

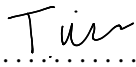
Reading Between the Lines: Modelling the Hydrogen Emission of T Tauri Stars

Thomas Josiah Garratt Wilson

Submitted by Thomas J. G. Wilson to the University of Exeter as a thesis for the degree of Doctor of Philosophy in Physics, September, 2022.

This thesis is available for Library use on the understanding that it is copyright material and that no quotation from the thesis may be published without proper acknowledgement.

I certify that all material in this thesis which is not my own work has been identified and that no material has previously been submitted and approved for the award of a degree by this or any other University.

Signed: 

Thomas J G. Wilson

Date: 13/09/2022.

Abstract

1st Supervisor: Prof. Sean Matt

2nd Supervisor: Prof. Tim Harries

T Tauri stars are young low-mass stellar objects. Studying how the progenitors of Sun-like stars form is vital to our understanding of stellar evolution and planetary formation. However, the mechanisms by which these stars accrete matter, power winds, and shed angular momentum remains elusive. Too distant and dim to probe with direct imaging or interferometry, the inner disks of T Tauri stars must be studied using spectroscopy. However, the atomic spectra of these stars are complex and highly variable. Radiative transfer modelling offers a powerful tool for understanding the physical processes that create T Tauri stars' enigmatic hydrogen emission lines.

In this thesis, I use the state-of-the-art radiative transfer code TORUS to explore synthetic T Tauri spectra. I present a detailed description of the radiative transfer code and the T Tauri model. Moreover, I develop and test a new polar stellar wind framework applicable to both axisymmetric and non-axisymmetric T Tauri simulations. In addition, I explore the effects of Stark and turbulent broadening. The optical and near-IR spectroscopy of 29 T Tauri stars is compared with a grid of synthetic line profiles created using TORUS . The archival T Tauri spectra, obtained with VLT/X-Shooter, provide simultaneous coverage of many optical and infrared hydrogen lines. The observations exhibit morphologies similar to those seen in other studies. The synthetic line profile grid was computed for the hydrogen transitions of $H\alpha$, $Pa\beta$, $Pa\gamma$, and $Br\gamma$ for a fiducial T Tauri model that included axisymmetric magnetospheric accretion and a polar stellar wind. Furthermore, I use the Reipurth classification scheme to study observed and synthetic profile morphology distributions.

I show that the modelled infrared lines are narrower than the observations by $\approx 80 \text{ km s}^{-1}$. In other words, the mean width of the synthetic lines is only ≈ 50 per cent of the observed mean width. Additionally, the models predict a significantly higher proportion (≈ 90 per cent) of inverse P-Cygni profiles. The radiative transfer models suggest that the frequency of P-Cygni profiles depends on the ratio of mass loss to mass accretion rates, and blue-shifted sub-continuum absorption is predicted for mass-loss

rates as low as $10^{-12} M_{\odot} \text{ yr}^{-1}$. Several modifications to the T Tauri models are explored, including the effects of rotation and turbulence on the synthetic hydrogen line profiles.

Finally, I present six 3D T Tauri models that include non-axisymmetric accretion flows and wind. For each model, line profiles are calculated at different azimuthal values, allowing me to study the rotational variability of the synthetic spectra. The models exhibit patterns of variability, correlation, and morphology, as seen in observations and previous theoretical studies. It was seen that non-axisymmetric accretion flows could reduce the frequency of inverse P-Cygni profiles and increase the HW10% of the infrared lines by $\approx 60 \text{ km s}^{-1}$. However, the width of both the infrared lines and H α increased simultaneously. Additionally, the 3D models predict trends in the variation of equivalent width and profile half-width that could be tested against T Tauri time-series spectroscopy.

The radiative transfer code developed in this work and the models presented in this thesis provide a modern foundation for future synthetic T Tauri line modelling. The models were shown to successfully reproduce the hydrogen line profile characteristics similar to those of T Tauri stars. Moreover, the radiative transfer modelling predicted trends in variability and profile morphology that observations could verify. However, this thesis also highlights several problems with the current models and discusses how future work may solve these obstacles so that radiative transfer modelling can be used effectively as an effective diagnostic tool for T Tauri systems.

Contents

List of Figures	6
List of Tables	8
Declaration	9
Acknowledgements	10
1 Introduction	11
1.1 Accretion and mass-loss process of T Tauri stars	13
1.2 Spectroscopic analysis of T Tauri stars	18
2 Radiative Transfer	22
2.1 Introduction to TORUS	23
2.2 Radiative transfer calculations	23
2.2.1 Statistical equilibrium	25
2.2.2 Synthetic line profiles	27
2.2.3 Stark broadening	31
2.3 T Tauri model	32
2.3.1 Accretion funnel	33
2.3.1.1 Accretion shock hot-spot	35
2.3.1.2 Accretion temperature	37
2.3.1.3 Photospheric continuum	37
2.3.1.4 Stellar wind	38
2.3.1.4.1 Wind density	39
2.3.1.4.2 Wind velocity	40
2.3.2 3D geometry	41
2.4 Model validation	45
2.4.1 Magnetospheric accretion only	45
2.4.2 Magnetosphere and stellar wind	47

3	Observations	50
3.1	X-Shooter instrument	51
3.2	X-Shooter data	52
3.2.1	Telluric corrections	53
3.2.2	Continuum and Gaussian fitting	55
3.3	Presentation of hydrogen spectra	56
3.3.1	Reipurth classification	61
3.3.2	Line profile characteristics	63
4	A Comparison of Synthetic and Observed Spectra	66
4.1	Synthetic line profile grid	66
4.2	Comparison of profile features	72
4.2.1	Reipurth classification	79
4.2.2	P-Cygni profiles	82
4.3	Modified T Tauri model	84
4.3.1	Turbulent line broadening	84
4.3.2	Rotational line broadening	86
4.3.3	Blue-shifted emission	90
4.4	Discussion	92
5	Non-Axisymmetric 3D Radiative Transfer	98
5.1	3D model geometry	100
5.2	Variability and morphology of 3D non-axisymmetric spectra	102
5.2.1	Quantitative analysis of the variability of time-series spectra	104
5.2.1.1	Accretion and temperature comparison	111
5.2.1.2	Geometry comparison	112
5.2.1.3	Mass-loss rate comparison	112
5.2.2	Correlation analysis of time-series spectra	113
5.3	Inverse P-Cygni profiles	115
5.4	Variability of the line profile widths	117
5.5	Discussion	120
6	Conclusions and Future Outlook	124
6.1	Future Outlook	128
	Bibliography	131
A	Atlas of Line Profiles from the Axisymmetric Accretion Models	136

B Spectral Variability Figures	146
C Auto-Correlation Maps	153

List of Figures

1.1	Cartoon of a T Tauri star	13
1.2	Magnetohydrodynamic T Tauri simulation	17
2.1	An overview of the capabilities of TORUS	24
2.2	Ray distribution	29
2.3	Datacube and spectrum from TORUS	31
2.4	A 3D density plot of the T Tauri model	33
2.5	T Tauri model diagram	34
2.6	Temperature, density, and velocity of the magnetosphere	36
2.7	Kurucz model atmospheres	39
2.8	Stellar wind β -law	42
2.9	Stellar wind velocity components	43
2.10	Offset magnetic dipole model	44
2.11	Comparison of radiative transfer models	46
2.12	Comparison of different wind models	48
3.1	X-Shooter echelle spectrum	52
3.2	Full X-Shooter spectra	55
3.3	Continuum and Gaussian Fitting	57
3.4	Hydrogen line correlation matrix	58
3.5	Spectra of T Tauri stars	59
3.6	Reipurth Classification of Observed Stars	63
3.7	Observed profile characteristics	64
4.1	Grid of synthetic models	69
4.2	Distribution of synthetic line centres	72
4.3	Convolution of synthetic spectra to observed resolution	73
4.4	Line profile best fit examples	74
4.5	Distribution of HW10% for different hydrogen transitions	76
4.6	FWHM versus HW10%	78
4.7	Ratio of Pa β to Br γ	80

4.8	Distribution of synthetic Reipurth types	81
4.9	Signal-to-noise ratios of the spectra	82
4.10	The fraction of P-Cygni profiles	83
4.11	The effect of turbulent broadening on the FWHM and HW10%.	85
4.12	Grid of turbulently broadened line profiles	87
4.13	The effect of rotation on the line profiles	89
4.14	Blue-side HW10%	93
5.1	A cartoon of the 3D accretion and wind model	100
5.2	H α images of the T Tauri model	102
5.3	Pa β images of the T Tauri model	103
5.4	3D non-axisymmetric line profiles	105
5.5	Variance of models	114
5.6	Auto-correlation maps	115
5.7	Inverse P-Cygni profiles versus phase	117
5.8	The HW10% at different phases	118
5.9	The change in HW10% and equivalent width versus phases	121
A.1	Atlas of the synthetic axisymmetric line profiles	137
B.1	Variance of the 3D models	147
C.1	Auto-correlation maps	153

List of Tables

3.1	The T Tauri stars	54
3.2	Stars classified as weak line T Tauri stars	61
3.3	Observed spectral line characteristics	65
4.1	Parameters of the grid of synthetic models	68
4.2	Best fit model parameters	75
4.3	Stellar rotation rates	91
4.4	Blue side HW10% differences	92
5.1	3D model parameters	101

Declaration

The work contained in Chapters [2](#), [3](#), and [4](#) incorporates research published in [Wilson et al. \(2022\)](#). The work was undertaken by myself with contributions from S. Matt, T. Harries, and G. Herczeg. The material in Chapter [5](#) is yet to be published.

Acknowledgements

First, I would like to acknowledge my supervisors, Sean Matt and Tim Harries, for their help and guidance in my work. Thank you for the inspiration and knowledge you gave me. I would also like to thank Gregory Herczeg for his council and valuable input into my research. Furthermore, I extend my gratitude to the whole AWESoMeStars team and the members of the Exeter Astrophysics Department for being such a friendly, supportive, and exciting group to work with.

The research contained in this thesis was made possible due to funding from the European Research Council (ERC) under the European Union's Horizon 2020 research and innovation program (grant agreement No. 682393; AWESoMeStars: Accretion, Winds, and Evolution of Spins and Magnetism of Stars; <http://empslocal.ex.ac.uk/AWESoMeStars>). My research has made use of the services of the ESO Science Archive Facility, including observations collected at the European Southern Observatory under ESO programme 084.C-1095(A). The simulations presented in this thesis made use of the University of Exeter High-Performance Computing (HPC) facility. I also made use of the SIMBAD database, operated at CDS, Strasbourg, France (Wenger et al. 2000). Furthermore, I would like to thank the developers of the Python packages Pandas (Reback et al. 2020) and Matplotlib (Hunter 2007) that I used extensively in this thesis for data analysis and presentation.

I owe tremendous gratitude to my parents. I could not have undertaken this journey without the incredible education, perspective, and thirst for knowledge you have given me since my earliest years. Thank you for the opportunities and wisdom you have gifted me.

Lastly, I'm immensely grateful to my partner, Diva Drissell. Not only for helping me proofread each chapter and teaching me how to use commas but also for always being there, supporting me and being patient in times of great stress.

Chapter 1

Introduction

*“Dwell on the beauty of life. Watch the stars,
and see yourself running with them.”*

Marcus Aurelius, ‘Meditations’.

Since our first ancestors, just under half of our existence has been spent living in the dark. The blackness of the sky and the sparks of light that appear each night to bejewel it have been a constant companion to all life on Earth. The stars of the night sky have played an intrinsic role in shaping our understanding of the world in which we exist. Before we knew what stars were, they provoked our imagination, inspiring our songs, stories, and beliefs. Early cultures identified stars with their gods and used their movements as prophecies of the future. Moreover, since ancient times, humans have been using the patterns and motion of stars to track the passage of time and to navigate across land and the ocean. The study of stars is one of the oldest sciences, which has its beginnings at the root of many cultures. Astronomy, in its modern form, is far removed from its ancient origins but still plays an integral role in our society. Not only does astronomy inspire us to look outwards, but it pushes the boundaries of science and technology. It gives us an insight into the immensity of the universe, entwining our view of Earth with the vastness and beauty of space. As astronomy has progressed, we have discovered many extraordinary phenomena; however, millennia on, the study of stars still provides us with intriguing discoveries that reveal secrets to our genesis.

Although stars are the most prominent and numerous objects observable in our sky, investigating them is a non-trivial problem. The difficulties arise from a disparity of scale. With terrestrial objects, we can generally poke things with a stick, look inside them, or watch them change over time. However, stars can live for billions of years, and the closest star to Earth, the Sun, is more than 150 million kilometres away. Therefore, we cannot observe a star over its entire lifetime to see how it changes and until very recently, when

the Parker Solar Probe dived through Sun's corona (Kasper et al. 2021), we had never poked one with a stick.

To overcome these challenges, astronomers analyse the star's movement, spectra, and neighbours to learn about their internal workings, and they use large samples of stars to piece together the different phases of their lives. For instance, the Sun is already over 4.5 billion years old. It is known to be in its main-sequence, a period characterised by the fusion of hydrogen into helium in the core, a phase that will last for approximately 10 billion years. In contrast, the pre-main-sequence evolution of Sun-like stars is brief, on the order of 10 million years, yet encompasses a broad range of physics that determines their future evolution. The time when these stars are free from an enshrouding cloud of debris and before they reach the main-sequence is only a few million years, making them rare to observe and, therefore, difficult to study. However, determining the mechanisms that govern the formation of young stars is pivotal to our understanding of the evolution of stars, their disks, and, ultimately, the formation of life-bearing planets such as the Earth.

The progenitors of Sun analogues are known as T Tauri stars and were originally defined by Joy (1945). T Tauri stars are low-mass $\lesssim 2 M_{\odot}$, young (~ 1 to 10 Myrs) pre-main-sequence stars that have strong magnetic fields (Johns-Krull 2007) on the order of a few kG. T Tauri stars are generally divided into two subgroups: classical T Tauri stars and weak line T Tauri stars. Classical T Tauri stars have an observed excess of infrared and ultraviolet continuum, and they show strong emission lines that can have complex kinematic profiles (Reipurth et al. 1996). Their continuum and line luminosity can be in excess of the photospheric luminosity and, furthermore, they display an enigmatic pattern of variability across the spectral regime (Hartmann et al. 2016). Weak line T Tauri stars have a similar age to classical T Tauri stars but show neither strong emission lines nor excess infrared emission. The strong hydrogen $H\alpha$ line, observed in classical T Tauri stars, correlates with the presence of an accretion disk; weak line T Tauri stars are thought to be not accreting.

For decades, the observed infrared excesses of T Tauri stars were taken as evidence for the presence of circumstellar disks (Mendoza V. 1968; Strom et al. 1989) and coronagraphic observations of T Tauri stars confirmed the presence of disk and outflows (e.g. Schneider et al. 2003). Furthermore, interferometric observations show the existence of a circumstellar disk around T Tauri stars, for example, Simon et al. (2000), and more recently, the survey by Anthonioz et al. (2015). However, the inner gaseous disk regions of T Tauri stars, where the dust is sublimated, are small ≈ 0.1 AU. Additionally, T Tauri stars are relatively faint, for example, in comparison to their larger counterparts, Herbig Ae/Be stars. Combined, the size and the brightness of T Tauri stars make interferometric observations of the inner disks challenging. Whilst modern interferometric observations

can probe the outer disk regions of T Tauri stars, for example, GW Orionis (Kraus et al. 2020), the inner disk regions and the processes of accretion are poorly constrained by observations.

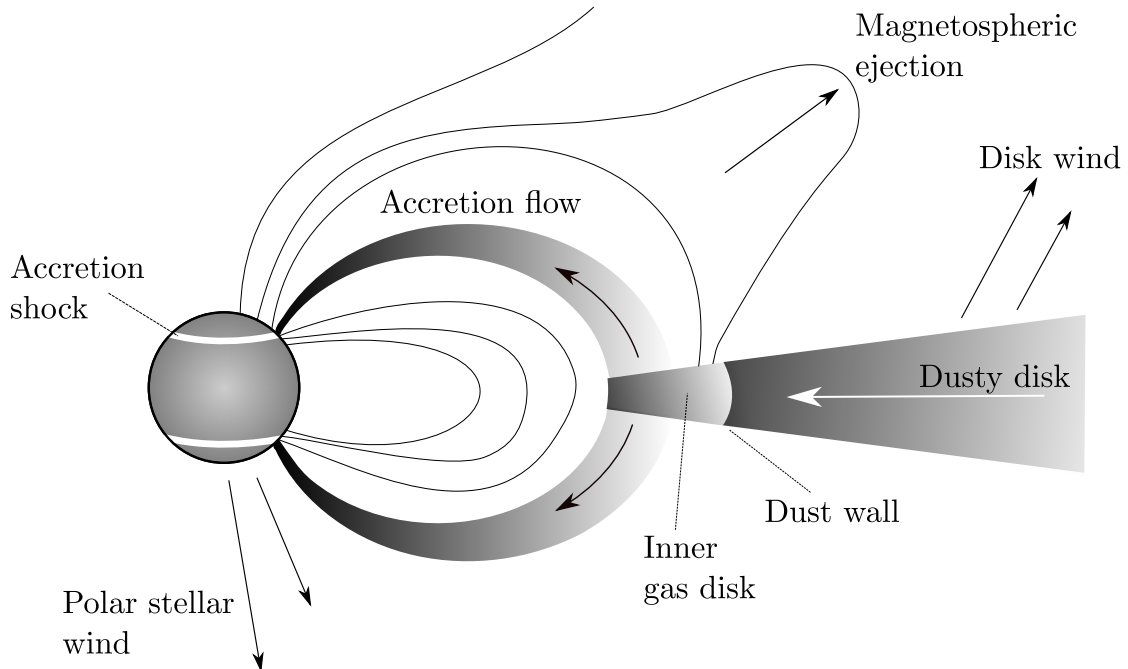


Figure 1.1: A cartoon of a T Tauri Star. The image shows the circumstellar disk, the magnetospheric accretion, and accretion shock zone. The possible mass outflows from the system are also marked. A magnetospheric ejection is indicated to be forming in an inflated magnetic field line.

1.1 Accretion and mass-loss process of T Tauri stars

The manner by which accreting matter moves from the disk to the stellar surface provides an interesting problem in T Tauri stars. The original disk-boundary layer model theorised that the accretion disk extended down to the star, where the material was rapidly decelerated, transferring angular momentum to the star (e.g. Hartmann et al. 1994). However, observations of T Tauri stars show that they are generally slow rotators (e.g. Bouvier et al. 2014). Therefore, there must be some mechanism to remove the angular momentum from the star, a process that is difficult to reconcile with the disk-boundary layer model. Furthermore, some of the observed spectra exhibit inverse P-Cygni features (e.g. Reipurth et al. 1996; Folha & Emerson 2001; Edwards et al. 1994); red-shifted sub-continuum absorption created by gas moving away from the observer, absorbing emission from beyond it. The boundary layer model cannot explain the broad high-velocity wings of the atomic spectra or the inverse P-Cygni profiles seen in some of the observed spectra.

Camenzind (1990) and Koenigl (1991) proposed that the accretion mechanism is similar to that of neutron stars, as theorised by Ghosh et al. (1977). In this formalism, known as magnetospheric accretion, the magnetic field truncates the disk at a radius R_{mi} , where the magnetic and material stresses are of the same order. The accreting material free-falls from the disk to the stellar surface along the magnetic field, creating an accretion column or funnel. The in-falling matter thermalises the kinetic energy as it impacts the stellar surface, forming a shock zone or “hot-spot”. The enormous energy release heats the gas to $\approx 10^6$ K and dissipates the energy as X-rays and extreme ultraviolet. The short-wavelength radiation is quickly reabsorbed in the optically thick accretion gas and re-emitted as longer wavelength radiation. This emission could be responsible for the high blue and UV excesses observed from T Tauri stars (e.g. see Muzerolle et al. 1998b; Hartmann et al. 2016, and references therein). The presence of an extended magnetosphere allows for mechanisms that transport angular momentum away from the star, which can help explain the observed slow T Tauri rotation (Bouvier et al. 2014). Furthermore, magnetospheric accretion can explain the inverse P-Cygni profiles. The accreting gas falling away from the observer at high velocity can absorb photospheric, continuum, and line emission from the star and magnetosphere.

Bouvier et al. (2007) firmly established the funnel-flow magnetospheric accretion paradigm as the generally accepted model for accretion in classical T Tauri stars. Blue-shifted sub-continuum absorption (the classical P-Cygni profile) is also observed and interpreted as evidence of the presence of mass outflows (e.g. Edwards et al. 2006; Kwan et al. 2007). Fig. 1.1 shows a cartoon depicting the standard model of T Tauri accretion and outflow. The figure shows the accreting disk, which sublimates from dust to gas at some radius. The magnetic fields of the star truncate the inner disk, and the gas free falls onto the star along the closed field lines. The figure points to three forms of mass outflow: stellar wind from the poles, disk wind, and magnetospheric ejections.

The truncation radius of the circumstellar disk is expected to be at the point where the magnetic and gas ram pressures roughly equate. For example, Koenigl (1991) theorised that the truncation radius R_{mi} of the disk would be where the magnetic stress is strong enough to remove the angular momentum of the Keplerian flow in a narrow region. This can be quantified as

$$R_{\text{mi}} = \frac{\beta \mu_*^{\frac{4}{7}}}{(2GM_*)^{\frac{1}{7}} \dot{M}_{\text{acc}}^{\frac{2}{7}}} \quad (1.1)$$

where μ_* is the magnetic dipole moment of the star, M_* and \dot{M}_{acc} are the mass of the star and the mass accretion rate of the disk, respectively. The parameter $\beta \lesssim 1$ is a proportionality coefficient that encapsulates effects such as the magnetic field geometry,

energy, and coupling to the disk. The material must be coupled to the magnetic field to truncate the disk. For instance, if the inner disk $\lesssim 0.1$ AU has a temperature of $\gtrsim 10^3$ K, then collisional ionisation should be sufficient to create a field-gas coupling (Koenigl 1991). For fiducial T Tauri values of $M_* = 0.5 M_\odot$, a stellar radius $R_* = 2 R_\odot$, and a magnetic field of $\approx 1 - 2$ kG, the truncation radius can be estimated to be $\approx 4 - 6 R_*$ at an accretion rate of $\dot{M}_{\text{acc}} = 10^{-8} M_\odot \text{ year}^{-1}$. Typical deduced T Tauri parameters and accretion rates lead to a truncation radii of $\sim 2-6 R_*$ (cf. Muzerolle et al. 2001; Hartmann et al. 2016).

The accreting matter will free fall from the truncation radius to the stellar surface, releasing the kinetic energy, which is assumed to radiate away. Calvet & Gullbring (1998) showed that the shock region forms near the photosphere, and the energy could be radiated away. Therefore, the excess luminosity from the accretion L_{acc} can be used to approximate the accretion rate of the star. The accretion rate can be determined from the accretion luminosity using the relationship (Calvet & Gullbring 1998)

$$L_{\text{acc}} = \frac{GM_*\dot{M}_{\text{acc}}}{R_*} \left(1 - \frac{R_*}{R_{\text{mi}}}\right). \quad (1.2)$$

During their evolution, the T Tauri star accretion rates are observed to be in the range of 10^{-9} to $10^{-7} M_\odot \text{ yr}^{-1}$ (Muzerolle et al. 2001). Material accreting from the disk will transfer angular momentum to the star, spinning it up. The spin-up torque on the star can be quantised as (Matt & Pudritz 2005b)

$$\tau_{\text{acc}} = \dot{M}_{\text{acc}} \sqrt{GM_* R_{\text{mi}}}. \quad (1.3)$$

Combined with the fact that the T Tauri stars are still contracting, the stars are expected to spin up to break-up velocities in $\sim 10^6$ yrs (Zanni & Ferreira 2009). However, T Tauri stars are generally slow rotators; a significant fraction of the stars have rotation rates of one to ten days, well below their rotation limit (Bouvier et al. 1993). Therefore, since the accretion and contraction processes are expected to spin up the T Tauri stars, and they are not usually observed to rotate near their break-up velocities, there must be an efficient mechanism by which the angular momentum is removed.

The process that brakes the rotation of T Tauri stars is still debated. Camenzind (1990) and Koenigl (1991) proposed that star-disk interactions could provide a spin-down torque. They suggested that the closed magnetic field lines threading the disk at radii greater than the corotation radius (where it is rotating slower than the star) exert a torque on the stellar surface, effectively braking its rotation. However, analytical and magnetohydrodynamic simulations show that the differential velocity between the star

and disk twists the magnetic fields, inflating them and opening the magnetosphere (e.g. [Uzdensky et al. 2002](#); [Matt & Pudritz 2005a](#)). This effect greatly reduces the spin-down torque efficiency of the extended magnetosphere (see [Ireland et al. 2021](#), and references therein). [Zanni & Ferreira \(2009\)](#) concluded that for their numerical example, the spin-down torque from the star-disk magnetic connection could only remove 10 per cent of the spin-up torque from the accretion.

Another mechanism for transporting angular momentum away from the stars arises from the opening and reconnecting of the magnetic field lines. This effect is caused by the inflation of magnetic fields induced by the difference in rotation velocities between the star and disk (e.g. [Zanni & Ferreira 2009](#); [Ireland et al. 2021](#)). The mechanism is known as magnetospheric ejections and can carry both angular momentum and mass away from the disk and the star. Magnetospheric ejections can provide a spin-up or spin-down torque depending on the relative location of the truncation and corotation radii. [Zanni & Ferreira \(2013\)](#) were able to show that for a mass-loss rate of 1–2 per cent of the accretion rate, magnetospheric ejections could balance 20–30 per cent of the accretion torque.

A further proposed mechanism to remove angular momentum is through the interaction of the magnetic field and a stellar wind (e.g. [Matt & Pudritz 2005b, 2008a](#)). Blue-shifted sub-continuum absorption (P-Cygni) features provide observational evidence of disk and stellar winds from T Tauri stars (e.g. [Edwards et al. 2003, 2006](#)). Typical mass outflow rates from T Tauri stars are on the order of $\sim 0.01 \dot{M}_{\text{acc}}$ ([Hartigan et al. 1995](#)), but can be as high as $\sim 0.2 \dot{M}_{\text{acc}}$ ([Cranmer 2008](#)). A stellar wind coupled to open magnetic field lines can produce a spin-down torque on the stellar surface.

As the star rotates, the wind is accelerated by the magnetic field, pushing it to rotate with the star, transporting angular momentum to the wind. [Matt & Pudritz \(2005b\)](#) characterised this stellar wind torque as

$$\tau_{\text{sw}} = -\kappa \dot{M}_{\text{sw}} \Omega_* R_A^2 \quad (1.4)$$

for a stellar wind mass-loss rate \dot{M}_{sw} and a stellar rotation rate Ω_* . κ is a dimensionless quantity that accounts for the geometry of the wind. The Alfvén radius R_A is the distance at which the wind velocity becomes super-Alfvénic. Beyond R_A , the magnetic interactions between the wind and the star are reduced. The spin-down torque from a stellar wind can be orders of magnitude greater than that provided by star-disk interactions (e.g. [Matt & Pudritz 2008b](#)).

However, [Matt & Pudritz \(2008b\)](#) showed that to balance accretion and wind torque, a mass-loss rate of ~ 10 per cent of the mass accretion rate is required. A mass-loss rate this high is difficult to achieve unless the wind is powered by a significant proportion

(~ 36 per cent) of the accretion power (Zanni & Ferreira 2009; Matt & Pudritz 2008b). Mass-loss rates of this size have been identified, but it is unclear what proportion of these winds originate from the star or disk (Matt & Pudritz 2008b). Furthermore, while there is a strong observed correlation between the accretion rate and the mass-loss rate, the

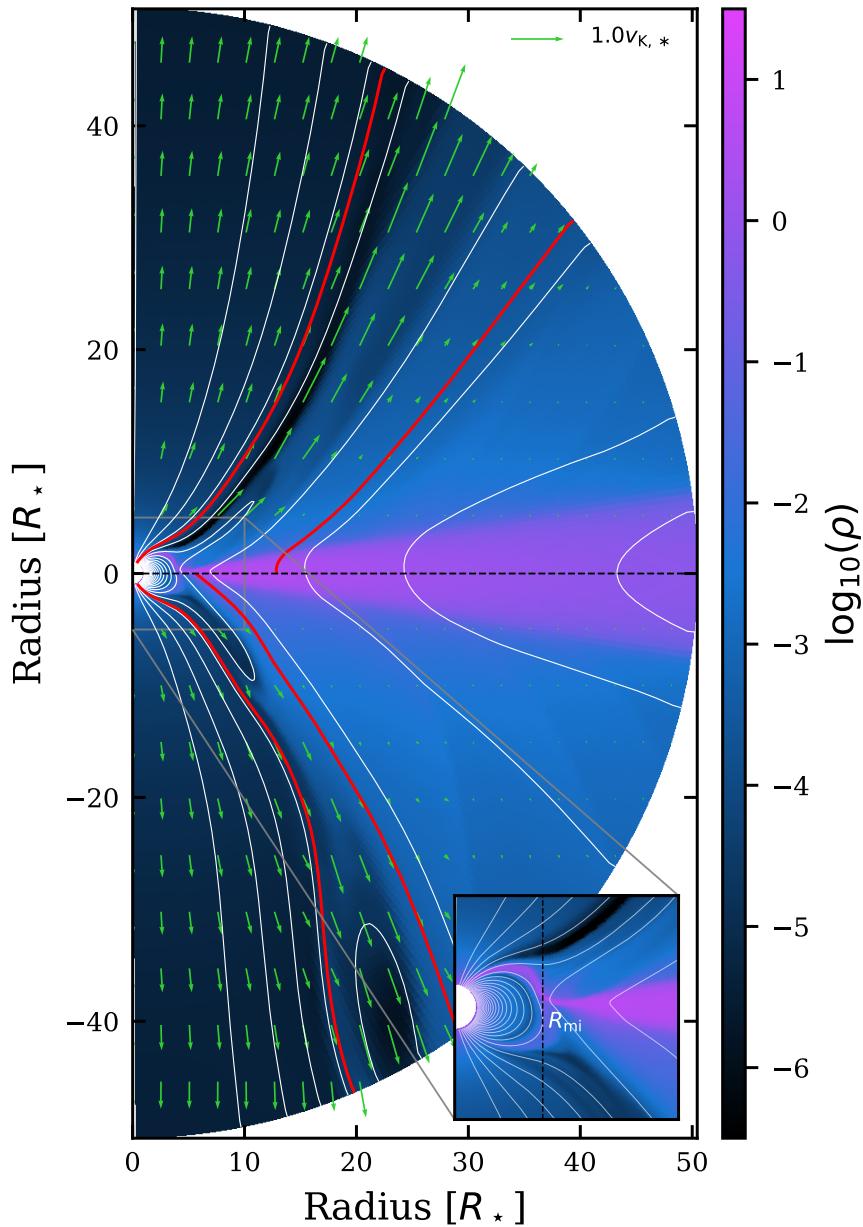


Figure 1.2: A logarithmic density colour map of a magnetohydrodynamic T Tauri model created from data produced by Ireland et al. (2021). The magnetic field is represented by the white lines. The red lines surround the area associated with magnetospheric ejections. The green arrows indicate the material velocity normalised by the Keplerian velocity. The magnified insert shows the magnetospheric accretion and the truncation radius $R_{mi} = 2.41 R_*$.

cause of this connection is debated. A limited amount of research has explored how the accretion energy could power a stellar wind. Cranmer (2008) and Cranmer (2009) showed that turbulent magnetic waves could work as a power transfer mechanism but could only achieve efficiency on the order of $\dot{M}_{\text{sw}}/\dot{M}_{\text{acc}} \approx 1$ per cent.

Fig. 1.2 shows a snapshot of a magnetohydrodynamic T Tauri model, created from the simulations of Ireland et al. (2021) and is representative of modern T Tauri magnetohydrodynamic simulations. The model shows a mass density map of an axisymmetric simulation of a T Tauri star. The white lines indicate the magnetic field lines, which near the star are closed and truncate the circumstellar disk, forming a magnetosphere. Despite the simulations being initialised with north-south symmetry, the accretion funnel predominantly prefers one hemisphere over the other, creating a non-axisymmetric magnetosphere. During the simulation run-time, the accretion funnel may remain in one hemisphere or switch as magnetic perturbations disturb it (Ireland et al. 2021, 2022). In Fig. 1.2, red boundary lines indicate the area corresponding to magnetospheric ejections. The figure shows magnetic field lines that are being stretched by the interaction of star and disk until they are disconnected and reconnected. The green arrows indicate the relative speed of the material in multiples of the star’s Keplerian velocity. Beyond a radius of $\sim 6 R_*$, the field lines threading the disk become open; in other words, they are stretched, effectively extending to infinity. A slow disk wind is seen flowing from the disk. Magnetocentrifugal forces may drive such a wind, accelerating matter along the open field lines where the angle between the disk and the field is less than 60° (Blandford & Payne 1982). Fig. 1.2 also shows a fast thermally driven stellar wind flowing from the poles of the star.

1.2 Spectroscopic analysis of T Tauri stars

Due to the physical size, distance, and brightness of T Tauri stars, direct and even interferometric observations of the inner disks remain challenging. Therefore, our understanding of the mechanisms of accretion and outflow in these stars must be inferred indirectly from alternative observations. One such observational metric is the analysis of atomic spectral lines associated with the release of accretion energy. The shock regions produce near X-ray, ultraviolet, optical, and infrared continuum emission. However, broad optical and infrared emission lines are most commonly associated with the extended magnetospheric accretion (Hartmann et al. 2016). The spectral lines contain the kinematic information required to understand these stars’ accretion and outflow processes. However, the observed spectra are complex, and disentangling the contributions from different T Tauri components is challenging. While extensive magnetohydrodynamic modelling of T Tauri stars has given valuable insight into the possible accretion and wind processes, better

observational diagnostics are needed to constrain the theory of T Tauri evolution. To do this, the radiative emission of these stars needs to be modelled to decipher the observed line profiles.

Complex radiative transfer models were first employed to study magnetospheric accretion in T Tauri stars by [Hartmann et al. \(1994\)](#). They used a two-level hydrogen model to show that magnetospheric accretion could explain the strong emission lines and blue excess of several T Tauri stars. [Muzerolle et al. \(1998b\)](#) further built on the T Tauri model of [Hartmann et al. \(1994\)](#) by using a 2D radiative transfer code that performed a multilevel statistical equilibrium calculation for eight hydrogen levels. They concluded that the Bry line profiles could be reproduced for embedded objects and that the Balmer line flux was consistent with observations. [Muzerolle et al. \(1998b, 2001\)](#) used radiative transfer simulations to constrain the temperature of the accretion column to the range 6000–10000 K and determined that Stark broadening may contribute to the observed broad H α wings (± 500 km s $^{-1}$). [Folha & Emerson \(2001\)](#) noted that the radiative transfer magnetospheric accretion models produced infrared lines (Paschen and Brackett) that were narrower than their observations by ≈ 100 km s $^{-1}$.

[Kurosawa et al. \(2006\)](#) introduced a disk wind and a polar stellar wind into their T Tauri radiative transfer simulations. They showed that the observed blue-shifted sub-continuum absorption profiles, interpreted as evidence of the presence of mass outflow (e.g. [Edwards et al. 2006](#); [Kwan et al. 2007](#)), could be reproduced by their wind models. Additionally, using wind and magnetospheric accretion models, [Kurosawa et al. \(2006\)](#) were able to produce the seven classical line profile classes defined by [Reipurth et al. \(1996\)](#). Furthermore, [Kurosawa et al. \(2011\)](#) showed that a bipolar stellar wind would produce broad P-Cygni absorption due to its high velocity and narrow P-Cygni absorption was the product of a slow disk wind. Both of these forms of P-Cygni profiles are observed (e.g. [Edwards et al. 2006](#)); although, it is not clear in which physical paradigms these outflow mechanisms are dominant or whether they coexist.

Another consideration for magnetospheric accretion is that the magnetic fields of T Tauri stars are never perfectly aligned with their poles (e.g. [McGinnis et al. 2020](#)). A magnetic obliquity will likely cause the accretion funnel to favour specific longitudes of the ascending nodes (e.g. [Espaillat et al. 2021](#)), restricting the azimuthal angle of the magnetosphere. A non-axisymmetric accretion funnel is likely to reduce the frequency of the observed inverse P-Cygni profiles and cause significant line and continuum variability as the hot-spots and accretion columns rotate with the star. [Symington et al. \(2005a\)](#) explored non-axisymmetric radiative transfer models and the rotational phase line variability. They showed that introducing a magnetic dipole offset induced greater line variability than was observed. [Kurosawa et al. \(2005\)](#) used similar models to compare synthetic spectra with

time series Pa β spectroscopy from SU Aurigae and were able to reproduce some of the observed velocity and equivalent width variability. Other studies have used magnetohydrodynamic models and post-processed them using radiative transfer simulations. For example, [Kurosawa et al. \(2008\)](#) and [Kurosawa & Romanova \(2012\)](#) successfully reproduced many of the commonly observed hydrogen line profiles and predicted similar line variability. Some studies have used magnetohydrodynamic models of stars with well-constrained stellar parameters to create radiative transfer models to study the observed emission. For instance, [Alencar et al. \(2012\)](#) successfully used a non-axisymmetric accretion model based on a magnetohydrodynamic simulation to perform a radiative transfer simulation of V2129 Oph* in H α and H β . Despite some similarities between the modelled emission and the observed spectroscopy, the authors could not reproduce the red-shifted absorption accurately.

Summary

T Tauri stars present an interesting problem in that their accretion and mass-outflow mechanisms remain elusive even with decades of observations and modelling. Modern radiative transfer simulations offer an opportunity to unlock the origins of the complex spectra. However, despite the relative success of radiative transfer studies, the T Tauri models still have multiple free parameters and chronic degeneracy. It is unclear how to disentangle the effects of geometry, accretion, and mass loss on the observed spectra. Consequently, although the evidence supports the magnetospheric paradigm, radiative transfer models need development. Therefore, while radiative transfer simulations can provide valuable insight into the spectra of T Tauri stars, there is still room for significant improvement of the models and their parameterisation.

The primary problems facing radiative transfer simulations are as follows. The constraints on the magnetospheric temperature and accretion rates are still vague because of a lack of a comprehensive theory for the heating of the accreting gas. Both stellar and disk winds have been modelled, but the dominant geometry, mass-loss rate, and temperature are still argued. [Folha & Emerson \(2001\)](#) noted that the synthetic infrared lines produced were too narrow. Furthermore, 3D radiative transfer simulations based on magnetohydrodynamic T Tauri simulations struggle to reproduce the observed red-shifted atomic line components. In this thesis, I use and develop a new generation of T Tauri models for the radiative transfer code TORUS, incorporating both polar stellar winds and an accelerated Monte Carlo processes. I explore a grid of synthetic hydrogen transitions using these models and compare them to the same atomic spectra from 29 T Tauri stars. The comparison aims to determine whether a range of accretion rates, mass-loss rates,

and temperatures based on observed parameters can reproduce the ensemble of observed T Tauri spectral characteristics.

This thesis aims to achieve two primary research goals. Firstly, I will scrutinise the radiative transfer T Tauri models presented in this thesis and consider possible modifications to improve the diagnostic capabilities via a comparison to observed spectra. Secondly, I will extend the 2D dimensional models to 3D and attempt to evaluate how non-axisymmetric accretion influences the spectral characteristics of the optical and infrared hydrogen lines. This research was undertaken to further the current theories on the evolution of Sun-like stars by improving T Tauri radiative transfer models.

In Chapter 2, the radiative transfer code TORUS (Harries et al. 2019) is presented and the new developments of the T Tauri model are described. Next, in Chapter 3, I reduce and show a set of hydrogen spectra from 29 T Tauri stars. Then, in Chapter 4, I examine the observed spectra in comparison to a grid of synthetic hydrogen line profiles produced using TORUS, focusing on the profile morphologies. Finally, in Chapter 5, I explore 3D non-axisymmetric T Tauri models and consider the rotational phase variability of the synthetic spectra.

Chapter 2

Radiative Transfer

Radiative transfer simulations attempt to reproduce the flow of electromagnetic energy through and around different media, the characterisation of which can reveal the complex physical process at play in the interaction of radiation and matter. Furthermore, it can be used to predict the observational characteristics of different theoretical physical phenomena. At the heart of these simulations is the radiative transfer equation,

$$\frac{dI_\nu}{d\tau_\nu} = S_\nu - I_\nu \quad (2.1)$$

where τ_ν is the optical depth of the medium at frequency ν . The specific intensity I_ν is the radiative energy flux per solid angle per frequency bandwidth, and S_ν is the source function, the ratio of the local absorption and emission coefficients. For all but the most simple systems, modelling the passage of light through a medium is a complex problem which has to be solved numerically (see [Steinacker et al. 2013](#)). The complexity of the system arises because the radiation field I_ν is coupled to the state of the medium S_ν by microphysical processes such as temperature, ionisation, and excitation. This coupling can be time-dependent and non-local due to the communication of physically distant regions via their radiation fields ([Harries et al. 2019](#)).

This chapter introduces the radiative transfer code TORUS in § 2.1 and discusses the theory behind the simulation of radiation around stars in § 2.2. The geometry and parameters of the T Tauri models used to create the synthetic spectra are discussed in § 2.3. Additionally, in § 2.4, we present two small grids of synthetic line profiles to validate the results of TORUS and our T Tauri model.

2.1 Introduction to TORUS

TORUS is a radiation transfer and radiation hydrodynamics code designed around the core tenet of flexibility. Originally written by Tim Harries, the code has been notably developed by Neil Symington, Ryuichi Kurosawa, Dave Acreman, and Tom Haworth. The core capabilities and programme flow are described in Fig. 2.1. The physical variables are stored in a grid structure. To balance efficiency with the accuracy of the solution, TORUS uses an adaptive mesh refinement (AMR) to vary spatial resolution in different computation domains. For example, areas of high optical depth, such as the T Tauri accretion funnel, require smaller grid cells to resolve accurately than the significantly less dense stellar wind that is far from the star. There are several physical processes that TORUS can simulate, including radiative dust equilibrium, radiative hydrodynamics, photoionisation, and statistical molecular and atomic equilibrium. The states of the radiation field I_ν and medium S_ν are then solved iteratively using either Monte Carlo photon packet tracing or ray tracing. TORUS can output several products, including Stokes intensity maps, spectral energy distributions (SED), and line spectra.

2.2 Radiative transfer calculations

TORUS has previously been used to model the emission from T Tauri stars (e.g. [Symington et al. 2005a](#); [Kurosawa et al. 2006, 2011](#)). However, the treatment of the radiation field that is used in this work has diverged significantly from prior versions. The latest exact integration method used to calculate the atomic (and molecular) statistical equilibrium is based on the accelerated Monte Carlo scheme developed by [Hogerheijde & van der Tak \(2000\)](#). This implementation was presented for molecular statistical equilibrium in TORUS by [Rundle et al. \(2010\)](#).

The original TORUS code calculated the atomic statistical equilibrium using the Sobolev approximation and geometric dilution based on the work of [Klein & Castor \(1978\)](#). The line profiles were then determined using traditional Monte Carlo radiative transfer. The Monte Carlo formalism uses photon packets originating from random positions (simulating the spontaneous emission) in the field that travel on random paths until they either escape the field or are absorbed. Other photon sources, such as stars and background radiation, are treated using separate photon packets. The passage of photon packets through a cell contributes to the local radiation field.

The accelerated Monte Carlo scheme of [Hogerheijde & van der Tak \(2000\)](#) is based on a cell-centric model, in which rays are propagated to random positions in a cell from random directions. Solving the radiative transfer equation along these rays to find the

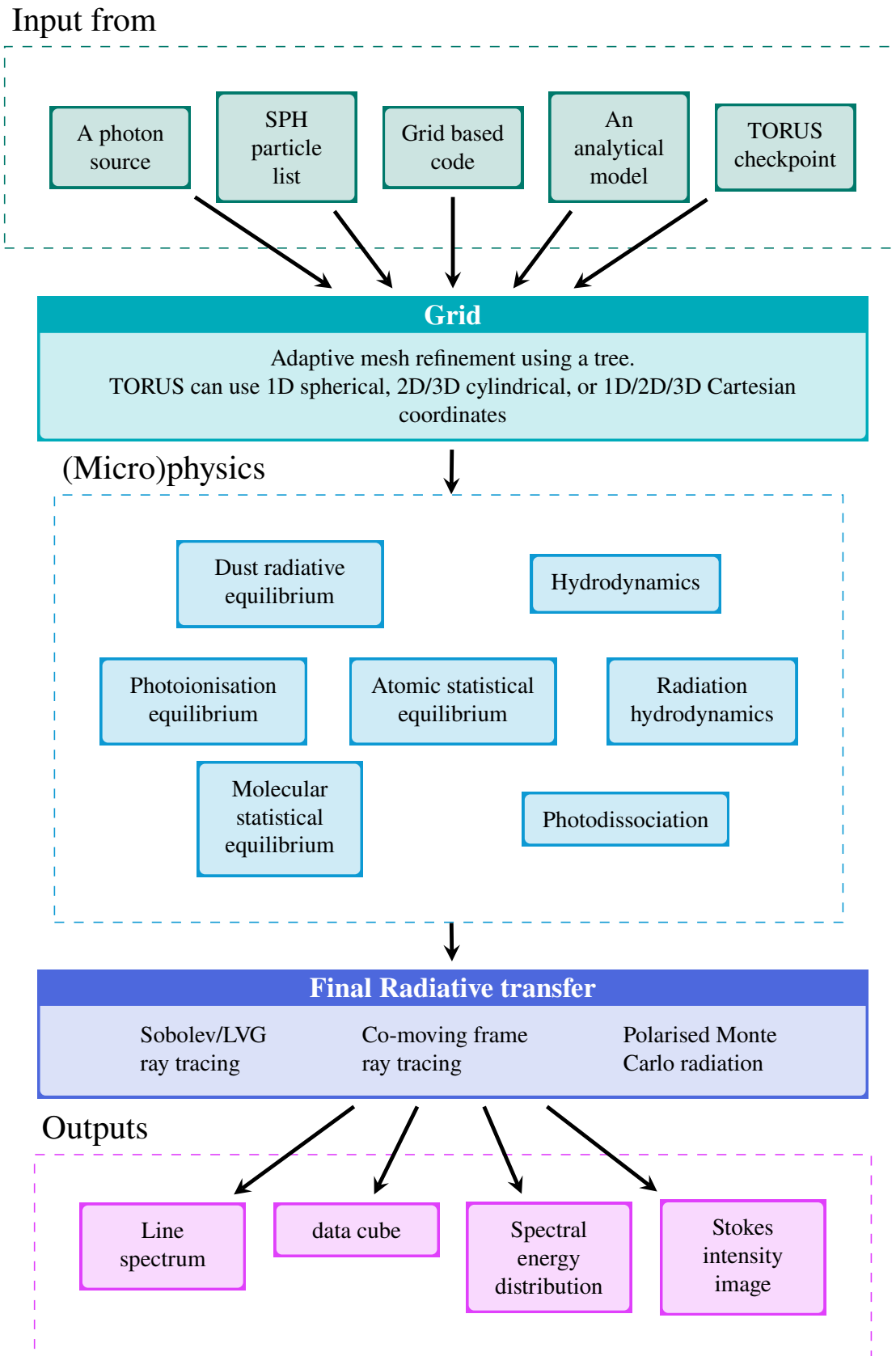


Figure 2.1: An overview of the capabilities of TORUS as described by Harries et al. (2019).

local radiation field accelerates the convergence of the simulation in areas of significant optical depth. In a full co-moving frame simulation, the rays are propagated from infinity or other intersection points (stars, disk, etc.) to the cell, the integrated radiation field along the rays is then used to calculate the statistical equilibrium. However, this is considerably computationally expensive and often the problem is simplified by using the Sobolev approximation (Sobolev 1957).

The Sobolev approximation works for a medium with large velocity gradients. It assumes that radiative interactions at any point are driven by the local vicinity due to the shift in the resonant frequencies of the emitting and absorbing atoms due to the velocity gradient (Grinin 2001). The Sobolev length or characteristic length s_0 of the local vicinity is given by the distance from a point such that the change in resonant frequency due to the velocity gradient is equal to the half-width of the spectral line profile given by the thermal or turbulent velocity v_t

$$s_0 = \frac{v_t}{|dv/ds|} \quad (2.2)$$

where dv/ds is the velocity gradient. If the velocity gradient is approximated as v/R , where R is the characteristic size of the system and v is the characteristic large-scale velocity, the Sobolev length can be estimated by $s_0 \approx R/(v/v_t)$.

The radiative transfer method used by TORUS in this thesis computes the line profiles in two stages. First, TORUS calculates the level populations using the Sobolev approximation and assuming statistical equilibrium. Second, TORUS computes the line profiles using full-frame co-moving ray tracing. This method is known as Sobolev with exact integration (SEI) (Harries et al. 2019).

2.2.1 Statistical equilibrium

TORUS calculates the level populations assuming the Sobolev approximation based on the method of Klein & Castor (1978). The electron energy level populations of the hydrogen atoms are solved for 15 levels, with 3 more held in local thermal equilibrium (LTE). The statistical equilibrium rate equation is a balance of R_l^L the net transition from the l^{th} level to lower levels, the transition from the l^{th} level to higher levels R_l^U , and the recombination and ionisation rates R_l^R and R_l^I , respectively. These components are balanced for each level, so that

$$R_l^L + R_l^U + R_l^R - R_l^I = 0. \quad (2.3)$$

Using the equations that define each term, the statistical equilibrium rate equation is as follows.

$$\begin{aligned}
 & \sum_{l < u} \left[N_l (B_{lu} \mathcal{J}_{lu} + N_e C_{lu}) - N_u (A_{ul} + B_{ul} \mathcal{J}_{lu} + N_e C_{ul}) \right] \\
 & + \sum_{l > u} \left[N_l (A_{lu} + B_{lu} \mathcal{J}_{lu} + N_e C_{lu}) - N_u (B_{ul} \mathcal{J}_{lu} + N_e C_{ul}) \right] \\
 & + N_u^* \left[\int_{\nu_u}^{\infty} \frac{4\pi}{h\nu} a_u(\nu) \left(\frac{2h\nu^3}{c^2} + J_\nu \right) \exp \left\{ \left(-\frac{h\nu}{k_B T_g} \right) \right\} d\nu + N_e C_{uk} \right] \\
 & - N_u \left[4\pi \int_{\nu_u}^{\infty} \frac{a_u(\nu)}{h\nu} J_\nu d\nu + N_e C_{uk} \right] = 0 \quad (2.4)
 \end{aligned}$$

where A_{lu} , B_{lu} are the Einstein coefficients and C_{lu} is the collision rate. N_u is the population of level u in statistical equilibrium and N_u^* the level population given by the Saha-Boltzmann equation for an electron density N_e and temperature T_g . J_ν is the angle average continuum mean intensity and term $a_u(\nu)$ refers to the photoionisation cross section of level u at frequency ν . The term k refers to the continuum state. The angle-averaged profile-weighted intensity of the radiation field in the line transitions between l and u is \mathcal{J}_{lu} and is determined using the Sobolev escape probability theory. \mathcal{J}_{lu} gives the probability that a photon is absorbed in the transition of $l \rightarrow u$ (Hubeny 2013) and for $l < u$ it is given by (cf. Harries et al. 2019; Kurosawa et al. 2011),

$$\mathcal{J}_{lu} = (1 - \beta_{lu}) \frac{2h\nu_{lu}^3}{c^2} \left[\frac{g_u N_l}{g_l N_u} - 1 \right]^{-1} + \beta_{c,lu} I_{c,lu}. \quad (2.5)$$

Here, g represents the level degeneracy, $I_{c,lu}$ the line frequency continuum intensity, and the variables β_{lu} and $\beta_{c,lu}$ are the Sobolev escape probabilities given by the expressions

$$\beta_{lu} = \frac{1}{4\pi} \oint_{4\pi} \frac{1 - e^{-\tau_{lu}}}{\tau_{lu}} d\Omega, \quad (2.6)$$

and

$$\beta_{c,lu} = \int_{\Omega_{\text{disk}}} \frac{1 - e^{-\tau_{lu}}}{\tau_{lu}} d\Omega. \quad (2.7)$$

The continuum escape probability $\beta_{c,lu}$ is calculated by integrating the Sobolev optical depth τ_{lu} across the solid angle subtended by the stellar photosphere Ω_{disk} , see § 2.3.1.3. The Sobolev optical depth for a velocity field \mathbf{v} projected along the unit vector \mathbf{n} is given by

$$\tau_{lu}(\mathbf{n}) = \frac{\pi e^2}{m_e c} (g_l f_{lu}) \frac{1}{v \mathbf{n} \cdot \nabla \mathbf{v}} \left(\frac{N_l}{g_l} - \frac{N_u}{g_u} \right). \quad (2.8)$$

Where m_e and e are the electron mass and charge, respectively. f_{lu} is the oscillator strength of the line transition. Only hydrogen is assumed to be present, so the electron density is $N_e = N(\text{H})^+$. Thus, the conservation equation is

$$\sum_{n=1}^{n_{\max}} N_n + \sum_{n=n_{\max}}^{n_{\max}+3} N_n^* + N(\text{H})^+ = \frac{\rho}{m_{\text{H}}}. \quad (2.9)$$

The above equations of statistical equilibrium are solved iteratively using a Newton-Raphson scheme on a cell-by-cell basis, assuming the starting conditions are either an LTE solution or a set of non-LTE solutions from a nearby cell. For each cell, a set of 1024 rays are generated that have randomly assigned frequencies, origins within the cell, and directions that are biased towards the photosphere. The total continuum intensity is summed along these rays to determine the local mean intensity. This has the advantage over the original [Klein & Castor \(1978\)](#) method of geometric dilution of photospheric flux, in that it can account for continuum attenuation by the intervening material in the mesh. The solution is taken to be converged when the level populations of more than 95% of the grid cells have a fractional change of less than 0.01% between iterations.

2.2.2 Synthetic line profiles

Once the level populations have been calculated (§ 2.2.1), TORUS can compute synthetic observations to model how the system will appear to the observer. Synthetic observations created in this thesis by TORUS are in the form of position-position-velocity (PPV) datacubes containing spectral and spatial information. The synthetic line profiles are calculated using full-frame co-moving ray tracing, which allows for pressure broadening of the lines and is better suited to dealing with regions of high optical depth when scattering is not significant. For atomic statistical equilibrium, TORUS does not account for scattering or Stokes intensities, and only the total intensity is considered. Pressure broadening is traditionally considered important because T Tauri Balmer lines can have wings that extend up to $\pm 500 \text{ km s}^{-1}$ (e.g. [Edwards et al. 1994](#)). These broad wings are hard to achieve with model geometry alone and may be the result of Stark broadening ([Muzerolle et al. 1998b, 2001](#)), see § 2.2.3.

TORUS creates the PPV datacubes using co-moving full frame ray tracing and further details can be found in [Harries et al. \(2019\)](#). To do this, a grid of bins is created, analogous to the pixels of a CCD. The number of bins and the position of the grid (distance, inclination, and angle around the midplane) are determined by the user. From each bin, a series of rays are generated that sample the AMR mesh. The total radiation flux at a frequency ν (or velocity) is integrated along these rays to obtain the observed flux.

TORUS generates multiple grids at discrete frequency intervals to build a PPV data cube. For a ray with path t , the total specific intensity I_ν at a frequency ν can be defined in terms of optical depth τ_ν to be

$$I_\nu = I_0 e^{-\tau_\infty} + \int_0^{\tau_\infty} S_\nu(\tau'_\nu) e^{-\tau'_\nu} d\tau'_\nu. \quad (2.10)$$

Here, I_0 is the boundary intensity, τ_∞ is the total optical depth along the ray and S_ν is the source function of the medium. The value of the initial boundary intensity I_0 depends on the intersection point of the path. If the ray hits the stellar photosphere, the value is computed from the Kurucz (1979) model atmosphere (§ 2.3.1.3). If the ray intersects with the accretion hotspot, the intensity is a sum of the model atmosphere intensity and the intensity given by a Planck function for a hot spot temperature of T_{hs} . Otherwise, if the ray intersects the disk or exits the simulation space, then $I_0 = 0$. Continuum emission from the disk is not considered in the models presented in this these, therefore, I_0 at the disk is zero.

The ray tracing starts from the defined data cube position-position-velocity bin (the observer) and moves across the AMR mesh until it exits the other side or hits something, for example, the photosphere or the accretion disk. As the integration progresses along the ray, the total optical depth τ_{total} between the current point and the observer is calculated. For a path segment ds , the optical depth along it is

$$d\tau_\nu = \int \phi_\nu \kappa_\nu ds \quad (2.11)$$

where κ_ν is the local transition-specific absorption coefficient. ϕ_ν is the line profile and is discussed in more detail below. The change across ds is then

$$I_\nu^{\text{new}} = I_\nu^{\text{old}} + S_\nu \left(1 - e^{-d\tau_\nu}\right) e^{-\tau_{\text{total}}}, \quad (2.12)$$

where the source function is the ratio of local emission j_ν and absorption,

$$S_\nu = \frac{j_\nu}{\kappa_\nu}. \quad (2.13)$$

The emission and absorption coefficients are calculated from the local-level populations by

$$j_\nu = \frac{h}{4\pi} \cdot A\nu_{lu} N_u \quad (2.14)$$

and

$$\kappa_\nu = \frac{h}{4\pi} \cdot (N_l B_{lu} - N_u B_{ul}), \quad (2.15)$$

where A and B are the Einstein coefficients.

Initially, each cell of the AMR mesh is divided into two ray segments, but this number doubles if $d\tau_\nu > 0.1$ and $d\tau_\nu < 20$. Furthermore, if the velocity gradient across the cell would cause the line resonance to be traversed or ν is close to the line resonance, the number of segments is set to 20.

The emission and absorption coefficients are affected by the local velocity, as a change in relative velocity could Doppler shift the line into resonance. This effect is contained within the line profile function ϕ_ν . If the intrinsic line broadening is negligible, then the profile is defined by thermal Doppler broadening and ϕ_ν is a Gaussian profile. For optically thick lines such as $H\alpha$, pressure broadening becomes important and a normalised Voigt profile is adopted, which is a convolution of a Gaussian and a Lorentzian (cf. [Vernazza et al. 1973a](#)). The Voigt profile is given as $\phi_\nu = \pi^{-1/2}H(a, y)$ where

$$H(a, y) \equiv \frac{a}{\pi} \int_{-\infty}^{\infty} \frac{e^{-y'^2}}{(y - y')^2 + a^2} dy' . \quad (2.16)$$

Here, $y = (\nu - \nu_0) / \Delta\nu_D$, $y' = (\nu' - \nu_0) / \Delta\nu_D$ and $a = \frac{\Gamma}{4\pi\Delta\nu_D}$ where ν_0 is the line centre frequency. $\Delta\nu_D$ is the Doppler linewidth of hydrogen given by

$$\Delta\nu_D = \frac{\nu_0}{c} \sqrt{\frac{2TK_B}{m_H} + v_{\text{turb}}^2} \quad (2.17)$$

here m_H is the hydrogen mass and v_{turb}^2 is the turbulent broadening factor ([de la Cruz Rodríguez & van Noort 2017](#)), set to zero for part of the present study. The damping constant Γ is discussed in § 2.2.3.

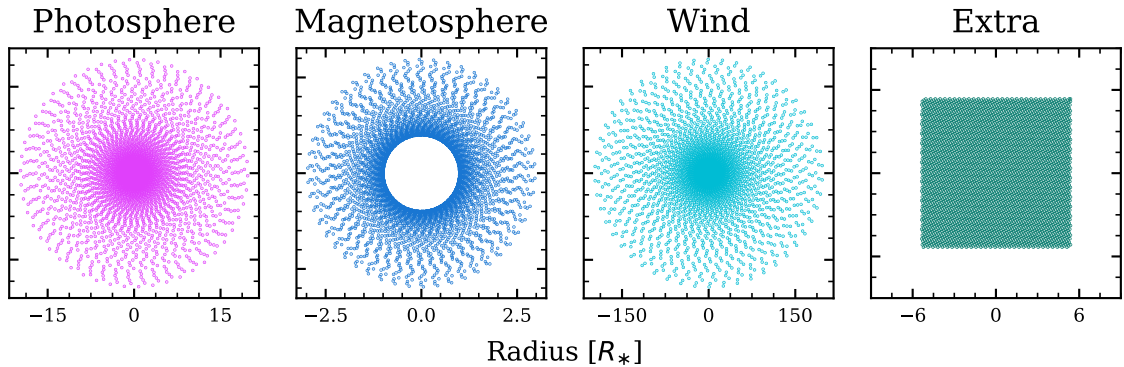


Figure 2.2: The distribution rays used in to calculate the line profiles. Note the aspect of the y-axis and x-axis are equal.

TORUS uses a set of rays that sample the photosphere, magnetosphere, and stellar wind. The rays are uniformly distributed radially and a random offset is applied to

the azimuthal distribution. Fig. 2.2 shows a typical arrangement of rays sampling the photosphere, magnetosphere, and stellar wind. For instance, the models presented in Chapter 4.2 used a total of 270000 rays spread over the 250×250 spatial bins; 10000 for the photosphere arranged with 100 radial points and 50 azimuthal points within a radius of $\leq R_*$ and another 100×50 rays between R_* and $20R_*$. The magnetosphere and wind have 100×50 rays each, and a further four rays per bin of the datacube frame are added to fill in any gaps in the coverage.

When TORUS uses the SEI method, it spends most of the computation time calculating the outputs. For example, the mean computer uptimes for the models presented in Chapter 4 were ≈ 12 min to determine level populations and ≈ 40 min to calculate a single data cube with 300 velocity bins and 250×250 spatial bins. For these datacubes, TORUS used 100 cores spread over five to six nodes with MPI parallelisation.

The datacubes output by TORUS contain position-position-wavelength flux maps centred around the central wavelength. Using the Doppler relationship, the wavelength λ axis can be converted to velocity v relative to the central wavelength λ_0 ,

$$v = \frac{c}{\lambda_0} (\lambda - \lambda_0). \quad (2.18)$$

By summing the total intensities of each position-position frame of the datacube and plotting this against the frame velocity, a spectral density plot can be created. This is demonstrated in Fig. 2.3, which shows a series of eight compound datacube frames and the spectrum they create. The original datacube had 400 wavelength bins, and the figure shows eight frames, which are compound images of 80 wavelength bins. The figure also shows the spectrum (or line profile) created from the datacube, and the contribution of the frames shown to the line profile. The line profile is plotted as the continuum-normalised flux versus relative velocity. The flux is normalised by the first wavelength frame of the datacube, which is assumed to be at the continuum level. Care was therefore taken to ensure the full extent of the line profiles were covered by the wavelength range of the datacubes, and the initial frames did not have any line emission in them.

Because the T Tauri models used in this work contain large velocity fields, the radiation field contains complex emission and absorption components from different areas of the mesh. For example, in Fig. 2.3, in frames two and three, the hot spot and star are obscured by the stellar wind moving towards the observer. The wind absorbs the emission and creates the blue-shifted sub-continuum absorption feature (P-Cygni profile) seen in the spectrum.

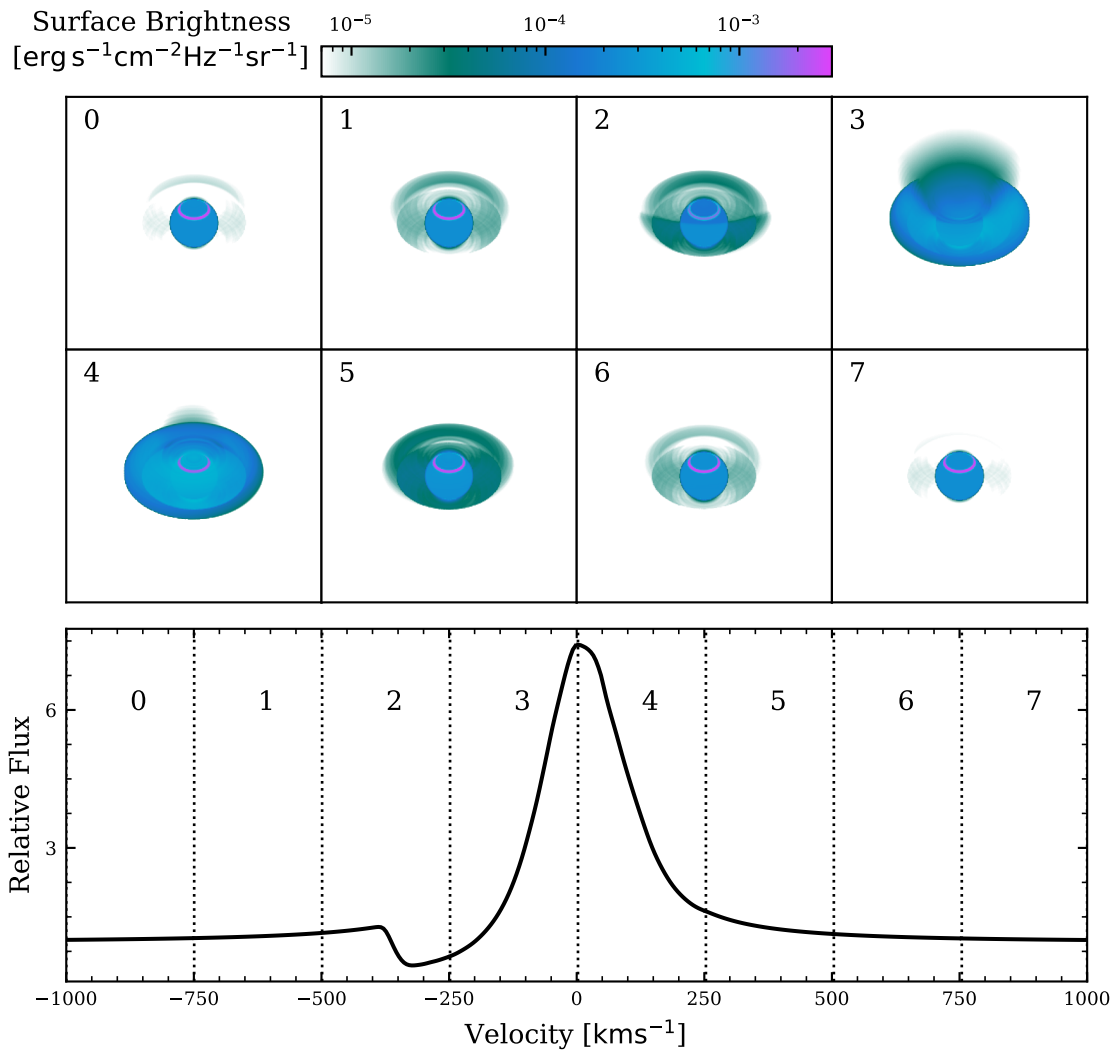


Figure 2.3: The top 8 frames are compound images of 80 wavelength bins from TORUS datacube centred around $\text{H}\alpha$. The colour scale indicates the $\text{H}\alpha$ flux, the brightest emission originates from the accretion hot-spot. The bottom subplot shows the line profile created from the datacube. The numbers correspond to the datacube frames and indicate their contribution to the spectrum.

2.2.3 Stark broadening

Stark broadening is caused by the local electric microfield of the plasma that perturbs the emission and absorption frequencies of the atomic energy levels. It is believed that Stark broadening is important for modelling hydrogen Balmer lines (Muzerolle et al. 1998b, 2001). Stark broadening is incorporated into the line transfer equations using the damping constant Γ , such that

$$\Gamma = C_{\text{rad}} + C_{\text{vdW}} \left(\frac{N_{\text{HI}}}{10^{16}} \right) \left(\frac{T}{5000} \right)^{0.3} + C_{\text{stark}} \left(\frac{N_{\text{e}}}{10^{12}} \right)^{\xi} \quad (2.19)$$

where C_{rad} , C_{vdW} , and C_{stark} are the radiative, van der Waals, and Stark broadening half-widths. N_{HI} is the neutral hydrogen density and T is the gas temperature in Kelvin. For $\text{H}\alpha$, the following broadening parameters were adopted from [Luttermoser & Johnson \(1992\)](#) $C_{\text{rad}} = 8.2 \times 10^{-3} \text{ \AA}$, $C_{\text{vdW}} = 5.5 \times 10^{-3} \text{ \AA}$, and $C_{\text{stark}} = 1.47 \times 10^{-2} \text{ \AA}$. ξ is the stark broadening type, [Kurosawa et al. \(2006\)](#) used a non-linear stark broadening, where $\xi = 2/3$. However, according to [Griem \(1964\)](#) and [Vernazza et al. \(1973b\)](#) hydrogen exhibits a linear Stark broadening $\xi = 1$. Therefore, in this thesis, we adopt the approach of [Luttermoser & Johnson \(1992\)](#); [Kurosawa et al. \(2011\)](#) and [Vernazza et al. \(1981\)](#) and use linear Stark broadening.

Stark broadening has a significant impact on the $\text{H}\alpha$ line widths at high accretion rates and funnel flow temperatures; see § 2.4. For lines other than $\text{H}\alpha$, I explored two methods to determine the Stark Broadening coefficients. Firstly, I determined the approximate line half-widths using the analytical solution proposed by [Sutton \(1978\)](#). Secondly, I used the extended Stark broadening tables of [Lemke \(1997\)](#) to calculate the half-widths of the hydrogen lines. For the infrared lines ($\text{Pa}\gamma$, $\text{Pa}\beta$, and $\text{Br}\gamma$), I concluded that the Stark broadening had a negligible effect on the synthetic line profiles. The dominant broadening effects come from the large velocity fields of the T Tauri model.

2.3 T Tauri model

TORUS uses an adaptive mesh refinement (AMR) system to create a numerical grid that represents the physical space of the simulation (see Fig. 2.4). The majority of the models presented in this work use a 2.5D coordinate system that is axisymmetric around the pole. However, TORUS can also use a 3D geometry for non-axisymmetric models, see § 2.3.2 and Chapter 5. The 2.5D geometry is defined using a 2D density field and a 3D velocity field. The third component is calculated symmetrically for a given azimuthal angle.

The T Tauri model populates the mesh with a star, an accretion flow, and a stellar wind; see Fig. 2.5. The disk used in our model is assumed to be geometrically thin and optically thick, any rays that intersect it are terminated at the disk, and $I_0 = 0$. The density, temperature, and velocity fields are defined as outlined in § 2.3.1 and § 2.3.1.4. The star, located at its origin, is defined by its radius R_* , mass M_* , and effective temperature T_{eff} . The coarseness of the grid with dimensions N is refined so that it starts with N^2 cells, which are split so that each cell contains a mass of $\leq 10^{10}$ g. The cells are subdivided no more than 10 times. The total size of the simulation space was set to be a 3D cylindrical mesh with a height and radius of 400×10^{10} cm (0.27 AU).

Fig. 2.4 shows a 3D density plot of the T Tauri model. A disk is illustrated; however, this is purely artistic and is included to indicate the position. In the simulation, the disk

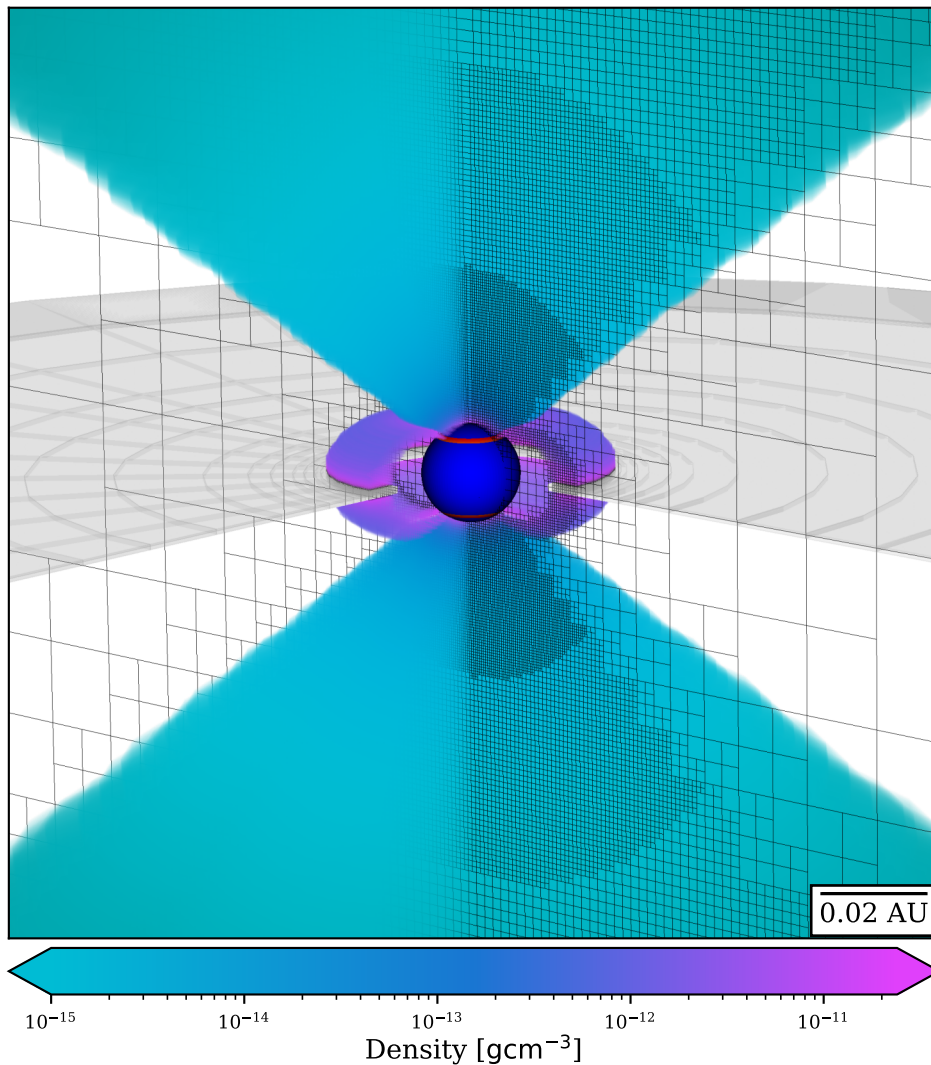


Figure 2.4: A 3D density plot of the T Tauri model, showing the density of the magnetosphere and the stellar wind. Note, the density colour scale applies purely to the magnetosphere and stellar wind. The accretion hot-spot highlighted in red on the surface of the star. A slice of the mesh is shown to illustrate the AMR system.

does not have any physical height or density. The colour of the star indicates the surface temperature, and the accretion hot-spot can be clearly seen. A slice of the AMR mesh is also displayed, which illustrates how the AMR system creates a finer grid for the higher-density regions of the magnetosphere and wind. Fig. 2.5 is a diagram of the model and the physical parameters used to define the geometry of the T Tauri model.

2.3.1 Accretion funnel

Magnetospheric accretion is the theory that the material accreting from the circumstellar disk to the star follows the magnetic field lines of the T Tauri star. The idea was first

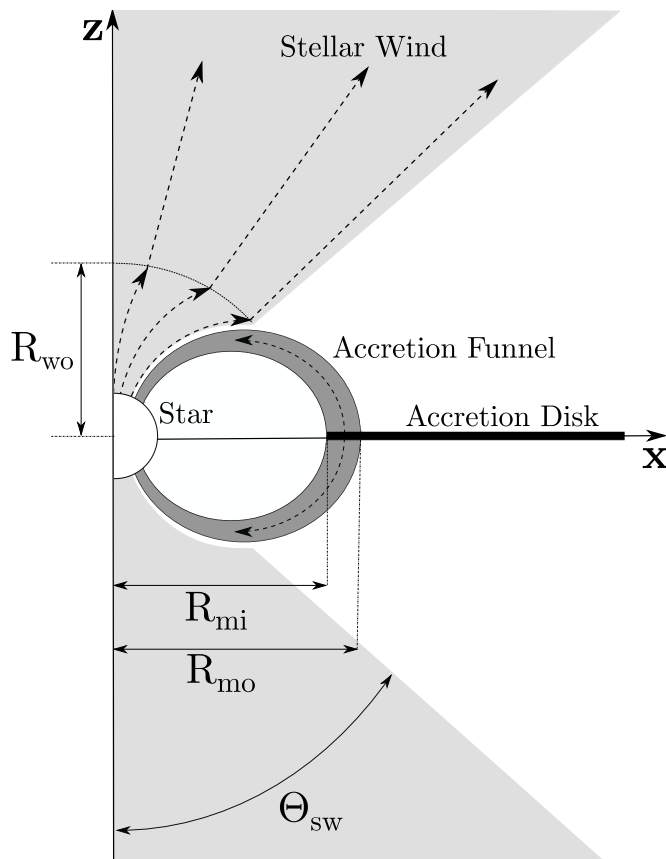


Figure 2.5: Diagram of the T Tauri Magnetospheric accretion model. The shaded regions indicate the areas populated with hydrogen in the TORUS model. Not to scale.

proposed by [Camenzind \(1990\)](#) and [Koenigl \(1991\)](#), based on the mechanism developed by [Ghosh et al. \(1977\)](#) for accretion around neutron stars. However, observational evidence of magnetospheric accretion was reported prior to the development of these concepts (e.g. [Bertout & Bouvier 1988](#)). In this formalism, the magnetic field truncates the accretion disk at some radius R_{mi} where the material and magnetic stresses balance each other. In the case of an axially aligned dipole field, the accreting material is lifted from the disk and free flows onto the star, sandwiched between two dipole field lines (see Fig. 2.5). In this thesis, we used the geometry of the accretion flow as described by [Hartmann et al. \(1994\)](#). MHD simulations predict a twisting of the magnetic field (e.g. [Uzdensky et al. 2002](#)) due to differential velocities between the star and disk; however, for simplicity, the magnetic field in our model is purely poloidal. The accreting matter flows freely along the field lines under gravitational acceleration. Where the accretion funnel impacts the star's surface, it creates a shock region known as the hot-spot.

The accretion funnel follows the magnetic dipole streamline given by

$$r = R_0 \sin^2(\theta) \quad (2.20)$$

where R_0 is the radius at the equator of the streamline that intersects the stellar surface at colatitude θ . The component of the poloidal magnetic field at radius r is

$$B_p(r, \theta) = \mu r^{-3} \sqrt{4 - 3 \sin^2(\theta)} \quad (2.21)$$

where μ is the magnetic dipole moment. Finding the unit vector of B_p and converting to Cartesian coordinates gives the components of the accretion flow unit vector

$$\hat{\mathbf{v}}_{\mathbf{p}} = \frac{1}{\sqrt{4 - 3 \sin^2 \theta}} \left(3 \sin(\theta) \sqrt{1 - \sin^2 \theta} \hat{\mathbf{x}} + (2 - 3 \sin^2 \theta) \hat{\mathbf{z}} \right). \quad (2.22)$$

The flow speed at r is calculated from the change in potential energy,

$$v_p(r, \theta) = \sqrt{2GM_* \left(\frac{1}{R_*} - \frac{\sin^2 \theta}{r} \right)}, \quad (2.23)$$

where R_* is the stellar radius. The velocity of the flow is $\mathbf{v}_{\mathbf{p}} = v_p \hat{\mathbf{v}}_{\mathbf{p}}$. For an accretion rate \dot{M}_{acc} the density at radius r is given to be (cf. [Hartmann et al. 1994](#))

$$\rho(r) = \frac{\dot{M}_{\text{acc}}}{4\pi(1/R_{mi} - 1/R_{mo})} \frac{r^{-5/2} \sqrt{4 - 3 \sin^2 \theta}}{\sqrt{2GM_*} \sqrt{1 - \sin^2 \theta}} \quad (2.24)$$

The velocity and density profiles can be seen in Fig. 2.6. In the figure, the density, velocity, and temperature (see § 2.3.1.2) are plotted for four field lines following the form of equation 2.20. The lines are a little uneven at lower radii because the values are lifted directly from the mesh without interpolation. The density is initially high, but as the material accelerates, the density rapidly decreases and then it begins to increase again as the field lines constrict the flow.

2.3.1.1 Accretion shock hot-spot

The hot-spot temperature T_{hs} is calculated from the potential energy liberated by the accreting material. The surface of the star is divided into a grid, each with its own SED, for which a [Kurucz \(1979\)](#) model atmosphere is used (see § 2.3.1.3). If a source grid cell coincides with the accretion funnel, the mass flux is determined from the AMR cells directly adjacent. The mass flux \dot{M}_{cell} , accretion velocity v , and the cell area A_{cell} can be used to determine the cell temperature,

$$T_{\text{hs}} = \left[\frac{v^2 \dot{M}_{\text{cell}}}{2\sigma A_{\text{cell}}} \right]^{\frac{1}{4}}, \quad (2.25)$$

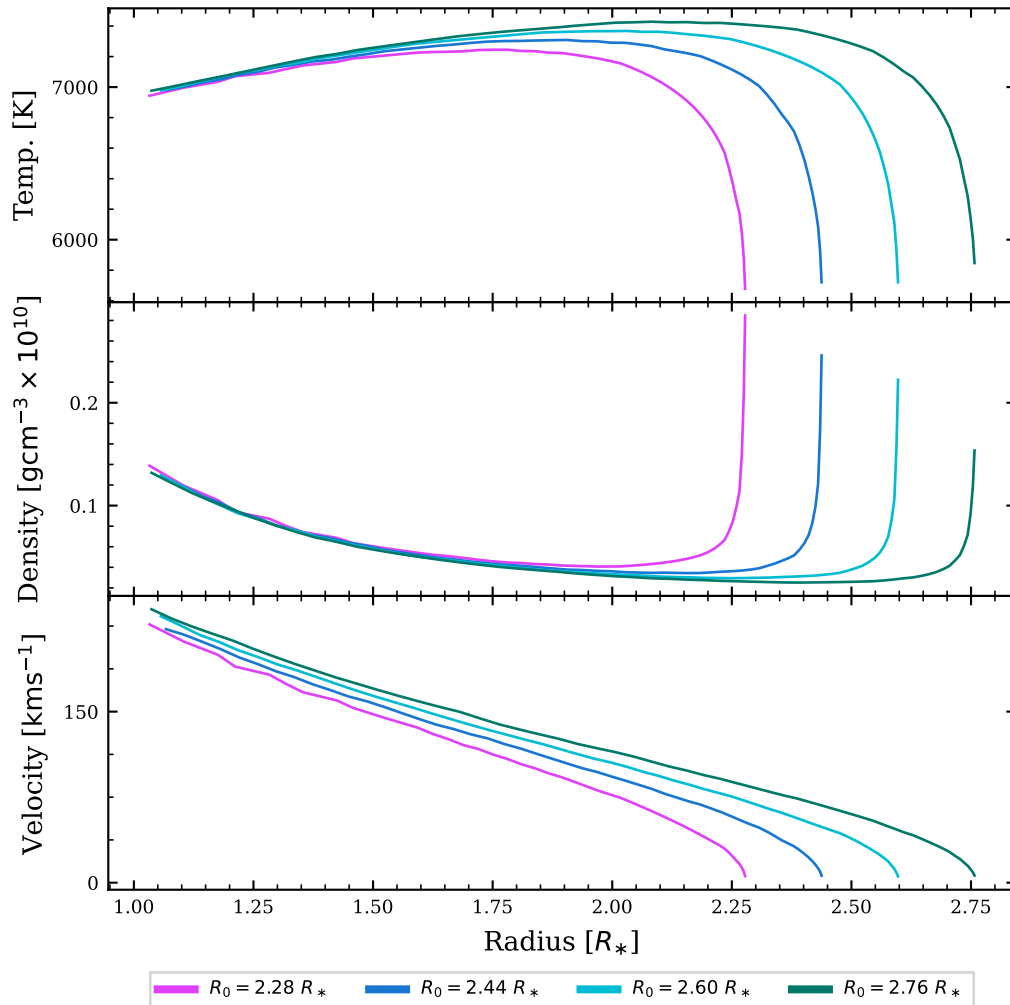


Figure 2.6: The three panels show the magnetospheric temperature (top), density (middle), and velocity (bottom) along four dipole field lines. The data is extracted from a TORUS mesh with a maximum accretion temperature of 7500 K and an accretion rate of $\log \dot{M}_{\text{acc}} = -7$. The wobbles in the lines are artefacts of the numerical grid.

here σ is the Stefan–Boltzmann constant. The temperature is used to determine a black-body SED, which is added to the photospheric SED. For example, in the instance of a star with a mass of $0.5 M_{\odot}$, a radius of $2 R_{\odot}$, and with accreting material falling from a distance of $3 R_*$ to the stellar surface intersecting at angle of 55° with accretion rates of $\dot{M}_{\text{acc}} = 10^{-7}$, 10^{-8} , and $10^{-9} M_{\odot} \text{yr}^{-1}$, the hotspot temperatures will be $T_{\text{hs}} \approx 6780$, 3810, and 2140 K, respectively.

By using a blackbody, it is assumed that the line emission and absorption from the hot spot are negligible. The model assumes that the energy radiated away from the shock zone is quickly reabsorbed in the optically thick accretion gas and re-emitted at longer wavelengths, as characterised by [Calvet & Gullbring \(1998\)](#). The accretion regions are

also expected to have line emission (e.g. [Dodin 2018](#)) that will contribute to the observed spectra; however, we neglect this due to the lack of available models. A complete radiative equilibrium treatment of the shock region and magnetosphere is necessary to fully constrain this effect.

2.3.1.2 Accretion temperature

The synthetic emission lines are very sensitive to the temperature distribution in the accretion funnel. However, the magnetospheric heating mechanisms are poorly understood, although it is assumed that they are magnetically driven; for instance, by the dissipation of Alfvén waves. The self-consistent thermal model produced by [Martin \(1996\)](#) used adiabatic compression to heat the accretion columns. However, [Muzerolle et al. \(1998b\)](#) showed that the model could not produce line profiles consistent with observations. Thus, the temperature is provided as an input parameter and the code does not solve for radiative equilibrium.

The temperature profiles adopted for this work are based on those used by [Hartmann et al. \(1994\)](#), who created a temperature structure using a volumetric heating rate $\propto r^{-3}$. The dissipation of Alfvén waves from inhomogeneous accretion could, for example, cause this heating rate. A schematic radiative cooling rate is used to balance the heating. The temperature structure used in our models is interpolated and scaled from the values given in fig. 6 of [Hartmann et al. \(1994\)](#). More details on heating and cooling rates can be found in [Hartmann et al. \(1982\)](#). The profiles are scaled by an input parameter of the maximum temperature in the accretion flow T_{acc} . A temperature profile from a TORUS model with $T_{\text{acc}} = 7500$ K is shown in Fig. 2.6. As gas falls towards the star from the disk, the temperature rapidly increases as the density decreases and then begins to get cooler as the field lines constrict and the density increases. The temperature drops near the disk and the star because the increase in density enhances the radiative cooling.

Without a self-consistent model of the accretion heating mechanism, the model can only be indicative of the temperature distribution. [Muzerolle et al. \(2001\)](#) further constrained these models by determining the range of T_{acc} that creates realistic line profiles for different accretion rates. Furthermore, in the words of L. Hartmann,

“our approach is merited if the adoption of a smooth, plausible temperature distribution results in line profiles which agree with observations” ([Hartmann et al. 1994](#))

2.3.1.3 Photospheric continuum

The photospheric continuum radiation from the star is calculated by interpolating the model atmospheres of [Kurucz \(1979\)](#). The [Kurucz \(1979\)](#) model atmospheres are com-

puted for a broad range of effective temperatures and stellar gravities, from a statistical distribution of nearly a million atomic lines. TORUS interpolates between the nearest models to determine an atmosphere that fits the input stellar parameters. Fig. 2.7 shows seven different models for a temperature range of 3500 – 6000 K and surface gravity of $\log(g_*/\text{cms}^{-2}) = 3.5$ which is close to the fiducial stellar gravity used in our models of $\log(g/\text{cms}^{-2}) = 3.53$. The locations of the primary hydrogen lines ($\text{H}\alpha$, $\text{Pa}\beta$, $\text{Pa}\gamma$, and $\text{Br}\gamma$) studied in this work are highlighted by the grey bars. The effective temperature of the fiducial star is 4000 K (see Chapter 4.1), at this temperature there is no significant continuum absorption or emission near the $\text{H}\alpha$, $\text{Pa}\beta$, $\text{Pa}\gamma$, and $\text{Br}\gamma$ hydrogen lines. However, at temperatures of 5000 K and above, there begins to be significant absorption present for the $\text{H}\alpha$, $\text{Pa}\beta$, $\text{Pa}\gamma$, and $\text{Br}\gamma$ transitions.

It is assumed that radiation from the high-temperature T_{hs} shock region created by the magnetosphere is absorbed and re-emitted by the cooler surrounding gas. As such, the hot-spot emission is treated simply as an addition to the continuum emission. See § 2.3.1 for a further discussion of the shock region. The continuum emission at a frequency ν from the hot-spot is calculated as the sum of the Kurucz model atmosphere and the blackbody spectral radiance $I_{\nu,\text{hs}}$ given by

$$I_{\nu,\text{hs}}(\nu, T_{\text{hs}}) = \frac{2h\nu^3}{c^2} \frac{1}{e^{\frac{h\nu}{k_{\text{B}}T_{\text{hs}}}} - 1}, \quad (2.26)$$

here, the terms have their usual meanings.

2.3.1.4 Stellar wind

We implemented a new stellar wind in TORUS that builds on the work by Kurosawa et al. (2011). Their model used a radial stellar wind launched from a spherical cap above the stellar surface so that a large opening angle could be achieved without interacting with the accretion funnel. However, the densest and radiatively significant part of the stellar wind should be closest to the star. The new wind geometry presented in this thesis, launches the outflow from the stellar surface, specifically, from the polar regions at latitudes higher than the accretion hot-spot. The wind and the accretion funnel do not intersect because the wind follows the dipole magnetic field lines until it reaches a specified opening angle Θ_{sw} , at which point the wind becomes radial (see Fig. 2.5). The parameterisation of Θ_{sw} automatically determines the radius R_{wo} where the wind transitions from following the dipole lines to becoming radial. This geometry approximates the wind behaviour observed in MHD simulations (e.g. Zanni & Ferreira 2009; Kurosawa & Romanova 2012; Ireland et al. 2021). Similarly to previous studies (e.g. Kurosawa et al. 2006, 2011), the wind is

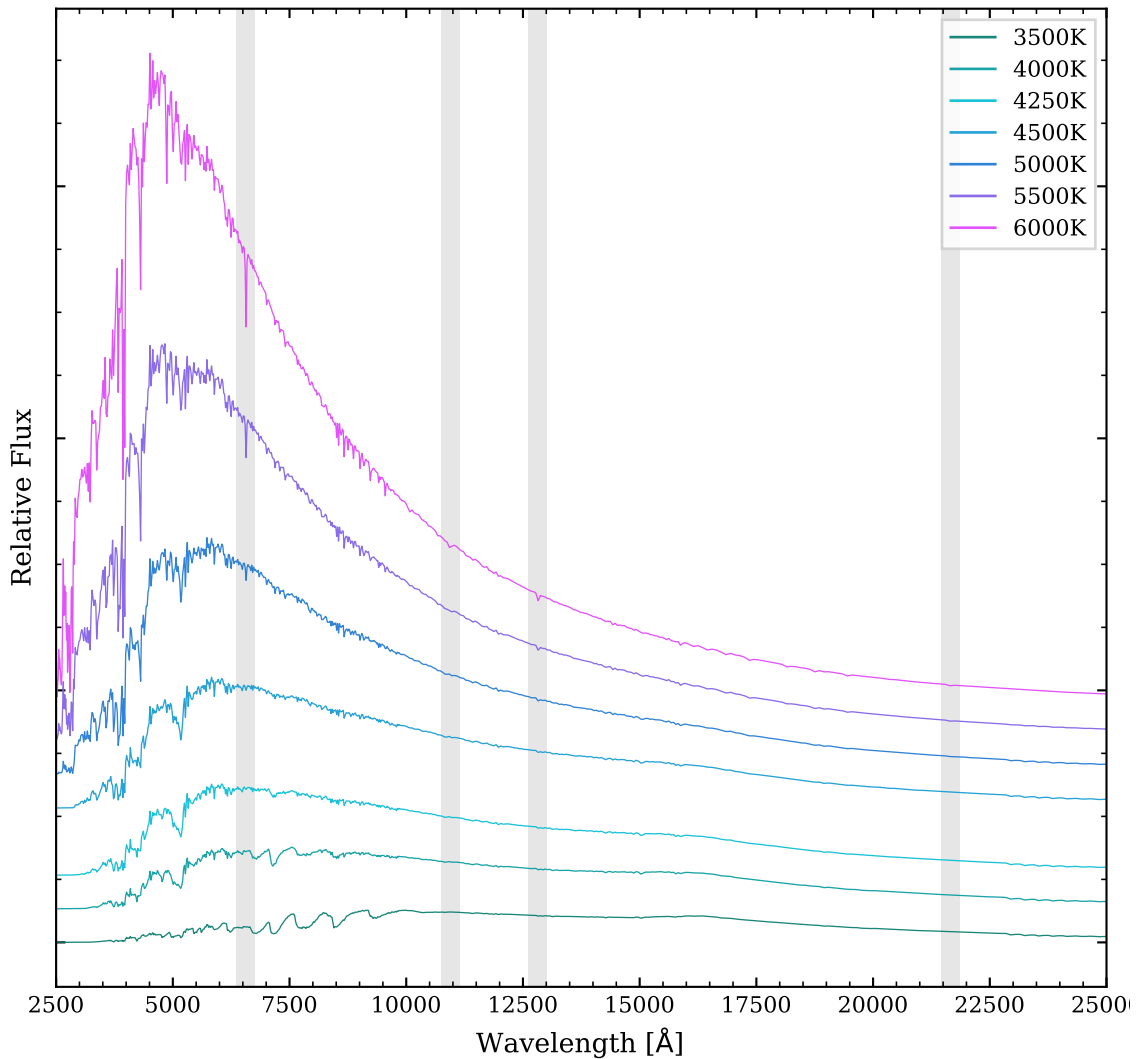


Figure 2.7: Kurucz (1979) model atmospheres for a surface gravity of $\log(g_*/\text{cms}^{-2}) = 3.5$ and seven different temperatures close to fiducial effective temperature used in Chapter 4. The vertical grey bars indicate the position of the four hydrogen lines ($H\alpha$, $Pa\gamma$, $Pa\beta$, and $Br\gamma$) studied in Chapter 3 and Chapter 4.

assumed to be isothermal and uses a β -law velocity profile.

2.3.1.4.1 Wind density

The density of the stellar wind is determined from the wind mass-loss rate \dot{M}_{sw} , a parameter set at run time. The density of the wind ρ_{sw} is proportional to $\dot{M}_{sw}/(v_{sw,r}A(r))$ where $A(r)$ is the surface at radius r through which the wind is moving with a radial velocity of $v_{sw,r}$. The area through which the wind is moving at a radius r depends on if the wind is moving with the magnetic field or flowing radially from the star. In the range $R_* < r \leq R_{wO}$, the wind is assumed to be contained within a diverging flux tube. The

field strength of a magnetic dipole diverges at a rate of $1/r^3$. Accordingly, the density is given by,

$$\rho_{sw}(r) = \frac{1}{2} \frac{\dot{M}_{sw}}{v_{sw,r} A_*} \left(\frac{R_*}{r} \right)^3 \quad (2.27)$$

where A_* is the surface area of the star from which the wind is launched. For radii greater than R_{wo} , the surface area $A(r)$ increases as a spherical cap (radial flow) with increasing radius. Hence,

$$A(r) = 2\pi r^2 (1 - \cos \Theta_{\text{open}}) \quad (2.28)$$

and so the density decrease is given by,

$$\rho_{sw}(r) = \frac{1}{2} \frac{\dot{M}_{sw}}{v_{sw,r} A_{wo}} \left(\frac{R_{wo}}{r} \right)^2. \quad (2.29)$$

Here, A_{wo} is the area of the spherical cap with radius R_{wo} . The value R_{wo} is the radius at which the wind velocity becomes radial such that

$$R_{wo} = \alpha (R_{mo} + \delta) \sin^2 \Theta_{\text{open}}. \quad (2.30)$$

The terms δ and α are input parameters that allow the wind coupling region to be adjusted. By default, these values are set to zero and unity, respectively. It should be noted, that while value R_{wo} is analogous to the Alfvén radius, R_{wo} is set solely by the geometry of the wind and magnetosphere and it is not based on the physical parameters of the Alfvén radius.

2.3.1.4.2 Wind velocity

The wind velocity v_{sw} is composed of two components: the poloidal velocity v_{pol} and the toroidal velocity v_{tor} . The most commonly used parameterization of poloidal wind velocity is the so-called β -law (cf. [Castor & Lamers 1979](#)). The β -law gives the magnitude of the poloidal component of the stellar wind velocity at a radius r to be

$$v_{\text{pol}}(r) = v_{\text{min}} + (v_{\text{max}} - v_{\text{min}}) \left(1 - \frac{R_*}{r} \right)^\beta \quad (2.31)$$

where v_{min} and v_{max} are the starting and end velocities of the wind. The free parameter β determines the steepness or acceleration of the wind. To obtain a physical grounding for the wind velocity, we used an MHD radial wind velocity profile (L. G. Ireland, personal communication, 5 March 2020), from [Ireland et al. \(2021\)](#) to fit equation 2.31. The MHD model had parameters similar to those of the fiducial radiative transfer model

with a truncation radius $R_{mi} = 2.41 R_{\odot}$. A least-squares regression fit was used to fit equation 2.31 to the MHD velocity profile. The lower bound of $v_{\min} = 1 \text{ km s}^{-1}$ was forced to match the launch velocity of the MHD wind. The fit was made using the PYTHON module `scipy.optimize.curve_fit`. This determined that a value of $\beta = 2.98$ best suited the MHD velocity profile. In comparison, Kurosawa et al. (2011) used a value of $\beta = 0.5$ for their wind models.

Fig. 2.8 shows the MHD velocity profile and the best fit. The fitted line closely resembles the MHD model velocity, which suggests that, although, the β -law is a relatively simple approach, it is an appropriate approximation for our model. The figure shows the difference in velocity and density profiles for $\beta = 0.5$ and $\beta = 2.89$. The higher β value produces a wind that accelerates slower, which creates a denser wind closer to the stellar surface. This dense wind close to the stellar surface will allow for greater absorption of the star's continuum and hot-spot emission.

The toroidal velocity component is derived from the star's rotation rate at the colatitude of wind launch. It assumes that the wind and magnetic field are perfectly coupled, and that the wind corotates as a rigid body with the star out to the wind corotation radius R_{wo} . Beyond this, the wind conserves the angular momentum and the toroidal component of the velocity decreases proportionally to $1/r$.

Fig. 2.9 shows the wind's poloidal, toroidal, and total velocity components along with the total velocity magnitude. The components shown here are for a star with a mass of $0.5 M_{\odot}$ and a radius of $2 R_{\odot}$ with an equatorial rotation rate of 40.2 km s^{-1} , which is approximately 15% of the stars breakup velocity. Additionally, Fig. 2.9 shows three images that display the wind velocity for x-y positions around the star. The star is located in the top left of each frame and the individual frames show the poloidal, toroidal, and magnitude of the velocity. The colour displays the wind velocity around the star assuming there is no magnetosphere. It can be seen that the poloidal component dominates the wind velocity magnitude apart from at radii close to the star. Even then, the largest toroidal effect is seen at high colatitude, an area that is mostly filled by the magnetosphere. The toroidal velocity has a more significant effect once the rotation rate is upped to $\approx 50\%$ of the break up velocity. Rotation and the effect it has on the synthetic line profiles are discussed further in Chapter 4.

2.3.2 3D geometry

The T Tauri model presented in § 2.3 can also be extended to full 3D simulations in TORUS. This enables us to create synthetic spectra from non-axisymmetric models. For example, this is useful for modelling a magnetosphere that does not fully extend around

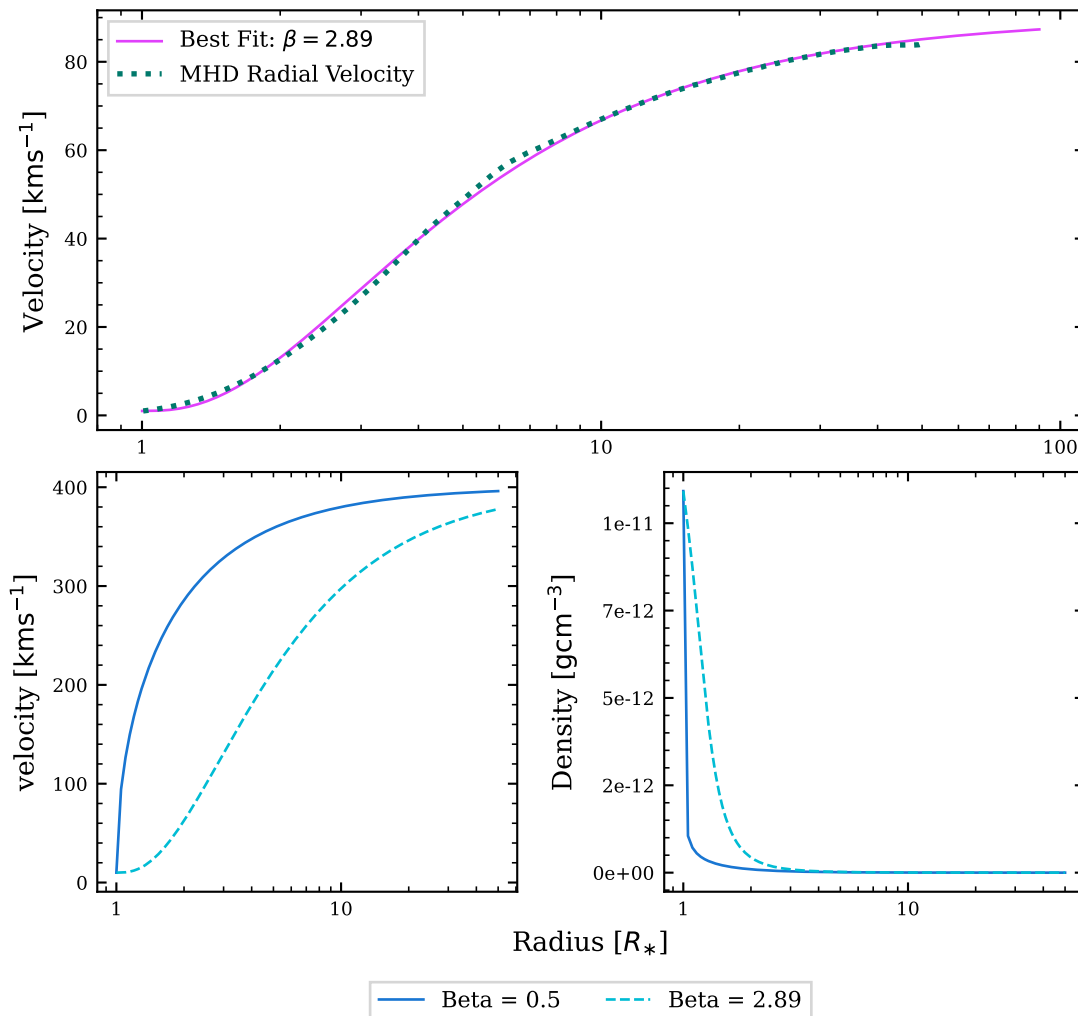


Figure 2.8: The top panel shows the fit of the velocity β -law, equation 2.31 and a wind velocity profile from an MHD simulation. A value of $\beta = 2.89$ was determined to be good match using a least-squares regression fit. The lower two panels shows the difference in velocity and density between beta values of $\beta = 2.89$ and $\beta = 0.5$, the latter being the value adopted by Kurosawa et al. (2011).

the star. This is a potentially likely scenario because the magnetic fields of T Tauri stars are rarely aligned with their poles (e.g. McGinnis et al. 2020). In the case of the magnetic dipole being offset from the rotation axis, the accreting matter will preferentially flow in half of each alternate hemisphere (e.g. Long et al. 2011). Moreover, the axisymmetric MHD simulations of Ireland et al. (2021) show that the magnetospheric flow tends to prefer one hemisphere and may change as permutations of the magnetic field develop. The dominance of accretion in one hemisphere in an axisymmetric MHD model can be seen in Fig. 1.2.

The T Tauri model is extended to 3D in TORUS by building the density, temperature,

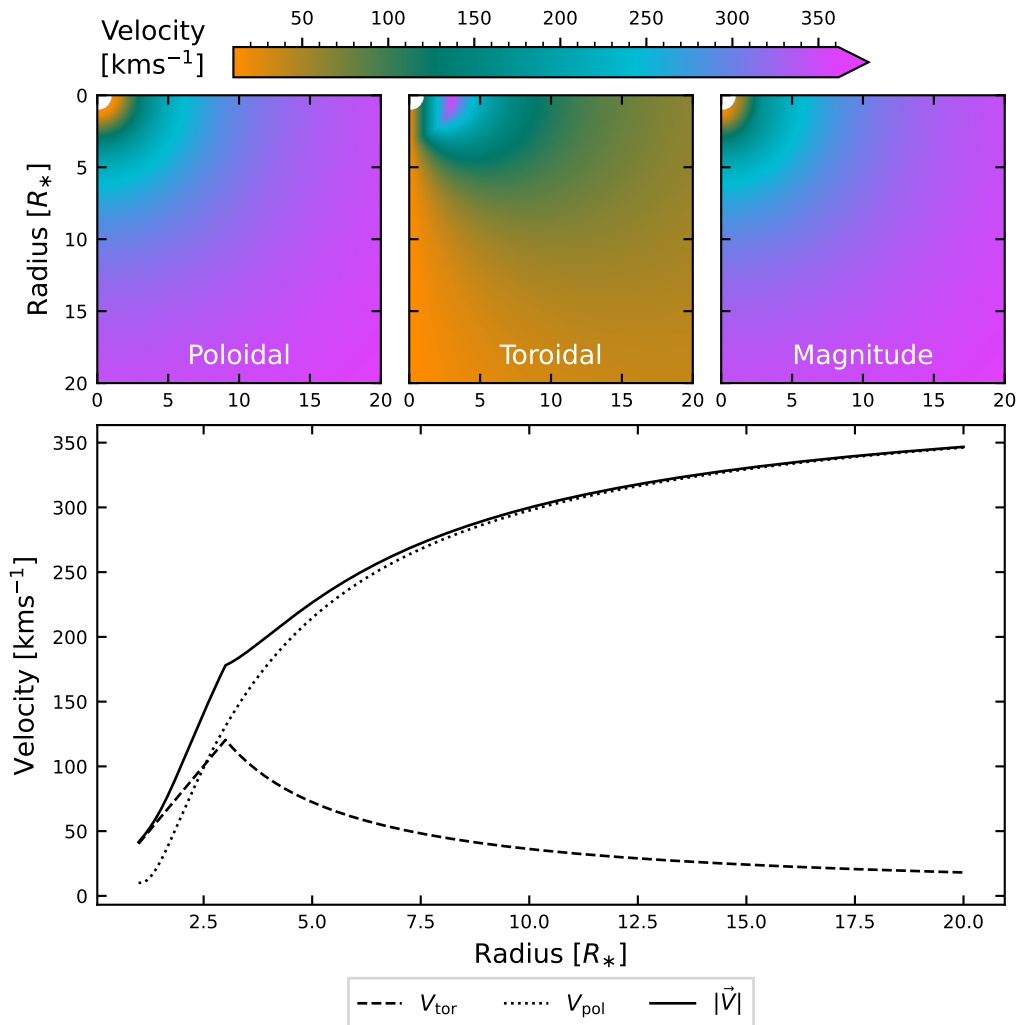


Figure 2.9: The lower frame shows the poloidal velocity, the toroidal velocity, and the velocity magnitude of the stellar wind. The rotation rate is 15% of the stars breakup velocity. The upper three panels display the wind velocity components as a 2D heat map. The star is located in the upper left corner.

and velocity fields in a 3D AMR mesh using the prescription laid out in § 2.3.1 and § 2.3.1.4. The complexity arises if a magnetic dipole offset is required. When the axis of the magnetic dipole is offset from the rotation axis (z-axis), the magnetosphere and the wind must similarly be rotated. Fig. 2.10 shows a slice of a 3D Cartesian T Tauri model from TORUS with a 10° dipole offset as indicated by the inclined black line. By default, when the magnetic dipole offset is greater than zero, the magnetosphere is limited to two opposing half-hemispheric accretion funnels; one in either hemisphere. The positions of the accretion funnels are chosen to minimise the distance from the disk to the star; see Fig. 2.10. The width of the two accretion funnels can be set as an input parameter. Previous iterations of TORUS have been used to model similar setups (e.g. Esau et al.

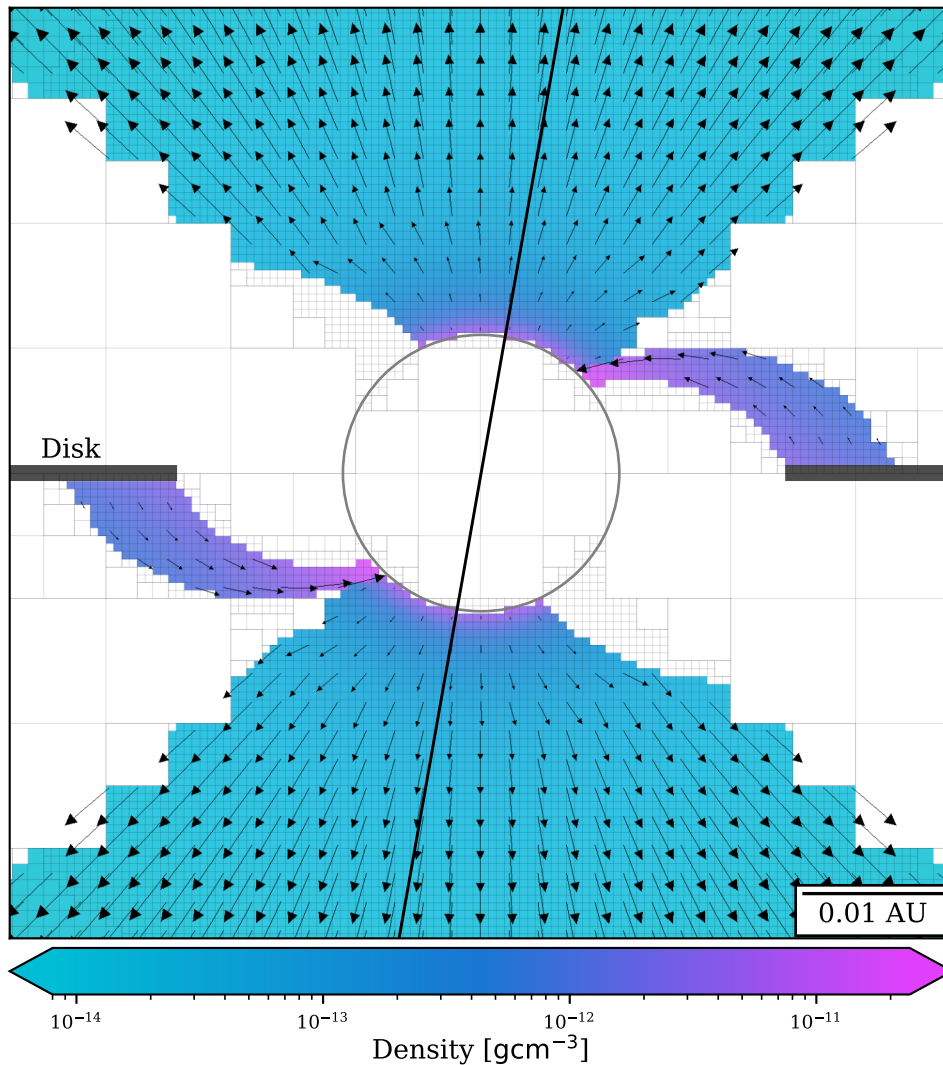


Figure 2.10: A slice of a 3D TORUS mesh where the magnetic dipole axis (inclined black line) has been rotated around the y-axis by 10° . The colour map denotes the density of the wind and magnetosphere. The arrows show the model velocity vector field.

2014; Symington et al. 2005a). However, these studies did not use the new implementation of radiative transfer described in § 2.2 or include a stellar wind.

The new stellar wind model in TORUS (see § 2.3.1.4) can also be used in a non-axisymmetric 3D model. The initial stage of the wind follows the magnetic field, which is rotated to match the magnetic dipole offset. After which, the wind becomes radial relative to the rotation axis. The wind flows along the field lines until it reaches the opening angle Θ_{open} ; which is relative to the rotation rather than to the dipole axis. If an offset is applied, the magnetic dipole rotates around the y-axis by an angle ξ . The disk remains fixed, therefore the length of the field lines is changed and the path of the wind must be

altered. The wind opening radius equation 2.30 is re-defined as,

$$R_{wo} = \alpha R_{\max} \sin^2 \Theta_{\text{open}}. \quad (2.32)$$

The term R_{\max} is the radius at which the outermost magnetic streamline intersects the disk, given by,

$$R_{\max} = \frac{R_{mo} + \delta}{\sin^2 \theta'_0}. \quad (2.33)$$

Where θ'_0 is the angle at which the field line intersects the disk in the rotated frame of reference. If $\theta_0 = \pi/2$ then,

$$\sin^2 \theta'_0 = \frac{1}{(1 + \tan^2 \xi \cos^2 \phi')} \quad (2.34)$$

here ϕ' is the azimuthal angle in the rotated frame of reference. The input parameters α and δ can be set to increase R_{wo} and the gap between the wind and magnetosphere, respectively.

The poloidal velocity vector field is shown in Fig. 2.10 overlaying a density map of the magnetosphere and wind. The mass-loss rate used in this simulation is $10^{-8} M_{\odot} \text{yr}^{-1}$ and an accretion rate of $10^{-7} M_{\odot} \text{yr}^{-1}$. The change from dipolar to radial velocity at R_{wo} can be seen. Assuming the wind and magnetic field are perfectly coupled, it is reasonable to assume that there would be minimal movement of the wind perpendicular to the field lines. The adaptive mesh refinement works as described in § 2.3 and a slice of the mesh can be seen in the figure.

2.4 Model validation

To validate the new radiative transfer routines implemented, I ran two separate model grids. The first contained only a magnetosphere and no outflow. The second included our new stellar wind model. The results were compared with previous radiative transfer simulations from literature. I was able to show that the new routines implemented in TORUS performed as expected and produced line profiles with morphologies, widths, and intensities similar to those seen in the literature. The results of the code validation are discussed below.

2.4.1 Magnetospheric accretion only

We used TORUS to reproduce the simple H α magnetospheric only model presented in fig. 3 of Kurosawa et al. (2006). The model used in fig. 3 of Kurosawa et al. (2006) is identical

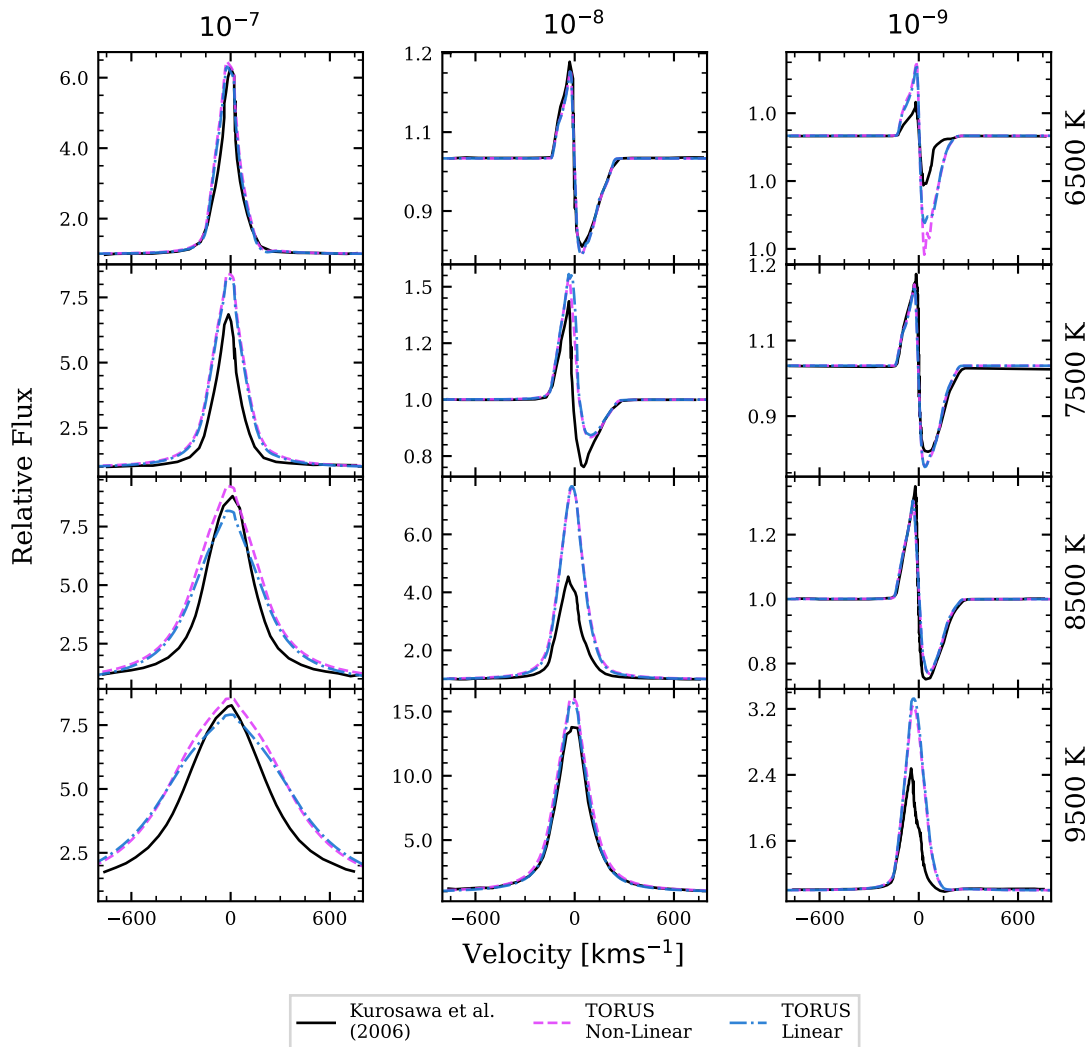


Figure 2.11: A comparison of synthetic H α line profiles produced by Kurosawa et al. (2006) (black lines) and TORUS . The models have magnetospheric accretion only and no form of mass outflows. Profiles arrange by accretion rate (columns) in values of $M_{\odot}\text{yr}^{-1}$ and accretion maximum temperature (rows) for a viewing colatitude of 55° . Two different Stark broadening parameterisations are used by TORUS ; linear (blue dot-dashed) and nonlinear (pink dashed) Stark broadening. Line strength increases with temperature and accretion rate, top-right to bottom-left.

to the setup described in § 2.3.1, and no outflows are included. The models were run with three different accretion rates of 10^{-7} , 10^{-8} , $10^{-9} M_{\odot}\text{yr}^{-1}$, four accretion maximum temperatures of 6500, 7500, 8500, 9500 K, and computed at an inclination of 55° . The model used a stellar mass of $0.5 M_{\odot}$, a stellar radius of $2 R_{\odot}$, and a magnetosphere stretching from $R_{mi} = 2.2 R_{*}$ to $R_{mo} = 3 R_{*}$. All other parameters are identical to those presented in Table 4.1. The only difference is that Kurosawa et al. (2006) used a nonlinear Stark broadening coefficient. Our TORUS model was run with both linear and nonlinear Stark broadening. In other words, the same fundamental physics is used by both

Kurosawa et al. (2006) and TORUS. This comparison therefore highlights the influence of the upgrades to TORUS discussed in § 2.2.

A comparison of the results produced by Kurosawa et al. (2006) and TORUS can be seen in Fig. 2.11. In the figure, it can be seen that the majority of the spectra share similar widths, shapes, and intensities. In general, the H α lines produced by TORUS are slightly broader, with peak intensities higher than those presented by Kurosawa et al. (2006). At higher temperatures and accretion rates, the non-linear Stark broadening produces spectra with marginally higher intensities at the line centre.

The general line profile trends shown by Kurosawa et al. (2006) are reflected by our TORUS models. The line strength and width increase with the accretion temperature and rates. The strongest lines for a given temperature are seen for the highest accretion rates $\log \dot{M}_{\text{acc}} = -7$. An exception to this trend is seen in Fig. 2.11 for the line profile produced with an accretion rate of $\log \dot{M}_{\text{acc}} = -8$ and $T_{\text{acc}} = 9500$ K. The line profile has a greater relative peak flux than the profile produced with an accretion rate of $\log \dot{M}_{\text{acc}} = -7$. This is because the continuum level from the hotspot is increased by the greater accretion rate, reducing the peak flux relative to the continuum. We see, in Fig. 2.11, that the width of the profiles increases with the rate and temperature of the accretion; it is unaffected by the continuum level.

2.4.2 Magnetosphere and stellar wind

The above comparisons did not include any outflows. Therefore, to assess our stellar wind geometry (§ 2.3.1.4), we ran an additional test to compare our model with the stellar wind geometry used by Kurosawa et al. (2011). The results are shown in Fig. 2.12. TORUS was used to run two models with identical stellar and magnetospheric parameters as those defined for fig. 10 of Kurosawa et al. (2011). Namely $M_* = 0.5 M_{\odot}$, $R_* = 2 R_{\odot}$, $R_{\text{mi}} = 2.2 R_*$ and $R_{\text{mo}} = 3 R_*$, all other stellar and magnetospheric parameters are as described in Table 4.1. The first models had an identical wind as Kurosawa et al. (2011); the wind launched from $3R_*$ above the star's surface. The second model used our wind geometry with the outflow being launched from the star's surface. We adopted the same outflow parameters of $T_{\text{sw}} = 8000$ K, $T_{\text{acc}} = 7500$ K, $\dot{M}_{\text{sw}} = 10^{-8} M_{\odot} \text{yr}^{-1}$, $\dot{M}_{\text{acc}} = 10^{-7} M_{\odot} \text{yr}^{-1}$, $v_{\text{min}} = 10 \text{ km s}^{-1}$, $v_{\text{max}} = 400 \text{ km s}^{-1}$, and $\Theta_{\text{open}} = 50^{\circ}$. The second model also used a value of $\beta = 1.6$ rather than $\beta = 0.5$ as this more closely replicated the wind acceleration and velocity of Kurosawa et al. (2011) at radii greater than $3 R_*$.

The differences in the line profiles produced by the two wind models are modest and comparable in magnitude to the variations seen in Fig. 2.11. For H α at low colatitude, the lines produced by our stellar wind model were broader at the peak by $\approx 20 \text{ km s}^{-1}$. For

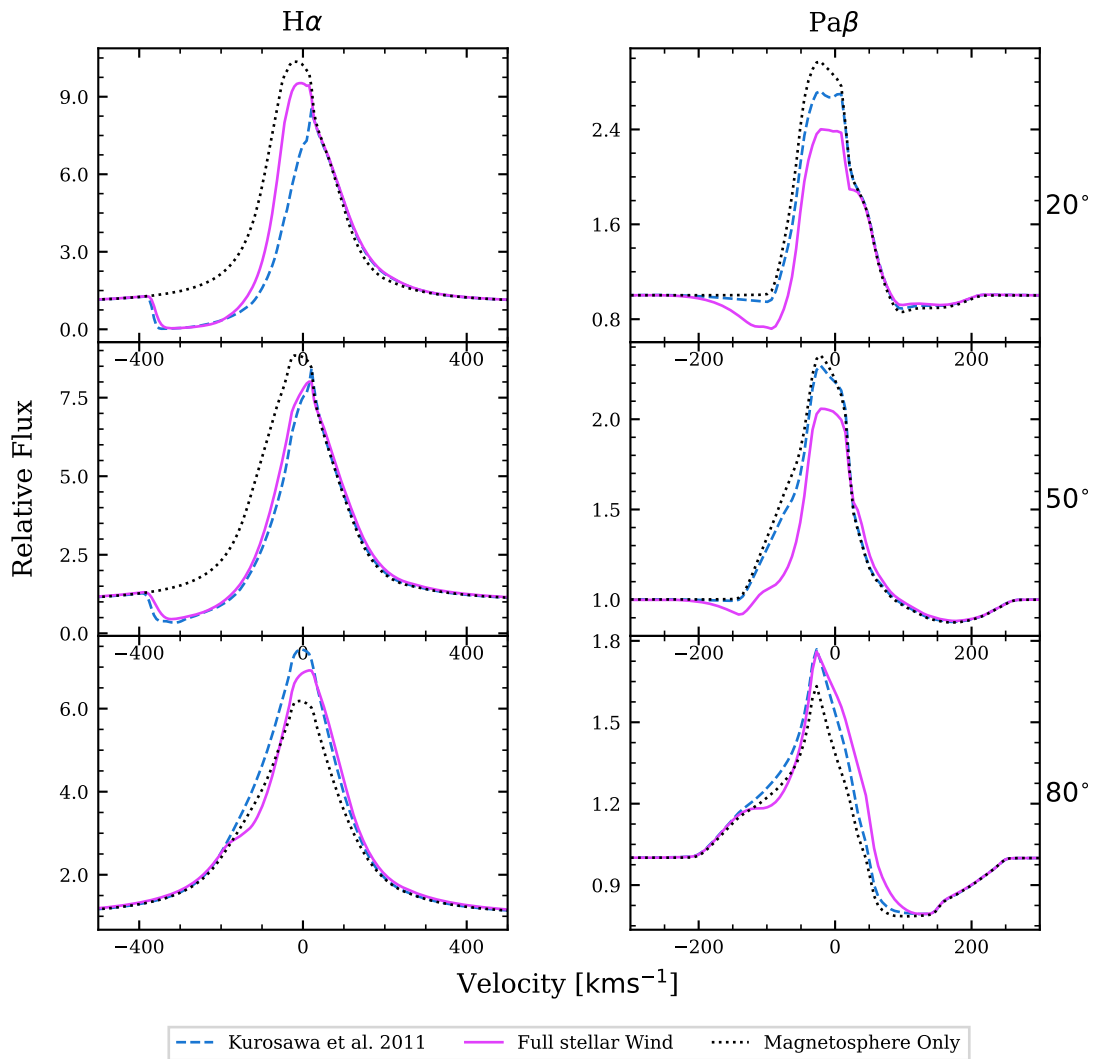


Figure 2.12: Three different models are shown here. A stellar wind model replicating the wind used by Kurosawa et al. (2011) and the new model developed in TORUS, see § 2.3.1.4. Additionally, the black dotted line is a magnetospheric only model is shown as. The rows are viewing inclinations and the columns show two different hydrogen lines.

high colatitudes, the lines were slightly narrower and exhibited small-scale blue-shifted absorption features not seen in the Kurosawa et al. (2011) wind model. For the infrared lines, at inclinations of 20° and 50°, the wind that extended to the star’s surface produced lines that were narrower and had a lower peak flux. Because the infrared lines are more optically thin, it is expected that they will be more sensitive to regions of denser gas. This effect can be seen in Fig. 2.11 where our wind model, which has denser regions of gas than the model of Kurosawa et al. (2011), produces deeper blue-shifted absorption features.

Summary

This chapter presented the radiative transfer code TORUS and the analytical T Tauri model used to create synthetic hydrogen spectra in Chapter 4. The statistical equilibrium and line profile routines of TORUS had been previously significantly updated but not verified. I further refined the code by removing bugs and enabling it to work on the available high-performance computing systems. Furthermore, I developed and tested a new polar stellar wind model framework applicable to axisymmetric and non-axisymmetric T Tauri simulations and expanded the Stark and turbulent broadening routines. This chapter showed that the upgrades to the physics and the accelerated Monte Carlo routines produced results congruent with previous studies. In the next chapter, we present a set of T Tauri observations and their line profiles, which are compared to synthetic line profiles from TORUS in Chapter 4.

Chapter 3

Observations

The size of the accreting region around T Tauri stars is on the order of a few stellar radii, too small to be directly resolved by current ground and space-based observatories. For example, ESO's Very Large Telescope Interferometer has a maximum resolution of ≈ 4 mas (milli-arcsecond), which at 150 pc, equates to the smallest discernible length scale of 0.6 AU or $130 R_{\odot}$. However, the technique of spectro-interferometry can be used to directly probe the gas kinematics to scales of a few stellar radii (e.g. [Bouvier et al. 2020](#); [Gravity Collaboration et al. 2020](#); [Kraus et al. 2008](#)). Nevertheless, spectro-interferometry is a complicated and modern process that requires highly sophisticated instrumentation and complex post-processing. Another more straightforward method for studying the accretion and outflow mechanisms of T Tauri stars is spectral analysis. Spectrometry has the advantage that T Tauri spectra are comparatively easy to observe, and an abundance of data is already available in archives.

Classical T Tauri stars are characterised by their hydrogen emission lines; see Chapter 1. Previous studies of hydrogen emission from T Tauri stars have predominantly focused on either the optical lines of $H\alpha$ and the Balmer series or the near-infrared lines of the Paschen and Brackett series. In this chapter, I examine the spectra of 29 T Tauri stars and compare the hydrogen lines of $H\alpha$, $Pa\gamma$, $Pa\beta$, and $Br\gamma$. T Tauri stars are variable (e.g. [Herbst et al. 2002](#); [Rucinski et al. 2008](#)) and their hydrogen lines can dramatically change over short periods. Therefore, when different spectra are compared, they must be observed simultaneously to avoid temporal divergence. I used spectra observed using the X-Shooter spectrometer (see § 3.1), which allows us to study both optical and infrared hydrogen lines from a single exposure.

A characteristic of T Tauri stars is their strong $H\alpha$ emission ([Joy 1945](#)). $H\alpha$ is normally the brightest of atomic emission lines from T Tauri stars and is considered an important probe of the circumstellar gas around the young stars ([Reipurth et al. 1996](#)).

It is an optical emission line caused by the hydrogen electron transition from 3 – 2 with a wavelength of 6565 Å (vacuum). The H α emission from T Tauri stars has been well studied, for example, [Hartmann \(1982\)](#); [Edwards et al. \(1994\)](#); [Reipurth et al. \(1996\)](#); [Muzerolle et al. \(1998a\)](#); [Alencar & Basri \(2000\)](#).

I also examine the near-infrared lines of Pa β , Pa γ , and Br γ . These lines are caused by the atomic transitions of Pa β 5 – 3, Pa γ 6 – 3, and Br γ 7 – 4. The transitions have vacuum wavelengths of 12821.6, 10941.1, and 21661.2 Å, respectively. These lines are generally optically thinner than H α and originate from denser regions of the hydrogen cloud and should be better tracers of the accretion than outflows because the winds are expected to have lower densities. Observations of these lines rarely show blue-shifted sub-continuum absorption, (e.g. [Folha & Emerson 2001](#); [Edwards et al. 2006, 2013](#)). For instance, a study by [Antoniucci et al. \(2011\)](#) showed that the relationship between Br γ luminosity and the accretion rate was more reliable than H α because there is less dispersion in Br γ luminosity when plotted as a function of stellar luminosity.

This chapter is structured as follows; I initially introduce the X-Shooter instrument § 3.1 and discuss the data reduction methods used in § 3.2. I then present the reduced hydrogen line profiles in § 3.3 and briefly discuss the general trends seen in the spectra.

3.1 X-Shooter instrument

X-Shooter is a second generation spectrograph fitted to Unit Telescope 2 of the Very Large Telescope (VLT) ([Vernet et al. 2011](#)). The instrument sits at the Cassegrain focus and has three independent cross-dispersed echelle spectrographs. Each spectroscopic arm contains its own detector, optimised optics, and dispersive elements. The three spectrographs can be used simultaneously to observe a wide wavelength range of 300 – 2480 nm. The three spectrographs have the following wavelength bands: *UVB*, 300 – 559.5 nm; *VIS*, 559.5 – 1024 nm; and *NIR*, 1024 – 2480 nm. The corresponding minimum slit widths are 0.5, 0.4, and 0.4 mas, respectively. For X-Shooter using the minimum slit widths, the spectral resolution of each arm is *UVB*, 9700; *VIS*, 18400; and *NIR*, 11600. The spectral resolution is defined as $R = \lambda/\Delta\lambda$, where $\Delta\lambda$ is the smallest difference in wavelengths that can be distinguished at a wavelength λ .

The principle of an echelle spectrograph is that it disperses the light into two orthogonal directions by using two dispersive elements. These elements may be prisms, gratings, or a combination of both. The general diffraction limited resolution R of a spectrograph using a grating is

$$R = \frac{Wn}{d}. \quad (3.1)$$

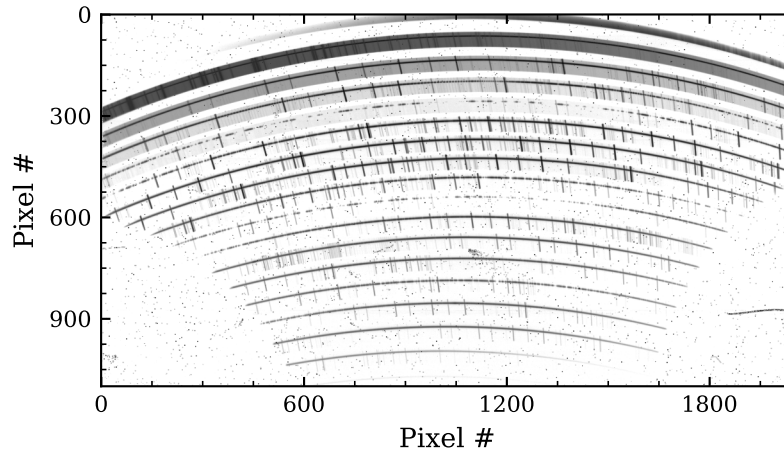


Figure 3.1: The unreduced image produced by the NIR echelle spectrograph of X-Shooter. The spectrum is dispersed in two orthogonal directions and darker regions indicate areas of greater intensity. The spectra is for Ass Cha T 2-23.

Here, W is the width of the grating, d is the grating groove spacing, and n is the diffraction order. Increasing W or decreasing d is limited by manufacturing technology and cost; accordingly, the easiest way to increase the resolution is by increasing n . Echelle spectrographs use an optimised grating to concentrate the energy in the higher orders. However, the free spectral range is reduced $\propto n^{-1}$, resulting in multiple orders overlapping. Therefore, a second dispersive element is used to sort the orders orthogonally to the original diffraction. This is especially useful for broadband or high-resolution spectral imaging because the otherwise wide spectra are “stacked” making full use of conventional 2D detectors. Fig. 3.1 shows an unreduced image from X-Shooter’s NIR detector or the Charge Coupled Device (CCD). Each stripe or arc is a different but overlapping section of the full wavelength range (1024 – 2480 nm). In the figure, the narrow curved bands are the stellar spectra, and darker regions indicate areas of high intensity. Atmospheric spectral contamination is seen as dark lines perpendicular to the arcs.

3.2 X-Shooter data

I selected 29 T Tauri stars from the ESO programme 084.C-1095(A) observed on 2010 January 18, 19, and 20 (PI G. Herczeg, see [Manara et al. 2016](#), [Rugel et al. 2018](#), [Schneider et al. 2018](#), and [Liu et al. 2016](#)). The observed targets were selected to have a broad range of accretion rates of four orders of magnitude; a complete list can be found in Table 3.1. The observations were made using X-Shooter ([Vernet et al. 2011](#)), see § 3.1. The spectra were obtained by nodding the telescope parallel to the slit to remove the sky background

from the images. A slit width of $0.4''$ was used for all stars except DG Tau, which used a width of $1.2''$.

Raw CCD images from the spectrograph (e.g. Fig. 3.1) were available in the archive already reduced using the ESO X-Shooter pipeline version v1.3.2 (Modigliani et al. 2010). The reduction used for these data followed a standard scheme of:

- Bias and dark frame subtraction.
- Flat-fielding, to normalise the response of the CCD pixels and correct for instrument-induced structures. This is done by using a dedicated halogen lamp (with appropriate balancing filters) for each spectrograph.
- Wavelength calibration, using Ar, Hg, Ne, and Xe Penray lamps.
- Background removal and spectra extraction.
- Flux calibration, using the standard spectrophotometric star GD-71 (Manara et al. 2016).

I further reduced the X-Shooter spectra by correcting for telluric contamination § 3.2.1 and extracting and fitting hydrogen lines § 3.2.2.

3.2.1 Telluric corrections

Ground based telescopes, such as VLT, observe through the Earth's atmosphere, the constituent molecules of which absorb or emit radiation that contaminates the astronomical spectra. These atmospheric features are called telluric lines and they are primarily a problem in the near-infrared regions of the spectrum (Fischer et al. 2016). Water vapour in the troposphere and stratosphere produces the greatest effect, however, molecules of carbon dioxide (CO_2), methane (CH_4), nitrous oxide (N_2O), and ozone (O_3) also produce significant telluric features. Due to the nature of the variable weather conditions and molecular abundances, the telluric features are unpredictable. Traditionally, to remove telluric features, science spectra are divided by the spectra of a photometric standard star observed as close as possible in time and airmass to the target. However, the observation of this calibration data is expensive and requires a standard star to be visible at a similar time and airmass as the target. A more recent method for removing telluric features is to use synthetic transmission spectra created using a radiative transfer code, based on atmospheric conditions at the time of observation. This is the method that was used in this chapter. To remove telluric contamination, I employed the MOLECFIT code from ESO (Smette et al. 2015; Kausch et al. 2015).

Fig. 3.2 is an example of the raw and telluric corrected spectra from X-Shooter. The spectra of all three X-Shooter arms are plotted, showing the full observed wavelength range.

Table 3.1: The 29 T Tauri stars used in this work. Here, the notes “B” or “T” denote that the star is listed in the literature as a binary or triple system respectively; a value of the angular separation is given where available. The complete SIMBAD name for Stars named T-# are Ass-Cha-T-2-#. The values and notes are adopted from: 1 [Manara et al. \(2016\)](#), 2 [Schneider et al. \(2018\)](#), 3 [Manara et al. \(2014\)](#), 4 [McGinnis et al. \(2015\)](#), and 5 [Rugel et al. \(2018\)](#).

Name	Type	T_{eff} [K]	A_V [mag]	Mass [M_{\odot}]	$\log \dot{M}$ [$M_{\odot}\text{yr}^{-1}$]	Notes	Ref.
ESO-Ha-562	M0.5+M0.5	3705	3.4	0.66	-9.3	B 0.28"	1
IQ-Tau	M0.5	3850	1.7	0.99	-8.2		1
V354-Mon	K4	4900	~	1.4	-8		2
T-33	K0	5110	2.7	0.95	-8.7	T 2.4"	1
T-11	K2	4900	0.8	1.32	8.3	B	3
VW-Cha	K7+M0	4060	1.9	1.24	-7.9	B 0.66"	1
V409-Tau	K5	4350	0.51	1.22	-7.8		3
CR-Cha	K0	5110	1.3	1.78	-8.7		1
T-52	K0	5110	1.0	1.4	-7.4	B 11.6"	1
T-38	M0.5	3780	1.9	0.71	-9.4		1
KV-Mon	K4	~	~	1.31	~		4
Sz-22	K5	4350	3.2	1.09	-8.4	T 17.6"	1
T-4	K7	4060	0.5	1.03	-9.5		1
DG-Tau	K5	4350	2.2	1.4	-7.7		1
T-23	M4.5	3200	1.7	0.33	-8.3		1
RECX-12	M3	3410	~	0.29	-9.8		5
Cha-Ha-6	M6.5	2935	0.1	0.1	-10.3		1
T-12	M4.5	3200	0.8	0.23	-8.8		1
CT-Cha-A	K5.	4350	2.4	1.4	-6.9		1
ESO-HA 442	M2	~	~	0.36	~		4
CHX18N	K2	4900	0.8	1.17	-8.1		1
TW-Cha	K7.	4060	0.8	1	-9	B	1
RECX-6	M3	3415	~	0.15	-11		5
T-49	M3.5	3340	1.0	0.36	-7.6	B 24.4"	1
T-35	K7	4060	2.9	0.96	-8.9		3
T-45a	K7	4060	1.1	0.97	-9.9	B 28.3"	1
RECX-9	M4.5	3085	~	0.15	-10.4		5
T-24	M0	3850	1.5	0.91	-8.7		1
Hn-5	M5	3125	0.0	0.16	-9.3		1

Note. ESO-HA 442 is also known as CID-0223980048.

The pink-shaded areas indicate the position of the four hydrogen lines $H\alpha$, $\text{Pa}\beta$, $\text{Pa}\gamma$, and $\text{Br}\gamma$. The areas of the spectra most affected by telluric features are 9000–10000, 11000–12300, 13000–15000, 17000–21000, and > 23000 Å. In particular, $\text{Pa}\beta$ (12821.6 Å) and $\text{Pa}\gamma$ (10941.1 Å) are at the edges of these regions. Telluric contamination introduces significant noise and distorts the continuum. MOLECFIT applied minimal corrections in

the regions of $H\alpha$ and $B\gamma$ because they lie in portions of the spectra that are relatively free of telluric features, as can be seen in Fig. 3.2.

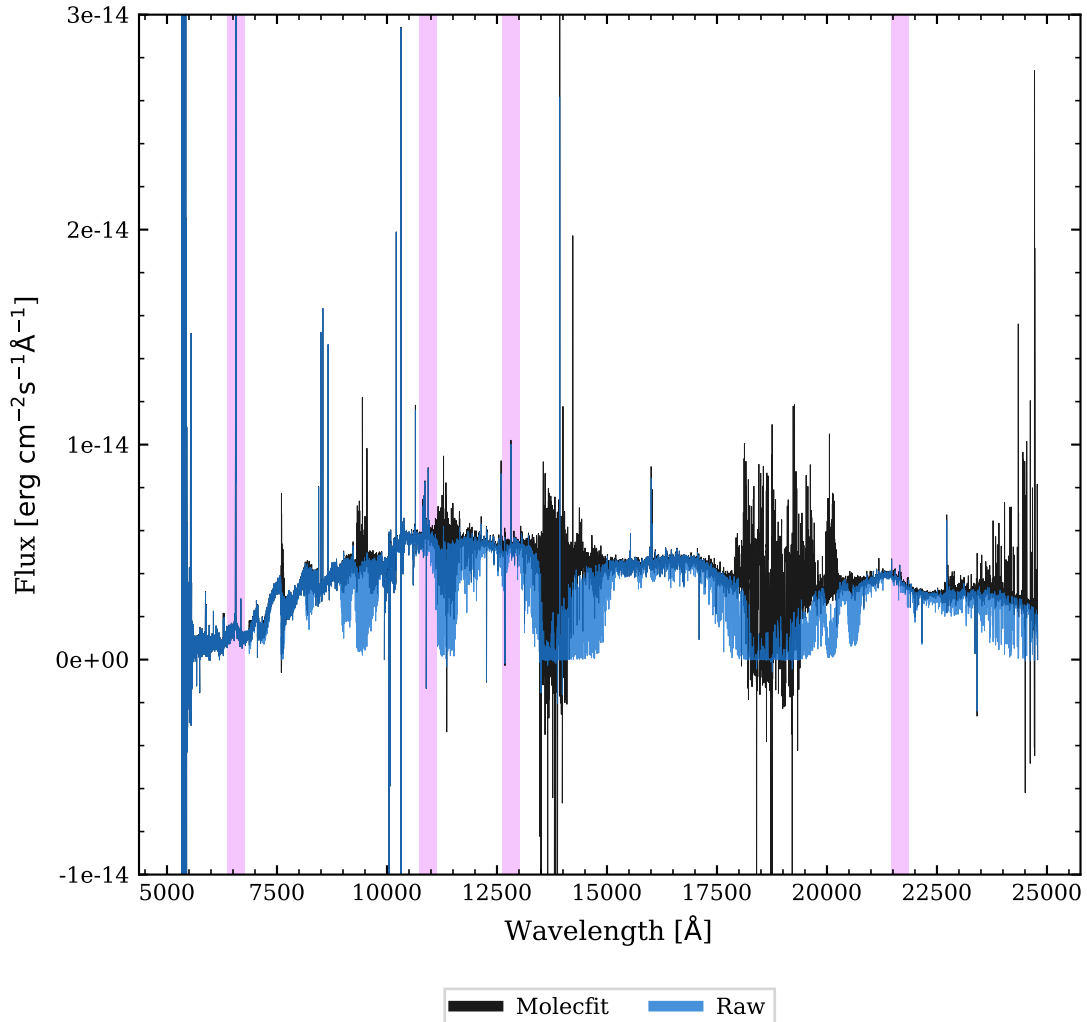


Figure 3.2: The raw and telluric feature corrected X-Shooter spectra. The pink shaded bars show the region of the four hydrogen lines extracted from the spectra. From left to right, these are $H\alpha$, $Pa\gamma$, $Pa\beta$, and $B\gamma$.

3.2.2 Continuum and Gaussian fitting

Once the telluric corrections had been applied, the regions of the hydrogen transitions ($\lambda_0 \pm 60 \text{ \AA}$) of interested were extracted from the full spectra. The line profiles were then further reduced by fitting the nearby continuum and creating a Gaussian fit to the profiles. The continuum fit is used to normalise the continuum to unity and remove any continuum features. Gaussian rather than spline fits were used for the emission profile to avoid problems with noise and to conform to standard data reduction methods.

The profiles were normalised by fitting a third-order polynomial to the nearby continuum. A demonstration of the continuum fit can be seen in the top panel of Fig. 3.3. The grey areas of the figure indicate the regions that were excluded from the fitting routine. An interactive PYTHON routine was programmed so that up to three separate areas could be selected (by clicking on the figure) to fit the continuum; this allowed line features to be excluded from the fit.

For the line profile fit, up to four Gaussians were used. A maximum of two Gaussians were used to fit the main emission feature, while a further two were used to fit the sub-continuum absorption. The fitting was done using the `astropy.modeling` module. The middle panel of Fig. 3.3 shows an example Gaussian fit and the central region (white) to which the Gaussian curves were fitted. Up to two such regions could be specified during the process to avoid fitting the Gaussians to spectral contaminants. The routine prioritised reproducing the line width and relative peak intensity.

The Gaussian fit was then used to determine several characteristics of the line profile. These were: full width at half maximum (FWHM), half width at 10% maximum (HW10%), equivalent width (W_λ), relative peak intensity, and the position of the line peak. Fig. 3.3 gives an example of the FWHM, HW10% and W_λ . The equivalent width is the width of a rectangle with a height from the continuum to zero that has an area equal to the integrated spectral line. Absorption lines are taken to have positive equivalent widths and emission as negative. In Fig. 3.3, the equivalent width is denoted by a vertical blue hashed bar (the full height is not shown), the area of which is equal to the blue hashed area under the line profile. The plotted bar has a width of 37.8 kms^{-1} , however, traditionally the equivalent width is given in the units of wavelength, and hence it is shown as $W_\lambda = -2.7 \text{ \AA}$.

3.3 Presentation of hydrogen spectra

The extracted and reduced hydrogen spectra from X-Shooter can be seen in Fig. 3.5. The figure shows the normalised line profiles for the target stars arranged in order of $H\alpha$ peak intensity. Each column displays the spectra for the individual objects listed in Table 3.1 at four different wavelengths: $H\alpha$, $Pa\beta$, $Pa\gamma$, and $Br\gamma$.

Veiling is the ratio of excess flux to photospheric flux. The excess flux from the accretion and shock zones changes the measured equivalent widths of the optical and infrared lines (Folha & Emerson 1999). The excess emission increases the continuum level and because the continuum level is used to normalise the line profiles, a higher continuum level will result in weaker relative emission and absorption. The scattering of light by the interstellar medium (ISM) is known as ISM extinction. The ISM extinction has a greater effect on shorter wavelengths, leading to a reddening of the observed spectra;

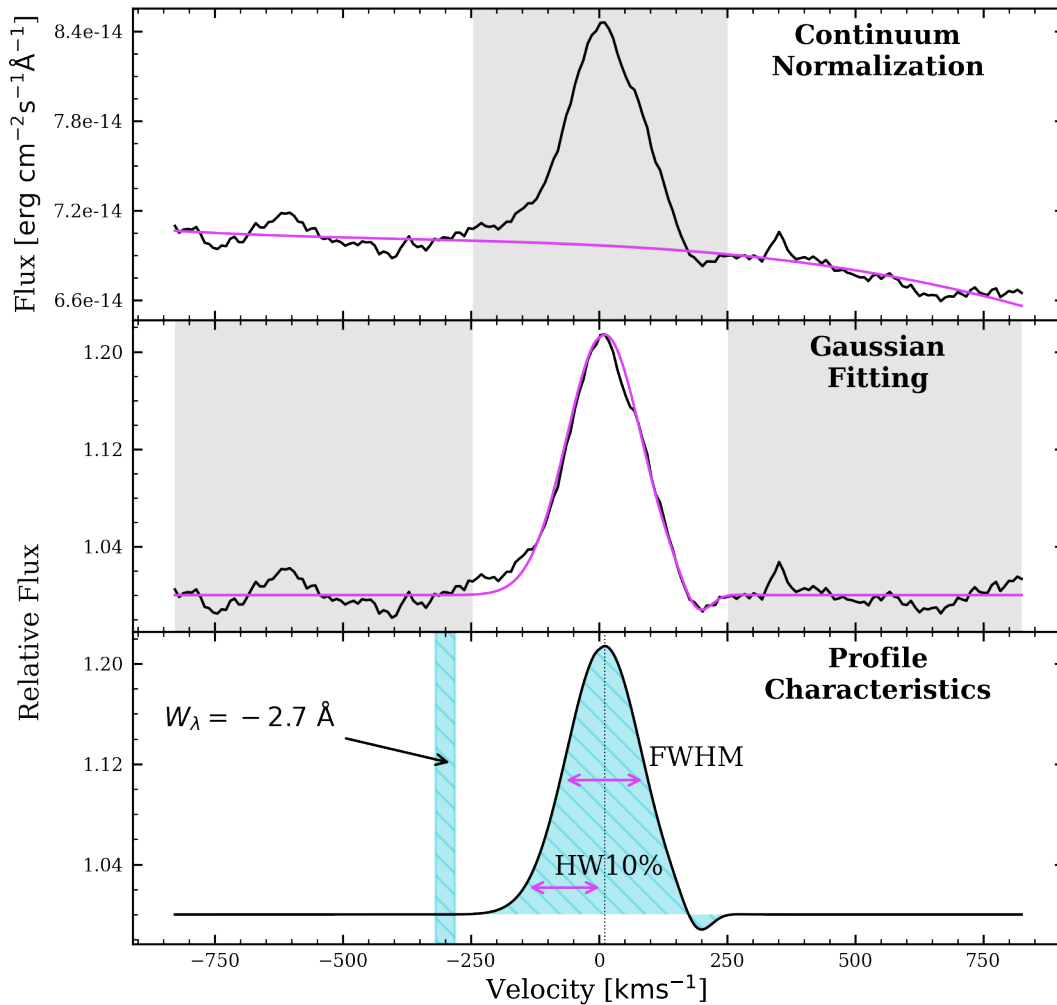


Figure 3.3: A diagram showing the continuum fit (top) to an observed profile, the Gaussian fit (middle) and extracted profile characteristics (bottom). Greyed areas in the top and middle panels indicate sections not used for fitting. The vertical blue hashed bar in the bottom panel indicates the equivalent width, for the purpose of clarity the full height is not shown and the bar is shifted up vertically.

the ratio of long to short-wavelength emission is increased by the extinction. The ISM extinction will influence the observed spectra fluxes. The star's [Cardelli et al. \(1989\)](#) extinction law reddening corrections are given in Table 3.1. However, the effects of veiling and extinction are not addressed in this thesis. Instead, the focus is on the line morphology and width; characteristics independent of veiling and extinction.

The strengths of the $H\alpha$ and infrared lines do not correlate well, as can be seen in Fig. 3.4. The figure shows the Spearman's rank correlation matrix of the equivalent width's between the different transitions; values close to unity suggest a good correlation. The different infrared lines correlate strongly with each other, but poorly with $H\alpha$. How-

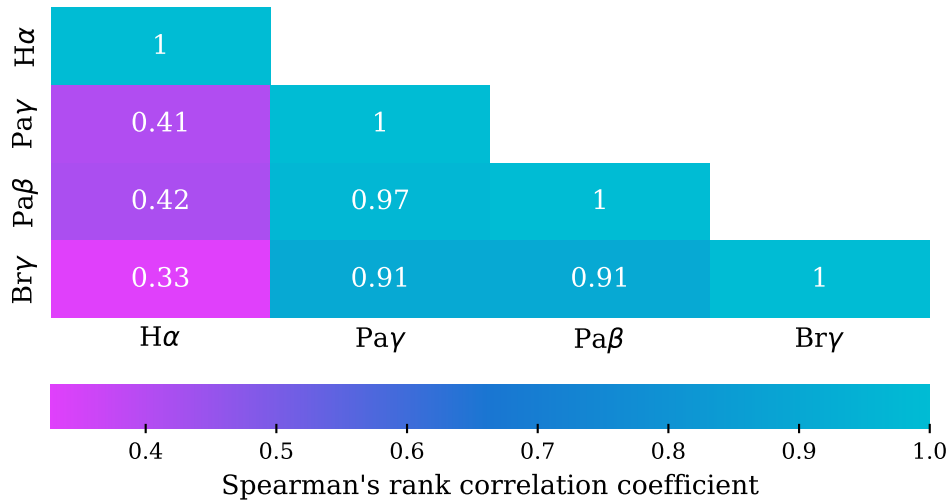


Figure 3.4: The correlation matrix between the equivalent widths of the different hydrogen transitions. The values are the Spearman's rank correlation coefficient, values close to unity suggest a strong correlation.

ever, the disparity seen in Fig. 3.5 cannot be accurately quantified because the effects of veiling and extinction have not been accounted for. Some stars with strong H α emission, e.g. Cha Ha 6, CID 0223980048 (ESO-HA 442), and Ass Cha T 2-33 have negligible emission in the Paschen and Brackett lines. The lack of Br γ lines in some spectra, while the Pa β and Pa γ are in emission, indicates that for these stars the population of level seven is negligible compared to the populations of five and six. Using the Boltzmann and Saha equations, we can calculate the hydrogen temperature at which the fraction in state seven is commensurate with states six and five to be ≈ 3700 K and ≈ 4500 K, respectively. We can then surmise that the Pa β and Pa γ emission from these stars are emitted from hydrogen at a temperature of < 4500 K. However, temperatures this low cannot explain the observed H α emission lines (Muzerolle et al. 1998b).

Four of the observed stars are classified as weak line T Tauri stars, according to the classification scheme of White & Basri (2003), because their half widths at 10 percent maximum (HW10%) are less than 135 km s^{-1} . The stars are RECX-6, Ass Cha T 2-45a, Ass Cha T 2-4, and RECX-12. In this work, I adopt the HW10% criterion because White & Basri (2003) showed it to be a reliable method of distinguishing between classical and weak line T Tauri stars and the HW10% criterion is unaffected by veiling.

In § 3.3.1, I discuss the classification and distribution of the different line profile structures. In § 3.3.2, I analyse the widths and general characteristics of the lines.

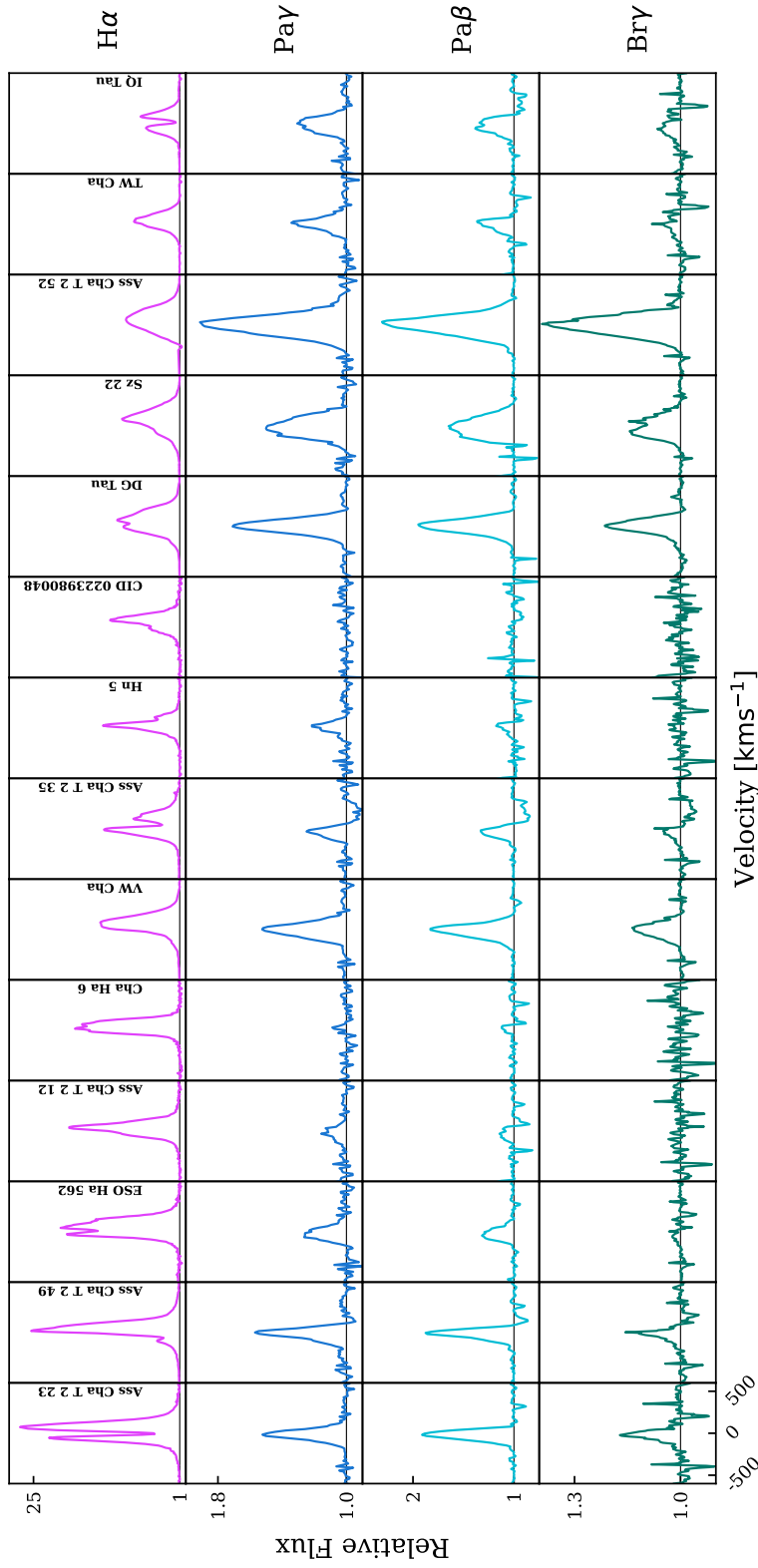


Figure 3.5: The normalised X-Shooter spectra of the objects (columns) listed in Table 3.1, at four different wavelengths: $H\alpha$; 6565 Å, $Pa\gamma$; 10938 Å, $Pa\beta$; 12818 Å, and $Br\gamma$; 21655 Å. The relative flux is plotted as a function of velocity, and each column has a width of $\pm 500 \text{ km s}^{-1}$. The stars are arranged from left to right by $H\alpha$ peak intensity.

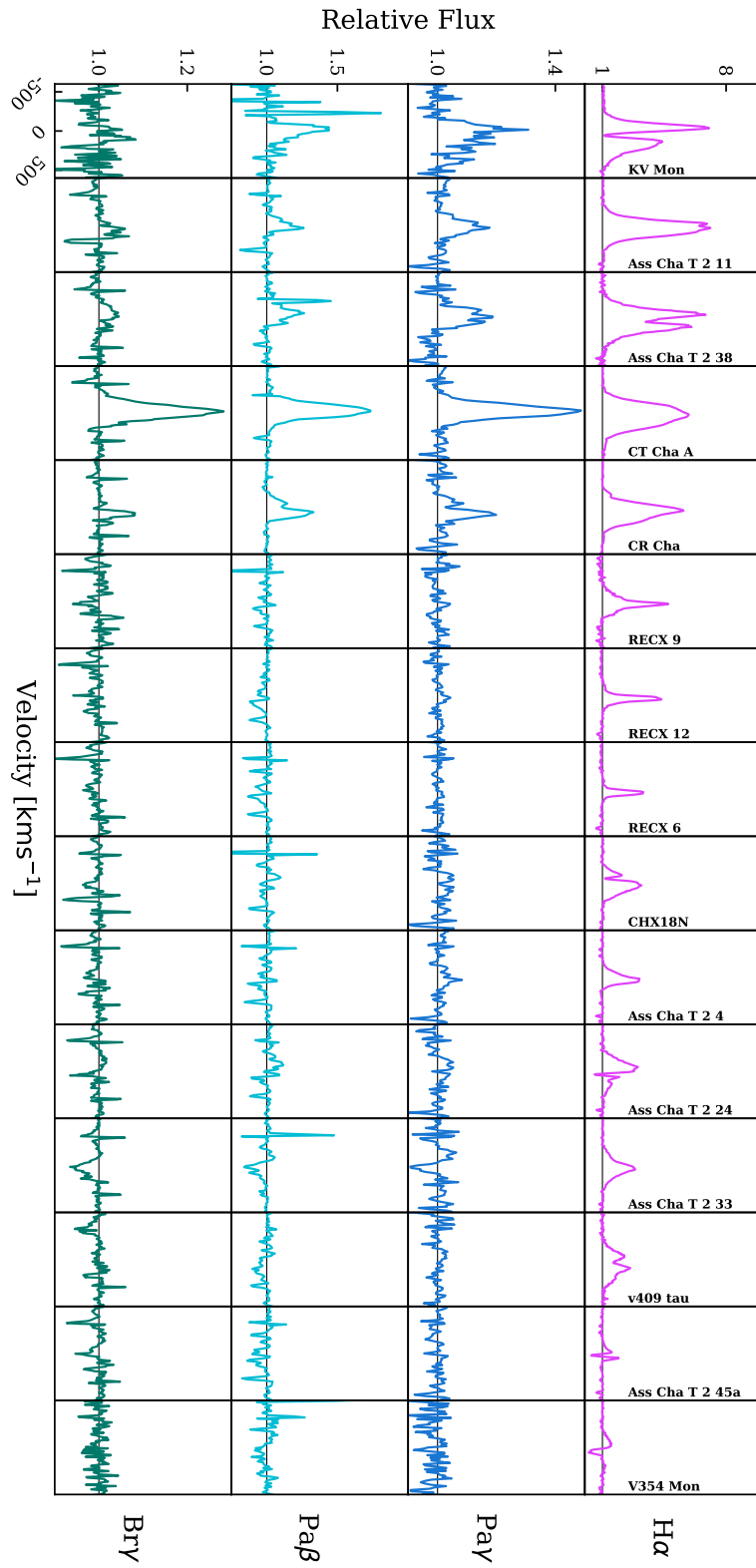


Figure 3.5: Continued. The stars are arranged from left to right by $H\alpha$ peak intensity. Note the different y-axis range.

Table 3.2: The half width at 10% maximum (HW10%) of the star's $H\alpha$ line profiles. Those stars with a width less than 135 km s^{-1} are classified as weak line T Tauri stars (WTTS) according to the approach of [White & Basri \(2003\)](#).

Name	HW10% [km s^{-1}]	WTTS
ESO-Ha-562	197.1	
IQ-Tau	187.3	
V354-Mon	178.2	
T-33	214.7	
T-11	191.0	
VW-Cha	209.3	
V409-Tau	283.3	
CR-Cha	220.8	
T-52	280.7	
T-38	219.2	
KV-Mon	228.9	
Sz-22	301.3	
T-4	125.0	Y
DG-Tau	271.3	
T-23	160.2	
RECX-12	85.7	Y
Cha-Ha-6	136.8	
T-12	159.8	
CT-Cha-A	272.8	
ESO-HA 442	166.3	
CHX18N	192.2	
TW-Cha	184.3	
RECX-6	63.1	Y
T-49	172.3	
T-35	205.5	
T-45a.	92.8	Y
RECX-9	149.1	
T-24	218.2	
Hn-5	161.2	

3.3.1 Reipurth classification

The hydrogen line profiles presented show a broad spectrum of different complex structures. The profile morphologies are important because they provide insight into the physical processes present in the T Tauri stars. [Reipurth et al. \(1996\)](#) devised a scheme to classify the $H\alpha$ T Tauri line profiles that not only simplified the data but also reflected the underlying physics of the spectra. The system established by [Reipurth et al. \(1996\)](#) characterises the spectra by the position and strength of a secondary peak relative to

the primary peak. The interplay between the peaks is assumed to be the product of a symmetric emission line and one or more absorbers.

Following the scheme described by [Reipurth et al. \(1996\)](#), the emission line profiles were classified as follows.

- *Type I*: symmetric profiles with few or no features.
- *Type II*: two peaks, the second greater than half the strength of the primary.
- *Type III*: two peaks, the second being less than half the strength of the primary.
- *Type IV*: sub-continuum absorption with no further significant emission beyond the absorption.

The types are subdivided into *B* and *R* because the secondary peak or absorption feature can be either blue or red-shifted relative to the primary peak. The classifications are illustrated in the top panels of [Fig. 3.6](#). The types *IVB* and *IVR* are equivalent to the P-Cygni and inverse P-Cygni profiles, respectively. The classification scheme is extended to the infrared lines because similar structures are seen for the higher lines and the underlying physics is assumed to be the same. Furthermore, the system has been used to categorise T Tauri spectra in previous studies, for example, [Folha & Emerson \(2001\)](#) and [Kurosawa et al. \(2006\)](#).

[Fig. 3.6](#) shows the Reipurth classification for the observations. Line profiles were classified by eye. The seven types of profile morphology defined by [Reipurth et al. \(1996\)](#) are seen in the data. For spectra in which the Reipurth type was not easily determined due to noise levels, the profiles were not classified and excluded from the results of this paper. Therefore, these unclassified spectra introduce uncertainty into the Reipurth distribution. The number of unclassified spectra are: 0 $H\alpha$, 10 $Pa\beta$, 14 $Pa\gamma$, and 18 $Br\gamma$. The sample of T Tauri stars is comparatively small, and a significant proportion of the infrared lines could not be classified. Consequently, the statistical significance of the distribution is ambiguous; however, it exhibits a similar distribution of morphologies as those seen in previous T Tauri studies (e.g. [Folha & Emerson 2001](#); [Reipurth et al. 1996](#)). The distribution concurs with previous results showing that the majority (≈ 43 per cent) of profiles are type *I* and the second highest population of Reipurth types for the infrared lines are type *IVR*.

There are several cases of inverse P-Cygni profiles in our data, the majority of which are seen for $Pa\beta$. There are two notable stars that contain prominent inverse P-Cygni signatures across all infrared lines. *Ass Cha T 2-35* has strong inverse P-Cygni absorption in all of the infrared lines, whereas the $H\alpha$ line only displays a red-shifted secondary

peak. Ass Cha T 2-49 has a narrow inverse P-Cygni absorption in the infrared lines and no significant $H\alpha$ red-shifted absorption. The single example of blue-shifted sub-continuum absorption is seen in the $H\alpha$ spectra of Ass Cha T 2-52, which has a narrow P-Cygni absorption profile consistent with a disk wind (Kurosawa et al. 2011). The infrared lines of Ass Cha T 2-52 exhibit no discernible blue-shifted absorption. None of the infrared lines exhibit discernible blue-shifted absorption.

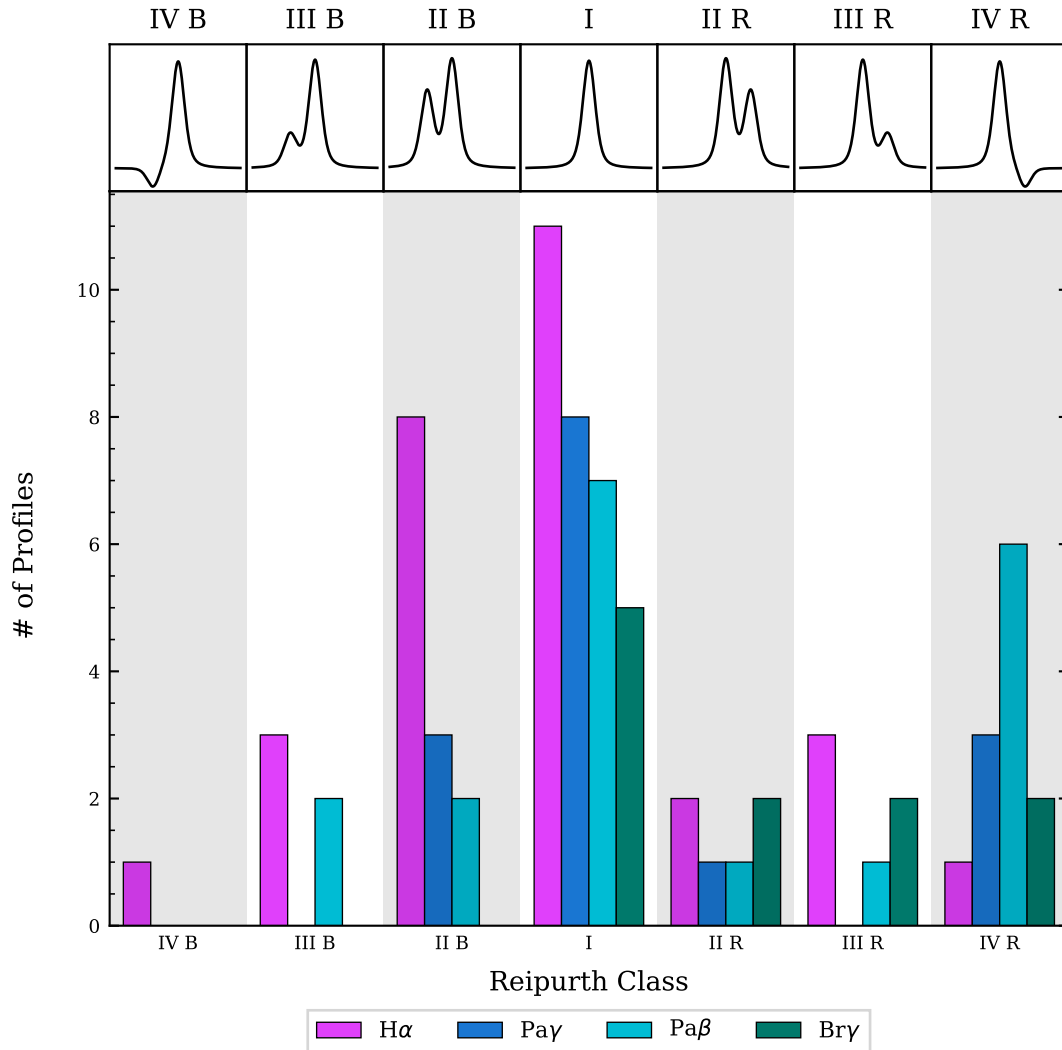


Figure 3.6: The distribution of Reipurth classification from the X-Shooter spectra. The results are subdivided by hydrogen emission line and example profiles are shown along the top.

3.3.2 Line profile characteristics

Fig. 3.7 shows the distribution of the central velocity of the primary peak, FWHM, HW10%, and the equivalent width as histograms subdivided by different categories of

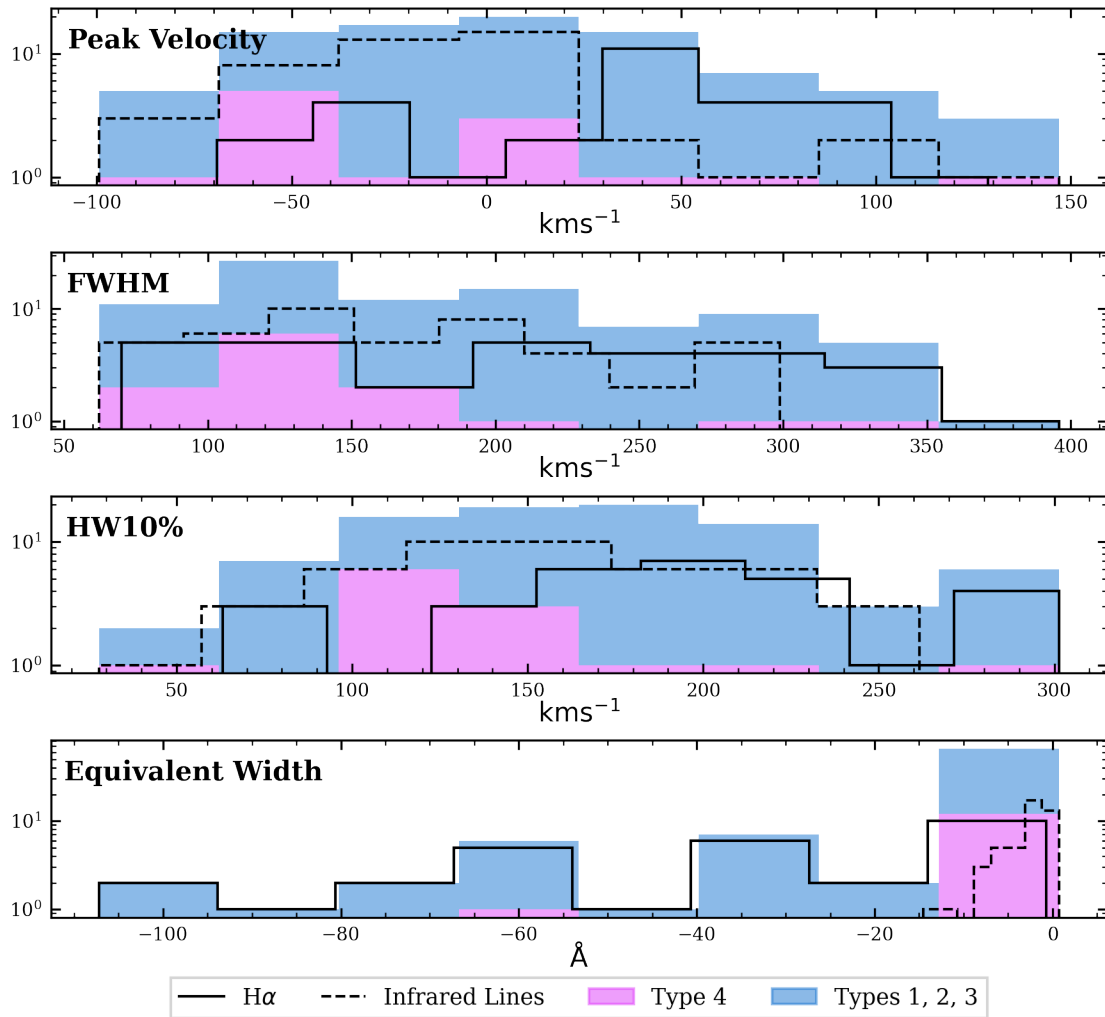


Figure 3.7: Histograms of the velocity of the line peak, the FWHM, the HW10%, and the equivalent width. The histograms are subdivided into the following categories: $\text{H}\alpha$, infrared lines, type IV, and types I–III.

observed spectra. The mean values for these subdivisions are shown in Table 3.3, along with the associated standard deviation. Generally, the $\text{H}\alpha$ profiles are wider than the infrared lines and have a greater equivalent width. The distribution of widths for $\text{H}\alpha$ is wider than for the infrared lines and the subsets have a large overlap. The central velocity of the primary peak is on average slightly (-8 kms^{-1}) blue-shifted from the rest velocity for the infrared lines. The $\text{Pa}\beta$ and $\text{Br}\gamma$ profiles presented by [Folha & Emerson \(2001\)](#) exhibited similar FWHM distributions and generally had slightly blue-shifted peak velocities. The mean $\text{H}\alpha$ peak velocity is 35 kms^{-1} , however, the distribution is bifurcated into two groups, one blue-shifted from the rest velocity and the other red-shifted.

The width of types I–III covers a broad range, but type IV profiles are on average

Table 3.3: The mean values of the primary peak’s central velocity, FWHM, HW10%, and equivalent width for four different subdivisions of the observed spectra. The standard deviation of each value is shown in brackets.

Category	Peak Vel. kms ⁻¹	FWHM kms ⁻¹	HW10% kms ⁻¹	W_λ Å
Type <i>IV</i>	-6 (60)	164 (74)	139 (59)	-8 (17)
Type <i>I–III</i>	9 (51)	184 (75)	170 (57)	-17 (26)
H α	35 (48)	208 (87)	191 (58)	-38 (31)
Pa β , Pa γ , Br γ	-8 (45)	169 (62)	157 (52)	-3 (3)

narrower by $\approx 26 \text{ kms}^{-1}$. The mean peak velocity is blue-shifted for type *IV* profiles and red-shifted for types *I–IV*, although they have similar standard deviations of 59 and 57 kms^{-1} , respectively. It is expected that the type *IV* profiles are narrower and blue-shifted because the inverse P-Cygni features reduce the line width, centring the emission slightly blueward.

Summary

This section presented the hydrogen line profiles of 29 different T Tauri stars observed using the X-Shooter instrument at the VLT. I explored the general characteristics of the profiles and saw that the H α line profiles were poorly correlated with the near-infrared lines of Pa β , Pa γ , and Br γ . At least four of the stars can be classified as weak line T Tauri from the H α half-width at 10%.

Using the line profile classification scheme set out by Reipurth et al. (1996), I found that our data produced a distribution of Reipurth types similar to previous studies of hydrogen lines. The most common type in our observations is type *I* for both H α and the infrared lines. The infrared lines have the highest proportion of inverse P-Cygni profiles (type *IV R*), and conversely, do not exhibit P-Cygni profiles (type *IV B*). This is because the generally low optical depth of the infrared lines creates absorption features only in high-density regions, such as the accretion funnel.

In the next chapter, I compare the observations to a grid of synthetic line profiles produced using the radiative transfer model (Chapter 2). The ensemble of the synthetic line profiles is compared with the general profile characteristics observed in this chapter, and it is seen that several discrepancies exist.

Chapter 4

A Comparison of Synthetic and Observed Spectra

In this chapter, I present a grid of synthetic line profiles (§ 4.1) produced using TORUS and the T Tauri model discussed in Chapter 2. Line profiles were produced using a set of parameters (see Table 4.1) intended to broadly span the range of predicted accretion rates and temperatures in T Tauri stars, based on observational constraints (e.g. [Muzerolle et al. 2001](#)).

The radiative transfer models have many unconstrained parameters, and the line profiles are highly degenerate. Therefore, in this chapter, I analyse the width and morphology of the ensemble of synthetic line profiles. I then compare our grid to the spectra of the 29 T Tauri stars presented in Chapter 3.

4.1 Synthetic line profile grid

The parameters used to create the synthetic line profile grid are described below. The models contain a single source star with an effective temperature of $T_{\text{eff}} = 4000$ K, a mass of $M_* = 0.5 M_{\odot}$, and a radius of $R_* = 2.0 R_{\odot}$. These parameters were chosen to be consistent with earlier work, for example, [Muzerolle et al. \(1998b, 2001\)](#); [Kurosawa et al. \(2006\)](#). Our grid covers a wide range of accretion rates of 10^{-7} , 10^{-8} , and $10^{-9} M_{\odot}\text{yr}^{-1}$ with mass-loss rates of 0.1, 0.01, and 0.001 of the accretion rate. These mass-loss rates were selected to be in the range required to provide a significant spin-down torque on the star ([Matt & Pudritz 2005b](#)) and are consistent with the range of values estimated from jets ([Nisini et al. 2018](#)). The source star parameters and the wind and magnetospheric geometries were not varied. For each model setup, line profiles were computed for three inclinations: 20° , looking down the pole through the wind; 60° , just outside of the wind's

opening angle; and 80° , looking along the disk through the magnetosphere. The line profiles were computed for the four hydrogen transitions presented in Chapter 3 of $H\alpha$, $Pa\beta$, $Pa\gamma$, and $Br\gamma$. The full list of parameters and their respective values can be found in Table 4.1.

Fig. 4.1 shows a subset of line profiles in the grid; only models with a wind temperature of 8000 K are included. The full atlas of the line profile can be seen in Appendix A. The figure arranges the line profiles by accretion rate and maximum magnetospheric temperature, subdivided by the hydrogen transition. The synthetic lines exhibit a broad range of different morphologies. $H\alpha$ has the highest peak intensity, and the subsequent strongest lines are $Pa\beta$, $Pa\gamma$, and $Br\gamma$, respectively. However, ≈ 7 per cent of the $Br\gamma$ lines at an inclination of 20° have a greater peak intensity than $Pa\beta$ and $Pa\gamma$. These lines occur for an accretion temperature of 9500 K and an accretion rate of $10^{-7} M_\odot \text{yr}^{-1}$. In general, the $H\alpha$ lines are wider than the infrared lines and some have broad wings $> 1000 \text{ km s}^{-1}$. The majority (≈ 83 per cent) of the infrared lines display red-shifted sub-continuum absorption. Blue-shifted sub-continuum absorption is not seen at high inclination, where the viewing angle is along the disk outside of the wind opening angle.

The general trends seen in the grid are outlined as follows. Higher accretion rates increase the line intensity. A high accretion rate of $10^{-6} M_\odot \text{yr}^{-1}$ was tested and the models produced structured $H\alpha$ absorption superposed on a broad ($\pm 1000 \text{ km s}^{-1}$) emission profile. Only a limited number of models were run with an accretion rate of $10^{-6} M_\odot \text{yr}^{-1}$ and the profiles are not included in this work. The line profiles intensity also increases with higher accretion flow temperature. The $H\alpha$ lines are dominated by Stark broadening for accretion flow temperatures of at least 7500 K at accretion rates of $10^{-8} M_\odot \text{yr}^{-1}$. The effect of Stark broadening is that the line width increases with temperature and accretion rate. For a temperature of 9500 K and an accretion rate of $10^{-7} M_\odot \text{yr}^{-1}$, the $H\alpha$ profiles are Stark broadened to have wings greater than $\pm 1000 \text{ km s}^{-1}$. In contrast, the infrared lines are almost completely unaffected by Stark broadening. The intensity and equivalent width of the infrared lines increases significantly with greater accretion rates and temperature. On the other hand, the full width at half maximum (FWHM) is less strongly affected by the accretion rate and temperature. The mean equivalent widths of the synthetic profiles are $H\alpha$, -34.5 ; $Pa\beta$, -2.3 ; $Pa\gamma$, -0.6 ; and $Br\gamma$, -2.3 .

$H\alpha$ exhibits inverse P-Cygni profiles for the accretion rates of $10^{-8} M_\odot \text{yr}^{-1}$ when $T_{\text{acc}} \leq 7500 \text{ K}$ and for $10^{-9} M_\odot \text{yr}^{-1}$ when $T_{\text{acc}} \leq 8500 \text{ K}$. For accretion rates and temperatures above this, the Stark broadening smooths over the absorption features. For the infrared lines, the inverse P-Cygni profiles are exhibited irrespective of the inclination, accretion rate, or temperature.

Fig. 4.2 shows the distribution of line peak velocities for the four different hydrogen

Table 4.1: Parameters of the grid of synthetic models

Parameter	Value	Unit	Description
M_*	0.5	M_\odot	Star mass
R_*	2.0	R_\odot	Star radius
T_{eff}	4000	K	Effective stellar temperature
R_{mi}	2.2	R_*	Truncation radius and inner magnetosphere connection point
R_{mo}	3.0	R_*	Outer connection point of magnetosphere
T_{acc}	6500, 7500, 8500, 9500	K	Maximum temperature of magnetosphere
\dot{M}_{acc}	$10^{-7}, 10^{-8}, 10^{-9}$	$M_\odot \text{yr}^{-1}$	Magnetospheric accretion rate
V_{rot}	0.0	kms^{-1}	Rotation velocity
Θ_{sw}	50	deg	Stellar wind opening angle
V_{min}	10	kms^{-1}	Velocity of wind at launch
V_{max}	400	kms^{-1}	Maximum wind velocity
β	2.89		Wind velocity scaling
\dot{M}_{sw}	0.1, 0.01, 0.001	\dot{M}_{acc}	Mass-loss rate as a fraction of accretion rate
T_{sw}	6000, 8000, 10000	K	Isothermal wind temperature
Synthetic inc	20, 60, 80	deg	Co-latitude of synthetic profile viewing angle
Profile λ	6562, 10938, 12818, 21655	\AA	Observed wavelengths: H α , Pa γ , Pa β , and Br γ respectively

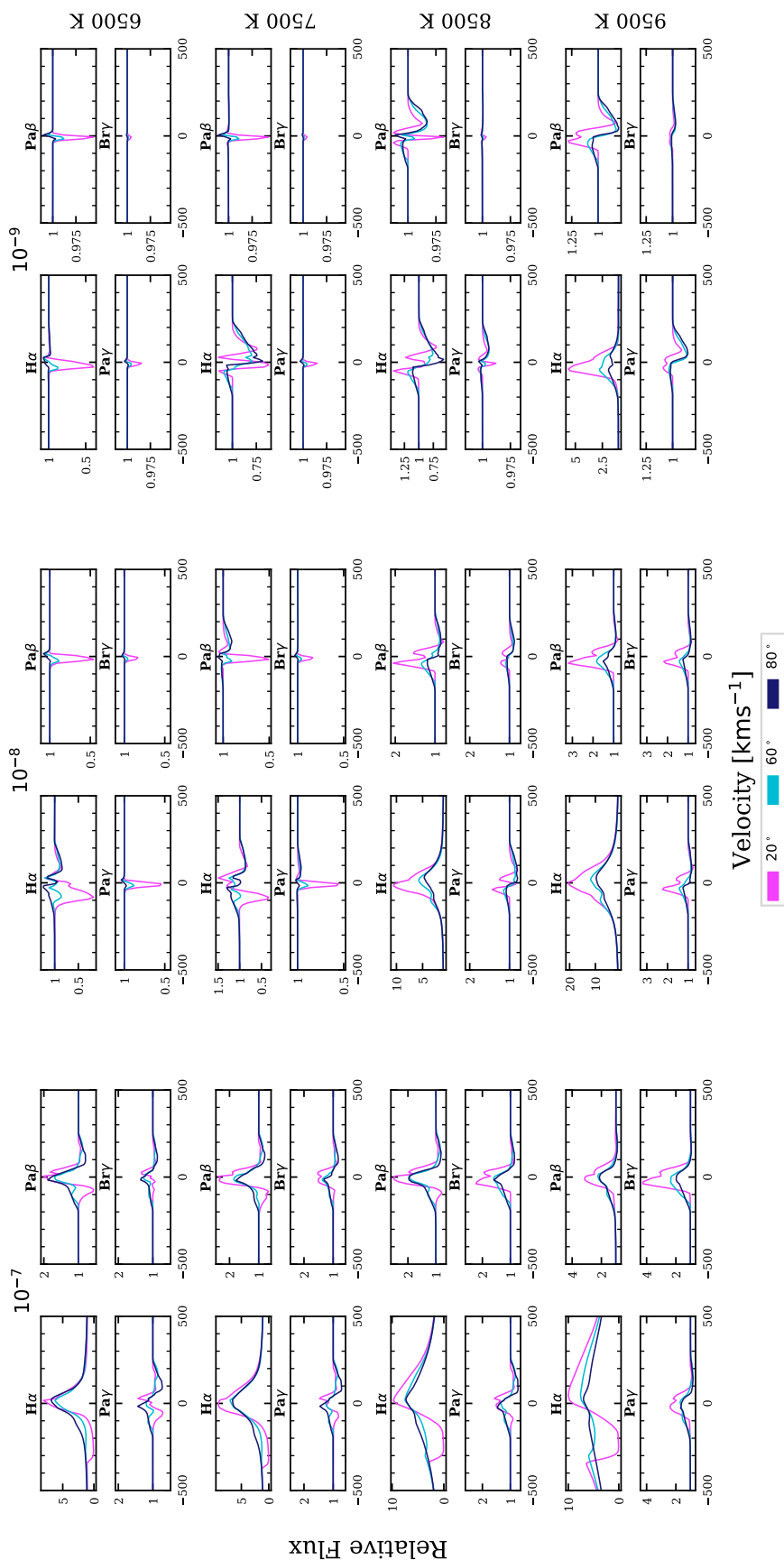
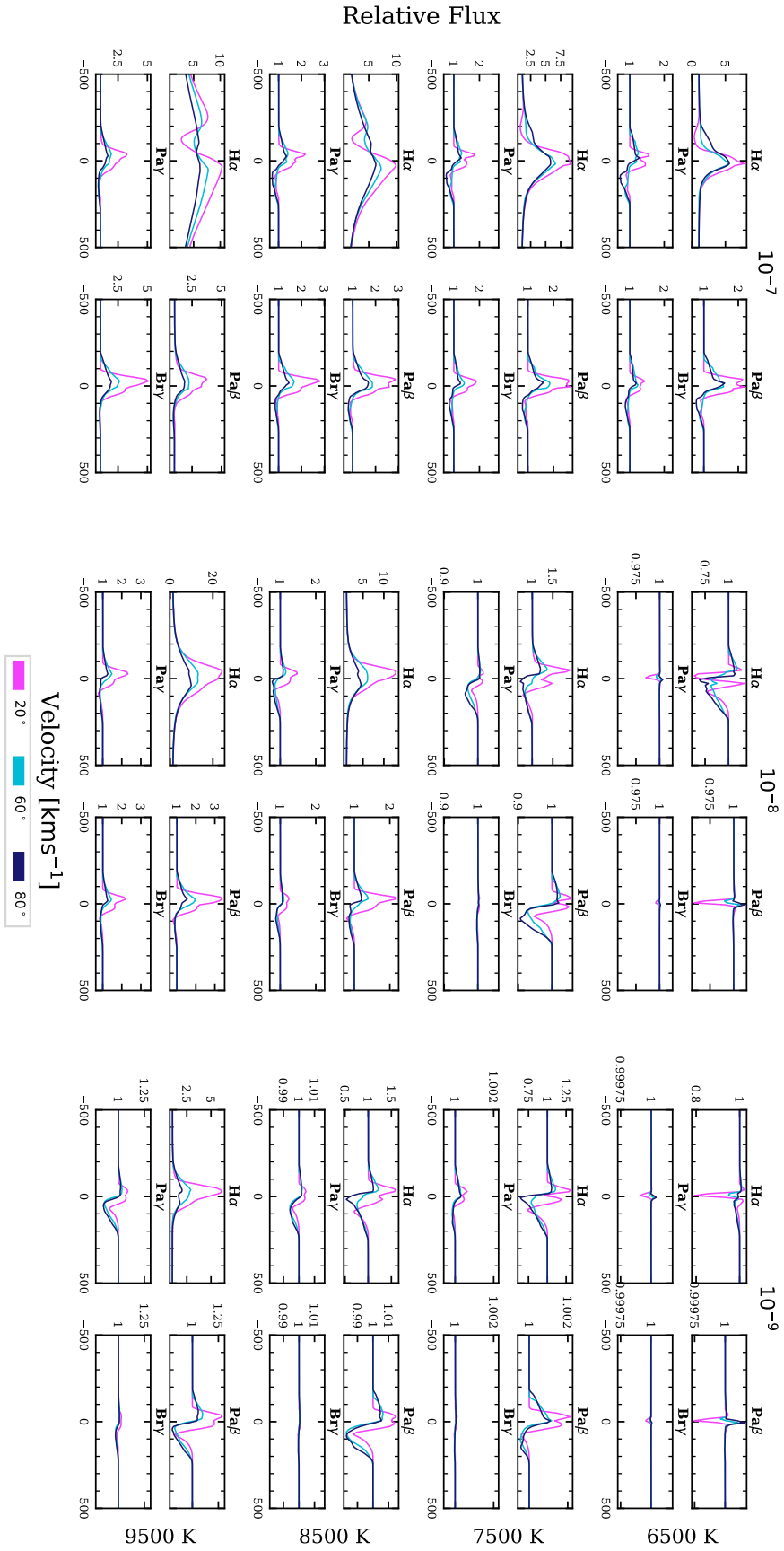


Figure 4.1: A sample of the line profiles produced by TORUS. The spectra are shown for $\dot{M}_{\text{sw}} = 0.1 \dot{M}_{\text{acc}}$ and $T_{\text{sw}} = 8000 \text{ K}$. The lines are arranged by \dot{M}_{acc} (columns) and T_{acc} (rows). Each section is subdivided by the hydrogen transition and shows the three different inclinations (colours). The y-axes of Pa β , Pa γ , and Br γ are present in most infrared lines. IPC profiles are present in most infrared lines. For hydrogen transitions at an inclination of 80° (outside of the stellar wind opening angle), there is less blue-shifted absorption and there are no P-Cygni features. H α profiles are broad, with some wings exceeding 500 km s^{-1} .



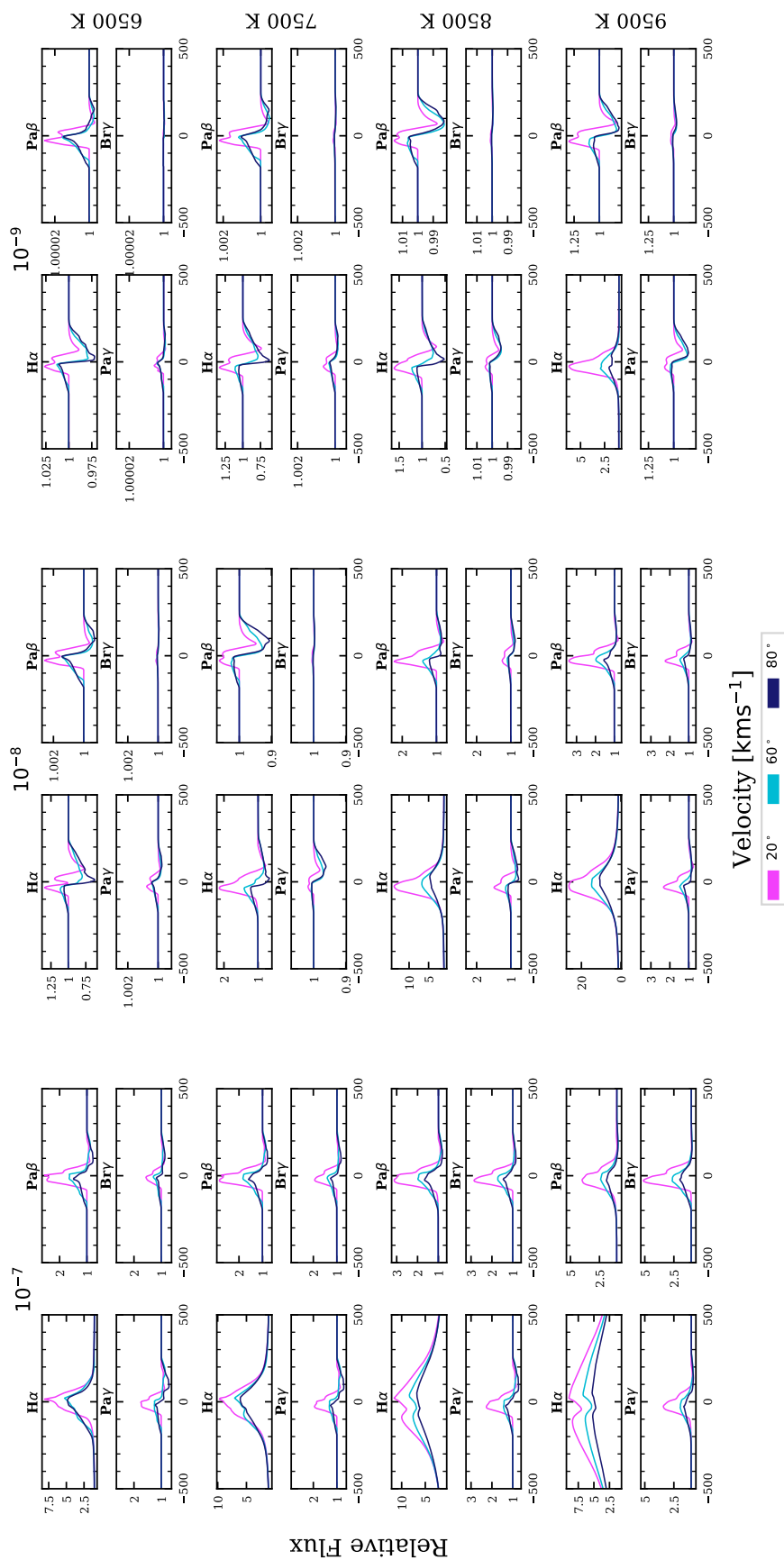


Figure 4.1: Continued. Models presented here for $\dot{M}_{\text{sw}} = 0.001 \dot{M}_{\text{acc}}$ and $T_{\text{sw}} = 8000 \text{ K}$.

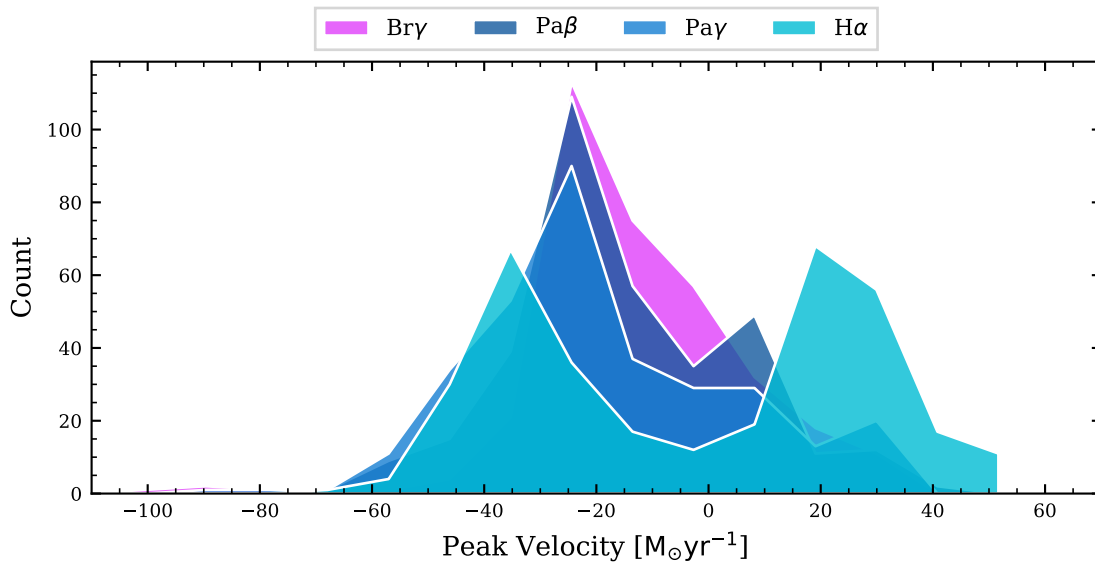


Figure 4.2: The distribution of synthetic line centres for the different hydrogen transitions. The infrared line centres are blue shifted, whereas the $H\alpha$ line centres are bi-modal with both red and blue-shifted peaks.

transitions. The infrared lines have mean peak velocities of -20.6 , -16.5 , and -14.5 kms^{-1} for $\text{Pa}\gamma$, $\text{Pa}\beta$, and $\text{Br}\gamma$, respectively. Whereas, the mean peak velocity for $H\alpha$ is -3 kms^{-1} . However, the distribution is divided into two sections of red-shifted peaks with a mean of $\approx 20 \text{ kms}^{-1}$ and blue-shifted peaks with a mean of $\approx -35 \text{ kms}^{-1}$. The red shifted peaks are the product of the high accretion rate models where $\log \dot{M}_{\text{acc}} = -7$ (the units of $\text{M}_{\odot}\text{yr}^{-1}$ are emitted for brevity) and the blue shifted peaks of the low accretion rate models ($\log \dot{M}_{\text{acc}} = -9$). Models with an accretion rate of $\log \dot{M}_{\text{acc}} = -8$ have peak velocities fairly evenly distributed from -60 to 40 kms^{-1} . The effect of Stark broadening is minimal at low accretion rates, which gives rise to greater red-shifted absorption, effectively shifting the peak velocity blueward.

In the following sections, I present a comparison of the characteristics (§ 4.2) and the structure (§ 4.2.1) of the ensemble of synthetic line profiles and the observed T Tauri stars.

4.2 Comparison of profile features

To analyse the synthetic and observed emission as an ensemble, I calculated the full width at half maximum (FWHM), the half width at 10% peak maximum (HW10%), equivalent width W_{λ} , the peak intensity, and the velocity of the peak intensity of the synthetic profiles. The FWHM and HW10% were calculated by fitting the synthetic line profiles with a linear spline using the PYTHON module `scipy.interpolate.interp1d`.

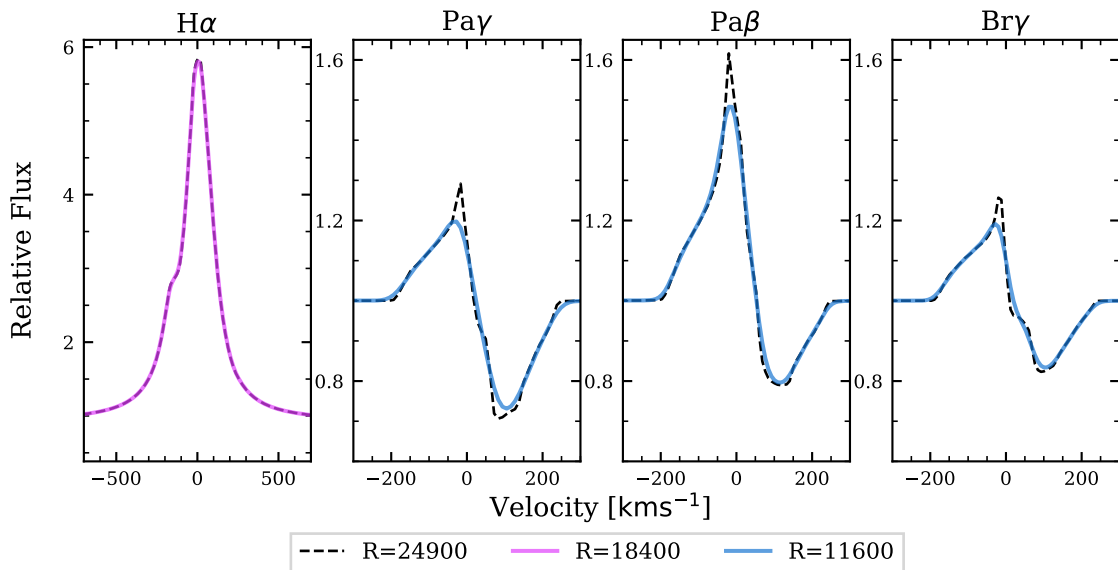


Figure 4.3: Convolution of synthetic spectra created with a velocity resolution of $\Delta v = 12.04 \text{ km s}^{-1}$ ($R = 24900$) to the observed resolutions of $R = 18400$ for $\text{H}\alpha$ and $R = 11600$ for $\text{Pa}\gamma$, $\text{Pa}\beta$, and $\text{Br}\gamma$.

The trapezium integrator provided by `scipy.integrate.trapz` was used to determine the area under the line profile to calculate W_λ . The synthetic profiles are smooth with negligible small scale fluctuations; therefore, a spline can accurately represent the line profile and a Gaussian fit is not required.

The synthetic line profiles were calculated for velocity increments of $\Delta v = 12.04 \text{ km s}^{-1}$, which corresponds to a spectral resolution of $R = 24900$. The observations were observed at resolutions of $R = 18400$ ($\Delta v = 16.3 \text{ km s}^{-1}$) for $\text{H}\alpha$ and $R = 11600$ ($\Delta v = 25.9 \text{ km s}^{-1}$) for the infrared lines. I explored the effect of applying a Gaussian convolution to the synthetic spectra to reduce their resolution to that of the observed spectra. However, the change in the morphology of the line profiles, particularly the FWHM and HW10% was negligible when the synthetic spectra were convolved. Fig. 4.3 shows the effect of convolving the synthetic spectra to the resolution of the observations using a Gaussian kernel. Therefore, the TORUS native resolution was kept and the resolution of the synthetic spectra were not convolved hereafter.

Although our model grid was not set up to fit any particular star, it is informative to directly compare the synthetic line profiles with the observed line profiles. As an example, I show the spectra of three stars (Sz 22, DG Tau, and Ass Cha T 2-52) in Fig. 4.4 and a corresponding model selected to match the $\text{H}\alpha$ line profiles. The models were chosen using a χ^2 fit test to find the closest $\text{H}\alpha$ profiles from the grid. The parameters of the chosen models are shown in Table 4.2. The models use our fiducial values of $T_{\text{eff}} = 4000 \text{ K}$ and $M_* = 0.5M_\odot$, whilst the effective photospheric temperature for Sz 22 is 4350 K, for

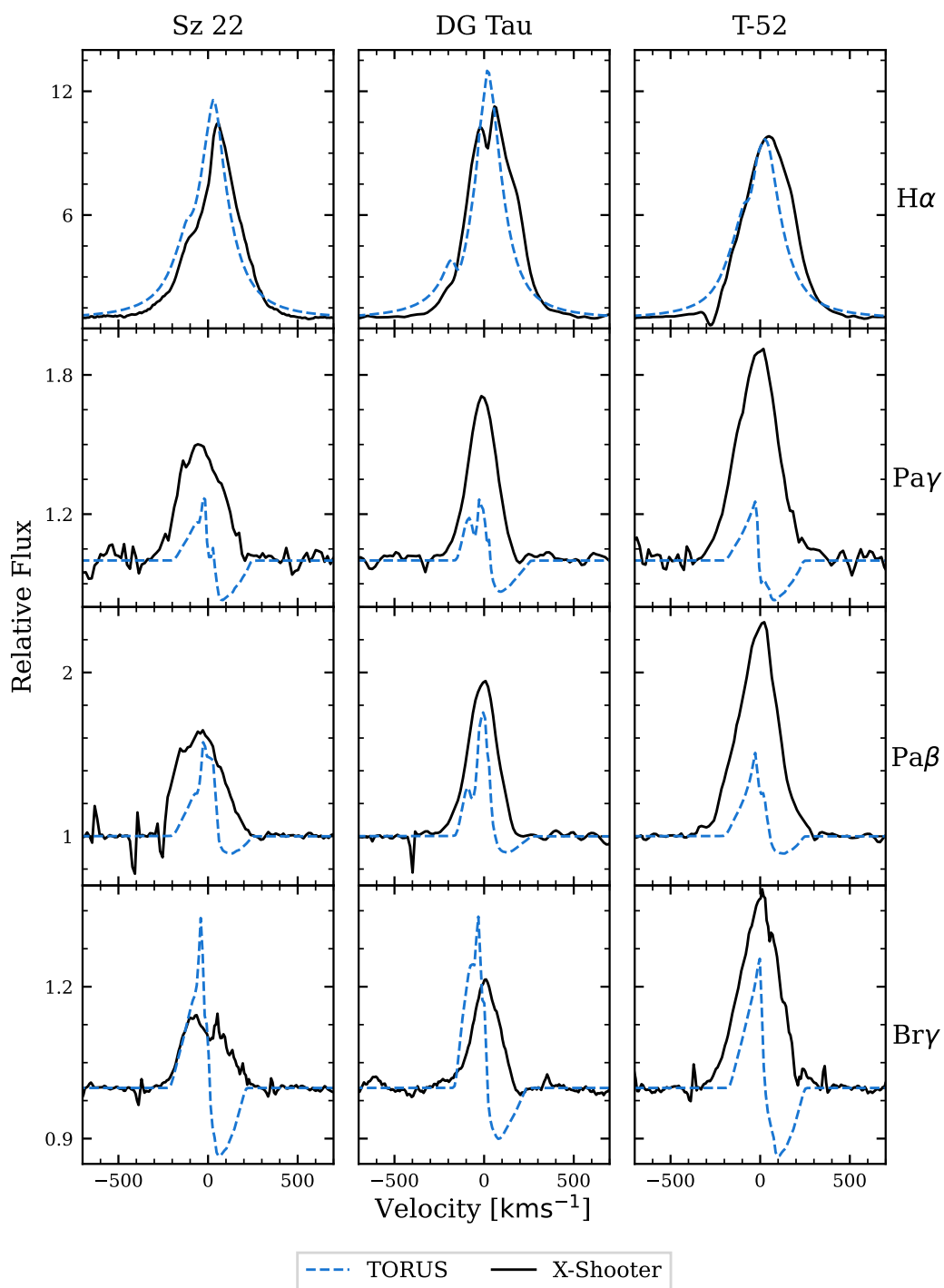


Figure 4.4: Three of the best cases of the grid matching the observed line profiles. The models have been chosen because they best reproduce the observed H α height and width. The observed spectra have been adjusted to compensate for each system's radial velocity.

DG Tau it is 4350 K, and for Ass Cha T 2-52 it is 5110 K (Manara et al. 2016; Nguyen et al. 2012). The stellar masses for Sz 22, DG Tau, and Ass Cha T 2-52 are 1.09, 1.4, and 1.4 M_{\odot} , respectively (Manara et al. 2016). The observed inclinations of DG Tau and Ass Cha T 2-52 are $< 30^{\circ}$ (Isella et al. 2010) and $35 \pm 10^{\circ}$ (Hussain et al. 2009), respectively. For Sz 22 the circumstellar disk is thought to be viewed edge on, suggesting a high inclination (Schmidt et al. 2013), which agrees with the fitted model. For DG Tau and Ass Cha T 2-52 the fitted models suggest a medium inclination compared to the observed low inclinations. However, the synthetic grid is coarse and the fitted models only crudely match the observed line profiles, especially for DG Tau and Ass Cha T 2-52. A close fit of the inclinations is not expected.

A caveat to direct comparison is that the veiling of the observed lines has not been considered. Whereas the effect of reddening is negated by the continuum normalisation, the influence of veiling is not. Nevertheless, Fig. 4.4 highlights a trend seen in the synthetic spectra grid. Namely, that while our method selects models with similar strengths and widths in $H\alpha$ to that observed, the models fail to reproduce the observed infrared lines. The synthetic infrared lines are too structured and narrow. The tendency of the ensemble of widths being too narrow for synthetic infrared lines is discussed below.

Table 4.2: The model parameters used in Fig.4.4

Object	Sz 22	DG Tau	T-52
$\log \dot{M}_{\text{acc}}$	-8	-8	-8
T_{acc}	9500 K	9500 K	9500 K
$\log \dot{M}_{\text{sw}}$	-9	-9	-9
T_{sw}	10000 K	10000 K	8000 K
Inclination	80°	60°	60°

Fig. 4.5 compares the distributions of synthetic and observed HW10% for the four hydrogen transitions. The upper quartile, the median, and the lower quartile are shown as horizontal dashed lines. The distribution of synthetic $H\alpha$ widths is much broader than that observed, ranging from close to zero to more than 1100 km s^{-1} . This broad range is a result of our parameter grid sampling a relatively uniform coverage of line profiles in this range. The right-hand figure shows a subset of our grid constrained such that only models with an $H\alpha$ HW10% between $60\text{--}350 \text{ km s}^{-1}$ are included. By constraining the synthetic models so that the $H\alpha$ HW10% lies in a range similar to that observed, it is easier to compare the ensemble of line profiles across the different hydrogen transitions. Even with the $H\alpha$ distribution constrained to match the observed widths, the median width of the synthetic infrared line is narrower than that in the observed sample. The differences in the median value of HW10% for the synthetic and observed $\text{Pa}\gamma$, $\text{Pa}\beta$, and $\text{Br}\gamma$ lines

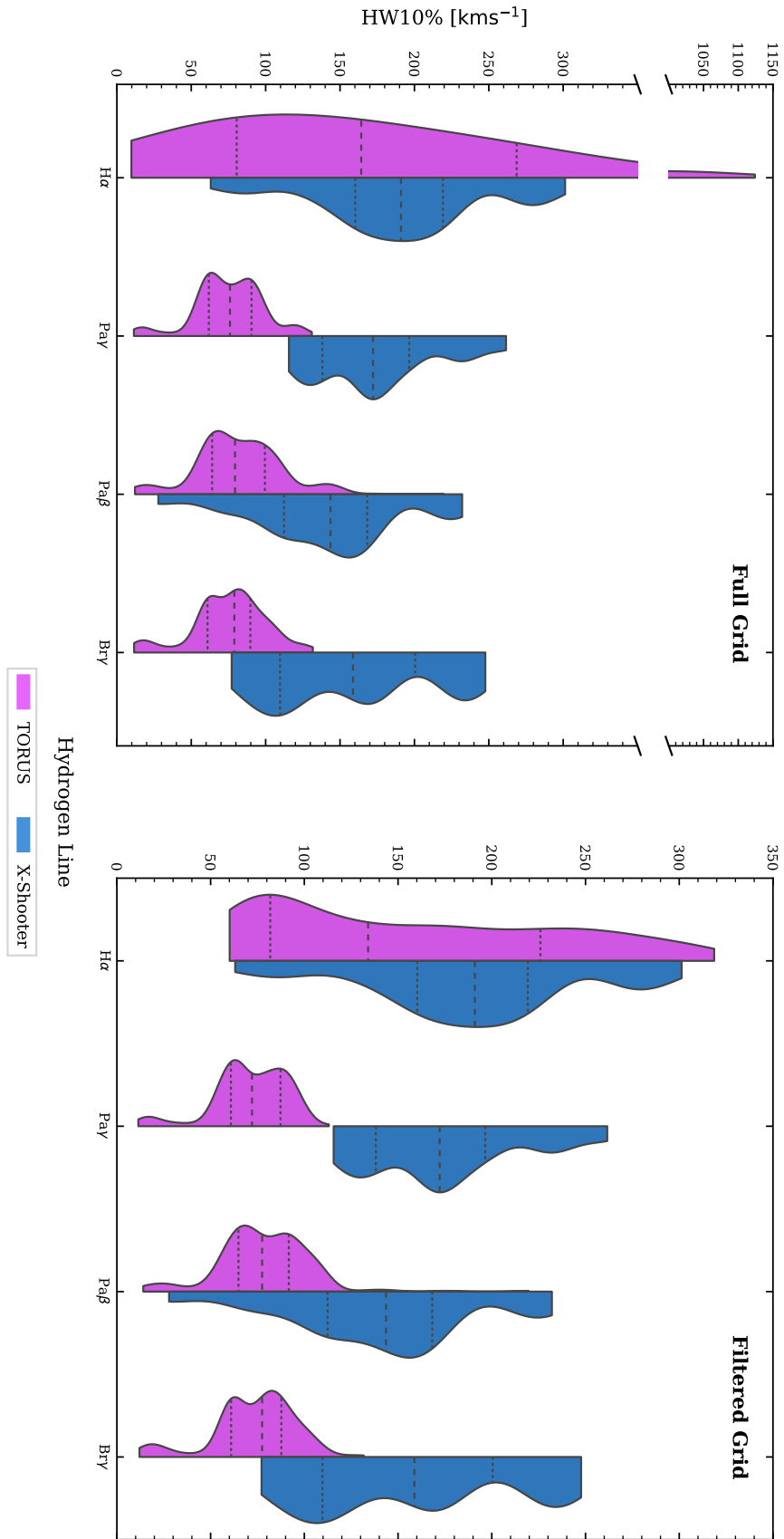


Figure 4.5: The HW10% distribution of the synthetic grid and observations are shown for each spectral line. The left panel shows the full grid (note the split of the y axis), and the right panel shows the filtered grid where $60 \leq \text{HW10\% H}\alpha < 350$. Horizontal lines indicate the 25th, median, and 75th percentiles

are 96, 64, and 80 kms^{-1} , respectively. In other words, for a range of models that predict line widths of $\text{H}\alpha$ in the same range as observations, the predicted widths for the infrared lines are systematically too narrow by $\approx 80 \text{ kms}^{-1}$. In § 4.3, I explore what modifications can be made to the models to bring these synthetic lines into better agreement with the observed sample.

Fig. 4.6 shows a plot of FWHM versus HW10% for the synthetic and observed spectra. Each point indicates a separate line profile; the colour and size indicate the accretion rate. The White & Basri (2003) $\text{H}\alpha$ HW10% distinction between the weak line and the classical T Tauri stars is shown by the vertical dotted line. For $\text{H}\alpha$, the FWHM and HW10% are strongly correlated for both observations and models. Both the synthetic and the observed data show that the widths depend on the accretion rate. However, the temperature of the accretion funnel and the viewing inclination have a significant influence on the widths of the models, scattering the FWHM and the HW10% for a given accretion rate. The relationship between FWHM and HW10% for a single Gaussian is

$$\frac{\text{FWHM}}{\text{HW10\%}} = \frac{2\sqrt{2 \ln 2}}{\sqrt{2 \ln 10}} \approx 1.1, \quad (4.1)$$

displayed in Fig. 4.6 by inclined solid black lines. The observed sample is scattered around this relationship. The synthetic $\text{H}\alpha$ spectra tend to have a smaller FWHM for a given HW10% than expected from the Gaussian relationship. The deviation from the Gaussian FWHM to HW10% relationship is due to Stark broadening. The synthetic $\text{H}\alpha$ lines take on a Voigt profile when Stark broadening is dominant (see Chapter 2.2.3). The Voigt form has wider wings and a narrower peak than a Gaussian curve. This effect is not observed in the higher lines, where Stark broadening is negligible. The widths of the observed line profiles were measured using a Gaussian fit; therefore, the deviation away from the expected FWHM to HW10% relationship for the observed data is due to the convolution of the multiple Gaussians components used.

For Pay and Bry, the observations exhibit a tighter correlation between the FWHM and HW10% than for $\text{Pa}\beta$. The $\text{Pa}\beta$ observations exhibit a larger scatter, suggesting a divergence away from the Gaussian form and more structure in the line profiles. This is corroborated by the fact that $\text{Pa}\beta$ has the highest frequency (63 per cent) of non-type *I* profiles (see § 4.2.1). In contrast to $\text{H}\alpha$, the FWHM and HW10% of the infrared lines in the observations and models exhibit little correlation with the accretion rate. The models shown in Fig. 4.6 have been selected so that the range of HW10% widths for $\text{H}\alpha$ roughly corresponds to the range of observational data. However, these models predict widths for the three higher lines that are, on average, much narrower than the observed widths. In general, for an accretion rate of $\log \dot{M}_{\text{acc}} = -7$ the synthetic lines have a lower ratio of

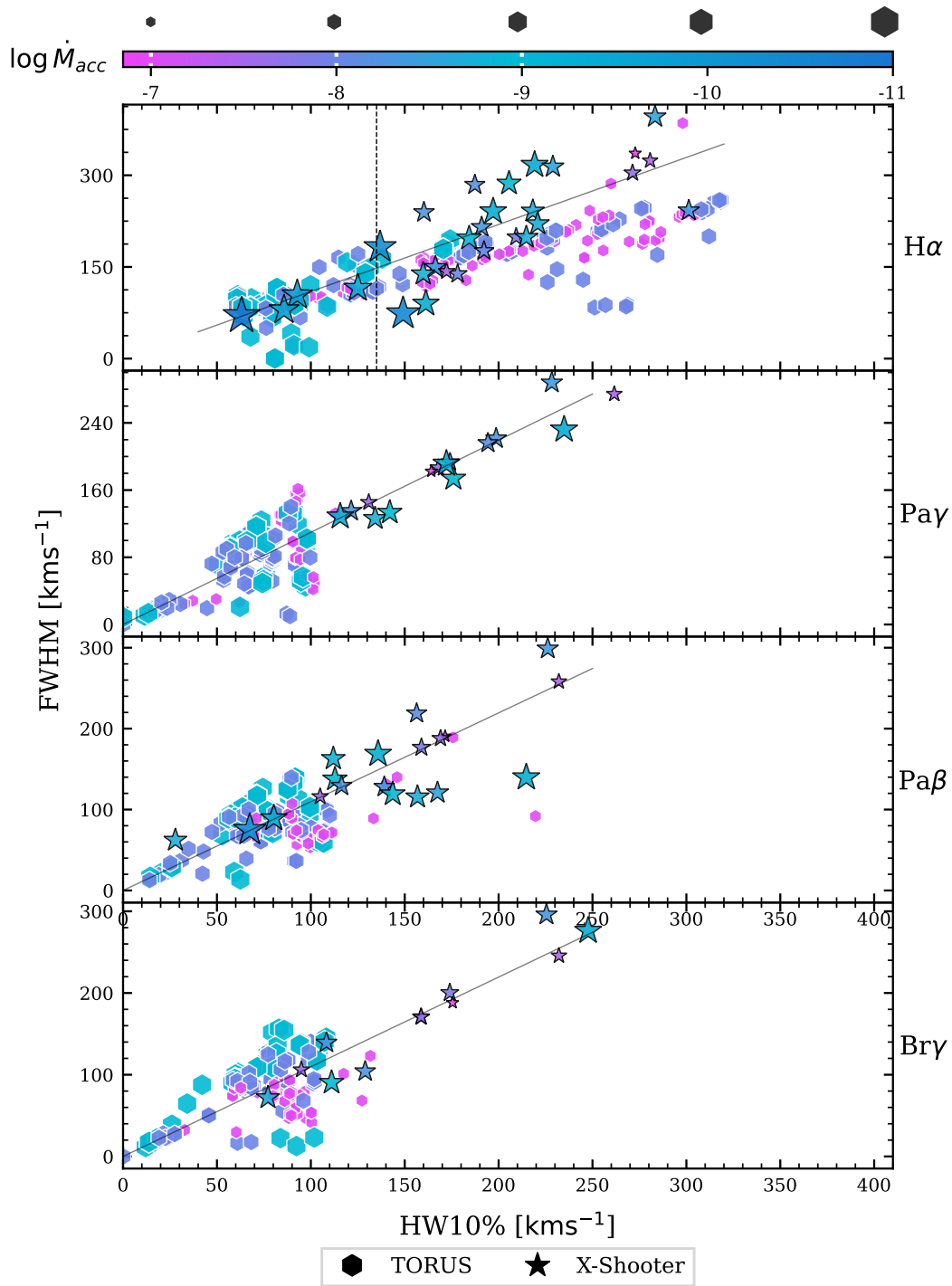


Figure 4.6: The FWHM vs. HW10% for observed (black outlined stars) and TORUS data (coloured hexagons). The colour denotes the accretion rate. The vertical dashed line shows the H α split between WTTS and CTTS (White & Basri 2003). The diagonal black line is the analytical Gaussian relationship between the FWHM and the HW10%.

FWHM/HW10% than other accretion rates.

Fig. 4.7 compares the ratio of the peak Pa β to Br γ versus the accretion rate for the synthetic and observed line profiles. Note that all synthetic Pa β and Br γ profiles in our complete grid are included in this figure. Because our T Tauri observations (see Chapter 3) are not corrected for veiling and ISM extinction, there is an uncertainty to the line ratios. Therefore, I have also included the line ratios of a sample of classical T Tauri stars from Muzerolle et al. (2001) and Muzerolle et al. (1998a). The observed line ratios of both data sets are in accord and typically have values between three and seven. Furthermore, the ratios are constant across a wide range of accretion rates ($\log \dot{M}_{\text{acc}} = -6.3$ to -9.4). The synthetic profiles show that as the accretion rate decreases, the ratio of Pa β to Br γ increases because the emission of Br γ decreases more rapidly. To duplicate the line ratios observed, higher temperatures are needed at lower accretion rates, which was also seen by Muzerolle et al. (2001). The constant line ratio observed across the range of accretion rates indicates that there may be a mechanism for increasing the temperature of the accretion flow as the accretion rate decreases.

4.2.1 Reipurth classification

Following the framework given by Reipurth et al. (1996) and outlined in Chapter 3.3.1, the synthetic line profiles were classified using a PYTHON routine. The code worked by finding peaks and troughs using a gradient search and using them to classify the lines with the following order of precedence: *IV*, *I*, *II*, and *III*. The programme defines type *IV* as being a sub-continuum absorption with no further emission greater than 0.01 of the maximum line flux. If the profile contains both red and blue-shifted absorption, the deepest feature is used to classify the line. Many profiles have type *II* or *III* features along with type *IV*. To avoid any classification bias, the synthetic spectra were classified using the same order of precedence as the X-Shooter observations.

Fig. 4.8 displays the results of the classification of synthetic spectra as hashed bars that overlay the distribution of the observed Reipurth types. The distribution of types for the synthetic H α lines shows a distribution similar to the observations, with the majority concentrated in type *I*. The H α distribution differs significantly from the observations for type *IVR*. Inverse P-Cygni profiles are seen in 35 per cent of the synthetic H α lines; whereas, only 3.4 per cent of the observations (1 spectra) exhibit this morphology. However, the H α inverse P-Cygni profiles are only present in models that would be classified as Weak Line T Tauri stars, based on the H α 10 per cent width criteria of White & Basri (2003). IPC profiles are seen in the spectra of one of the 29 T Tauri stars (Reipurth et al. (1996) observed two out of a sample of 43), approximately 3.4 per cent. From Fig. 4.5, it can be seen that

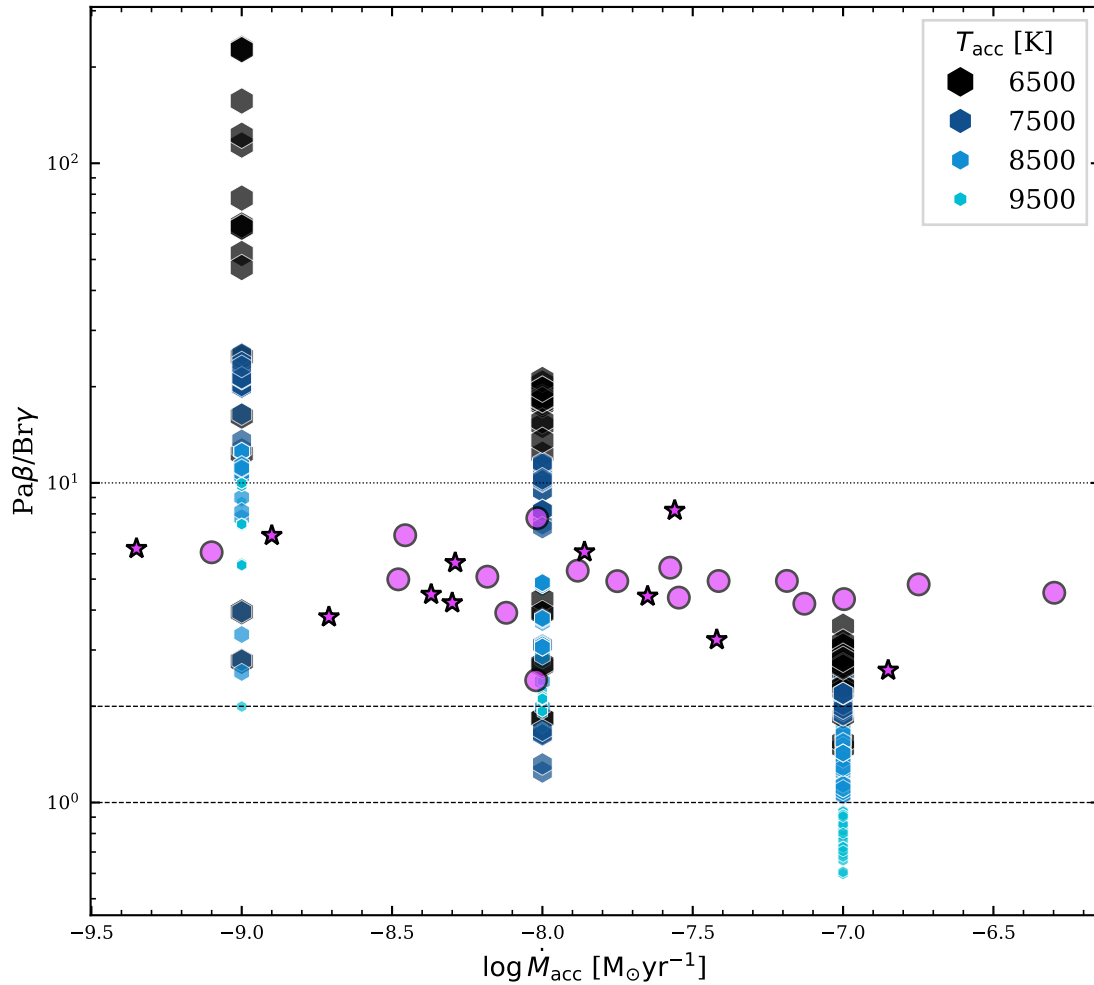


Figure 4.7: Ratio of Pa β to Br γ versus accretion rate the X-Shooter data (pink stars) the T Tauri sample of Muzerolle et al. (2001) (pink circles) and the synthetic line profiles (hexagons). The horizontal dotted lines indicate the Pa β /Br γ ratios of 1, 2, and 10. The colour of the hexagons indicate the magnetospheric temperature.

despite the uniform grid of parameters, the HW10% distribution is not uniform. A greater number of profiles are produced with a lower HW10%, these profiles predominantly have inverse P-Cygni features and account for the excess of type *IVR* profiles. Blue-shifted sub-continuum absorption (type *IVB*) is relatively rare for H α and only seen in 7 per cent of synthetic profiles; see § 4.2.2 for further discussion.

Unlike the relative agreement seen for H α , synthetic infrared lines predict a significantly higher frequency of P-Cygni profiles; ≈ 98 per cent are of type *IVR* or *IVB*. However, across all three infrared lines, the mean frequency of IPC profiles in the X-Shooter sample is ≈ 23 per cent and none of the infrared observations exhibit blue-shifted sub-continuum absorption. Comparatively, Folha & Emerson (2001) saw a frequency of type *IVR* profiles

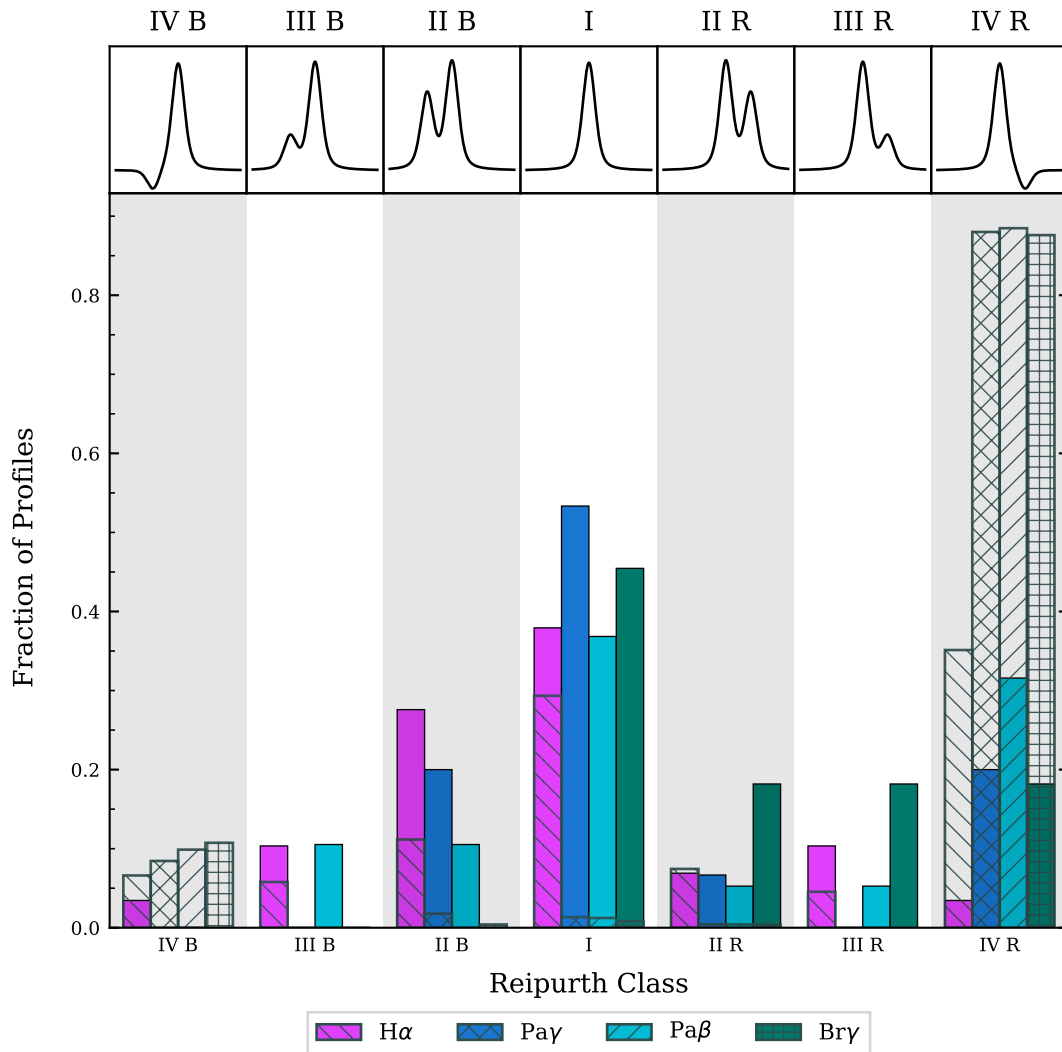


Figure 4.8: Relative fraction of Reipurth types. The coloured bars indicate the results for the X-Shooter observations and the hashed bars for the synthetic TORUS grid. The results are subdivided by hydrogen transition and an example profile of each type is shown at the top. The hashed bars over plotted are the classification of the corresponding hydrogen transition.

of 34 and 20 per cent for Pa β and Pa γ , respectively. Furthermore, they did not observe any type *IVB* profiles in their sample of 50 T Tauri stars. For the chosen parameters of our model grid, the synthetic line profiles show a much higher occurrence of deep-absorption features than that present in our observed sample. I explore possible modifications to the model in § 4.3 and further discuss them in § 4.4.

The mean signal-to-noise ratio (SNR) of the X-Shooter spectra is ≈ 70 for the VIS arm and ≈ 108 for the NIR. These values are taken as the mean over the whole VIS and NIR arms of X-Shooter. The mean ratio of the peak emission to the depth of the sub-continuum absorption (EAR) for the synthetic type *IV* profiles is ≈ 3 and ≈ 4 for the optical and infrared lines, respectively, see Fig. 4.9. Hence, the sub-continuum absorption features in

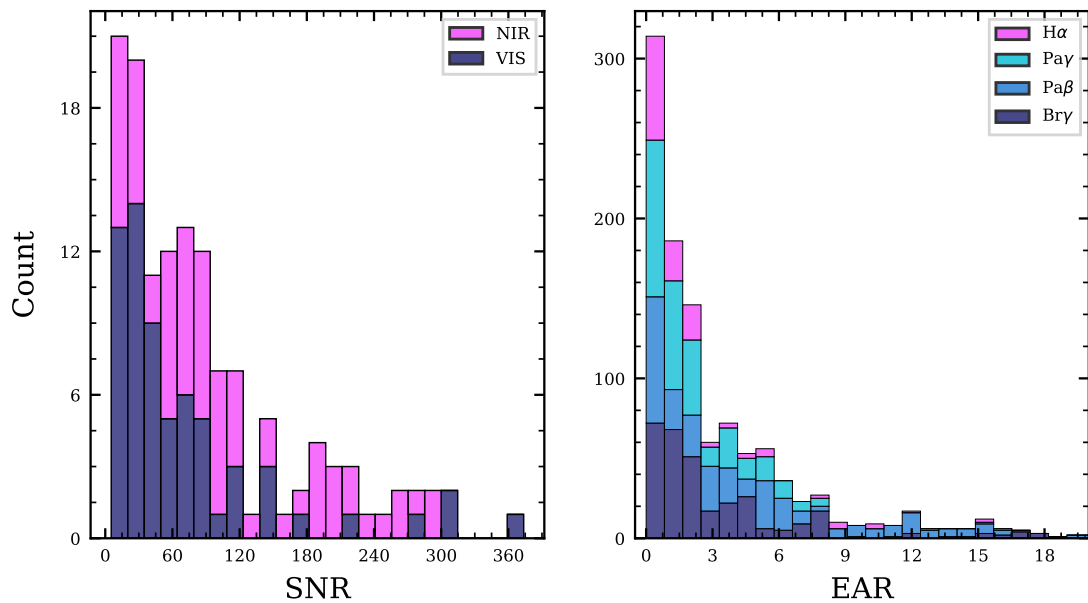


Figure 4.9: Left-hand panel shows the distribution of SNR for the VIS and NIR arms of X-Shooter. The right-hand panel shows the distribution of the ratios of the peak emission to the depth of the sub-continuum absorption (EAR) for the different hydrogen wavelengths in the synthetic data.

the synthetic grid are 18 – 25 times greater than the observed noise level. Consequently, the effect of the noise is not expected to significantly influence the Reipurth classifications of the synthetic profiles.

4.2.2 P-Cygni profiles

Blue-shifted sub-continuum absorption (a P-Cygni profile) is created in our model by the outflowing gas and is a good tracer of the stellar wind. In the observed T Tauri stars, there is a single P-Cygni profile for the $H\alpha$ spectra of Ass Cha T 2-52. As can be seen in Fig. 4.8, the frequency of P-Cygni profiles in our grid is ≈ 10 per cent. The blue-shifted sub-continuum absorption features in our grid are broad ($\approx 100 \text{ km s}^{-1}$), consistent with line profiles produced by the stellar wind models of Kurosawa et al. (2011).

P-Cygni profiles are seen in our grid at all three inclination of 20° , 60° , and 80° , but the majority is seen at 20° . $H\alpha$ P-Cygni profiles are primarily (92 per cent) seen for an inclination 20° ; the other eight per cent at an inclination of 60° . The depth of the blue-shifted absorption increases with the wind temperature and the largest fraction of P-Cygni profiles are seen with a wind temperature of 10^4 K . The line emission peak is inversely correlated with the wind temperatures. This is particularly apparent for the infrared lines because the higher energy levels five, six, and seven become depopulated before the upper $H\alpha$ level (three). This inverse relationship does not hold at a high wind

temperature (2×10^4 K), where the wind emission dominates the emission of the accretion funnel. Fig. 4.10 presents the fraction of synthetic lines that exhibit P-Cygni profiles as

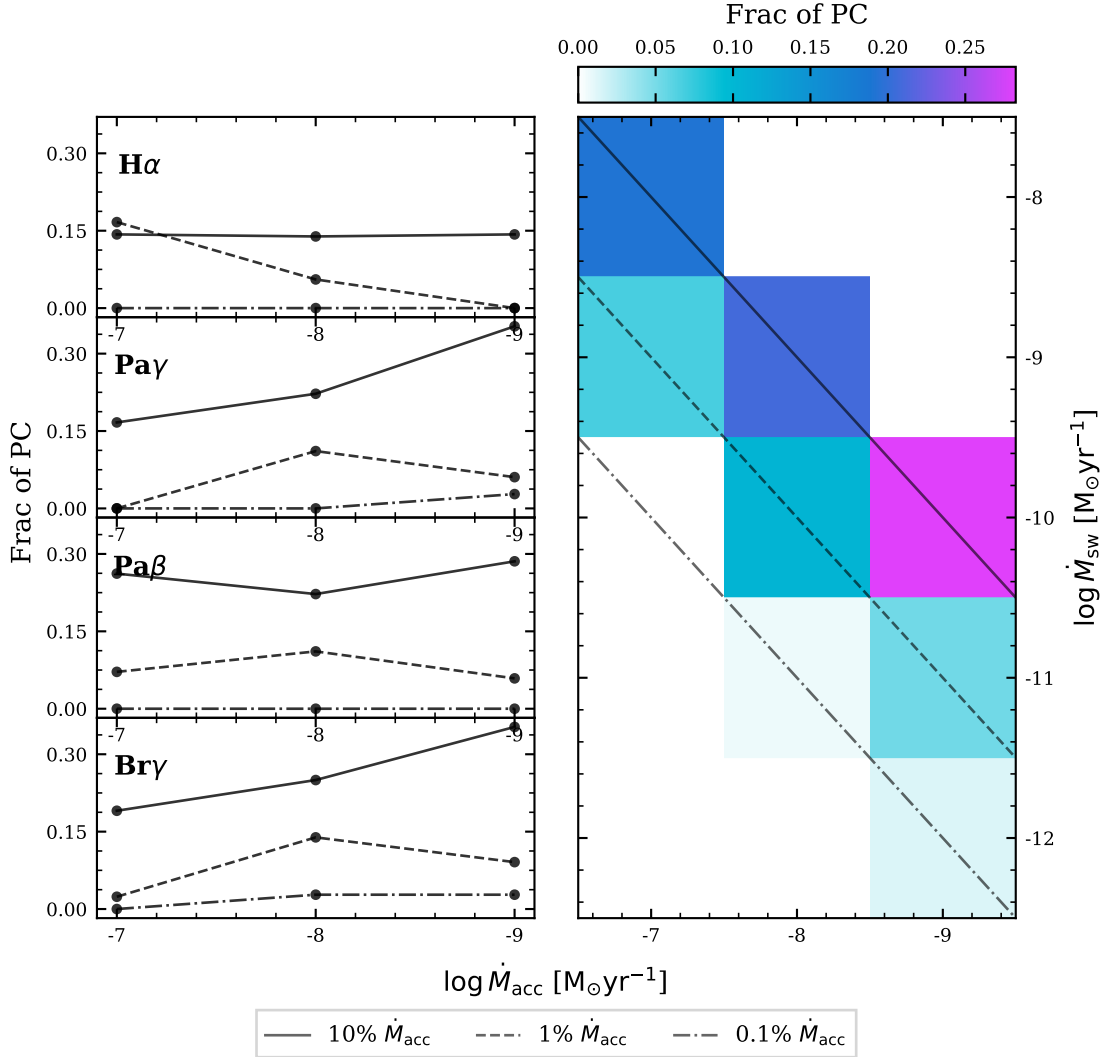


Figure 4.10: The right hand panels is a heatmap showing the total fraction of P-Cygni profiles for accretion rate versus mass-loss rate in the synthetic grid. The diagonal lines indicate constant mass-loss rates relative to the accretion rate. The left hand panel shows the fraction of P-Cygni profiles for different mass-loss rate subdivided by hydrogen transition.

a function of the rates of accretion and mass loss. It can be seen that the frequency of P-Cygni profiles is correlated with the ratio of $\dot{M}_{\text{sw}}/\dot{M}_{\text{acc}}$ and not \dot{M}_{sw} alone. For example, at a high accretion rate of $\log \dot{M}_{\text{acc}} = -7$, P-Cygni profiles are only observed at mass-loss rates of $\log \dot{M}_{\text{sw}} = -8$ and -9 . Whereas, for an $\log \dot{M}_{\text{acc}} = -8$ P-Cygni profiles are seen for mass-loss rates of $\log \dot{M}_{\text{sw}} = -9$, -10 and -11 with decreasing frequency. Similar results are seen for an accretion rate of $\log \dot{M}_{\text{acc}} = -9$. P-Cygni profiles were produced for mass-loss rates as low as $10^{-12} \text{ M}_{\odot} \text{yr}^{-1}$.

Additionally, Fig. 4.10 shows the fraction of P-Cygni profiles for different accretion

rates at the three fractions of the mass-loss rate, subdivided by hydrogen transition. Although a mass loss of 10% \dot{M}_{acc} generally produces the highest fraction of P-Cygni profiles, at an accretion rate of $\log \dot{M}_{\text{acc}} = -7$ a mass-loss rate of 1% \dot{M}_{acc} creates a larger frequency of H α P-Cygni profiles. A mass-loss rate of 0.1% \dot{M}_{acc} has the lowest proportion of P-Cygni profiles, and they are seen primarily for an accretion rate of $\log \dot{M}_{\text{acc}} = -9$. The higher optical depth of H α should make it a good tracer of the low-density stellar wind. However, in contrast to the expected and observed P-Cygni frequency, the H α profiles produce P-Cygni profiles with a frequency lower than that of the infrared lines.

4.3 Modified T Tauri model

The model grid does not adequately reproduce the observed frequency of the infrared line profile structures or the observed range of profile widths (§ 4.2). In the following section, I explore the effects of a few different modifications to the models in an attempt to discover the possible reasons for the discrepancies. In § 4.3.1, the effects of introducing turbulent broadening are examined. The influence of rotation on synthetic lines is introduced in § 4.3.2. Finally in § 4.3.3, the widths are re-evaluated, considering only the blue-shifted side, to determine the consequence of the high proportion of sub-continuum absorption on the widths of the line profiles.

4.3.1 Turbulent line broadening

It is expected that there will be unresolved small-scale motion in the T Tauri systems on top of the bulk gas flows. For instance, from unsteady accretion or wind flow, instabilities in the accretion, or post-accretion shock gas. The effect of Stark broadening on the infrared lines is negligible and so it was considered that the small-scale motion in conjunction with Stark broadening could broaden the observed lines and reduce the frequency of sub-continuum absorption features.

To explore the effect of turbulent broadening on the infrared line widths, the effect of this small-scale motion was incorporated into the models. I assume that the unresolved velocity is everywhere in the grid and acts like a form of turbulence, i.e. a Maxwell–Boltzmann velocity distribution. I used a value of $v_{\text{turb}} = 100 \text{ km s}^{-1}$, which is approximately the largest difference in the median HW10% of the observed and synthetic infrared lines; see § 4.2. There is little physical justification for the turbulent velocity to be as high as 100 km s^{-1} , other than it is the required velocity to sufficiently broaden the ensemble of line profiles.

Fig. 4.11 shows the FWHM versus the HW10% for the Stark and turbulently broad-

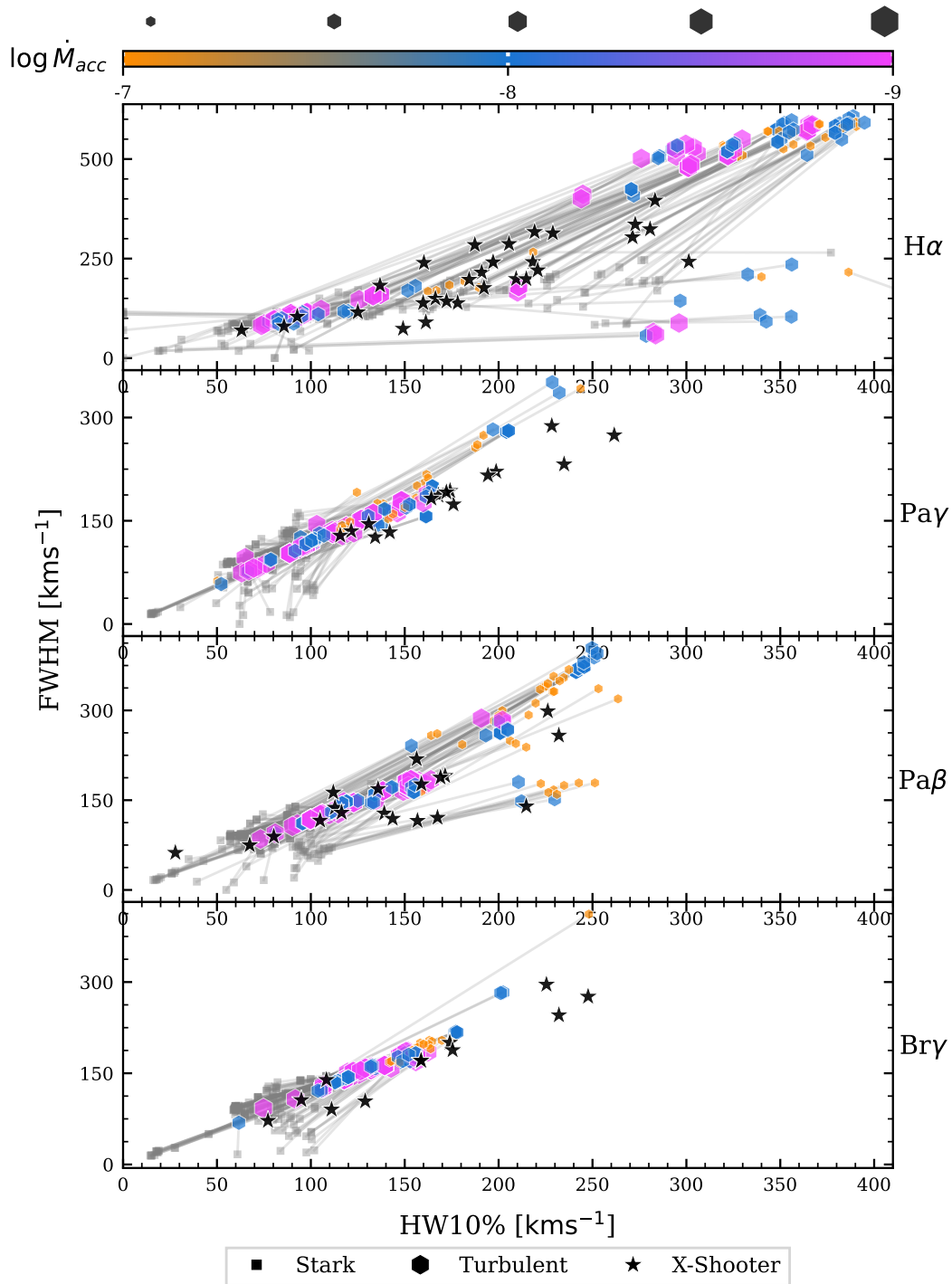


Figure 4.11: The effect of combining 100 km s^{-1} of turbulent broadening with Stark broadening. Grey squares are the original Stark only broadened profiles from TORUS, and the coloured hexagons are the Stark and turbulent broadened profiles. The grey lines connect the two different models.

ened lines and the Stark-only broadened lines. Similarly to Fig. 4.6, the profiles are filtered so that only models with a $H\alpha$ HW10% between $60 - 400 \text{ km s}^{-1}$ are included. Turbulent broadening increases the $H\alpha$ line too much, pushing the median value of HW10% to $\approx 320 \text{ km s}^{-1}$. The effect on the infrared lines is to bring the range of predicted values to be largely overlapping with the observed data. Turbulent broadening increases the number of synthetic lines that have HW10% greater than 400 km s^{-1} by 4%.

The full set of turbulently broadened line profiles can be seen in Fig. 4.12. The figure shows the line profiles organised by spectral line (columns) and inclination (rows). The effect of the turbulence is to create a boxier profile; steep sides with flat tops. The added turbulent velocity increases the resonant range of the transition wavelength, broadening both the emission and absorption features. This “top-hat” morphology is not seen in the observed data. The distribution of the Reipurth classifications is not significantly changed by the turbulence and a high proportion of inverse P-Cygni profiles are still predicted. The boxier profiles increase the ratio between the FWHM and the HW10%, creating a steeper relationship than seen for a Gaussian or a Voigt profile.

In conclusion, the turbulent broadening produces an infrared range of line widths in better agreement with the observations. This modification causes the width of the $H\alpha$ lines to become boxy, a morphology not reflected in the observations. A smaller value of v_{turb} will reduce the top-hat like morphology but will not increase the width of infrared line profiles sufficiently. Furthermore, the frequency of sub-continuum absorption is not significantly changed, suggesting that incorporating unresolved small-scale motions into the simulations cannot solely account for the lack of width in the infrared lines. This is especially true since there is no strong physical motivation for the turbulent motion to be as high as 100 km s^{-1} .

4.3.2 Rotational line broadening

The line profiles presented in § 4.1 are computed for a non-rotating T Tauri model. In principle, the Doppler shift from rotational motion should broaden the line profiles. Thus, to explore whether this improved the fit of the model to the data, I ran a small grid of rotating models with a wind velocity as prescribed in Chapter 2.3.1.4.2. The magnetosphere is treated as a solid body that rotates with the star. The models were computed at two rotation velocities, $0.05 v_{\text{br}}$ (13.4 km s^{-1}) and $0.5 v_{\text{br}}$ (134 km s^{-1}), where v_{br} is the stellar break-up velocity, taken to be the balance of gravitational and centrifugal forces without considering the effects of an equatorial bulge such that

$$v_{\text{br}} = \sqrt{GM R_*^{-1}}. \quad (4.2)$$

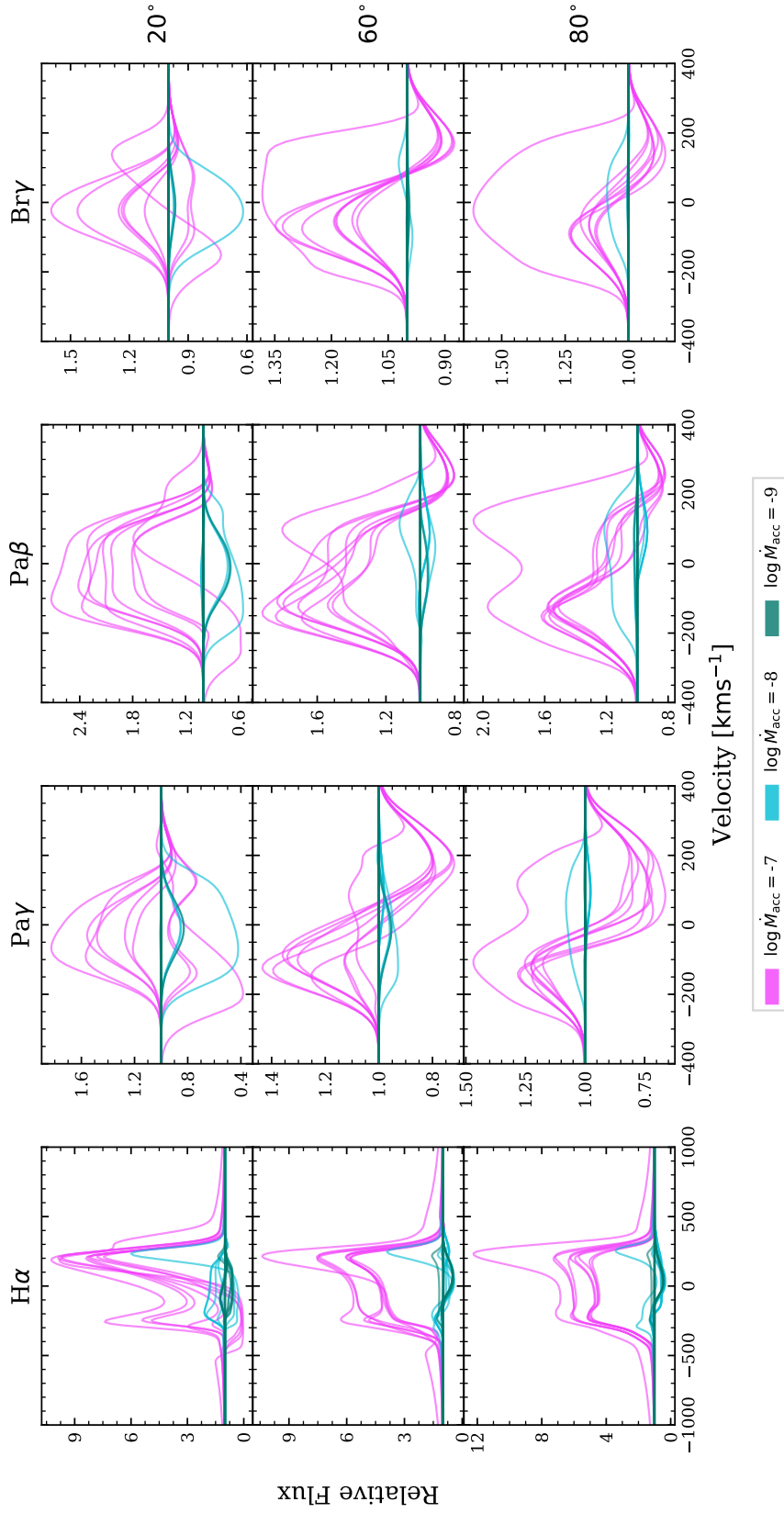


Figure 4.12: Turbulently broadened TORUS line profiles arranged by wavelength (column) and inclination (row). The profiles are boxy with a 'top-hat' like appearance and the sub-continuum absorption features are broadened. Note that the ranges on the axes vary. Models presented here for accretion temperatures of $T_{\text{acc}} = 6500$ and 7500 K.

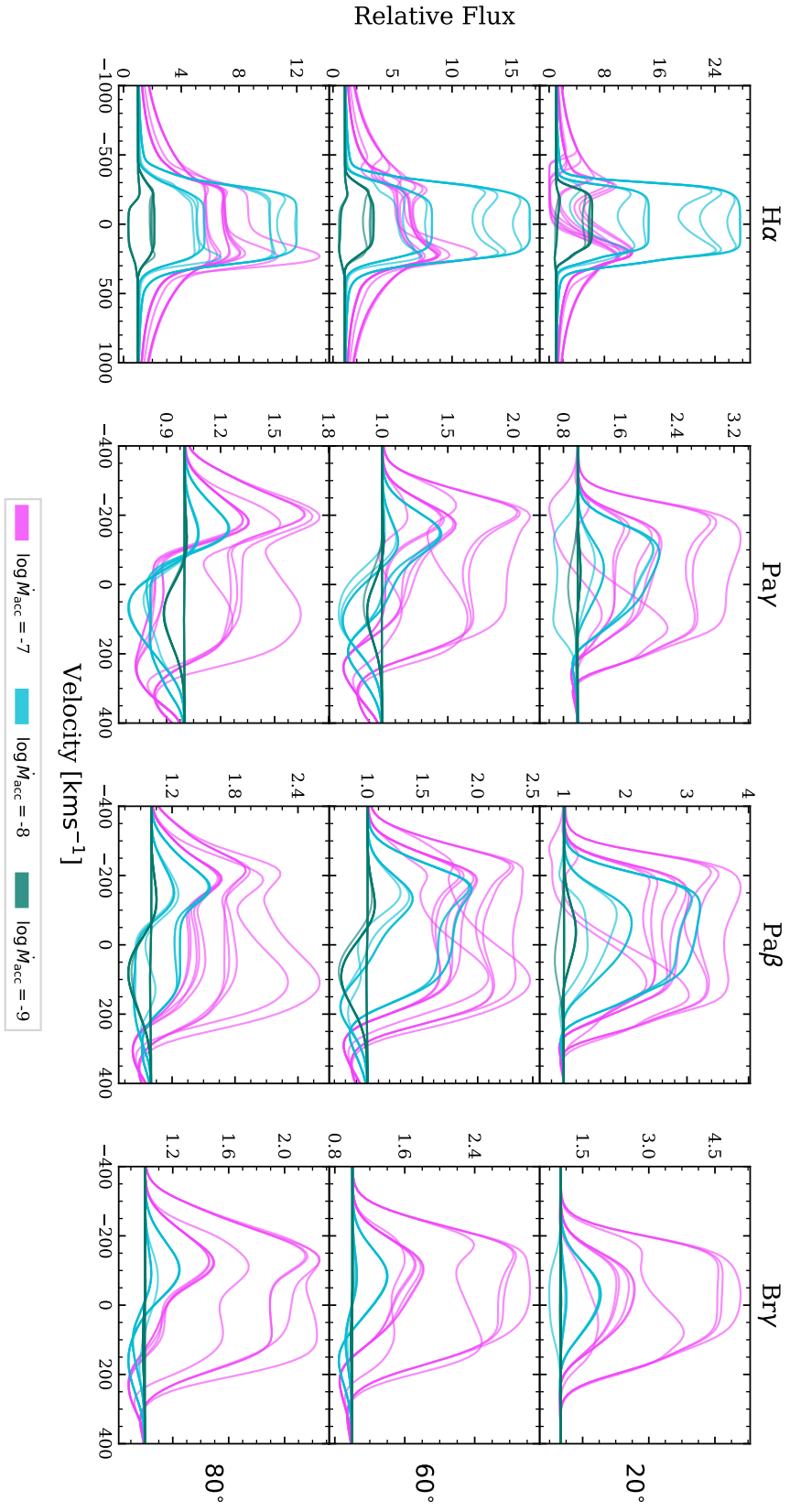


Figure 4.12: Continued. Models presented here for accretion temperatures of $T_{acc} = 8500$ and 9500 K.

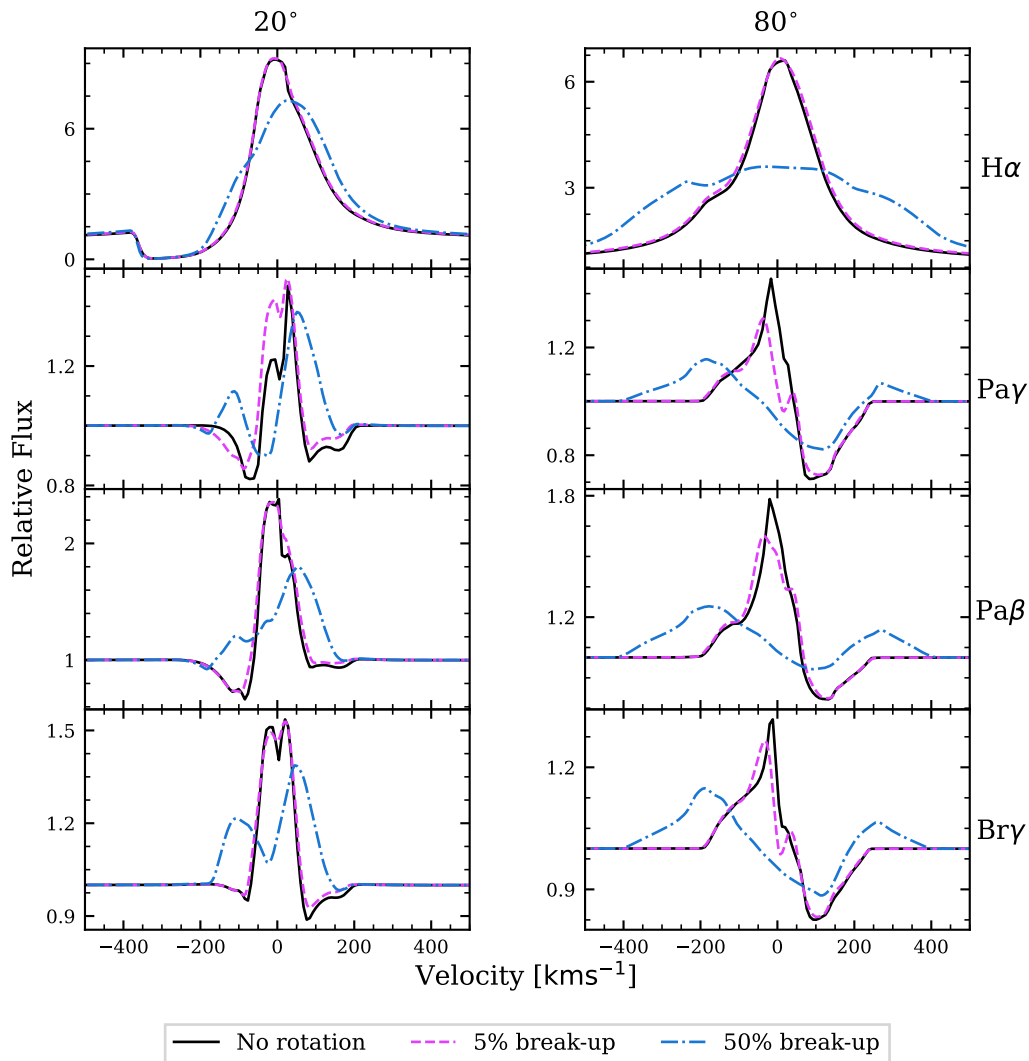


Figure 4.13: The effect of rotation on line profiles. The profiles are shown for three different rotation rates: no rotation (solid line), $0.05 v_{\text{br}}$ (pink dashed line), and $0.5 v_{\text{br}}$ (blue dash-dotted line). The profiles are arranged by viewing inclination (columns) and wavelength (rows). At high rotation rates, the profiles are flattened and broadened.

T Tauri stars are typically slow rotators (e.g. [Bouvier et al. 2014](#)). However, I include a model with a rotation rate of $0.5 v_{\text{br}}$ so as to be able to compare the effect of an extreme case with a more realistic rotation rate. The models have an accretion rate of $\log \dot{M}_{\text{acc}} = -7$, a mass-loss rate of $\dot{M}_{\text{sw}} = 0.1 \dot{M}_{\text{acc}}$, a maximum accretion funnel temperature of $T_{\text{acc}} = 7500$ K, and a stellar wind temperature of $T_{\text{sw}} = 8000$ K. Fig. 4.13 shows the line profiles for the rotating and the non-rotating case.

The profiles are smoothed and broadened by rotation. However, this effect is negligible unless the rotation is at a significant proportion of the stellar break-up velocity. For example, a rotation velocity of $0.05 v_{\text{br}}$ had no effect on $\text{H}\alpha$, while for $\text{Pa}\gamma$ and $\text{Pa}\beta$, the peak intensity was reduced by ≈ 10 per cent for an inclination of 80° . On the other hand,

a rotation rate of $0.5 v_{\text{br}}$ significantly broadens the synthetic profiles when viewed from a high colatitude. The peaks are shifted away from the rest velocity as the hot, high-density gas in the magnetosphere dominates the emission. Estimates of $v \sin i$ and the rotation as a fraction of the break-up velocity for the X-Shooter stars are shown in Table 4.3. V354-Mon has the highest rotation rate in the data set with a velocity of $v \sin i = 40.9 \text{ km s}^{-1}$, only 11 per cent of the star's break-up velocity. The rotation rates in our observed data set are not large enough to cause significant line broadening. Therefore, rotational broadening cannot explain the mismatch between the observed and synthetic line widths.

4.3.3 Blue-shifted emission

More than 80 per cent of the synthetic infrared line profiles have inverse P-Cygni features, significantly more frequent than the ~ 23 per cent seen in the observations; see § 4.2.1. The red-shifted sub-continuum absorption reduces the width of the emission profiles. Thus, if the model were modified to reduce the frequency of red-shifted sub-continuum absorption, we can expect that the average line widths would also increase. A possible mechanism for removing the red-shifted absorption is by introducing a non-axisymmetric accretion flow where the accreting column only periodically intersects with the line of sight. For example, Esau et al. (2014) used a non-axisymmetric accretion flow to reproduce the Balmer variations seen for AA Tau successfully; this effect is discussed further in § 4.4.

To estimate how much the inverse P-Cygni absorption might affect the line widths in our models, I calculated the HW10% values using only the blue side of each synthetic line profile (HW10%_{Blue}). I employed a linear interpolation of the line that was blue-shifted from the peak to determine values of the profile width. Fig. 4.14 shows the HW10%_{Blue} versus the true HW10%. The diagonal line (black dashed) shows the one-to-one ratio; points below the diagonal indicate that the width decreased when considering only the blue side. The points are coloured, denoting the inclination of the model. For a viewing angle of 20° , the majority of line widths decreased when only the blue-shifted emission was considered. The blue sides of these modelled lines are narrower than the red because of the strong blue-shifted absorption from the stellar wind, which lies along the line of sight at this inclination. Fig. 4.14 also shows the distribution of the width change ($\Delta \text{HW10\%}$) as a series of histograms. The mean change in HW10% for all models with inclination of 60° or 80° is 48 km s^{-1} . When only models with a low mass-loss rate ($0.001 \dot{M}_{\text{acc}}$) are considered, the average increase in width is $\approx 50 \text{ km s}^{-1}$ for inclinations of 60° and 80° . The change in measured HW10% is consistent across all four hydrogen lines, H α is broadened similarly to the infrared lines. The mean changes in width for different inclinations and hydrogen transitions are tabulated in Table 4.4.

Table 4.3: Stellar rotation rates

Table showing the rotation rates for the observed X-Shooter stars. References are: 1 [Nguyen et al. \(2012\)](#), 2 [Baxter et al. \(2009\)](#), 3 [Frasca et al. \(2015\)](#), 4 [Kounkel et al. \(2019\)](#), 5 [Malo et al. \(2014\)](#), 6 [Manara et al. \(2016\)](#), 7 [Schneider et al. \(2018\)](#), 8 [Manara et al. \(2014\)](#), 9 [McGinnis et al. \(2015\)](#), and 10 [Rugel et al. \(2018\)](#).

Name	L_* [L_\odot]	R_* [R_\odot]	$V \sin i$ [kms^{-1}]	$\frac{V \sin i}{V_{br}}$	Reference
ESO-Ha-562	0.12	0.8	40	0.1	1,6
IQ-Tau	0.75	1.9	14.4	0.05	1,6
V354-Mon	1.67	1.8	40.9	0.11	2,7
T-33	0.69	1.1	16.5	0.04	3,6
T-11	1.45	1.7	14.1	0.04	3,8
VW-Cha	1.64	2.6	13	0.04	1,6
V409-Tau	1.17	1.5	34	0.09	1,8
CR-Cha	3.26	2.3	35	0.09	1,6
T-52	2.55	2.0	28	0.08	1,6
T-38	0.13	0.8	18.7	0.05	1,6
KV-Mon	~	~	24.25	~	4,9
Sz-22	0.51	1.3	~	~	6
T-4	0.43	1.3	12.4	0.03	1,6
DG-Tau	1.55	2.2	24.7	0.07	1,6
T-23	0.32	1.8	9.6	0.05	3,6
RECX-12	0.23	1.4	6.4	0.03	5,10
Cha-Ha-6	0.07	1.0	~	~	6
T-12	0.15	1.3	10.7	0.06	1,6
CT-Cha-A	1.5	2.2	7.8	0.02	1,6
ESO-HA-442	~	~	~	~	
CHX18N	1.03	1.4	26.5	0.07	1,6
TW-Cha	0.38	1.2	11.3	0.03	1,6
RECX-6	0.1	0.9	~	~	10
T-49	0.29	1.6	8.2	0.04	1,6
T-35	0.33	1.2	21	0.05	1,8
T-45a	0.34	1.2	12.4	0.03	1,6
RECX-9	0.095	1.1	~	~	10
T-24	0.4	1.4	10.5	0.03	1,6
Hn-5	0.05	0.8	7.8	0.04	1,6

The above analysis suggests that if the models were modified in some way to reduce the prevalence of inverse P-Cygni absorption, the synthetic line profiles would become significantly wider by an average of $\approx 48 \text{ kms}^{-1}$. A mean increase of $\approx 80 \text{ kms}^{-1}$ (see § 4.2) is needed to shift the HW10% of the synthetic infrared lines into agreement with the observations. Therefore, while this effect cannot account for the whole disparity of widths on its own, when combined with other mechanisms, such as turbulence and rotation, it

Table 4.4: The mean differences between HW10\% and $\text{HW10\%}_{\text{Blue}}$.

Inclination	$\text{H}\alpha$	$\text{Pa}\gamma$	$\text{Pa}\beta$	$\text{Br}\gamma$
		[kms^{-1}]		
20°	-0.7	-5.9	-4.3	-5.7
60°	40.1	40.7	39.8	41.7
80°	52.8	57.4	54.1	58.4

may be sufficient.

4.4 Discussion

A significant caveat to our comparison of the observed and synthetic line profiles is the possibility that our observed data are incongruous and not representative of the consensus of T Tauri stars. However, our sample of 29 stars appears to be consistent with other observational data. For example, the sample has a fraction of Reipurth classes similar to the distributions reported by Reipurth et al. (1996) for $\text{H}\alpha$ and Folha & Emerson (2001) for $\text{Pa}\beta$ and $\text{Br}\gamma$. Furthermore, the peaks of the $\text{Pa}\beta$ and $\text{Br}\gamma$ lines are slightly blue shifted, in agreement with Folha & Emerson (2001), although the mean FWHM of our line profiles is smaller than the mean FWHM reported by Folha & Emerson (2001). The lines profiles observed showed little correlation between the strength of $\text{H}\alpha$ and the strength of the infrared lines. No correction for veiling has been applied to the spectra in Fig. 3.5 making this result difficult to interpret. However, some stars, e.g. Cha Ha 6, have $\text{H}\alpha$ emission but no infrared emission. This demonstrates that the fourth electron level is relatively populated in some stars, while the gas does not have a significant proportion of hydrogen with electrons in levels five, six and seven.

A second caveat is that our grid of synthetic line profiles was not adjusted to agree with any particular observation; a singular stellar mass, radius, and temperature were used. Broadly speaking, the synthetic line profile morphology is determined by the magnetosphere's geometry, accretion rate, and temperature. Consequently, our grid was designed to encompass the broad range of parameters predicted for T Tauri accretion and outflow (e.g. Hartmann et al. 1994; Muzerolle et al. 1998b, 2001; Kurosawa et al. 2006; Lima et al. 2010; Kurosawa & Romanova 2012). In turn, our T Tauri sample has an extensive range of accretion rates and stellar parameters, making it an appropriate initial data set for a comparison with the ensemble of synthetic spectra.

Our models predict a greater number of $\text{H}\alpha$ inverse P-Cygni profiles than observed. However, our grid of models can reproduce the observed fraction of $\text{H}\alpha$ Reipurth types after the lines classified as weak line T Tauri stars (≈ 40 per cent) are removed. The models

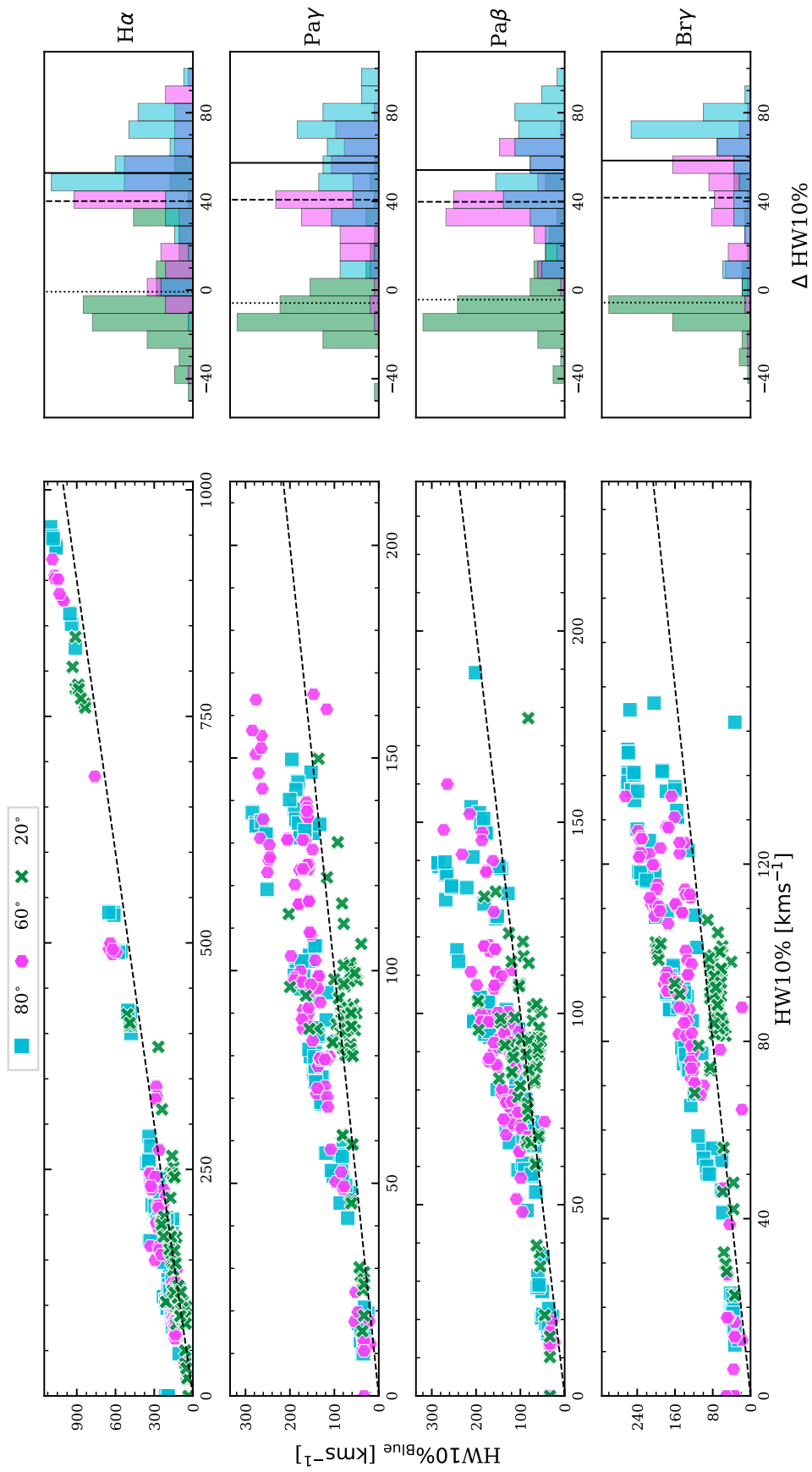


Figure 4.14: Comparison of the true $HW10\%$ and half width measured only for blue-shifted emission. The dashed diagonal line has a gradient of unity; the points above it are broader when only the blue-shifted emission is considered. The colour and style of the points denote the inclination of the model. On the right are histograms showing the difference of the two measured widths. The vertical lines indicate the respective means: 20° dotted, 60° dashed, and 80° solid.

can be classified as Weak Line T Tauri stars based on the equivalent width criterion of 10 \AA (Herbig & Bell 1988) or the HW10% criteria of White & Basri (2003) to the same effect. By removing the weak line T Tauri models, I discard the $H\alpha$ models that contain red-shifted sub-continuum absorption. Hence, for our model grid, inverse P-Cygni profiles are only produced by models that would be classified as Weak Line T Tauri stars. This result is substantiated by Kurosawa et al. (2006) who demonstrated that the inverse P-Cygni profiles in $H\alpha$ were only produced in ≈ 5 per cent of their sample. Moreover, in these cases, the accretion rate was low enough that the lines would be consistent with a weak line T Tauri classification.

The same models that correctly reproduce the observed $H\alpha$ Reipurth types predict a very high frequency of inverse P-Cygni profiles for $Pa\beta$, $Pa\gamma$, and $Br\gamma$. For $H\alpha$, Stark broadening smooths out the synthetic spectra, masking the absorption features (Muzerolle et al. 2001). However, for the infrared lines, the effect of Stark broadening is negligible at the temperatures and densities expected in T Tauri accretion. A possible reason for the dearth of observed inverse P-Cygni profiles is non-axisymmetric accretion flow. A magnetic obliquity from the stellar pole could cause the accretion funnel to form “curtains” that rotate with the star. Inverse P-Cygni profiles would then be seen intermittently when the accretion curtain intersects the line of sight. Observations support this effect; for example, McGinnis et al. (2020) measured a magnetic obliquity of $18^{\circ+8}_{-7}$ for DK Tau and observed an inverse P-Cygni profile for two of the eight epochs. Accretion funnel “curtains” have also been explored in radiative transfer studies. For instance, Symington et al. (2005a) used a 3D non-axisymmetric model to reproduce some of the observed variability seen in T Tauri stars, but in general, the models produced results that were too variable. Esau et al. (2014) successfully modelled variable Balmer emission from AA Tau with a non-axisymmetric accretion model, and Alencar et al. (2012) reproduced Balmer lines from V2129 Oph over several stellar rotational cycles. Further analysis of T Tauri time-series spectroscopic surveys would be helpful in better quantifying the variability of inverse P-Cygni profiles across multiple wavelengths.

In addition to the red-shifted features of the magnetosphere, some interesting blue-shifted features were created by the stellar wind. The stellar wind produced the characteristic broad sub-continuum absorption feature noted by Kurosawa et al. (2011). P-Cygni features occur in ≈ 10 per cent of the synthetic profiles, whereas P-Cygni profiles are rare in our observations, with none exhibited for the infrared lines. The infrared lines are optically thinner than $H\alpha$, and therefore less sensitive to the lower-density wind. P-Cygni profiles were also observed to be rare by Folha & Emerson (2001) and Edwards et al. (2006). The reason why these mass-outflow signatures are scarce in the observations could be due to the geometry, temperature, or mass-loss rate. Geometry should signif-

icantly reduce the frequency of fast wind absorption since these winds are likely to be collimated (Edwards et al. 2006) and therefore may not intersect the line of sight at high inclinations. $H\alpha$ is optically thicker than the infrared lines, making it a better tracer of low-density gas, such as the wind. However, the infrared lines of our grid produced a higher frequency of P-Cygni profiles than $H\alpha$, ~ 11 and ~ 8 per cent, respectively. This may be due to Stark broadening effects smoothing out the absorption features for $H\alpha$ and the relatively high density ($\approx 5 \times 10^{-12} \text{ g cm}^{-3}$) gas at the foot of the wind being optically thick for $\text{Pa}\gamma$, $\text{Pa}\beta$, and $\text{Br}\gamma$. Lima et al. (2010) showed that for $H\alpha$ a mass-loss rate from the inner disk of at least $10^{-9} M_{\odot} \text{ yr}^{-1}$ was needed for the blue-shifted absorption features to be shown. However, for our polar stellar wind, the models produced $H\alpha$ blue-shifted sub-continuum absorption for mass-loss rates as low as $10^{-12} M_{\odot} \text{ yr}^{-1}$. Additionally, our results suggest that the frequency of synthetic P-Cygni profiles depends on the ratio of mass loss to mass accretion, not the mass-loss rate alone. This is because higher accretion rates increase magnetospheric and hot-spot emission, which masks the absorption features from the wind.

Muzerolle et al. (2001) noted that the ratio of $\text{Pa}\beta$ to $\text{Br}\gamma$ was consistent for a sample of T Tauri stars at different accretion rates. The ratio of the peak fluxes of $\text{Pa}\beta$ to $\text{Br}\gamma$ from our sample of T Tauri stars was compared with the sample from fig. 15 of Muzerolle et al. (2001) and found to be in agreement despite the lack of veiling and ISM extinction corrections to our spectra. Similarly to the results of Muzerolle et al. (2001), our models show that for the synthetic line ratio of $\text{Pa}\beta$ to $\text{Br}\gamma$ to correspond to the observed line ratio, the magnetospheric temperature must increase as the accretion rate decreases. This is because the emission of $\text{Br}\gamma$ abates rapidly with the decrease in density produced by lower accretion rates. There must be a mechanism in the T Tauri systems that links the accretion temperature to the accretion rate.

Another factor seen in § 4.2 is that the infrared widths (FWHM and HW10%) of the synthetic and observed data do not agree. The models that produce $H\alpha$ profiles that lie within the observed range create Paschen and Brackett spectra that are too narrow by $\approx 80 \text{ km s}^{-1}$. Alencar & Basri (2000) suggested that rotation and turbulence may play an important role in the formation of the width of the line profiles. In agreement with Muzerolle et al. (2001), our results demonstrated that stellar rotation has a negligible effect on the line widths at the rotation rates seen in our observed sample. Furthermore, the level of turbulent motion needed to broaden the synthetic lines sufficiently to account for the difference in infrared line widths is very high ($\approx 100 \text{ km s}^{-1}$). Not only is there no apparent physical justification for such a considerable value of turbulence, but the spectra produced are broad and flat-topped, a morphology not seen in observations.

In addition to turbulence and rotation, I attempted to quantify the reduction in the

width of the spectra due to red-shifted absorption by calculating the width using only the blue-shifted emission; an approach similar to that adopted by [Alencar et al. \(2012\)](#) to compensate for poorly fitting red-shifted absorption. As expected ([Bouvier et al. 2007](#); [Alencar et al. 2012](#)), our analysis suggested that a significant change in the model geometry that could remove the inverse P-Cygni absorption, such as non-axisymmetric accretion, would account for a substantial increase in the infrared line widths. Alone, such a method may not be sufficient to account for the disparity between the synthetic and observed hydrogen profiles. However, if the models were to include some combination of stellar rotation, turbulence, and non-axisymmetric accretion, the synthetic profiles may be shifted into accord with the observations. Conversely, [Folha & Emerson \(2001\)](#) showed that, for their sample of Pa β and Br γ T Tauri spectra, the FWHM of Reipurth type *I* and type *IVR* profiles were not significantly different. This would indicate that spectra with inverse P-Cygni profiles are generally broader than those without them or that the sub-continuum absorption does not significantly narrow the spectra. There is not a sufficient population of type *IVR*'s in our sample to confirm this result.

Another factor not considered is the line emission from the accretion shock region. This work treats the accretion shock zone as a black body heated by the release of gravitational potential energy that adds to the continuum. However, the accretion regions will also have line emission (e.g. [Dodin 2018](#)) that will contribute to the observed spectra. A complete radiative equilibrium treatment of the shock region and magnetosphere is necessary to constrain this effect fully, which requires the development of a self-consistent theory of the heating and cooling mechanisms in the magnetosphere.

Summary

I presented a grid of synthetic T Tauri line profiles, computed using the radiative transfer code TORUS . The models are based on the magnetospheric accretion configuration originally developed by [Hartmann et al. \(1994\)](#) and developed further by [Muzerolle et al. \(1998b, 2001\)](#); [Symington et al. \(2005a\)](#); [Kurosawa et al. \(2006\)](#); [Lima et al. \(2010\)](#); [Kurosawa et al. \(2011\)](#). Our models also included a polar stellar wind launched from the star's surface, a more realistic development to the stellar wind used by [Kurosawa et al. \(2011\)](#). I compared our ensemble of models to the spectra of 29 T Tauri stars. The medium-resolution spectra covered a broad range of wavelengths that allowed me to simultaneously compare the H α , Pa β , Pa γ , and Br γ lines. The following conclusions are drawn.

- The observations exhibited similar Reipurth classifications, widths, and mean line

centres to those seen in other studies (e.g. [Folha & Emerson 2001](#); [Reipurth et al. 1996](#); [Edwards et al. 2006](#)).

- For $H\alpha$, our synthetic line profile grid was able to reproduce the observed distribution of Reipurth classifications and line widths. However, for the same models, the infrared lines could not reproduce the observed emission. The modelled lines were too narrow by $\approx 80 \text{ km s}^{-1}$, and the majority (≈ 90 per cent) had inverse P-Cygni profiles.
- The ratio of synthetic $\text{Pa}\beta$ to $\text{Br}\gamma$ peak intensities showed that higher magnetospheric temperatures are needed at lower accretion rates to match the observed infrared line ratios.
- I explored the effect of rotation and turbulence and determined that they could not sufficiently broaden the synthetic infrared line profiles or remove the inverse P-Cygni features. The red-shifted sub-continuum absorption was determined to narrow the HW10% of the lines by $\approx 48 \text{ km s}^{-1}$.
- The polar stellar wind produced the characteristic broad P-Cygni profiles as suggested by [Kurosawa et al. \(2011\)](#). Our models produced blue-shifted sub-continuum absorption with mass-loss rates as low as $10^{-12} M_{\odot} \text{ yr}^{-1}$. Furthermore, our results suggested that the frequency of P-Cygni profiles depends on the ratio of mass loss to mass accretion rate; the increased emission from higher accretion rates masks the blue-shifted absorption. Despite the higher optical depth of $H\alpha$, synthetic infrared lines produced a higher frequency of P-Cygni profiles than $H\alpha$.

In the next chapter, radiative transfer simulations of non-axisymmetric T Tauri models are presented and consideration is made to the phase-dependent variability seen in the synthetic line profiles.

Chapter 5

Non-Axisymmetric 3D Radiative Transfer

In Chapter 4, I presented axisymmetric T Tauri models; however, such a system is a special case. It is more probable that the magnetic and rotation axes are not aligned but offset by at least a few degrees. For example, [McGinnis et al. \(2020\)](#) saw a mean offset of 11.4° for their sample of 10 classical T Tauri stars with an RMS dispersion of 5.4° . [McGinnis et al. \(2020\)](#) measured the offset by monitoring the radial velocity variations, produced by the accretion shock, of the He I $\lambda 5876$ Å line. Magnetohydrodynamic models show that even when the magnetic field and rotation axes are aligned, the accretion funnel preferentially flows through one hemisphere over the other. Magnetic perturbations can shift the flow between hemispheres ([Ireland et al. 2021, 2022](#)). Therefore, a magnetic obliquity necessarily causes a non-axisymmetric magnetosphere, where the accretion flow adopts the most energy-efficient path to accrete from the disk to the star. Magnetohydrodynamic simulations of T Tauri stars with an offset magnetic dipole commonly predict a paradigm in which the alternate accretion columns (azimuthally constrained) form on either side of the star in opposite hemispheres (e.g. [Romanova et al. 2003](#); [Long et al. 2011](#)).

Non-axisymmetric accretion flow may account for some of the observed variability of T Tauri stars. As the T Tauri stars rotate, the accretion columns and hot spots move through the line of sight, altering the observed continuum and line emission. For instance, inverse P-Cygni profiles are only expected when the accretion column intersects the line of sight. In Chapter 4, I speculated that a reduction in the frequency of synthetic inverse P-Cygni profiles could explain the narrowness of the infrared line ensemble. Non-axisymmetric accretion flow may, by reducing red-shifted absorption, bring the widths of the infrared line profiles into better agreement with the observations.

[Symington et al. \(2005a\)](#) presented the first 3D radiative transfer models of T Tauri

stars with non-axisymmetric accretion flows. The authors showed that by confining the azimuthal extent of the accretion columns, the models produced spectral variations similar to those observed in T Tauri stars. However, [Symington et al. \(2005a\)](#) concluded that the rotational variability produced by the radiative transfer simulations was greater than that seen in the observations. In particular, they stated that the accretion model suggested by magnetohydrodynamic simulations (two accretion columns, one in each hemisphere on either side of the star) produced excessive variability at odds with observations. [Kurosawa et al. \(2005\)](#) compared time-series Pa β spectroscopy of SU Aurigae with non-axisymmetric accretion radiative transfer simulations. Their models used either a magnetosphere formed by modifying an axisymmetric accretion curtain by tilting it 10° relative to the rotation axis or by removing three equally spaced 10° gaps. They showed that their models could reproduce the variability of the equivalent width and the red-shifted absorption. [Kurosawa et al. \(2008\)](#) used the results of a magnetohydrodynamic model mapped onto a radiative transfer grid to study the induced variability of H α , Pa β , and Br γ . [Kurosawa et al. \(2008\)](#) showed that, in contrast to the conclusions of [Symington et al. \(2005a\)](#), the synthetic spectra predicted line variability in good agreement with observations. Additionally, their results demonstrated that the spectra of [Folha & Emerson \(2001\)](#) were consistent with models where the magnetic offset was small ($< 15^\circ$).

Clearly, 3D non-axisymmetric radiative transfer models are necessary for adequately simulating T Tauri accretion. For instance, both [Alencar et al. \(2012\)](#) and [Esau et al. \(2014\)](#) successfully reproduced some of the time-series spectroscopy variability of V2129 Oph and AA Tau, respectively, by using radiative transfer simulations based on magnetohydrodynamic models. [Dmitriev et al. \(2019\)](#) presented 3D radiative transfer models of T Tauri stars with an inclined magnetic dipole and introduced magnetospheric heating from accretion shock, based on the work of [Dodin \(2018\)](#). Using their new models, [Dmitriev et al. \(2019\)](#) demonstrated rotational modulation of synthetic spectra and line profiles that were similar to the theoretical results of [Muzerolle et al. \(1998b\)](#) and [Muzerolle et al. \(2001\)](#). However, extending the models to three dimensions only increases the degeneracy of the synthetic spectra and adds further free parameters to the already complex models. Therefore, a better understanding of how the geometry and accretion parameters shape spectral variability is paramount.

This chapter examines several non-axisymmetric 3D T Tauri models and the variability of the hydrogen spectra produced at different viewing inclinations, azimuthal angles, and wavelengths. In § 5.1, I present the models and the parameters used. § 5.2 analyzes the spectra and considers their variability. In § 5.3 and § 5.4, I attempt to quantify the changes in the Reipurth type and the width of the line profile in different rotational phases. Finally, in § 5.5, we discuss the results and attempt to quantify whether the 3D geometry

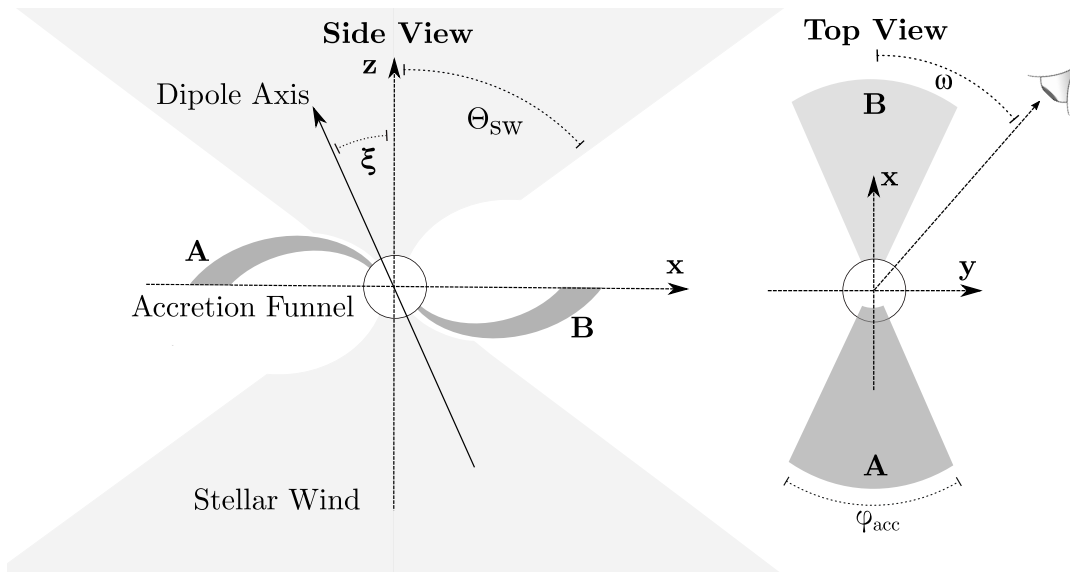


Figure 5.1: A cartoon showing the 3D accretion and wind model. The left-hand diagram shows a side view of the magnetosphere and wind, indicating the offset magnetic axis. The right-hand diagram gives a top-down view of the magnetosphere and indicates the azimuthal constraint φ_{acc} . The labelled regions **A** and **B** correspond to the same accretion funnels in the left and right diagram. Note that the cartoons are not to scale, and the wind is not included in the right-hand cartoon.

may address the problems seen in Chapter 4.

5.1 3D model geometry

This chapter investigates the variability of hydrogen spectra induced by azimuthally structured accretion flows. To this effect, a magnetic axis offset ξ was introduced into the fiducial T Tauri model used in Chapter 4. Fig. 5.1 shows a cartoon representation of the magnetosphere and stellar wind model used in this chapter. The accretion flow takes the shortest distance along the dipole field lines from the accretion disk to the stellar surface. By default, TORUS creates two accretion curtains, one in either hemisphere, with an azimuthal angular width $\varphi_{acc} = 180^\circ$. The stellar wind is mostly unchanged by the dipole offset, moving along the dipole field lines until the specified opening angle Θ_{sw} is achieved, at which point the wind’s velocity becomes radial.

This setup of the model is similar to the “A30” model used by [Symington et al. \(2005a\)](#), who concluded that such a model produced spectra “sufficiently at odds with spectroscopic observations that this form of MHD model may be rejected”. However, despite the findings of [Symington et al. \(2005a\)](#), these models are extensively predicted by magnetohydrodynamic simulations (e.g. [Romanova et al. 2003](#); [Long et al. 2011](#); [Ireland et al. 2021](#)) and have been subsequently used to relatively successfully reproduce observed

T Tauri spectral variability (e.g. [Kurosawa et al. 2005](#); [Alencar et al. 2012](#); [Esau et al. 2014](#)). Therefore, this chapter further explores this form of accretion and the line profiles produced.

Table 5.1: The parameters of the 3D models.

Model	$\log \dot{M}_{\text{acc}}$ [$M_{\odot} \text{yr}^{-1}$]	\dot{M}_{sw} [\dot{M}_{acc}]	T_{acc} [K]	φ_{acc} [deg]	ξ [deg]
0	-7	0.1	7500	180	10
1	-7	0.1	7500	90	10
2	-7	0.1	7500	30	10
3	-7	0.01	7500	30	10
4	-8	0.1	8500	30	10
5	-8	0.01	8500	30	10

In this chapter, I present six different models all with a magnetic obliquity of $\xi = 10^\circ$, the model parameters are shown in Table 5.1. Three models (**0**, **1**, and **2**) have an accretion rate $\log \dot{M}_{\text{acc}} = -7$, a magnetospheric maximum temperature of 7500 K and a mass-loss rate of $0.1 \dot{M}_{\text{acc}}$. These models explore the effect of the azimuthal width on the synthetic spectra and have values of $\varphi_{\text{acc}} = 180^\circ$, 90° , and 30° , respectively. Model **3** has a lower mass-loss rate of $\dot{M}_{\text{sw}} = 0.01 \dot{M}_{\text{acc}}$ and was run to explore the effects of the stellar wind where $\log \dot{M}_{\text{acc}} = -7$ and $\varphi_{\text{acc}} = 30^\circ$. The last two models (**4** and **5**) have a lower accretion rate of $\log \dot{M}_{\text{acc}} = -8$, but a higher maximum accretion temperature of 8500 K. The hotter temperature is so that the models can reproduce the typically observed $\text{H}\alpha$ strength ([Muzerolle et al. 2001](#)). Models **4** and **5** have a narrow accretion curtain of $\varphi_{\text{acc}} = 30^\circ$ and different mass-loss rates of $0.1 \dot{M}_{\text{acc}}$ and $0.01 \dot{M}_{\text{acc}}$, respectively. All of the models have a slow rotation speed of 13.4 km s^{-1} (five per cent of their break of velocity) and an isothermal wind temperature of 8000 K. All other input parameters are as defined in Table 4.1.

For each model, 30 different viewing angles around the model were chosen, using all combinations of three colatitudes of 20° , 60° , and 80° at ten different azimuthal angles ω around the z-axis. At each position, synthetic spectra were computed for the four hydrogen transitions $\text{H}\alpha$, $\text{Pa}\beta$, $\text{Pa}\gamma$, and $\text{Br}\gamma$. The z-axis is the rotational axis or pole of the models. Therefore, different values of ω are analogous to the rotational phase of the T Tauri model.

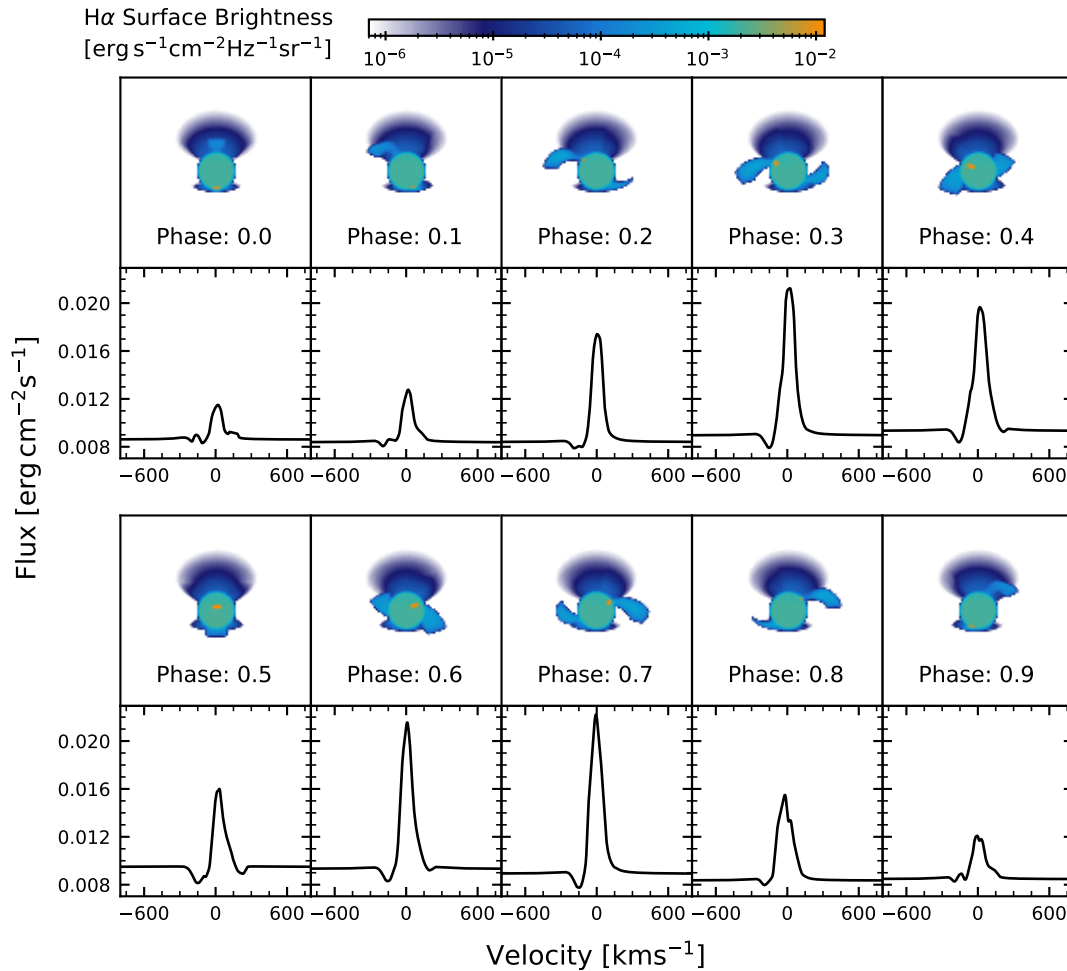


Figure 5.2: $H\alpha$ surface brightness colour maps, which show model 4 at an inclination of 60° and ten different phases. Below each image is the integrated line profile. The spectra are not continuum normalised, and as the hot-spot rotates into view, the continuum level increases. The peak flux is seen when the accretion columns are perpendicular to the line of sight.

5.2 Variability and morphology of 3D non-axisymmetric spectra

The line profiles produced by the 3D non-axisymmetric models have a high degree of phase variability and exhibit large changes in morphology when viewed from different angles. The following sections outline the trends in variability and morphology seen in the synthetic spectra. An example of rotational variability can be seen in Figs. 5.2 and 5.3. The figures show the synthetic images and line profiles of model 4 with an inclination of 60° for $H\alpha$ and $\text{Pa}\beta$. The $\text{Pa}\gamma$ and $\text{Br}\gamma$ lines are not shown as they are similar to $\text{Pa}\beta$. The line profiles are not normalised and share a common flux axis; the continuum

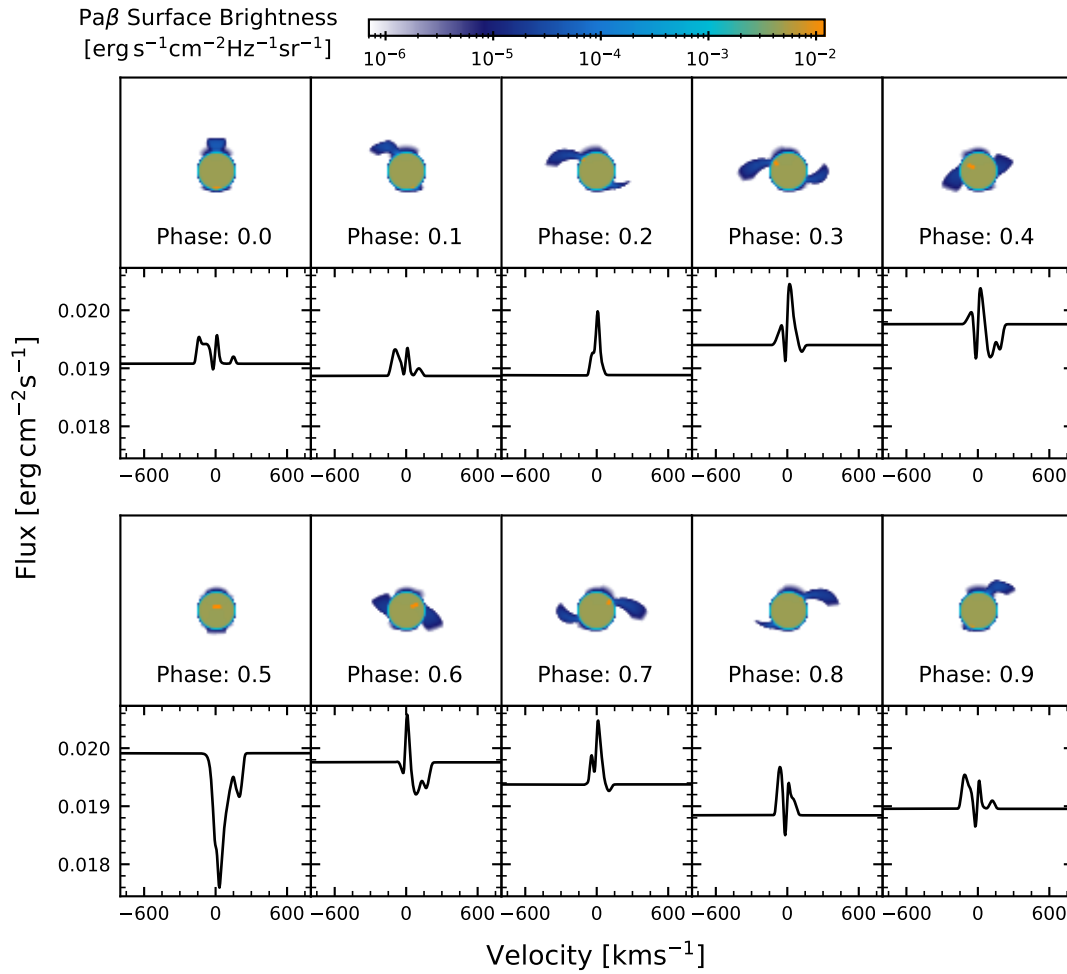


Figure 5.3: The same model and inclination as as Fig. 5.2 but for the hydrogen transition Pa β .

level increases as the hot spot rotates into view. The strongest emission is seen when the accretion columns are aligned to be perpendicular to the line of sight, lessening the magnetospheric absorption. The narrower the magnetosphere, the higher the gas density. This increases the surface brightness of the accretion gas. For example, the H α surface brightness of the magnetosphere with an accretion rate of $\log \dot{M}_{\text{acc}} = -7$ and $\varphi_{\text{acc}} = 30^\circ$ is ≈ 10 times greater than the photospheric surface brightness; a similar magnitude of surface brightness as the hot-spot. As φ_{acc} increases, the strength of the magnetospheric surface brightness decreases. For models 4 and 5 which have an accretion rate of $\log \dot{M}_{\text{acc}} = -8$, the stellar continuum has a higher surface brightness than the magnetosphere. This is always the case for the infrared lines, where the photospheric surface brightness is several orders of magnitude greater than the line flux in all the models presented here.

Fig. 5.4 shows the complete atlas of the line profiles produced by the six models. For each model, there are 120 spectra arranged by wavelength and inclination. The ten

spectra produced at different phases are plotted. Phases 0.0 and 0.5 are shown in bold, highlighting the phases when the magnetosphere is aligned with the observer. The $H\alpha$ line shows more extended emission, originating further away from the star in regions of more rarefied gas. This is especially apparent for the stellar wind, where $Pa\beta$, $Pa\gamma$, and $B\gamma$ emission from the outflow is limited to within 1 – 2 stellar radii. However, blue-shifted absorption and emission features are seen at an inclination of 20° in all the models presented here.

5.2.1 Quantitative analysis of the variability of time-series spectra

A common metric used by observers to quantify the variability of time series spectra is the temporal variance spectrum (TVS) (Fullerton et al. 1996). The method statistically determines the variance at each velocity bin of the series of spectra using a weighted function inversely proportional to the signal-to-noise level of the continuum. However, given that our synthetic spectra have no continuum noise, an alternative method is used. In this work, we quantify variance versus velocity using a range-normalised root mean square deviation (RMSD) distribution. This is defined for the i^{th} velocity bin as

$$\text{RMSD}_i = \left(\bar{f}_{i,\text{max}} - \bar{f}_{i,\text{min}} \right)^{-1} \sqrt{\frac{\sum_j^N \left(\bar{f}_i - f_{ij} \right)^2}{N}}, \quad (5.1)$$

where \bar{f} is the mean line intensity across the N rotational phases. f_{ij} is the flux in the i^{th} velocity bin of the j^{th} spectra. $\bar{f}_{i,\text{max}}$ and $\bar{f}_{i,\text{min}}$ are the maximum and minimum intensities of the mean profile, respectively. Fig. 5.5 shows, for each inclination and wavelength, the mean line profile, the RMSD distribution, and an image showing the quotient of the spectra at each phase. The continuum level versus rotational phase is also plotted. The minimum and maximum of the grey scale is given for each image. The flux of the mean line profile is normalised by the continuum. The spectra of model 3 are shown in Fig. 5.5, similar figures for models 0, 1, 2, 4, and 5 can be seen in Appendix B.

$B\gamma$ exhibits the strongest spectral variability relative to the mean profile range. The next strongest in decreasing order are $Pa\gamma$, $Pa\beta$, and $H\alpha$. The $H\alpha$ flux is significantly greater than the infrared, and the percentage change in the profiles is smaller than the relative change in the infrared lines. Generally, the largest variability is at the line centre for all wavelengths and inclinations. For an inclination of 20° , the RMSD distributions of the lines exhibit three peaks: one at the rest velocity, one blue-shifted, and the other red-shifted. These three points of increased variability are created by absorption from the stellar wind and the magnetosphere. Because of the magnetic offset, the magnetosphere

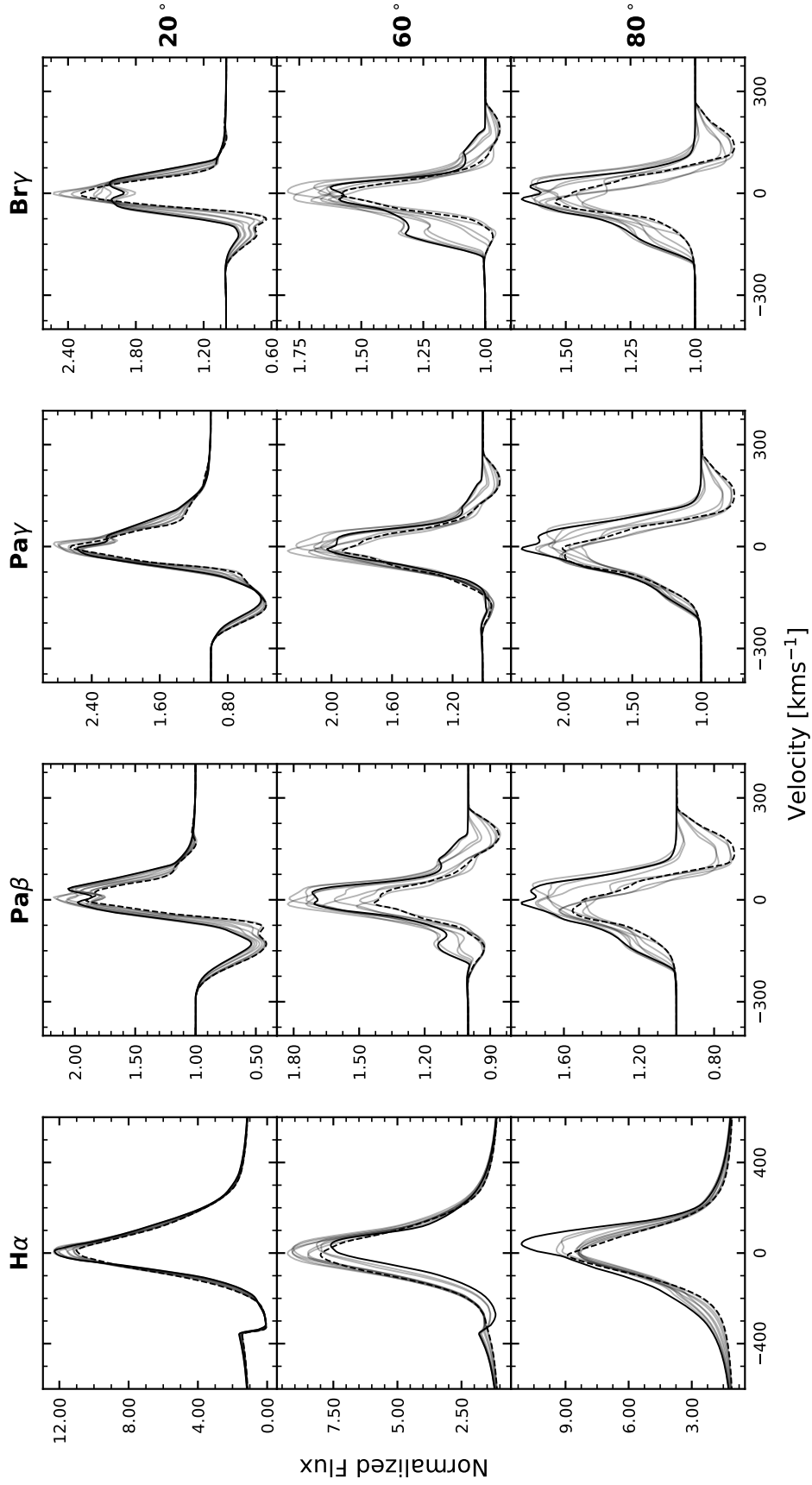


Figure 5.4: The line profiles from model **0** are arranged by inclination (rows) and wavelength (columns). The phases 0.0 (solid) and 0.5 (dashed), which are 180° apart, are highlighted bold.

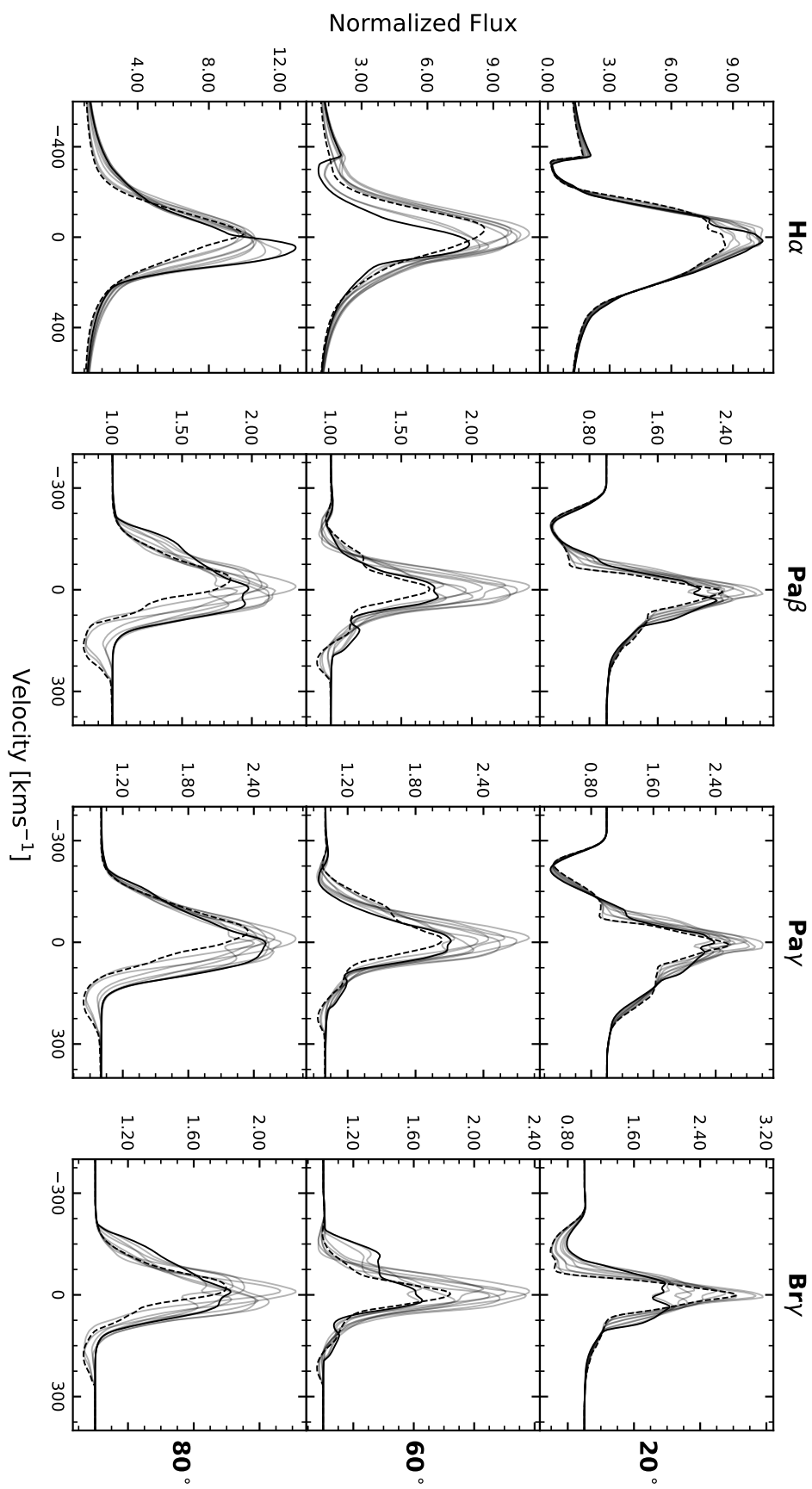


Figure 5.4: Continued. Line profiles for model 1.

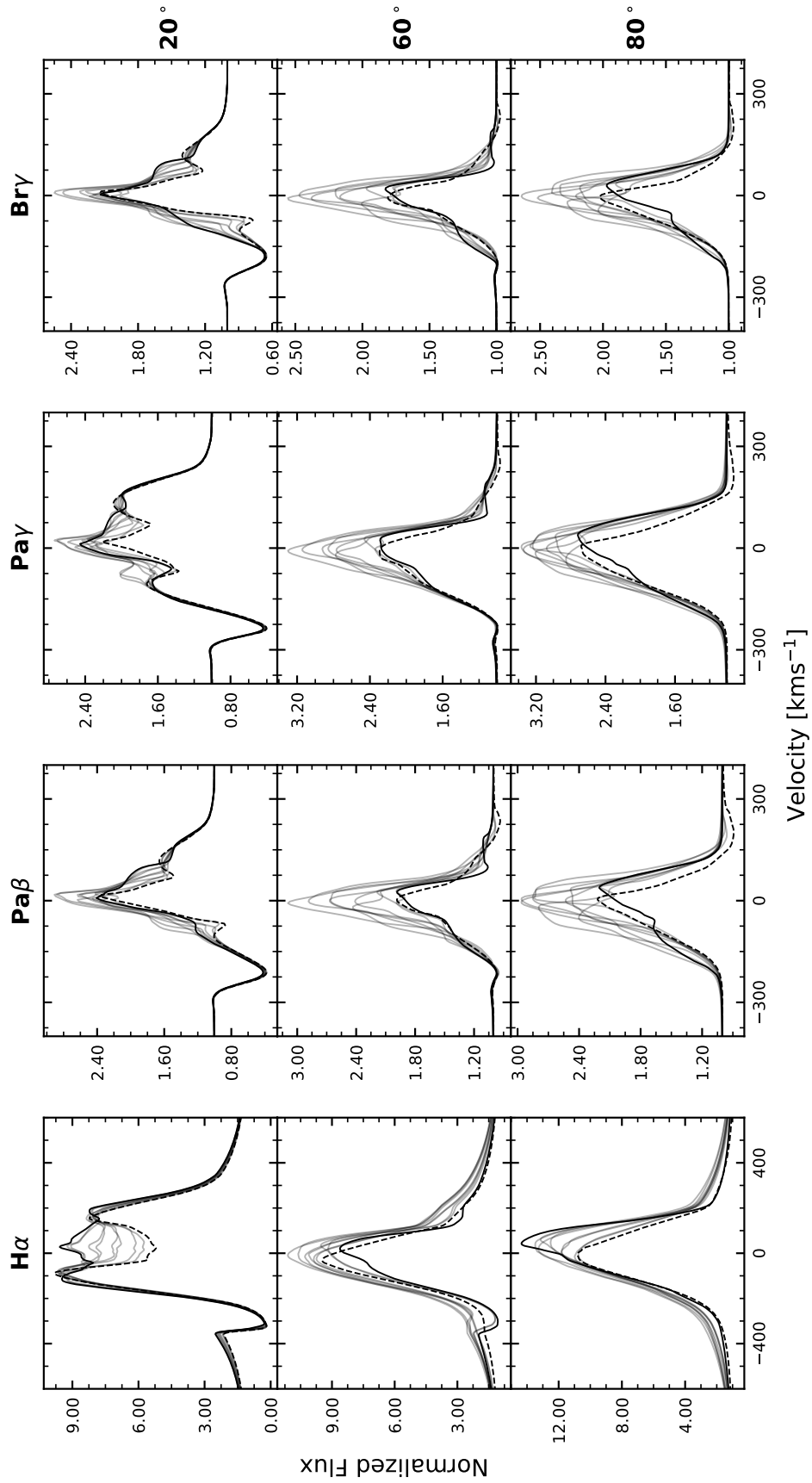


Figure 5.4: Continued. Line profiles for model 2.

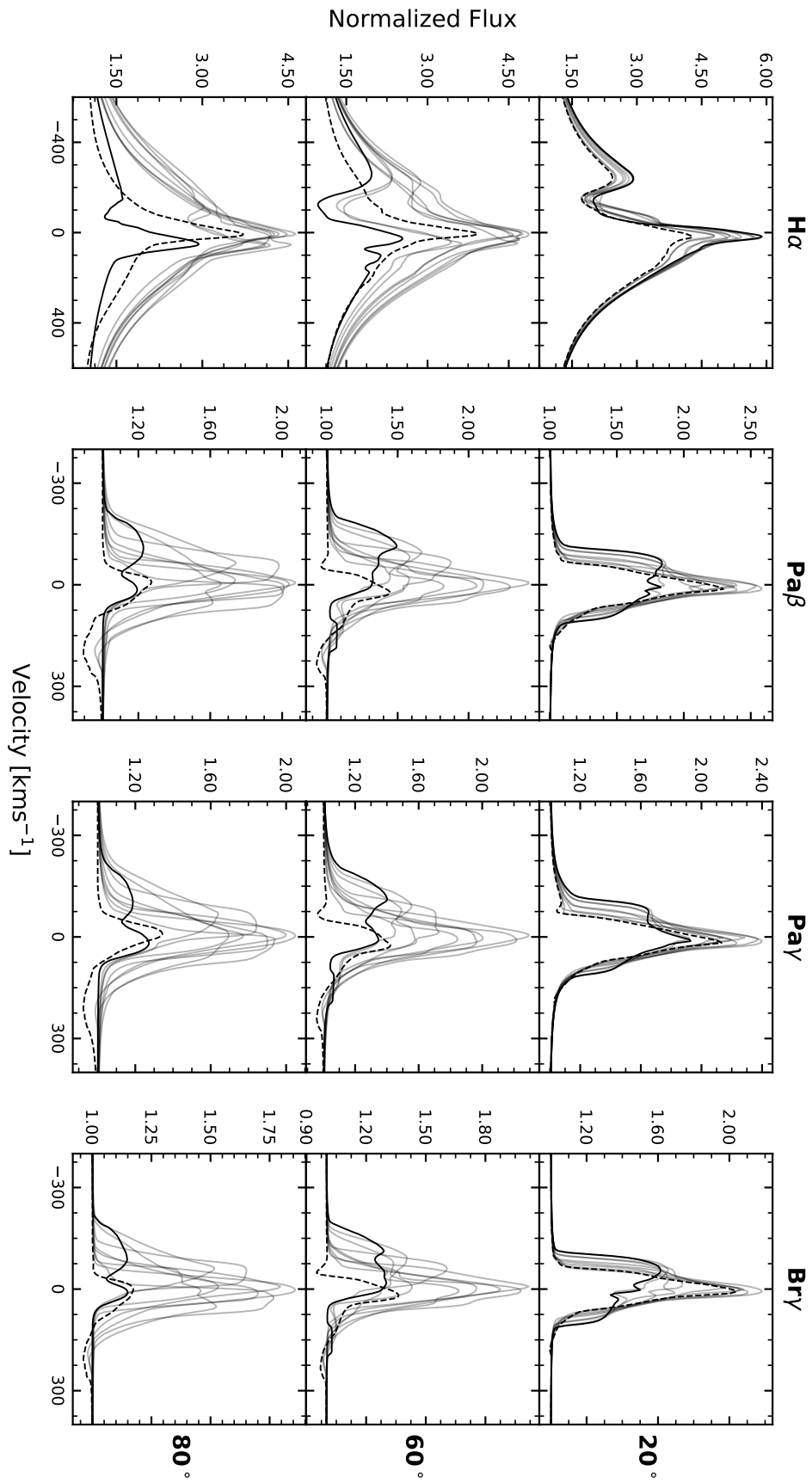


Figure 5.4: Continued. Line profiles for model 3.

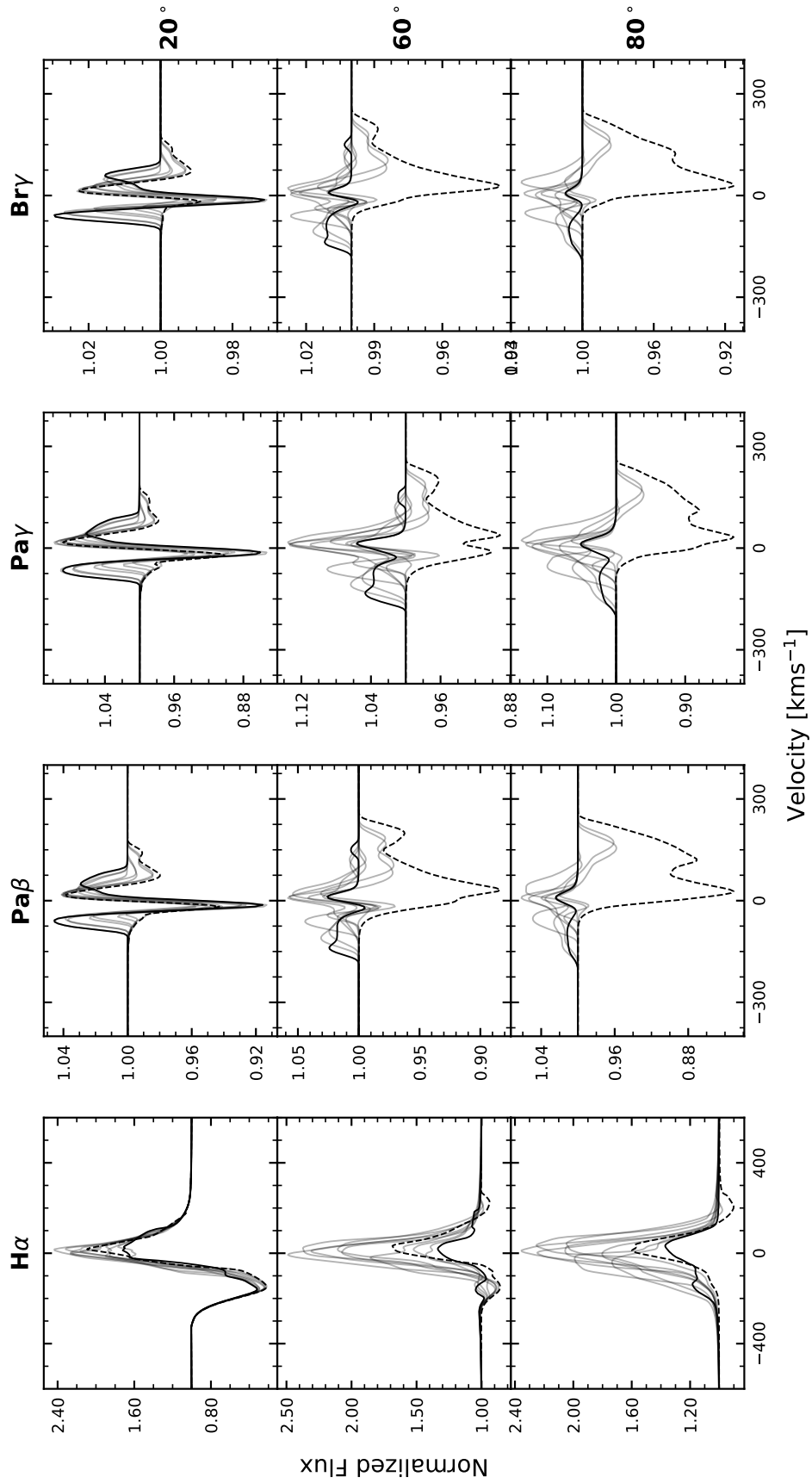


Figure 5.4: Continued. Line profiles for model 4.

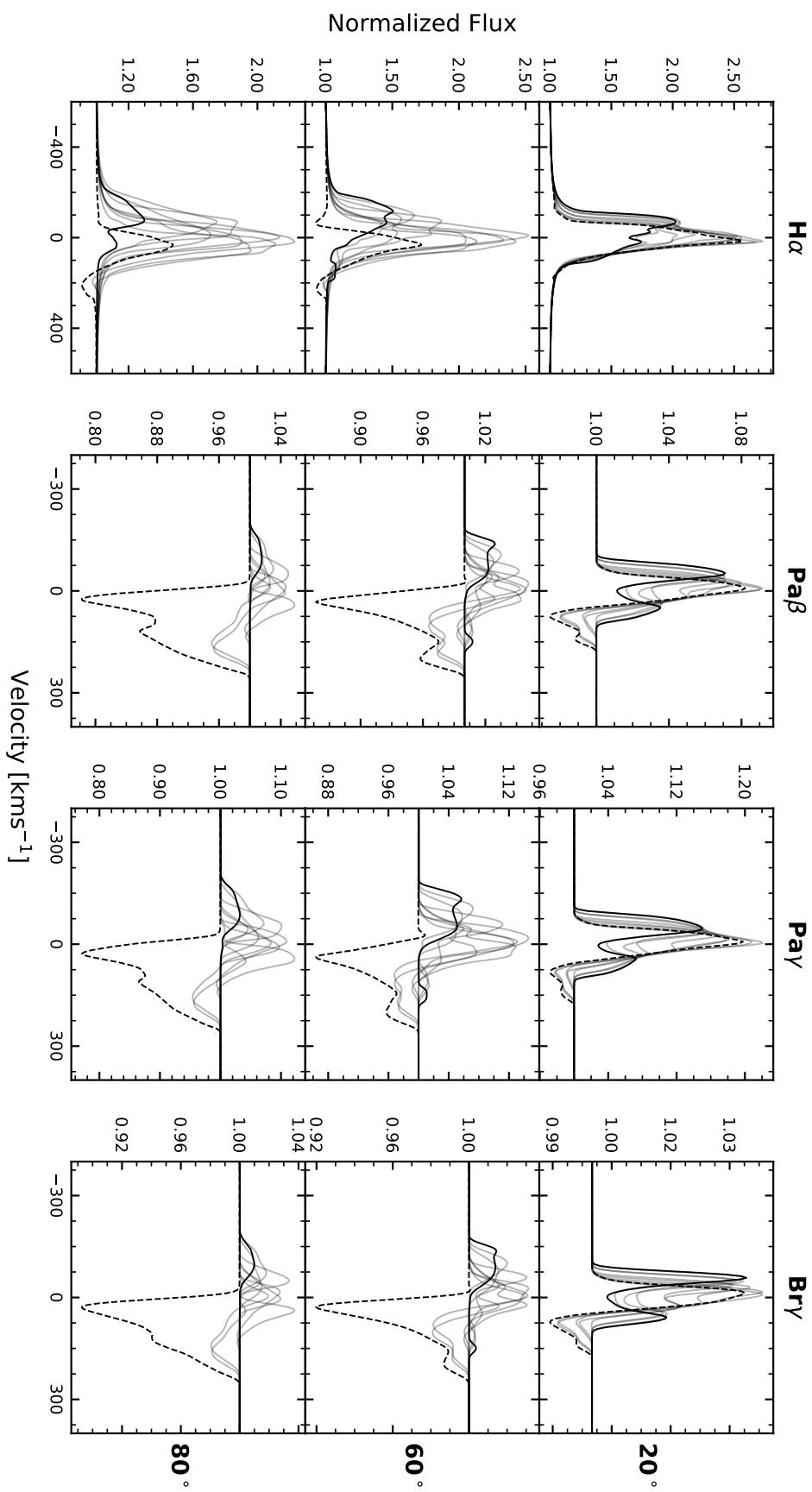


Figure 5.4: Continued. Line profiles for model 5.

intersects with the line of sight to the hot-spot in phases 0.3 – 0.7, creating the red-shifted RMSD peak. At 80° , the magnetosphere rotates through the line of sight, increasing the variability of red-shifted absorption and emission. Thus, the RMSD distribution is red-shifted at this high inclination.

The synthetic continuum emission in the spectra is simulated only for the star, hotspot and magnetosphere; see Chapter 2. Infrared continuum emission from the disk is not included and the rotational phase changes in the continuum arise solely from the hotspot and accretion column. The continuum level of the spectra increases when the accretion hot-spot is visible, peaking at a phase of 0.5. For an inclination of 60° , the hot-spot on the star’s far side creates a secondary continuum peak at phase 0.0. The change in the magnitude of the continuum is calculated according to the following equation

$$\Delta m = -2.5 \log_{10} \frac{f_{\max}}{f_{\min}} . \quad (5.2)$$

where f_{\max} and f_{\min} are the maximum and minimum continuum values in the series. The change in the continuum near $H\alpha$ is dependent on the inclination; it increases at higher colatitudes. For an inclination 20° and an accretion rate of $\log \dot{M}_{\text{acc}} = -7$, the continuum near $H\alpha$ changes in magnitude by ≈ 0.28 . However, at 80° , the change in magnitude is ≈ 0.7 . For the lower accretion rate of $\log \dot{M}_{\text{acc}} = -7$, the maximum magnitude change for $H\alpha$ is ≈ 0.2 at 80° and half that at 20° . The change in the magnitude of the continuum near the infrared lines is smaller but follows a trend similar to $H\alpha$. The mean changes in the magnitude of the continuum near the infrared lines are: ≈ 0.16 , ≈ 0.12 , and ≈ 0.06 for $\text{Pa}\gamma$, $\text{Pa}\beta$, and $\text{Br}\gamma$, respectively.

5.2.1.1 Accretion and temperature comparison

The models **2** and **4** have the same geometry but different accretion rates and temperatures. For the infrared lines, reducing the accretion rate increases the variability of the spectra relative to the intensity of the line profile. At an inclination of 20° , the peak value of the RMSD for model **2** is ≈ 50 per cent of that for model **4**. However, this decreases to ≈ 10 per cent at higher inclinations. There is a similar change in the variability of the $H\alpha$ profiles but to a lesser extent. At 80° , a difference of 40 per cent is observed between the RMSD’s of the two models. Models **3** and **5** exhibit comparable trends in variability.

The increased variability seen in models **4** and **5**, relative to **2** and **3**, is red-shifted. Whereas, the rotational variability of the blue-shifted side of the line profiles is unchanged by the different accretion rates. The infrared line profiles of models **4** and **5** at a phase of 0.5 and inclinations of 60° and 80° show no emission, only sub-continuum absorption; see Fig. 5.4. This is because the line emission for $\text{Pa}\beta$, $\text{Pa}\gamma$, and $\text{Br}\gamma$ is dominated by the

magnetospheric absorption of the photospheric and hot-spot continua. On the other hand, in the models **2** and **3**, the higher accretion rate of $\log \dot{M}_{\text{acc}} = -7$ creates accretion funnels with significant line emission that dominates the continuum absorption. For $\text{H}\alpha$, there is an increase in the rotational variability as the accretion rate decreases; however, at the phases calculated, the line profiles all had emission components.

Models with accretion rates of $\log \dot{M}_{\text{acc}} = -8$ show significantly less change in their continua than models with an accretion rate of $\log \dot{M}_{\text{acc}} = -7$. For instance, the $\text{H}\alpha$ continuum magnitude change of models **2** and **4** at an inclination of 80° are ≈ 0.6 and ≈ 0.2 , respectively. The differences in the continua are due to the stronger hot-spot continuum emission, created by the higher accretion rate.

5.2.1.2 Geometry comparison

For the infrared lines, the smaller the azimuthal extent of the accretion curtain φ_{acc} , the lesser the phase variability of the red-shifted emission. This is because the wider the accretion column, the greater the proportion of red-shifted absorption at each rotational phase. For example, stronger and more frequent red-shifted absorption features are seen in model **0** than in model **2**. In general, the larger the value of φ_{acc} , the broader the RMSD spectrum. At an inclination of 60° , the narrower accretion columns produce more variability. Whereas, at 80° , the wider accretion columns create a higher peak RMSD. For $\text{H}\alpha$, the effect of φ_{acc} on the RMSD spectra is negligible. The $\text{H}\alpha$ RMSD distributions have strong red-shifted peaks at 80° and blue-shifted peaks at an inclination of 60° . This is due to the increased sensitivity of $\text{H}\alpha$ to the stellar wind.

The continuum levels of the $\text{H}\alpha$ spectra have a consistent variation and magnitude change across the phases, independent of φ_{acc} . However, the wider the accretion columns, the stronger the continuum is at all phases for the infrared lines. Additionally, the change in magnitude of the continuum increases with φ_{acc} . At an inclination of 60° , model **0** does not show a secondary peak in the continuum at phase 0.0. This is because a hot-spot in either the upper or lower hemisphere is visible at all phases.

5.2.1.3 Mass-loss rate comparison

Models **2** and **3** have different mass-loss rates of $0.1 \dot{M}_{\text{acc}}$ and $0.01 \dot{M}_{\text{acc}}$, respectively. Similarly, models **4** and **5** have the same ratios of mass loss to mass accretion rates. The variability of the models increases as the mass-loss rate reduces. This effect is more pronounced between models **2** and **3**, which have the larger accretion rate of $\log \dot{M}_{\text{acc}} = -7$. The wind absorbs emission from the magnetosphere and hot-spot, creating blue-shifted absorption features in the line profiles. The wind's emission and absorption decrease with

lower mass-loss rates as the wind density reduces.

5.2.2 Correlation analysis of time-series spectra

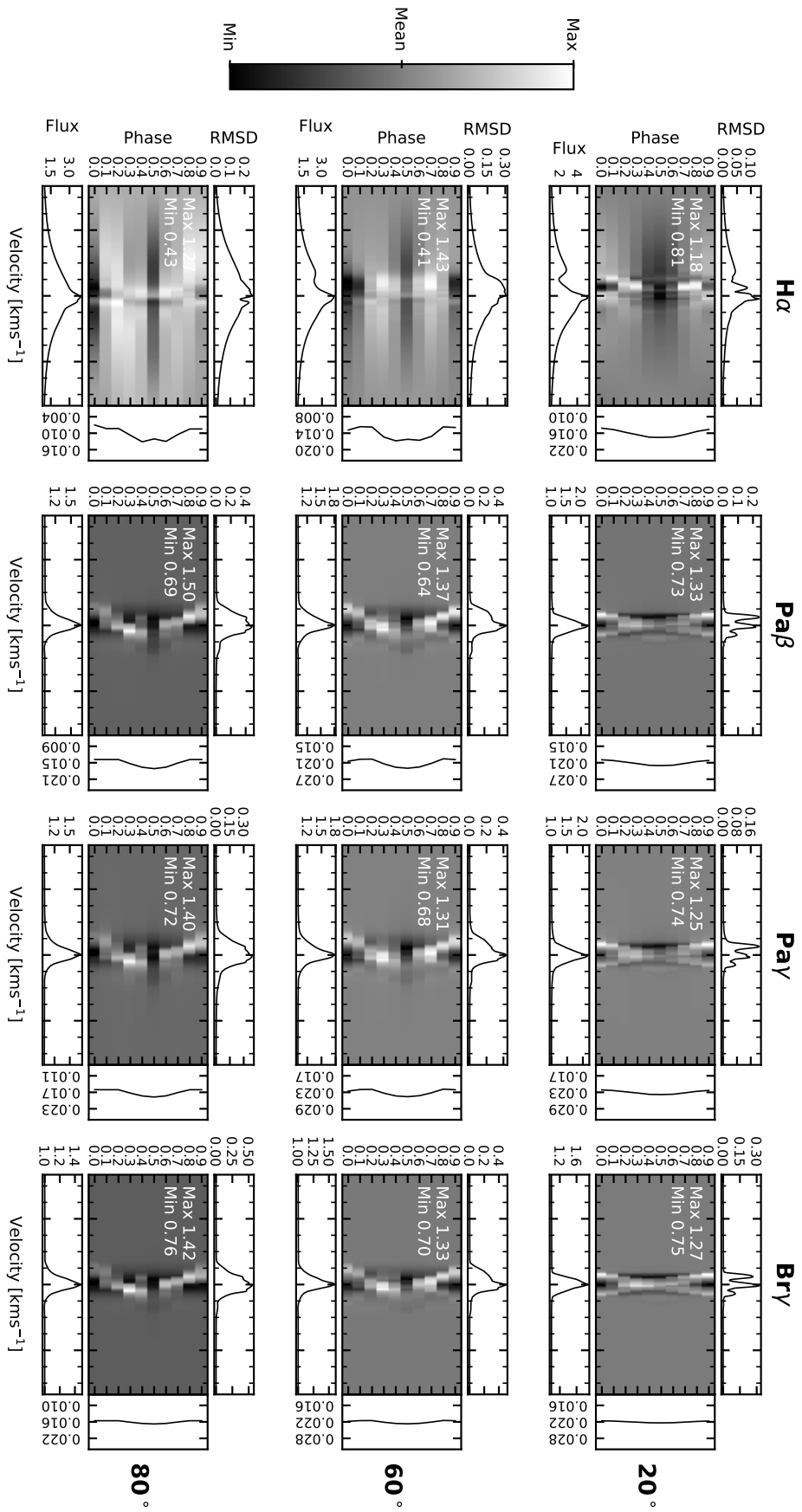
A common method for analysing the often complex changes in the morphology of time-series spectra are auto-correlation images. Using the technique pioneered by [Johns \(1994\)](#) and [Johns & Basri \(1995\)](#), auto-correlation images or maps are created to examine the correlation of the variability of each velocity bin with the rest of the spectra. This correlation is quantified by the coefficient C_{ij} for the i^{th} row and j^{th} column as

$$C_{ij} = \frac{1}{N} \sum_{m=1}^N \frac{(S_{mi} - \bar{S}_i)(S_{mj} - \bar{S}_j)}{\sigma_i \sigma_j}. \quad (5.3)$$

Where N is the number of spectra in the series and S_{mi} is the signal of the i^{th} velocity bin of the m^{th} spectra. σ_i and \bar{S}_i are the standard deviation and average values of the i^{th} velocity bin across the series, respectively. The correlation coefficient has values in the range of -1 to 1 , the former representing areas of strong anti-correlation and the latter strong correlation.

The auto-correlation maps are useful for visually determining what regions of the spectra correlate with each other. [Fig. 5.6](#) shows an example auto-correlation map for model **2**. The white areas represent correlation and the black anti-correlation. The auto-correlation maps for all six models can be seen in [Appendix C](#). The images show a complex correlation distribution dependent on the wavelength and inclination. In general, at an inclination of 80° , the red-shifted section of the spectra ($> 0 \text{ km s}^{-1}$) is anti-correlated with the blue side of the line ($< 0 \text{ km s}^{-1}$). As the single accretion column rotates, it shifts from being blue-shifted to red-shifted, translating the peak emission from negative to positive velocity. Another trend is that the width of the blocks of correlation and anti-correlation increases with the inclination. This is because for the higher inclinations there is greater line-sight velocity from the accretion flow.

At an inclination of 20° , models **0** to **3** exhibit a red-shifted band ($\approx 100 \text{ km s}^{-1}$ to 150 km s^{-1} , the width and position vary between models) of anti-correlation with the entire profile. The anti-correlation band arises because the accretion column is orientated such that at certain phases, it absorbs emission from the photosphere and hot-spot. This causes a narrow absorption band to appear in the line profiles as the overall line emission increases simultaneously. This effect is not seen in models **4** and **5**, where the lower accretion rate reduces the column density, decreasing the absorption and emission properties of the magnetosphere. Furthermore, at 20° , many of the images show an anti-correlation



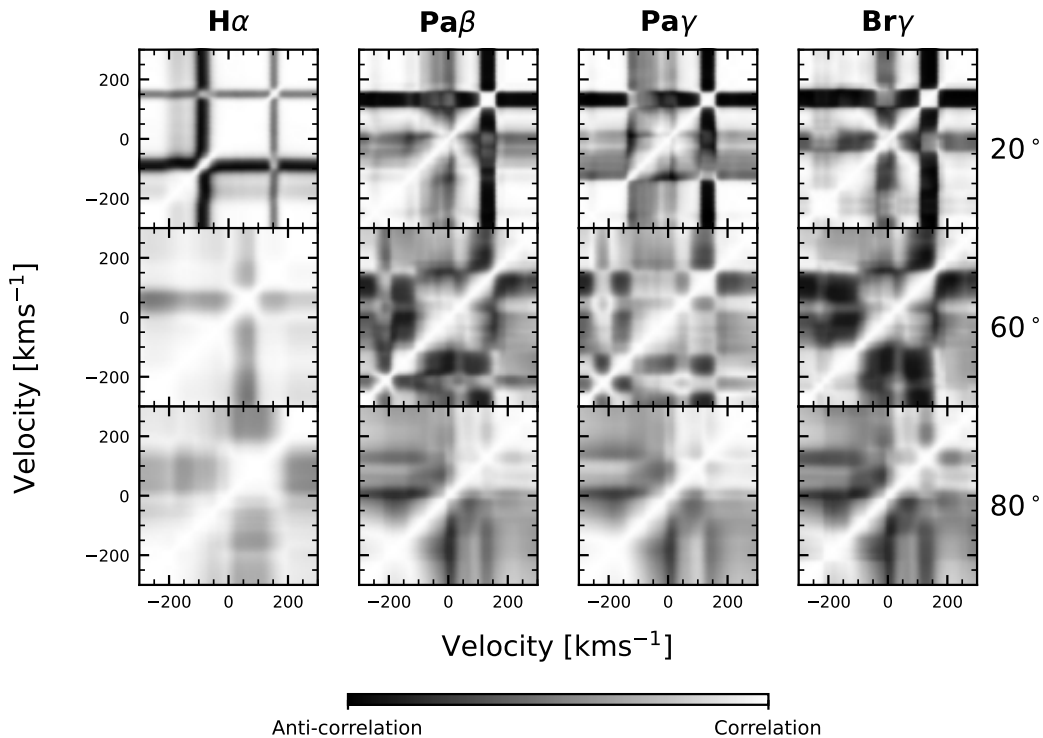


Figure 5.6: Auto-correlation maps for model 2. White areas correspond to a strong correlation and black areas strong anti-correlation. The images are symmetrical along the x-y diagonal. The maps are arranged by wavelength and inclination. The $\text{Pa}\beta$, $\text{Pa}\gamma$, and $\text{Br}\gamma$ lines share similar patterns for each inclination. For instance, at 80° , the red side of the infrared lines is anti-correlated with the blue side.

between the line centre ($\pm 25 - 50 \text{ km s}^{-1}$) and the wings. This effect is not seen as strongly in the $\text{H}\alpha$ profiles, which more commonly show a blue-shifted anti-correlation.

The above evaluation is intended to provide only a rudimentary analysis of these correlation maps, and a complete analysis is beyond the scope of this thesis. I discuss the auto-correlation maps and briefly compare them with those from literature in § 5.5.

5.3 Inverse P-Cygni profiles

One of the problems with the grid of synthetic line profiles presented in Chapter 4 was that ≈ 90 per cent of the infrared line profiles were classified as type *IVR* (inverse P-Cygni). This is a significantly greater value than the observed frequency of inverse P-Cygni profiles (≈ 35 per cent) seen in both in our sample of T Tauri stars and that of [Folha & Emerson \(2001\)](#). In Chapter 4, it was proposed that a possible method to reduce the frequency

of the inverse P-Cygni profiles was to use non-axisymmetric accretion. It was postulated that the induced rotational variation from such a model might reduce the frequency of the red-shifted sub-continuum absorption. To quantify this effect, I used a PYTHON script to classify the spectra at each phase into the types defined by Reipurth et al. (1996). In Chapter 4, the strongest absorption feature was used to distinguish between types *IVR* and *IVB* for profiles that contained both red and blue-shifted absorption. Whereas, in this section, only type *IVR* profiles are considered, and as such, any spectra that contain red-shifted sub-continuum absorption are classified as *IVR*. Fig. 5.7 shows two histograms (optical and infrared) representing the fraction of inverse P-Cygni profiles seen in our synthetic spectra at different phases. The bars are sub-divided by the azimuthal extent of the accretion column φ_{acc} . It is immediately apparent that the occurrence of inverse P-Cygni profiles is centred around phase 0.5, where the magnetosphere is directly in the observer's line of sight. The maximum fraction of spectra from all six models that show red-shifted sub-continuum absorption at any given phase is 0.5 for $\text{H}\alpha$ and 0.23 for the combined infrared lines. For $\text{H}\alpha$ (optical), the red-shifted sub-continuum absorption is only seen in our spectra at phases of 0.4 – 0.6. The type *IVR* $\text{H}\alpha$ profiles primarily come from models 4 and 5 where the accretion rate is $\log \dot{M}_{\text{acc}} = -8$. The lower accretion rate reduces the influence of Stark broadening on the line profiles.

For the infrared lines $\text{Pa}\beta$, $\text{Pa}\gamma$, and $\text{Br}\gamma$, the distribution of inverse P-Cygni profiles is centred around a phase of 0.5. Models 0, 1, 2, and 3 have a total proportion of inverse P-Cygni profiles of 0.47, 0.29, 0.13, and 0.17, respectively. As the value of φ_{acc} decreases, the phases at which the magnetosphere intersects the line of sight are reduced. This can be seen in Fig. 5.7, where the inverse P-Cygni profiles are predicted for the phases 0.2 – 0.8 for $\varphi_{\text{acc}} = 180^\circ$. Whereas, the inverse P-Cygni profiles occur only between phases 0.3 to 0.7 for $\varphi_{\text{acc}} = 90^\circ$ and 30° . The lower accretion rate models 4 and 5 have a total proportion of infrared P-Cygni profiles of 0.49 and 0.5, respectively. In these models, the fraction of inverse P-Cygni profiles is produced equally between the phases 0.3 to 0.7. The lower accretion rate produces less line emission, increasing the absorption of the continuum. There is also evidence to suggest that reducing the mass-loss rate from 0.1 to 0.01 \dot{M}_{acc} increases the proportion of inverse P-Cygni profiles; however, additional models are needed to verify this result.

The mean fractions of infrared inverse P-Cygni profiles for all phases and models are 0.44, 0.41, and 0.16 for the inclinations 80° , 60° , and 20° , respectively. For $\text{H}\alpha$, inverse P-Cygni profiles are only predicted at inclinations of 80° and 60° and both with a mean fractional occurrence of 0.08.

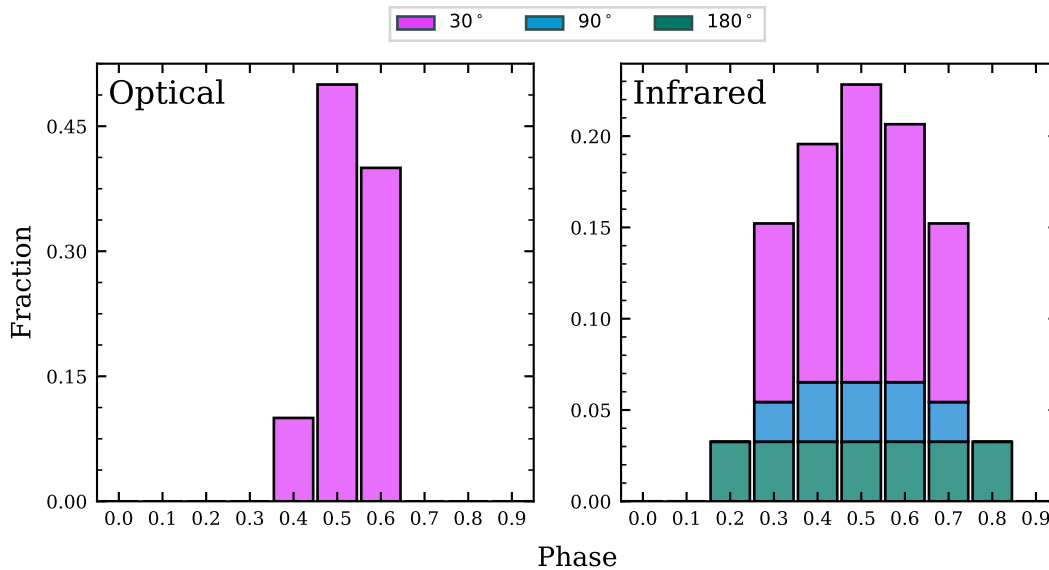


Figure 5.7: The fraction of synthetic line profiles with inverse P-Cygni features for all models and inclinations at the ten different phases. The left-hand figure shows the fraction for $H\alpha$ and the right-hand figure for the infrared lines. The fraction is subdivided by the azimuthal extent of the accretion column. The wider the accretion funnel, the more phases contain inverse P-Cygni features. The most significant fraction occurs at a phase of 0.5 when the near-side accretion column is between the observer and the star.

5.4 Variability of the line profile widths

In Chapter 4, it was seen that the synthetic spectra grid could reproduce the observed $H\alpha$ line widths. However, the same models produced infrared lines that, on average, had $HW10\%$ approximately 80 km s^{-1} narrower than the observed T Tauri spectra. This section considers how the widths of the line profiles change when the 3D models are rotated. We quantify the width using the $HW10\%$ and the equivalent width.

Fig. 5.8 shows two polar plots displaying the $HW10\%$ (radius) at different angles around the z-axis for $H\alpha$ and $Pa\beta$. The line profiles from models 2–5 were determined for an inclination of 60° . The greyed sections indicate the location of the accretion columns; the darker section is the column on the near side of the disk. In the figure, it can be seen that the narrowest spectra occur when the magnetosphere is directly in the line of sight, an angle of $\omega = 180^\circ$ corresponding to a phase of 0.5. The narrowing of the line is caused by the increased continuum absorption of the magnetosphere. However, for an accretion rate of $\log \dot{M}_{\text{acc}} = -7$ and mass-loss rate of $0.1 \dot{M}_{\text{acc}}$, the narrowest $Pa\beta$ spectra occurs at $\omega = 72^\circ$ and 252° . This is where the accretion columns are side on, minimising the velocity component of the accreting gas relative to the viewing angle.

Fig. 5.9 shows the residual change of the $HW10\%$ and the equivalent width of the

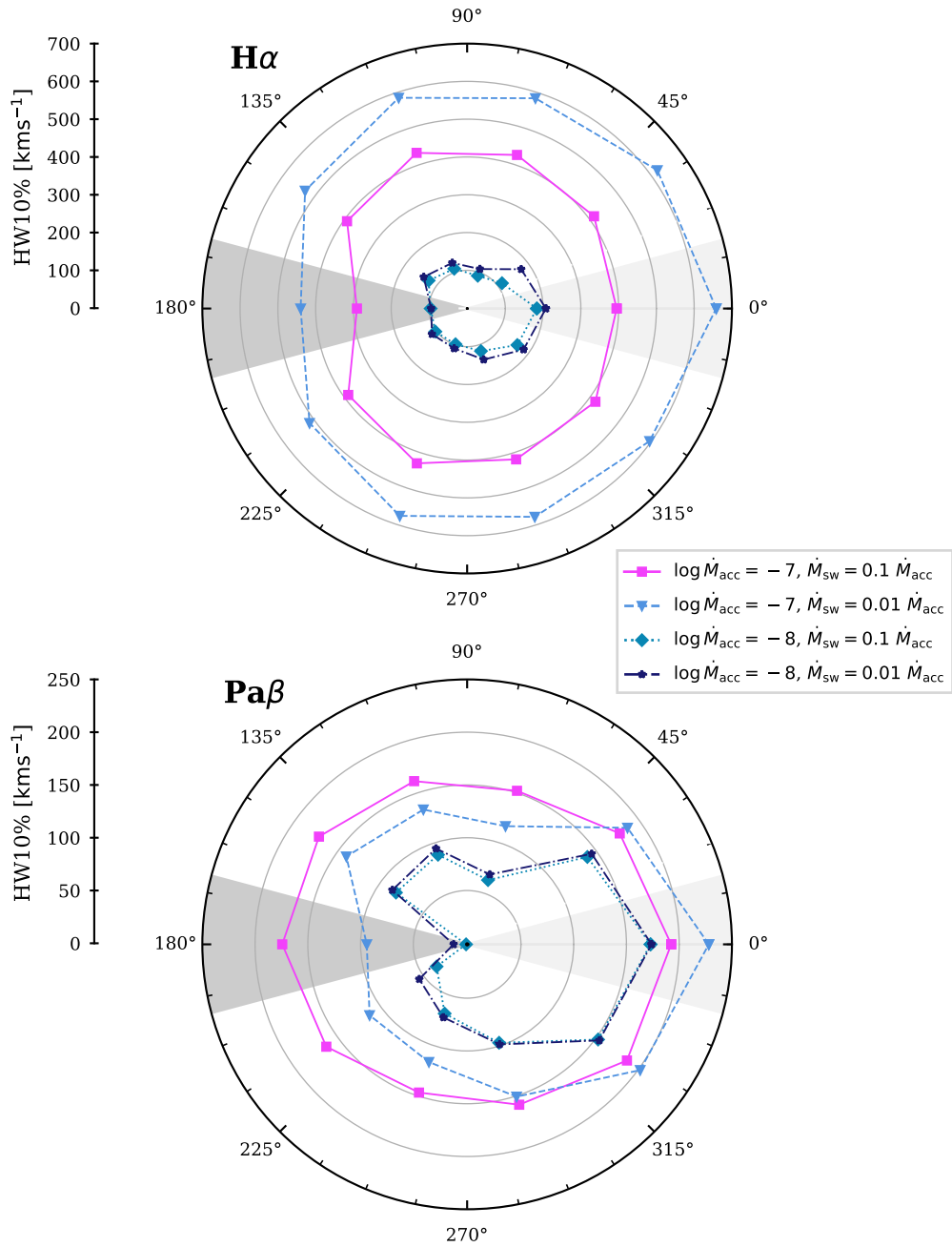


Figure 5.8: Polar plots showing the HW10% (radius) at different phases for H α (top) and Pa β (bottom). The plots show spectra observed at an inclination of 60° from models with $\varphi_{\text{acc}} = 30^\circ$. The dark grey section indicates the near side magnetosphere, and the light grey is the far side.

$H\alpha$ and infrared spectra. The residual is calculated by subtracting the smallest width from the phase series. The figure shows the mean change and the minimum and maximum ranges. As the azimuthal extent of the accretion column decreases, so does the change in the infrared HW10%. Reducing the accretion rate of the models, increases the change in the infrared HW10% by ≈ 2 times and reduces the change seen in $H\alpha$ by 100 km s^{-1} . The change in the $H\alpha$ HW10% in model **3** is significantly greater than in model **2**, the only difference being a lower rate of mass loss. However, there is a negligible difference between the HW10% residuals of models **4** and **5**. Therefore, the change in HW10% is coupled with the accretion and mass-loss rates. Spectra produced at a low inclination (20°) exhibit the least change in HW10%. Changes in equivalent width follow trends similar to those of HW10%. Decreasing φ_{acc} , increases the change in the equivalent width at different phases, as does increasing the accretion rate.

The HW10% is narrowest for $H\alpha$ and the infrared lines when the magnetosphere is between the observer and the star; a phase of 0.5. Whilst this orientation should give the largest width due to the magnetospheric velocity, the absorption from the accretion funnel dominates and significantly reduces the line width. The broadest infrared HW10% occurs at a phase of 0.0, when the near-side accretion column is on the star's far side. The same is true for the $H\alpha$ spectra produced by models with an accretion rate of $\log \dot{M}_{\text{acc}} = -8$. However, when the accretion rate is $\log \dot{M}_{\text{acc}} = -7$, a secondary HW10% minimum occurs at a phase of 0.0 caused by increased absorption of emission from the accretion curtain by the stellar wind. The effect is more noticeable at higher mass-loss rates because the wind is denser, and lower values of φ_{acc} which increases the surface brightness of the accretion funnel.

Similar to the HW10%, the equivalent width is narrowest when the near-side magnetosphere is directly aligned with the observer at a phase of 0.5. The absorption features and continuum level are maximised in this orientation, reducing the equivalent width. When $\varphi_{\text{acc}} = 180$ and the inclination is 20° or 60° , the broadest equivalent width is seen at a phase of 0.0 when the accretion funnel is behind the star. In this orientation, the maximum velocity broadening is obtained from the accretion flow, absorption by the magnetosphere and wind are minimised, and there is no increase in the continuum level. However, a secondary equivalent width minimum forms at a phase of 0.0 as φ_{acc} decreases. This secondary equivalent width minimum does not appear in the spectra produced for an inclination of 20° when $\log \dot{M}_{\text{acc}} = -7$. The secondary equivalent width minima are caused by a combination of strong absorption features and an increase in the continuum levels due to the visibility of the far-side hot-spot. In models **4** and **5**, where $\log \dot{M}_{\text{acc}} = -8$, the secondary equivalent width minimum is seen for all inclinations. This is because of the deep absorption features seen in the spectra produced by these models at a phase of

0.0. The equivalent width at a phase of 0.0 is correlated with the inclination, accretion rate, mass-loss rate, and the azimuthal extent of the magnetosphere.

The width variability of the infrared lines is at least dependent on the accretion rate, mass-loss rate, and inclination. From our models, it can be seen that changes in the line HW10% of up to $\approx 240 \text{ km s}^{-1}$ are possible by introducing non-axisymmetric accretion flow. However, both the infrared lines and H α get broader when the accretion flow is not in the line of sight. For an accretion rate of $\log \dot{M}_{\text{acc}} = -7$, the majority of the H α spectra are broadened more than the infrared lines. On the other hand, when $\log \dot{M}_{\text{acc}} = -8$, the infrared lines are broadened more than H α ; this may be due to the effect of Stark broadening. Therefore, while the non-axisymmetric accretion flow broadens the infrared lines sufficiently to account for the HW10% disparity observed in Chapter 4, the effect also broadens H α shifting the distributions out of agreement with the observations.

5.5 Discussion

The six 3D models presented in this chapter provide a preparatory study into the spectral modulation caused by the rotation of non-axisymmetric T Tauri models. The parameters are not adjusted to fit any specific observations but are taken as illustrative cases from the synthetic grid described in Chapter 4 and magnetohydrodynamic simulations (e.g. [Romanova et al. 2003](#); [Long et al. 2011](#); [Alencar et al. 2012](#); [Ireland et al. 2021](#)). This chapter builds on the work of [Symington et al. \(2005a\)](#) and [Kurosawa et al. \(2008\)](#), who presented models with accretion columns in alternate hemispheres. This chapter augments previous radiative transfer studies by including a mass outflow in the T Tauri models in the form of a polar stellar wind.

The 3D models produced spectra with similar profile characteristics and morphological variability to that seen in T Tauri observations, (e.g. [McGinnis et al. 2020](#); [Alencar et al. 2018](#)). From the limited number of models presented, it is apparent that the synthetic spectra's rotational phase modulation depends on the magnetospheric temperature and accretion rate, inclination, wavelength, and mass-loss rate. Our results show that decreasing the accretion rate increases the line variability; the line profiles of model 4 and 5 have a greater relative change than models 0 – 3. In contrast, [Johns & Basri \(1995\)](#) showed that for their sample of seven T Tauri stars, the profile variance increased with the accretion rate. Further radiative transfer models are needed to unravel the effects of the accretion rate and magnetospheric temperature.

The primary variability of the synthetic spectra lies near the line centre. However, the red-side line variability is generally more significant than that on the blue-side due to strong emission and absorption by the magnetosphere. [Alencar et al. \(2001\)](#) noted that

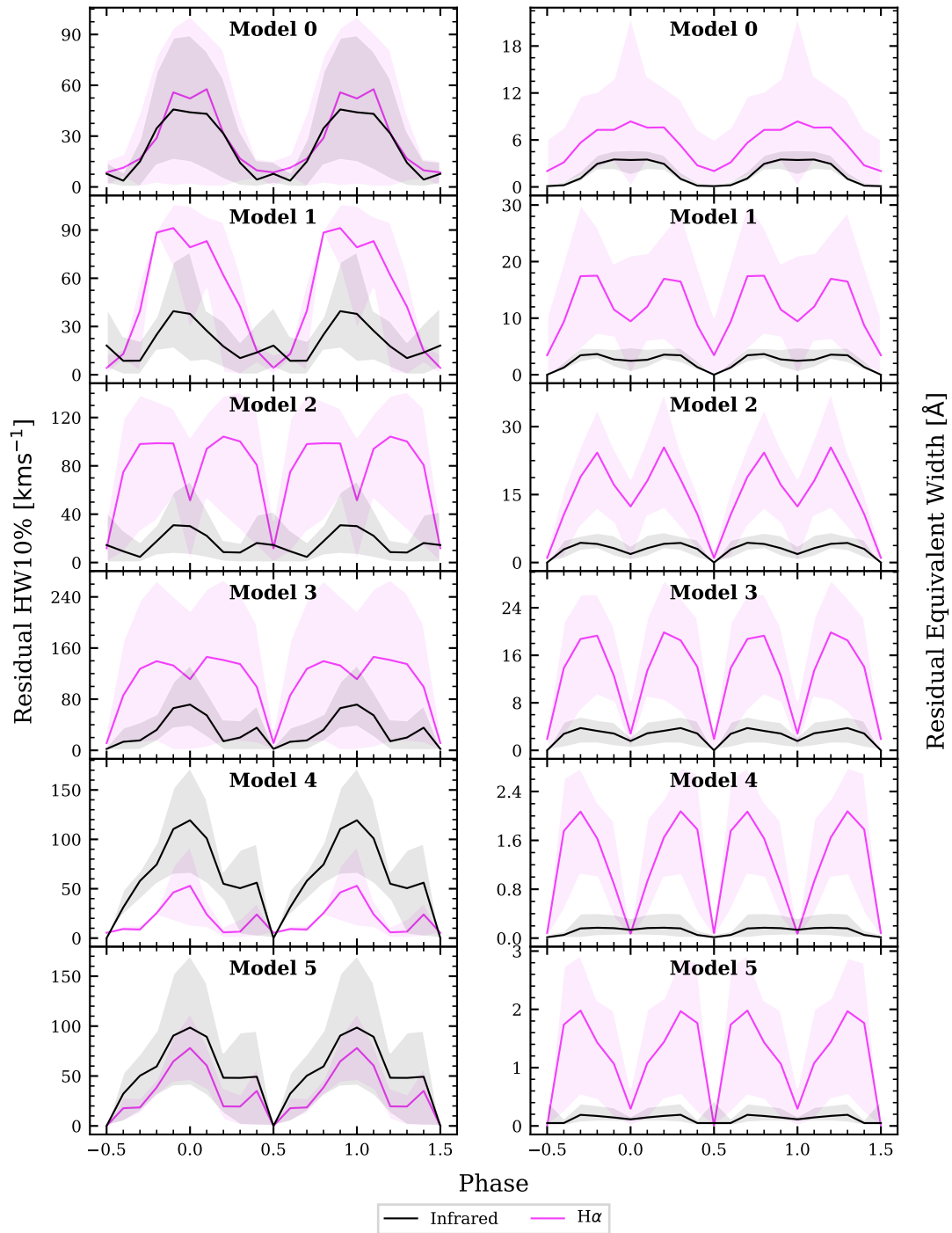


Figure 5.9: Plots showing the residual change in HW10% (left) and the equivalent width (right) of H α (pink) and the infrared lines Pa β , Pa γ , and Br γ (black). The mean change for all the inclinations and wavelengths is illustrated by the solid line and the maximum and minimum range denoted by the shaded area. The x-axis shows two full phases from -0.5 to 1.5 .

for the pole-on spectra of DR Tau, the hydrogen line variability was mostly blue-shifted. In our models, spectra produced at a low inclination (pole-on) have increased blue-shifted variance due to the stellar wind. The spectral variability seen in the models depends on the mass-loss rate, and a lower mass loss relative to the accretion rate significantly increases the spectral variability. Additionally, at high inclinations, the azimuthally constrained magnetosphere changes from being blue-shifted to red-shifted, creating substantial variability on both sides of the synthetic spectra.

An analysis of the correlation between different components of the line profiles was undertaken using auto-correlation images. The images reproduced share similar patterns to those created by radiative transfer models from literature ([Symington et al. 2005a](#) and [Kurosawa et al. 2005](#)). Models **1**, **2**, and **3** showed an anti-correlation between the red and blue sides of the spectra. This is caused by the rotation of the magnetosphere through the line of sight. Similar features can be seen in some cross-correlation maps of observed spectral series (e.g. [Pouilly et al. 2020](#); [Alencar et al. 2012](#); [Oliveira et al. 2000](#)). In [Alencar et al. \(2018\)](#), the authors noted that the H α line centre was anti-correlated to the high-velocity blue wing; a feature they could not explain. A similar anti-correlation is seen in the H α maps of models **4** and **5** at inclinations of 60° and 80°. In our models, this relationship is caused by the rotation of the narrow magnetosphere. The maximum line intensity is achieved when the accretion flow is perpendicular to the line of sight, minimising absorption by the magnetosphere. At this point, the line intensity is centred because the velocity components of the accretion flow relative to the observer are at a minimum. When the accretion column is on the far side of the star, the dominant line emission source is from the magnetosphere and is strongly blue-shifted as it falls towards the star. The emission from the near side accretion column is predominately blocked by the disk. As the star rotates, the accretion column emission becomes red-shifted; simultaneously, the red-shifted absorption of the line and continuum increase. These effects work in tandem to maintain a peak line centre close to zero. Additionally, as the hot-spot becomes visible, the blue-shifted sub-continuum absorption from the stellar wind increases, further decreasing the blue-side emission strength. Combined, these effects produce correlation maps that show the line centre to be anti-correlated with the blue-side wing. Although this may not be the cause of the correlation seen in [Alencar et al. \(2018\)](#), it is useful to see how the correlation images may be used to diagnose the complex phenomenon seen in the time-series variability of T Tauri spectra.

In Chapter **4**, it was shown that the primary problem with the synthetic line profile grid was that the infrared line widths were too narrow when compared to the observed spectra. One of the proposed solutions was that non-axisymmetric accretion might lower the frequency of synthetic inverse P-Cygni profiles. In § **5.3**, we saw that the mean

occurrence rate of infrared inverse P-Cygni profiles in all models and inclinations was ≈ 34 per cent. This is considerably lower than predicted for axisymmetric models (see Chapter 4) and similar to the observed frequency. These sub-continuum absorption features depend on the phase, inclination, accretion rate, and column width. The associated predicted phase-modulated change in the width of the spectra was similarly dependent on the model, wavelength, and inclination. The models produced changes in the infrared HW10% of up to 170 km s^{-1} with a mean change of $\approx 60 \text{ km s}^{-1}$. These values could account for the disparity of width seen between the synthetic and observed infrared lines. However, both the width of the infrared and $\text{H}\alpha$ lines change concurrently. Therefore, while the infrared widths can be brought into agreement with the observed range of HW10%, the $\text{H}\alpha$ spectra are shifted out of accord with the observed range. For models with $\log \dot{M}_{\text{acc}} = -7$, the $\text{H}\alpha$ lines change more than the infrared lines, probably due to the effect of Stark broadening. At a lower accretion rate of $\log \dot{M}_{\text{acc}} = -8$, the infrared lines show a greater change in width over the phase. Further study should be undertaken to explore this effect for a wide range of accretion rates and temperatures to determine how the ensemble of models behave.

Lastly, the models suggested that the minima of the equivalent width and the HW10% occur when the velocity broadening should be at its highest. In addition, a secondary minimum of width occurs at a half phase from the narrowest width. This secondary reduction in width is created by combinations of an increased continuum level and stronger absorption from the accretion flow and wind. The feature is strongly dependent on the inclination, accretion rate, mass-loss rate, and the azimuthal extent of the accretion column. Time-series spectroscopic surveys of T Tauri stars may provide observational evidence of this predicted feature.

Summary

In conclusion, this chapter presents a preparatory radiative transfer study of six 3D T Tauri models that include non-axisymmetric accretion and polar stellar winds. The models exhibit patterns of variability, correlation, and morphology, as seen in observations and previous theoretical studies. The models produce a phase modulation of the HW10% and equivalent width within a range similar to that observed (e.g. [Alencar et al. 2012](#)). Furthermore, the 3D models predicted two points of minimum equivalent width and HW10% created by the interplay of absorption and continuum level. Further work needs to be undertaken to create a more extensive set of synthetic spectra from 3D models and to compare them to existing or new times-series of hydrogen spectra.

Chapter 6

Conclusions and Future Outlook

Radiative transfer simulations present an invaluable tool for understanding the complex and variable spectroscopic observations of T Tauri stars. While modern radiative transfer codes are well tested and understood, the exact form the T Tauri models should take remains an enigma. Magnetospheric accretion is the accepted paradigm for circumstellar accretion, but the heating mechanisms and geometry of the funnel flow are still poorly constrained. Observations show that there are mass outflows from T Tauri stars, but it is still unknown whether the dominant flows come from the star, disk, or magnetosphere. These unknowns lead to a large number of free parameters in T Tauri radiative transfer simulations and degeneracy of the synthetic spectra produced as similar spectra can be created with multiple different inputs. Our theoretical understanding of T Tauri stars is refined by constraining the radiative transfer input parameters. This is vital for providing better observational diagnostic tools and for developing our theory of T Tauri stellar evolution. Understanding how T Tauri stars accrete matter, drive outflows, and manage the angular momentum problem is integral to establishing how low-mass stars evolve and produce planetary systems.

Radiative transfer studies in the literature have produced synthetic atomic spectra similar to the observed line profiles from T Tauri stars. A significant limitation to these studies is that they are plagued by a plethora of free parameters and unknowns. For instance, radiative transfer simulations show that the line profiles are susceptible to the temperature distribution of the accretion funnel. However, the heating mechanism of the accretion funnel is unknown. Current simulations use a model proposed by [Hartmann et al. \(1994\)](#) that is based on a volumetric heating rate balanced by radiative cooling. Furthermore, there are few modern radiative transfer studies of T Tauri stars, despite an increase in the availability of high-resolution spectroscopy. To address this, in this thesis, I have presented new developments to a state-of-the-art radiative transfer code TORUS and

the associated T Tauri model, which includes a polar stellar wind.

Nominally, this thesis uses the radiative transfer code TORUS and verifies the atomic hydrogen line transfer calculations for a 2.5D and 3D non-axisymmetric T Tauri model. However, the work also builds on T Tauri radiative transfer studies from the literature, implementing a more physically realistic stellar wind geometry and comparing the synthetic line profiles to multiple simultaneously observed hydrogen transition lines. Through this comparison, it was shown that current radiative transfer models could not concurrently reproduce the observed $H\alpha$ and infrared spectra. This led to the exploration of several modifications to the T Tauri model and the initial investigation into a set of 3D non-axisymmetric models, including a polar stellar wind. The 3D radiative transfer study led to several T Tauri rotational variability predictions, preparing the field for further study. Moreover, the thesis presents an atlas of $H\alpha$, $Pa\beta$, $Pa\gamma$, and $Br\gamma$ line profiles for a broad range of accretion rates, mass-loss rates, temperatures, and viewing inclinations.

During the work of this thesis, the non-LTE atomic statistical equilibrium calculation routines of TORUS were verified by reproducing results similar to those of [Kurosawa et al. \(2006\)](#). Furthermore, the polar stellar wind model was tested against the wind models of [Kurosawa et al. \(2011\)](#). The more physically realistic wind model presented in this thesis produced spectra noticeably different from the results seen in the literature. Notably, compared to [Kurosawa et al. \(2011\)](#), our model produced a greater $H\alpha$ emission close to the line centre and deeper blue-shifted sub-continuum absorption features in the infrared lines. This justifies using the more complex stellar wind, and I suggest that future radiative transfer studies implement a similar wind model.

Using TORUS and the T Tauri model, I compared a large grid of synthetic hydrogen line profiles to a set of spectra from 29 T Tauri stars observed with the X-Shooter instrument on VLT. Due to the broad wavelength range of X-Shooter, I was able to compare the simultaneously observed $H\alpha$, $Pa\beta$, $Pa\gamma$, and $Br\gamma$ line profiles with synthetic spectra of the same hydrogen transitions. T Tauri stars are spectroscopically variable; therefore, if multiple lines are to be compared accurately, they must be observed concurrently. Whilst the ensemble of $H\alpha$ line profiles produced spectra with the same range of widths and morphologies as seen in the observations, the infrared lines ($Pa\beta$, $Pa\gamma$, and $Br\gamma$) created profiles that had a mean HW10% narrower than the observed spectra by $\approx 80 \text{ km s}^{-1}$. Moreover, the synthetic infrared spectra showed an extremely high frequency (≈ 90 per cent) of inverse P-Cygni profiles, whereas the observed prevalence is ≈ 30 per cent (e.g [Folha & Emerson 2001](#)). A caveat to this comparison is that the observed sample of T Tauri stars is statistically ambiguous. This is because the sample is comparatively small and the simulation grid was not designed to directly probe the parameter space covered by the observations. However, the sample does show a very similar distribution of

Reipurth types, as seen in other studies (e.g. [Reipurth et al. 1996](#); [Folha & Emerson 2001](#)). Furthermore, the observations highlight that the majority of lines should be symmetrical, and only approximately 25 per cent of infrared lines should show inverse P-Cygni profiles.

To increase the width of the infrared line profiles and reduce the frequency of inverse P-Cygni profiles, we explored three modifications to our radiative transfer model. Firstly, it was shown that the broadening of the line profiles due to the stellar rotation has a negligible effect on the synthetic spectra unless the rotation rate is a significant proportion of the stellar break-up velocity. Secondly, I investigated whether small-scale motions in the accretion and wind flows could increase the width of the infrared line profiles. To do this, I incorporated the small-scale motions as turbulence using a Maxwell–Boltzmann velocity distribution. While increasing the turbulence could broaden the lines to the observed range, there was no physical justification for the large value of turbulence required ($\sim 100 \text{ km s}^{-1}$). Moreover, the resulting line profiles were boxy (broad peaks and bases), a morphology not commonly observed in T Tauri spectra. Lastly, I considered whether the high frequency of inverse P-Cygni profiles decreased the mean ensemble width of the infrared line profiles. For the inclinations of 60° and 80° , it was shown that considering only the blue side of the line profiles, the mean HW10% increased by 48 km s^{-1} . However, at an inclination of 20° (within the wind opening angle), the widths decreased when only the blue-side emission was considered due to greater absorption by the stellar wind. Therefore, it was concluded that, independently, none of the above modifications could fully bring the synthetic infrared lines into an agreement with the observed range of profile widths. Nevertheless, the combination of rotation, turbulence, and a reduced inverse P-Cygni frequency may be sufficient to explain the discrepancy in the widths of the spectra.

The high frequency of inverse P-Cygni profiles can be reduced by introducing non-axisymmetric accretion flow. For instance, if there is an obliquity to the magnetic field so that it is misaligned with the stellar pole, the accretion funnel will favour one hemisphere. In fact, the accretion column may prefer to flow in one hemisphere even when the magnetic and rotation axes align ([Ireland et al. 2021, 2022](#)). If the accretion column is non-axisymmetric, the line and continuum emissions are expected to vary as the star rotates. This has previously been shown in several radiative transfer simulations, for example, [Symington et al. \(2005a\)](#), [Kurosawa et al. \(2005\)](#), and [Kurosawa et al. \(2008\)](#). In this thesis, I expanded upon the literature by including a stellar wind in the 3D models, analysing the effect of mass loss and accretion rate, and quantifying the change in profile morphology. It was seen that on average, inverse P-Cygni profiles occur only in ≈ 34 per cent of the infrared profiles and, as expected, are phase-dependent. This is close to the observed frequency of inverse P-Cygni profiles ([Folha & Emerson 2001](#)).

I showed that, by using fiducial 3D radiative transfer T Tauri models, I could produce

synthetic hydrogen spectra that had similar morphologies and time-series variation as seen in observations. The rotational variability of the line profiles is dependent on the wavelength, inclination, accretion rate, and mass-loss rate of the models. As the accretion rate decreased, the change in the line profiles in different phases increased. The phase change in HW10% and the equivalent width of the synthetic line profiles are similar in range to the observed time-series data. The auto-correlation maps produced for our line profiles agree with the general areas of correlation and anti-correlation seen in previous radiative transfer studies and some observations. The auto-correlation maps also allowed me to make a prediction as to the origin of the anti-correlation between the high-velocity blue wing of H α and its line centre observed in LkCa 15 (Alencar et al. 2018). The mean change in HW10% of the infrared lines is $\approx 60 \text{ kms}^{-1}$, less than the necessary width increase seen in Chapter 4. Only six models are presented, and the maximum change in the infrared HW10% over the rotational phase is $\approx 170 \text{ kms}^{-1}$. However, both the infrared and H α spectra are broadened concurrently. This shifts the infrared lines into better agreement with the observed range of widths while simultaneously making the H α profiles too wide. The effect is exacerbated by Stark broadening. A more extensive set of models is needed with a wide range of accretion rates temperatures to determine if a non-axisymmetric geometry can solve the narrow infrared lines.

In conclusion, the 3D models presented in this thesis build on the work of Symington et al. (2005a) and Esau et al. (2014) by focusing on a magnetospheric geometry with accretion columns in alternate hemispheres and exploring this paradigm for a range of accretion rates and azimuthal extents. Furthermore, the models also include a non-axisymmetric stellar wind, the mass-loss rate of which has a significant effect on the spectral variability and line correlations. Lastly, the models predict line width and morphology variations, which could be verified with current or future time-series data. Specifically, it would require a time-series monitoring of T Tauri stars (e.g. Sousa et al. 2021; Pouilly et al. 2020; Alencar et al. 2018) over a few rotation periods using a high spectral resolution and broad wavelength coverage, ideally producing flux-calibrated spectra.

The observed Pa β to Br γ flux ratio for T Tauri stars, both in our data and in that of Muzerolle et al. (2001), is constant across a wide range of accretion rates. I showed that for the models to produce synthetic line profiles with a Pa β to Br γ flux ratio similar to the observed stars, the magnetospheric temperature must increase as the accretion rate decreases; this confirmed the results of Muzerolle et al. (2001). Finally, it was seen that the frequency of the P-Cygni profiles was correlated not just with the mass-loss rate but with the ratio of mass loss to mass accretion. This is because the increased emission from higher accretion rates masks the blue-shifted absorption. A further effect seen in our synthetic hydrogen profiles is that, despite the larger optical depth of H α , the frequency

of the P-Cygni profiles was higher in the infrared hydrogen lines.

In summary, in this thesis, I demonstrate that the T Tauri axisymmetric radiative transfer models cannot simultaneously reproduce the observed distributions of width and morphology for $H\alpha$, $Pa\beta$, $Pa\gamma$, and $Br\gamma$. The addition of rotation and turbulence to the fiducial models cannot sufficiently broaden the infrared lines, while the rotation and turbulent velocities are constrained to physically realistic values. By introducing a non-axisymmetric magnetosphere, the half-widths of the synthetic spectra can be increased by a mean of 50 per cent. However, both the infrared and $H\alpha$ lines are broadened simultaneously. Finally, from the radiative transfer simulations, several predictions have been made. For instance, the frequency of P-Cygni profiles, the sensitivity of the hydrogen spectra to a stellar wind mass-loss rate, and the variability of the HW10% and the equivalent width. Although there are still improvements to be made with the models developed in this thesis, the research presented shows the current state of the modern radiative transfer simulations and pushes the field closer to a better understanding of T Tauri spectroscopy.

6.1 Future Outlook

As this thesis has demonstrated, while radiative transfer simulations can provide valuable insight into the radiative emission of T Tauri stars, some phenomena are challenging to reproduce. The first and most tempting recourse is to throw more physics into the computational melting pot. However, the radiative transfer models of T Tauri stars already suffer from a surfeit of free parameters. Adding further elaborations has the potential to increase the degeneracy of the simulated emission without adding any real insight into the origins of the observed spectra. Moreover, given a sufficient number of parameters, a model can be constructed to fit any observed spectra. Therefore, the addition of further complexity to T Tauri radiative transfer models must be done carefully and, if possible, with observational and theoretical constraints.

Nevertheless, several areas of improvement and research should be investigated in future radiative transfer studies. These can be broadly split into two categories: observations of T Tauri stars to add constraints to the models and developments to the radiative transfer simulations. Future radiative transfer models would benefit from constraints gained from the following comparison, either from pre-existing data or new observations.

- Further comparisons should be made between synthetic line profiles and large data sets of high-resolution, optical, infrared, and UV spectra. For example, from the GIARPS infrared spectrometer. Simultaneous observations of multiple atomic transition lines are desirable to remove uncertainty from the spectral variability. Further-

more, as an improvement over the spectra presented in this thesis, the observations should be corrected for veiling and extinction. This would allow for comparisons between the flux and the equivalent width of the observed and synthetic data.

- High-cadence time-series spectroscopy of T Tauri stars is necessary for constraining the 3D non-axisymmetric magnetospheric radiative transfer models. The observations should be used to test predictions such as the variability of the equivalent width and the HW10%.
- Spectro-interferometry surveys and spectro-astrometry of T Tauri spectra could probe the geometry of the magnetosphere and winds by providing sub-seeing spatial information. This may add constraints to the size and location of line-forming regions around the T Tauri star.
- Observations characterising the surface magnetic fields of T Tauri stars, for example, ZDI maps, may further constrain the magnetospheric geometry.

Future radiative transfer models should attempt to reduce the degeneracy of the synthetic spectra and further curtail their free parameters by constraints based on T Tauri observations. However, subsequent studies should consider the following areas of research.

- In this thesis, I considered the four hydrogen transition lines of $H\alpha$, $Pa\beta$, $Pa\gamma$, and $Br\gamma$. However, future work would benefit from modelling more lines in both hydrogen and helium. For example, the He I $\lambda 10830$ Å triplet, is optically thick and very sensitive to absorption from winds and the magnetosphere (e.g. [Kwan et al. 2007](#)). To this end, TORUS already contains much of the necessary code to extend the models to the helium lines, making this an ideal project for future work.
- An outstanding issue with the T Tauri model is the unknown heating mechanisms of the accretion column and its temperature distribution. [Martin \(1996\)](#) developed a self-consistent theory of heating using adiabatic compression, but it was shown by [Muzerolle et al. \(1998b\)](#) that it did not produce line profiles in agreement with the observations. Therefore, it is imperative that work is undertaken to create a self-consistent theory of heating in the accretion column. Codes such as TORUS can then be used to test heating mechanisms by performing radiative equilibrium calculations to determine magnetospheric temperature distributions and emission.
- Further radiative transfer simulations may benefit from including continuum emission from dust in the circumstellar disk, which is an important factor for infrared lines, in particular, $Br\gamma$.

- The model presented in this thesis considers the hot-spot as producing only continuum emission. However, line emission is expected from these regions (e.g. [Dodin 2018](#)) and its inclusion may be significant in the simulated spectra.
- The models could be used to create synthetic spectro-astrometric and spectro-interferometric observations to give insight into the spatial separation and orientation of the line emission regions.
- Spectropolarimetry has been used to show that the T Tauri emission lines originate from within a structured magnetic field (e.g. [Symington et al. 2005b](#)). A possible extension to such observations is to use the radiative transfer simulations to compute the Stokes vectors. Adding a magnetic field configuration to the grid (e.g. from magnetohydrodynamic models) would allow for the simulation of synthetic circular spectropolarimetry and more accurate diagnostics of observed magnetic fields.

Finally, several studies of T Tauri line emission have used the output of a magnetohydrodynamic simulation to map the density and velocity distributions onto a radiative transfer grid to produce synthetic line profiles (e.g. [Kurosawa et al. 2008](#); [Kurosawa & Romanova 2012](#); [Alencar et al. 2012](#)). These forms of simulation offer the benefits of both dynamic and radiative modelling. However, the temperature distributions of the magnetohydrodynamic models are not realistic, as they lack a comprehensive treatment of radiative heating and cooling. Therefore, these models have to use modified temperature distributions based on radiative transfer models such as the one presented in this thesis. Future radiative transfer studies should incorporate the velocity and density distributions of magnetohydrodynamic simulations. For instance, by using multiple time slices of magnetohydrodynamic simulations, such models could study the time-series variability induced by fluctuating accretion, winds, and magnetospheric ejections.

Bibliography

- Alencar S. H. P., Basri G., 2000, [AJ](#), 119, 1881
- Alencar S. H. P., Johns-Krull C. M., Basri G., 2001, [AJ](#), 122, 3335
- Alencar S. H. P., et al., 2012, [A&A](#), 541, A116
- Alencar S. H. P., et al., 2018, [A&A](#), 620, A195
- Anthonioz F., et al., 2015, [A&A](#), 574, A41
- Antonucci S., et al., 2011, [A&A](#), 534, A32
- Baxter E. J., Covey K. R., Muench A. A., Fűrész G., Rebull L., Szentgyorgyi A. H., 2009, [AJ](#), 138, 963
- Bertout C., Bouvier J., 1988, in European Southern Observatory Conference and Workshop Proceedings. pp 69–75
- Blandford R. D., Payne D. G., 1982, [MNRAS](#), 199, 883
- Bouvier J., Cabrit S., Fernandez M., Martin E. L., Matthews J. M., 1993, [A&A](#), 272, 176
- Bouvier J., Alencar S. H. P., Harries T. J., Johns-Krull C. M., Romanova M. M., 2007, in Reipurth B., Jewitt D., Keil K., eds, Protostars and Planets V. p. 479 ([arXiv:astro-ph/0603498](#))
- Bouvier J., Matt S. P., Mohanty S., Scholz A., Stassun K. G., Zanni C., 2014, in Beuther H., Klessen R. S., Dullemond C. P., Henning T., eds, Protostars and Planets VI. p. 433 ([arXiv:1309.7851](#)), [doi:10.2458/azu_uapress_9780816531240-ch019](#)
- Bouvier J., et al., 2020, [A&A](#), 636, A108
- Calvet N., Gullbring E., 1998, [ApJ](#), 509, 802
- Camenzind M., 1990, [Reviews in Modern Astronomy](#), 3, 234
- Cardelli J. A., Clayton G. C., Mathis J. S., 1989, [ApJ](#), 345, 245
- Castor J. I., Lamers H. J. G. L. M., 1979, [ApJS](#), 39, 481
- Cranmer S. R., 2008, [ApJ](#), 689, 316
- Cranmer S. R., 2009, [ApJ](#), 706, 824
- Dmitriev D. V., Grinin V. P., Katysheva N. A., 2019, [Astronomy Letters](#), 45, 371
- Dodin A., 2018, [MNRAS](#), 475, 4367
- Edwards S., Hartigan P., Ghandour L., Andrusis C., 1994, [AJ](#), 108, 1056
- Edwards S., Fischer W., Kwan J., Hillenbrand L., Dupree A. K., 2003, [ApJ](#), 599, L41

- Edwards S., Fischer W., Hillenbrand L., Kwan J., 2006, *ApJ*, 646, 319
- Edwards S., Kwan J., Fischer W., Hillenbrand L., Finn K., Fedorenko K., Feng W., 2013, *Protostars and Planets VI*, p. 2
- Esau C. F., Harries T. J., Bouvier J., 2014, *MNRAS*, 443, 1022
- Espartero C. C., Robinson C. E., Romanova M. M., Thanathibodee T., Wendeborn J., Calvet N., Reynolds M., Muzerolle J., 2021, *Nature*, 597, 41
- Fischer D. A., et al., 2016, *PASP*, 128, 066001
- Folha D. F. M., Emerson J. P., 1999, *A&A*, 352, 517
- Folha D. F. M., Emerson J. P., 2001, *A&A*, 365, 90
- Frasca A., et al., 2015, *A&A*, 575, A4
- Fullerton A. W., Gies D. R., Bolton C. T., 1996, *ApJS*, 103, 475
- Ghosh P., Lamb F. K., Pethick C. J., 1977, *ApJ*, 217, 578
- Gravity Collaboration et al., 2020, *Nature*, 584, 547
- Griem H. R., 1964, *Plasma spectroscopy*. McGraw-Hill Book Company
- Grinin V. P., 2001, *Astrophysics*, 44, 402
- Harries T. J., Haworth T. J., Acreman D., Ali A., Douglas T., 2019, *Astronomy and Computing*, 27, 63
- Hartigan P., Edwards S., Ghandour L., 1995, *ApJ*, 452, 736
- Hartmann L., 1982, *ApJS*, 48, 109
- Hartmann L., Avrett E., Edwards S., 1982, *ApJ*, 261, 279
- Hartmann L., Hewett R., Calvet N., 1994, *ApJ*, 426, 669
- Hartmann L., Herczeg G., Calvet N., 2016, *ARA&A*, 54, 135
- Herbig G. H., Bell K. R., 1988, *Third Catalog of Emission-Line Stars of the Orion Population : 3 : 1988*. Lick Observatory
- Herbst W., Bailer-Jones C. A. L., Mundt R., Meisenheimer K., Wackermann R., 2002, *A&A*, 396, 513
- Hogerheijde M. R., van der Tak F., 2000, *A&A*, 362, 697
- Hubeny I., 2013, *Stellar Atmospheres*. Springer Netherlands, Dordrecht, pp 51–85, doi:10.1007/978-94-007-5615-1_2, https://doi.org/10.1007/978-94-007-5615-1_2
- Hunter J. D., 2007, *Computing in Science & Engineering*, 9, 90
- Hussain G. A. J., et al., 2009, *MNRAS*, 398, 189
- Ireland L. G., Zanni C., Matt S. P., Pantolmos G., 2021, *ApJ*, 906, 4
- Ireland L. G., Matt S. P., Zanni C., 2022, *ApJ*, 929, 65
- Isella A., Carpenter J. M., Sargent A. I., 2010, *ApJ*, 714, 1746
- Johns C. M., 1994, PhD thesis, University of California, Berkeley
- Johns C. M., Basri G., 1995, *AJ*, 109, 2800

- Johns-Krull C. M., 2007, *ApJ*, 664, 975
- Joy A. H., 1945, *ApJ*, 102, 168
- Kasper J. C., et al., 2021, *Phys. Rev. Lett.*, 127, 255101
- Kausch W., et al., 2015, *A&A*, 576, A78
- Klein R. I., Castor J. I., 1978, *ApJ*, 220, 902
- Koenigl A., 1991, *ApJ*, 370, L39
- Kounkel M., et al., 2019, *AJ*, 157, 196
- Kraus S., et al., 2008, *A&A*, 489, 1157
- Kraus S., et al., 2020, *Science*, 369, 1233
- Kurosawa R., Romanova M. M., 2012, *MNRAS*, 426, 2901
- Kurosawa R., Harries T. J., Symington N. H., 2005, *MNRAS*, 358, 671
- Kurosawa R., Harries T. J., Symington N. H., 2006, *MNRAS*, 370, 580
- Kurosawa R., Romanova M. M., Harries T. J., 2008, *MNRAS*, 385, 1931
- Kurosawa R., Romanova M. M., Harries T. J., 2011, *MNRAS*, 416, 2623
- Kurucz R. L., 1979, *ApJS*, 40, 1
- Kwan J., Edwards S., Fischer W., 2007, *ApJ*, 657, 897
- Lemke M., 1997, *A&AS*, 122, 285
- Lima G. H. R. A., Alencar S. H. P., Calvet N., Hartmann L., Muzerolle J., 2010, *A&A*, 522, A104
- Liu C.-F., Shang H., Herczeg G. J., Walter F. M., 2016, *ApJ*, 832, 153
- Long M., Romanova M. M., Kulkarni A. K., Donati J. F., 2011, *MNRAS*, 413, 1061
- Luttermoser D. G., Johnson H. R., 1992, *ApJ*, 388, 579
- Malo L., Artigau É., Doyon R., Lafrenière D., Albert L., Gagné J., 2014, *ApJ*, 788, 81
- Manara C. F., Testi L., Natta A., Rosotti G., Benisty M., Ercolano B., Ricci L., 2014, *A&A*, 568, A18
- Manara C. F., Fedele D., Herczeg G. J., Teixeira P. S., 2016, *A&A*, 585, A136
- Martin S. C., 1996, *ApJ*, 470, 537
- Matt S., Pudritz R. E., 2005a, *MNRAS*, 356, 167
- Matt S., Pudritz R. E., 2005b, *ApJ*, 632, L135
- Matt S., Pudritz R. E., 2008a, *ApJ*, 678, 1109
- Matt S., Pudritz R. E., 2008b, *ApJ*, 681, 391
- McGinnis P. T., et al., 2015, *A&A*, 577, A11
- McGinnis P., Bouvier J., Gallet F., 2020, *MNRAS*, 497, 2142
- Mendoza V. E. E., 1968, *ApJ*, 151, 977
- Modigliani A., et al., 2010, in Silva D. R., Peck A. B., Soifer B. T., eds, Society of Photo-Optical Instrumentation Engineers (SPIE) Conference Series Vol. 7737, Observatory Operations: Strategies, Processes, and Systems III. p. 773728, doi:10.1117/12.857211

- Muzerolle J., Hartmann L., Calvet N., 1998a, *AJ*, 116, 455
- Muzerolle J., Calvet N., Hartmann L., 1998b, *ApJ*, 492, 743
- Muzerolle J., Calvet N., Hartmann L., 2001, *ApJ*, 550, 944
- Nguyen D. C., Brandeker A., van Kerkwijk M. H., Jayawardhana R., 2012, *ApJ*, 745, 119
- Nisini B., Antonucci S., Alcalá J. M., Giannini T., Manara C. F., Natta A., Fedele D., Biazzo K., 2018, *A&A*, 609, A87
- Oliveira J. M., Foing B. H., van Loon J. T., Unruh Y. C., 2000, *A&A*, 362, 615
- Pouilly K., et al., 2020, *A&A*, 642, A99
- Reback J., et al., 2020, pandas-dev/pandas: Pandas 1.0.3, doi:10.5281/zenodo.3715232, <https://doi.org/10.5281/zenodo.3715232>
- Reipurth B., Pedrosa A., Lago M. T. V. T., 1996, *A&AS*, 120, 229
- Romanova M. M., Ustyugova G. V., Koldoba A. V., Wick J. V., Lovelace R. V. E., 2003, *ApJ*, 595, 1009
- Rucinski S. M., et al., 2008, *MNRAS*, 391, 1913
- Rugel M., Fedele D., Herczeg G., 2018, *A&A*, 609, A70
- Rundle D., Harries T. J., Acreman D. M., Bate M. R., 2010, *MNRAS*, 407, 986
- Schmidt T. O. B., Vogt N., Neuhäuser R., Bedalov A., Roell T., 2013, *A&A*, 557, A80
- Schneider G., Wood K., Silverstone M. D., Hines D. C., Koerner D. W., Whitney B. A., Bjorkman J. E., Lowrance P. J., 2003, *AJ*, 125, 1467
- Schneider P. C., Manara C. F., Facchini S., Günther H. M., Herczeg G. J., Fedele D., Teixeira P. S., 2018, *A&A*, 614, A108
- Simon M., Dutrey A., Guilloteau S., 2000, *ApJ*, 545, 1034
- Smette A., et al., 2015, *A&A*, 576, A77
- Sobolev V. V., 1957, *Soviet Ast.*, 1, 678
- Sousa A. P., et al., 2021, *A&A*, 649, A68
- Steinacker J., Baes M., Gordon K. D., 2013, *ARA&A*, 51, 63
- Strom K. M., Strom S. E., Edwards S., Cabrit S., Skrutskie M. F., 1989, *AJ*, 97, 1451
- Sutton K., 1978, *Journal of Quantitative Spectroscopy and Radiative Transfer*, 20, 333
- Symington N. H., Harries T. J., Kurosawa R., 2005a, *MNRAS*, 356, 1489
- Symington N. H., Harries T. J., Kurosawa R., Naylor T., 2005b, *MNRAS*, 358, 977
- Uzdensky D. A., Königl A., Litwin C., 2002, *ApJ*, 565, 1191
- Vernazza J. E., Avrett E. H., Loeser R., 1973a, *ApJ*, 184, 605
- Vernazza J. E., Avrett E. H., Loeser R., 1973b, *ApJ*, 184, 605
- Vernazza J. E., Avrett E. H., Loeser R., 1981, *ApJS*, 45, 635
- Vernet J., et al., 2011, *A&A*, 536, A105
- Wenger M., et al., 2000, *A&AS*, 143, 9
- White R. J., Basri G., 2003, *ApJ*, 582, 1109

- Wilson T. J. G., Matt S., Harries T. J., Herczeg G. J., 2022, [MNRAS](#), 514, 2162
- Zanni C., Ferreira J., 2009, [A&A](#), 508, 1117
- Zanni C., Ferreira J., 2013, [A&A](#), 550, A99
- de la Cruz Rodríguez J., van Noort M., 2017, [Space Sci. Rev.](#), 210, 109

Appendix A

Atlas of Line Profiles from the Axisymmetric Accretion Models

The full set of line profiles that are generated in [Chapter 4](#) using an 2.5D axisymmetric T Tauri model.

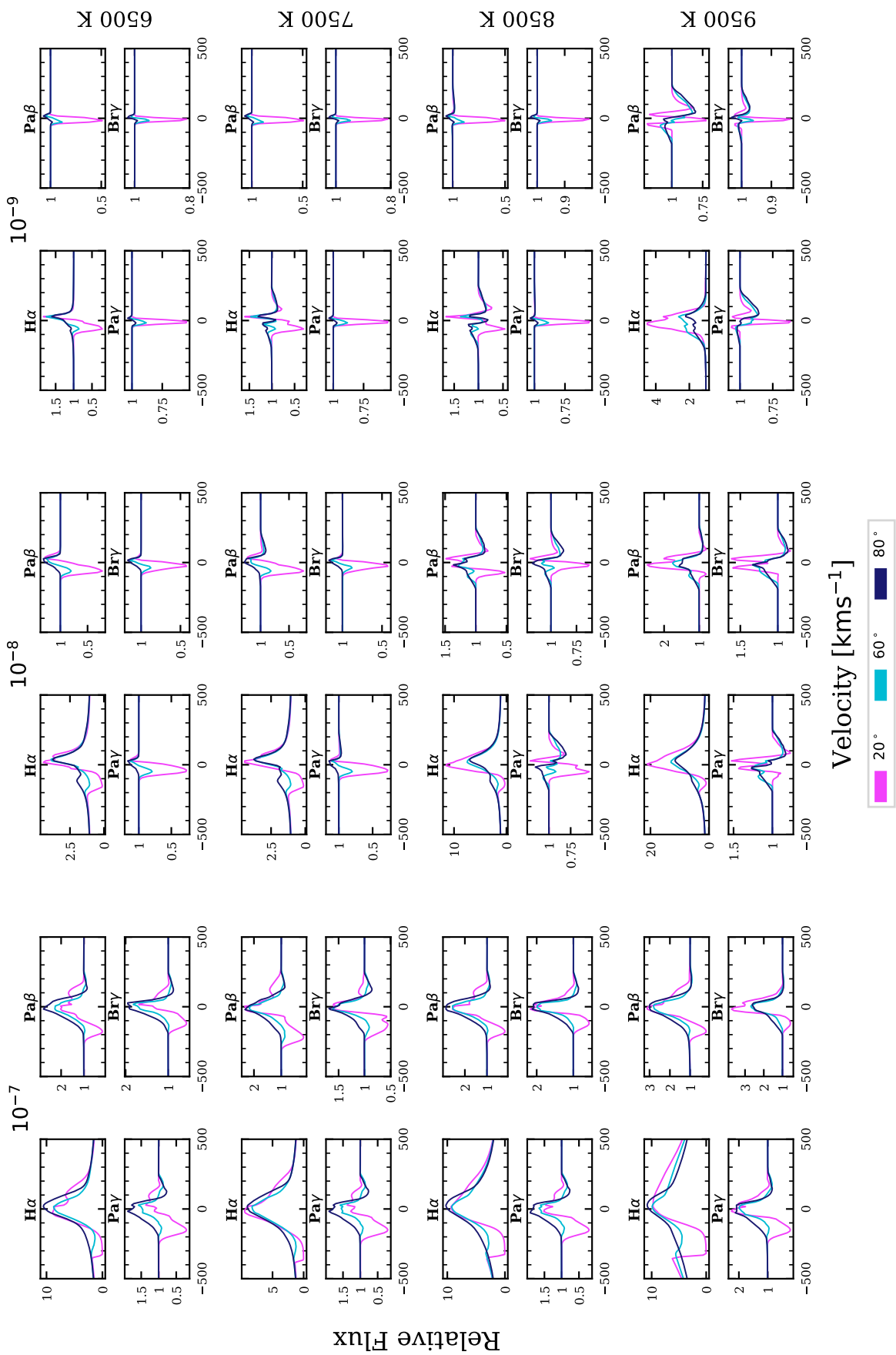


Figure A.1: A sample of the line profiles produced by TORUS . The spectra are shown for $\dot{M}_{\text{sw}} = 0.1 \dot{M}_{\text{acc}}$ and $T_{\text{sw}} = 10000 \text{ K}$. The lines are arranged by \dot{M}_{acc} (columns) and T_{acc} (rows). Each section is subdivided by hydrogen transition and shows the three different inclinations (colours).

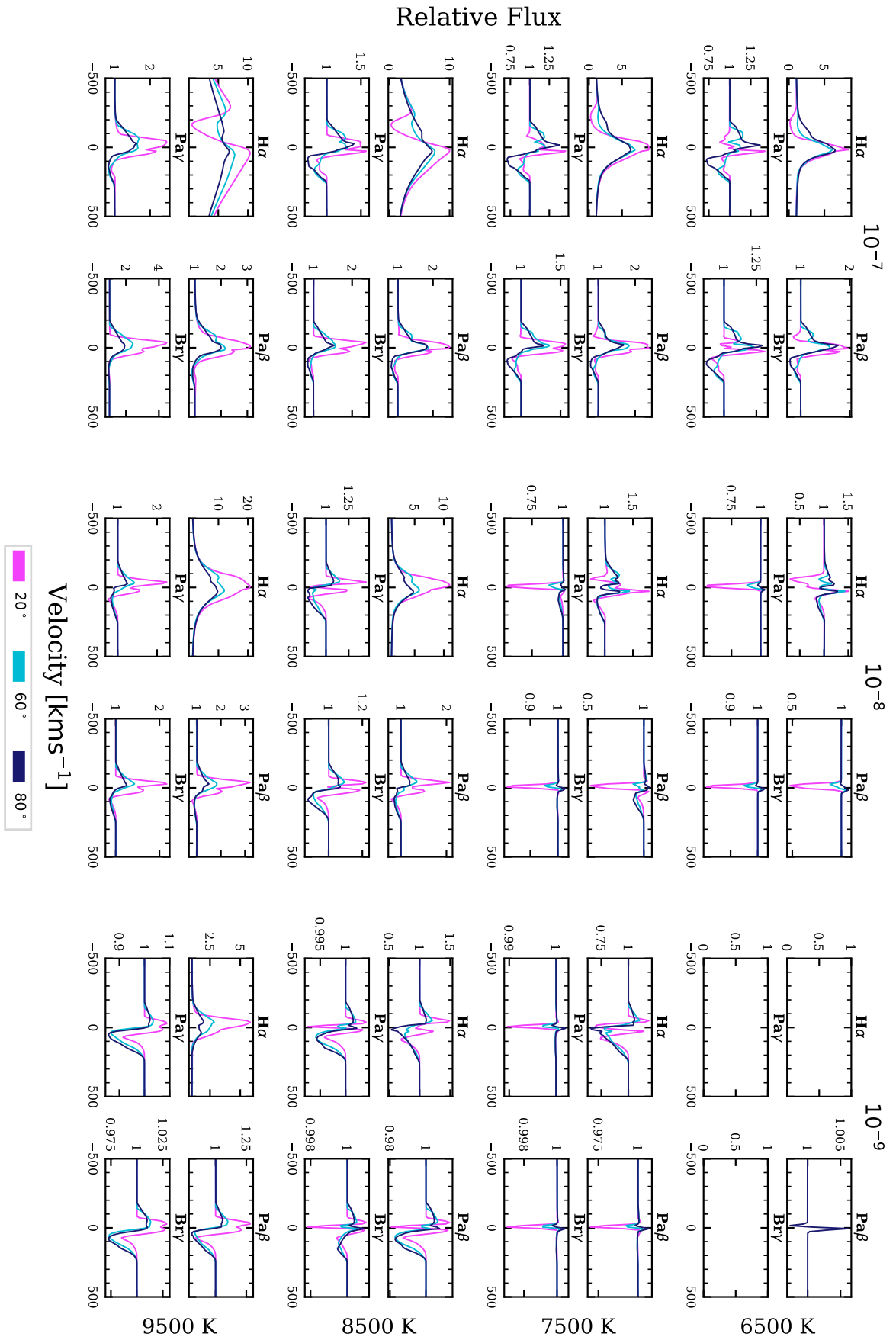


Figure A.1: Continued. Models presented here for $\dot{M}_{\text{sw}} = 0.01 \dot{M}_{\text{acc}}$ and $T_{\text{sw}} = 10000$ K.

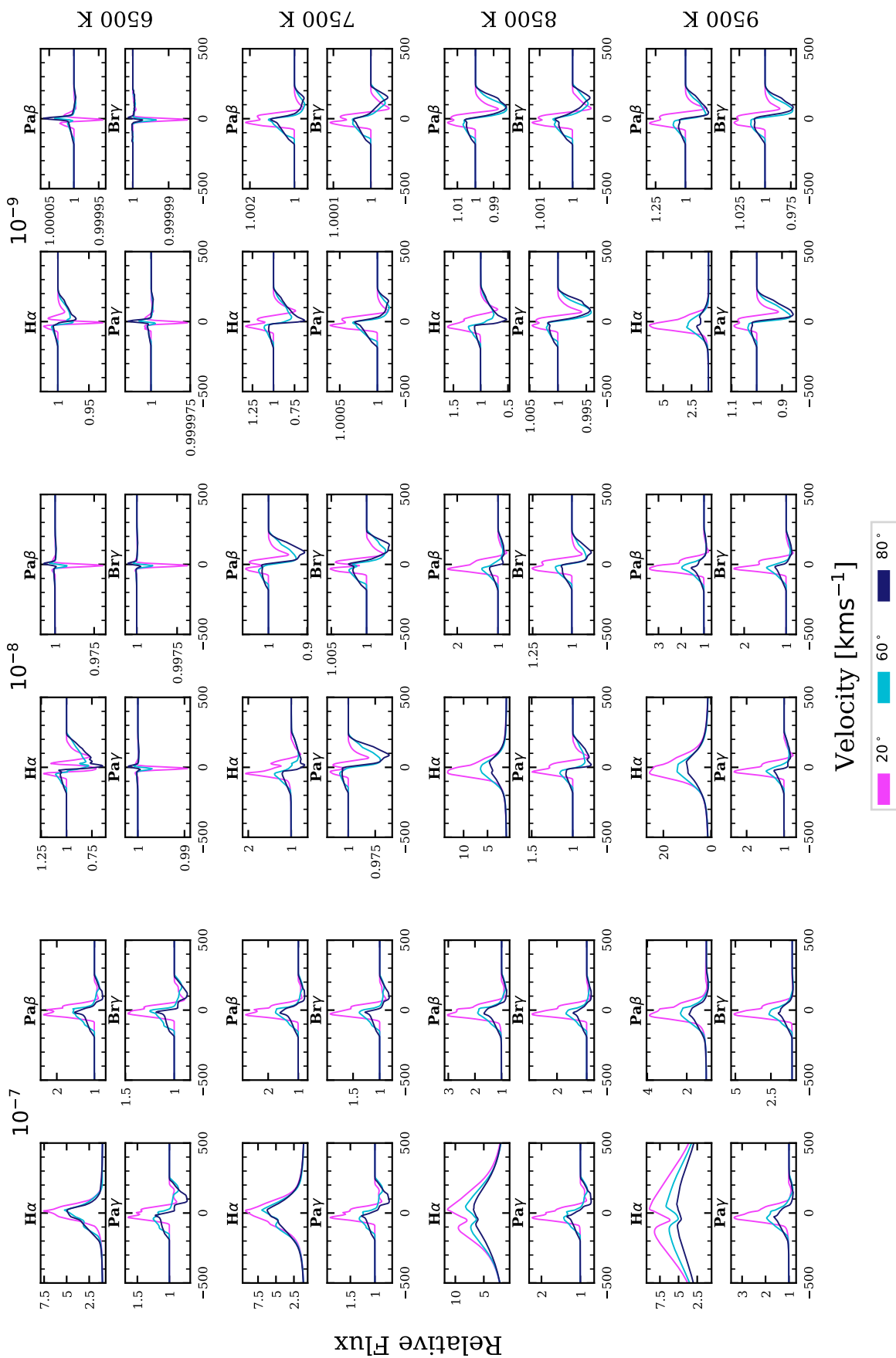


Figure A.1: Continued. Models presented here for $\dot{M}_{\text{sw}} = 0.001 \dot{M}_{\text{acc}}$ and $T_{\text{sw}} = 10000 \text{ K}$.

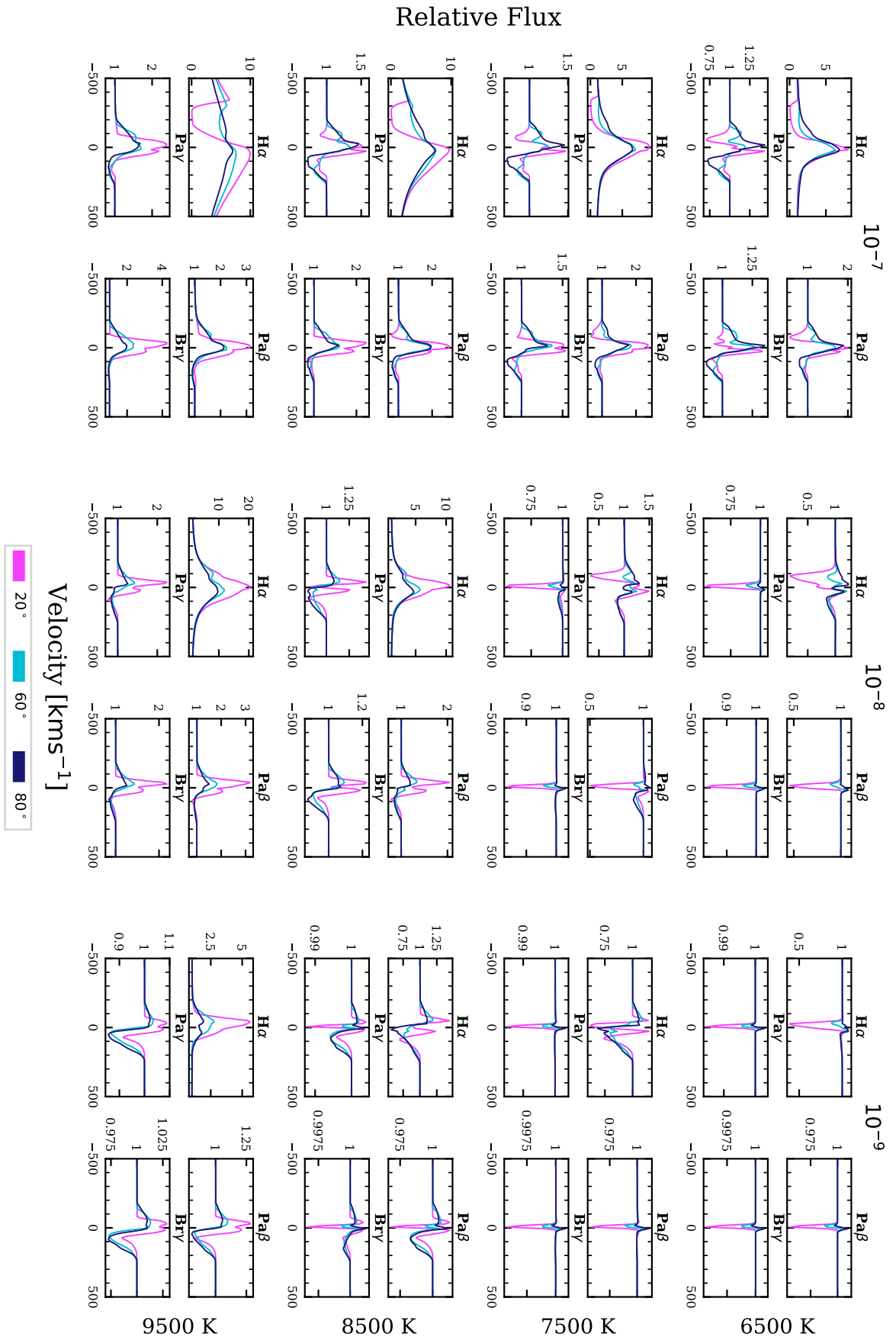


Figure A.1: Continued. Models presented here for $\dot{M}_{\text{sw}} = 0.1 \dot{M}_{\text{acc}}$ and $T_{\text{sw}} = 8000$ K.

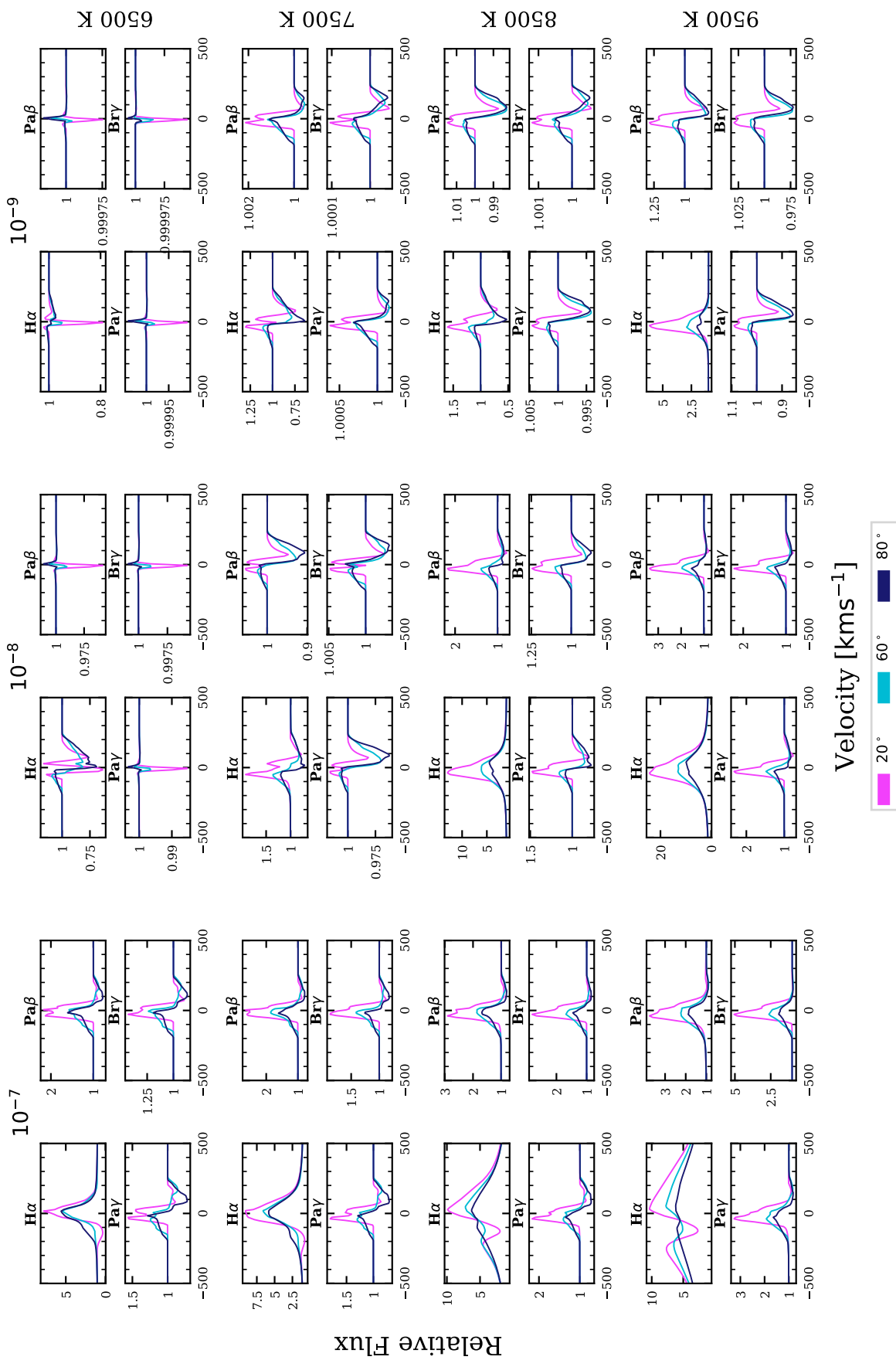


Figure A.1: Continued. Models presented here for $\dot{M}_{\text{sw}} = 0.01 \dot{M}_{\text{acc}}$ and $T_{\text{sw}} = 8000$ K.

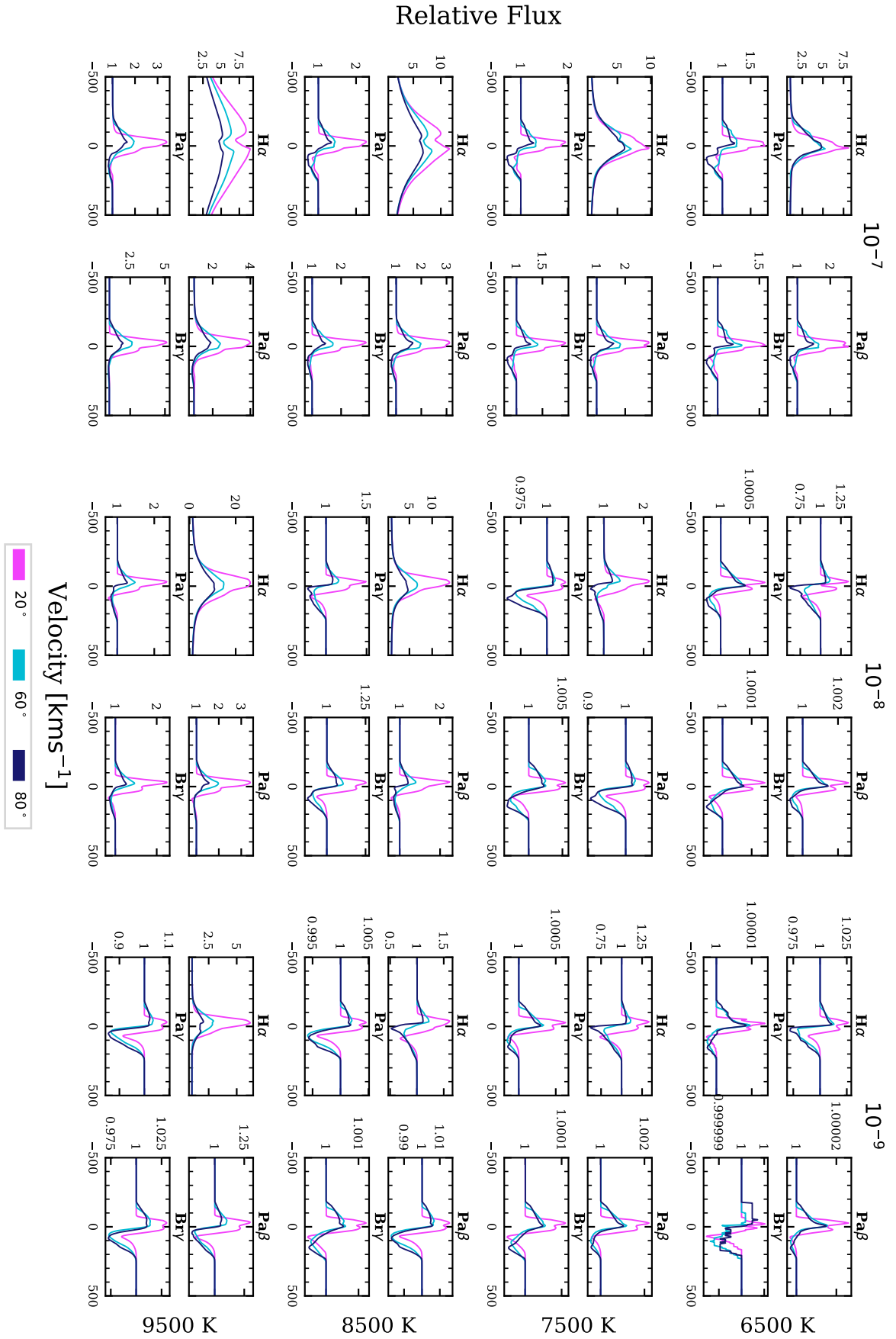


Figure A.1: Continued. Models presented here for $\dot{M}_{\text{sw}} = 0.001 \dot{M}_{\text{acc}}$ and $T_{\text{sw}} = 8000$ K.

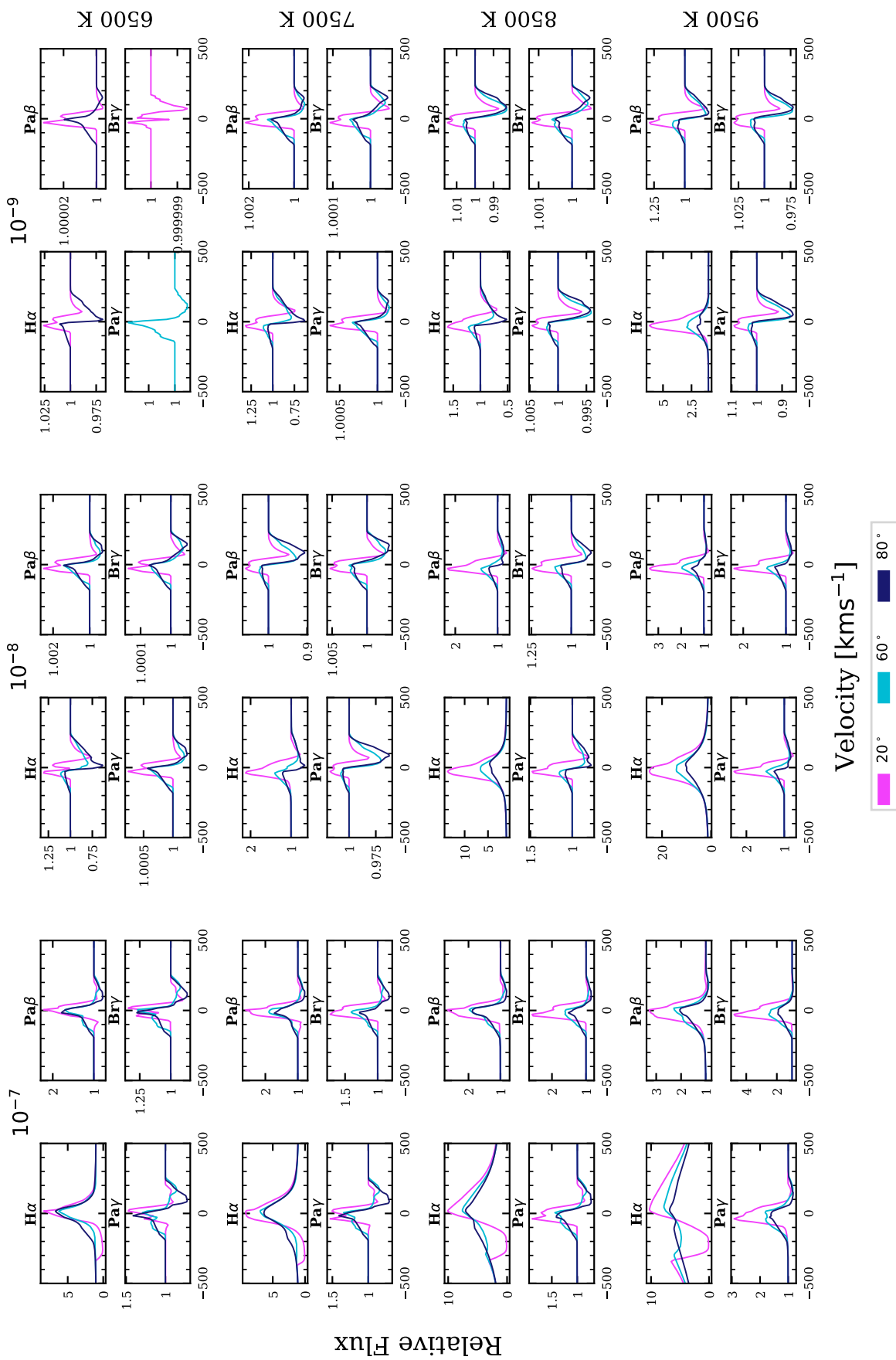


Figure A.1: Continued. Models presented here for $\dot{M}_{sw} = 0.1 \dot{M}_{acc}$ and $T_{sw} = 6000$ K.

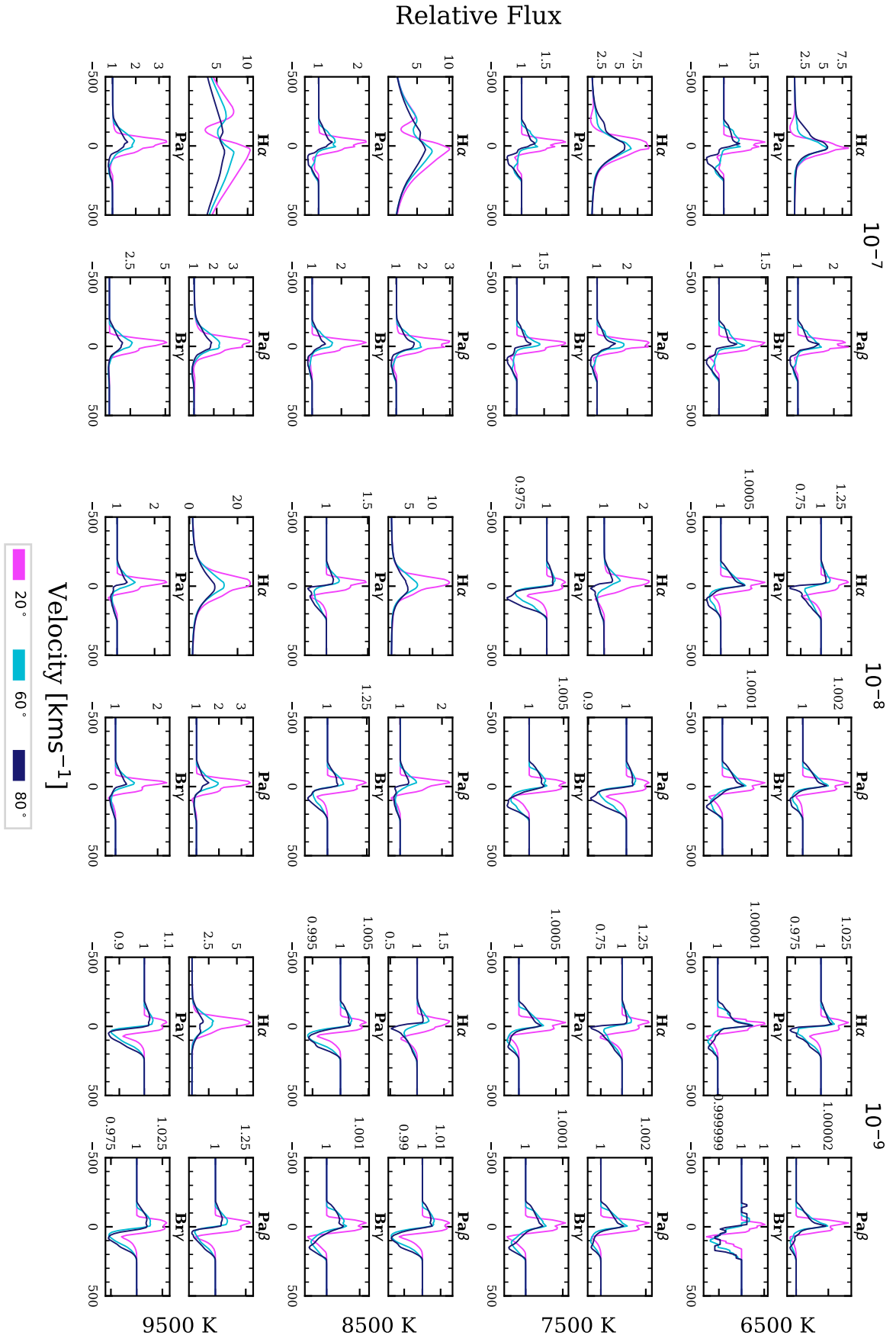


Figure A.1: Continued. Models presented here for $\dot{M}_{\text{sw}} = 0.01 \dot{M}_{\text{acc}}$ and $T_{\text{sw}} = 6000$ K.

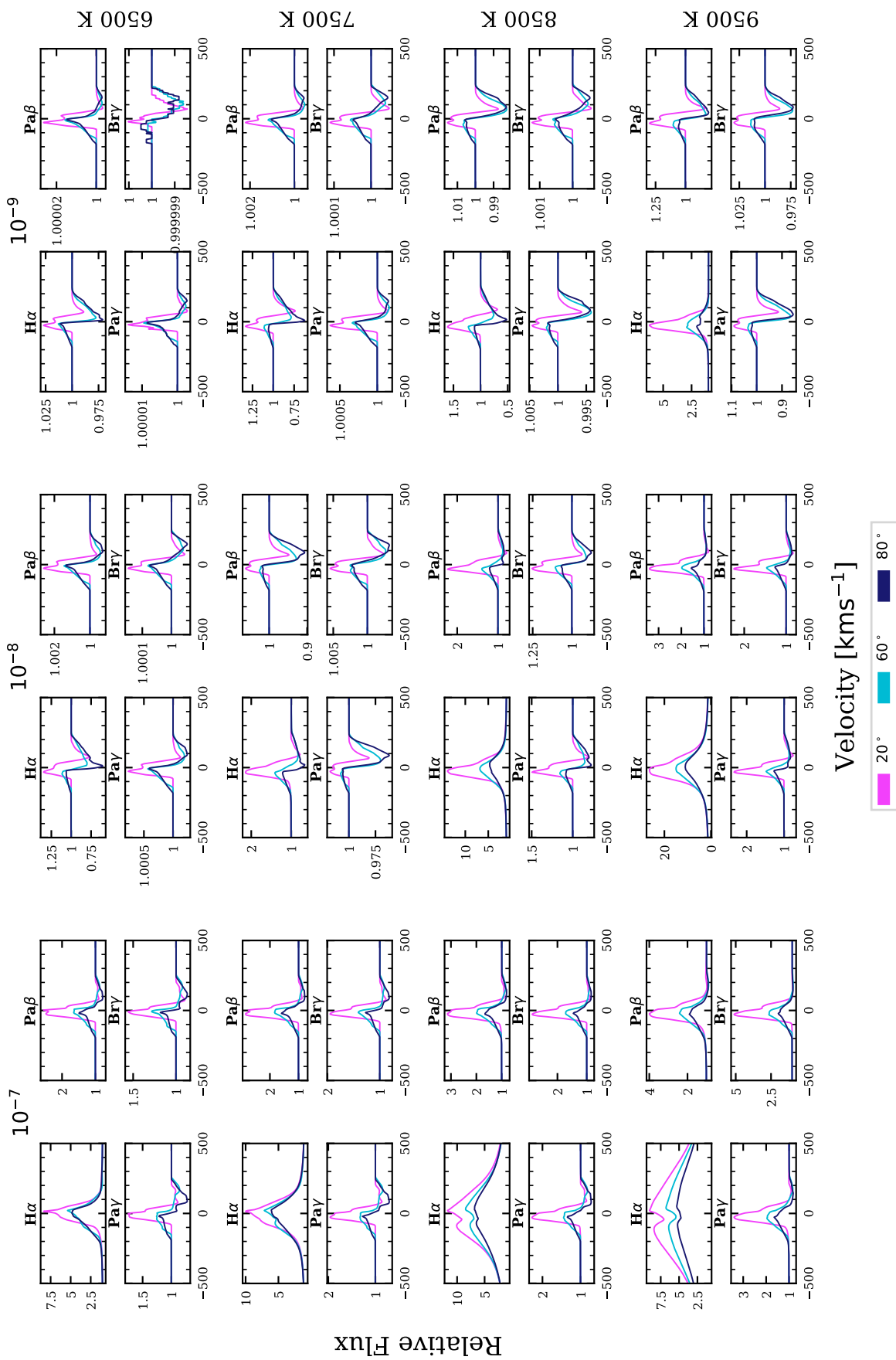


Figure A.1: Continued. Models presented here for $\dot{M}_{\text{sw}} = 0.001 \dot{M}_{\text{acc}}$ and $T_{\text{sw}} = 6000 \text{ K}$.

Appendix B

Spectral Variability Figures

Figures showing the mean line profile, the RMSD, the continuum level, and quotient spectra for the 3D non-axisymmetric models presented in [Chapter 5](#).

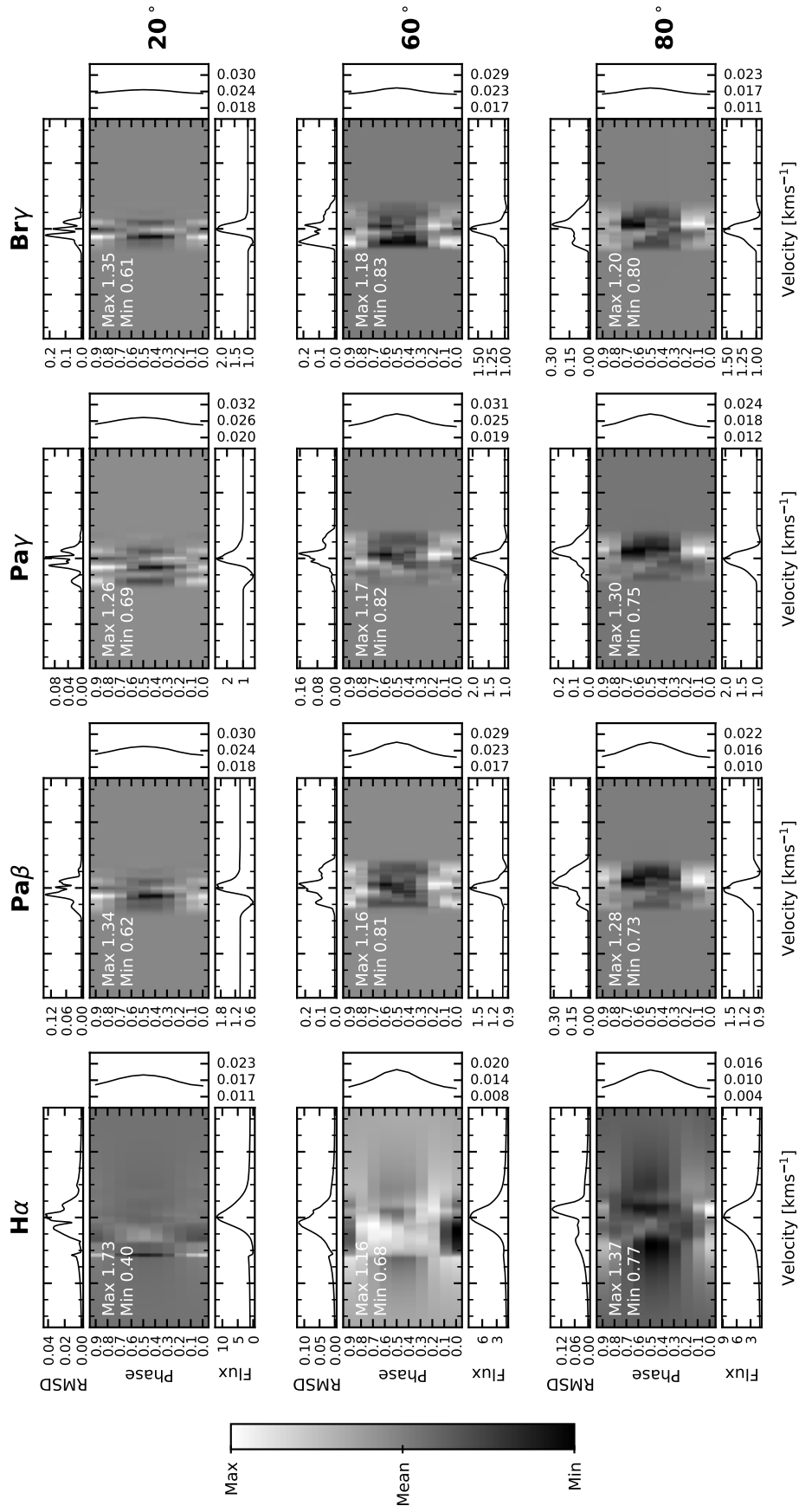


Figure B.1: Spectra from model 0, arranged by inclination and wavelength. The bottom plot shows the mean spectrum, the grey-scale image is the quotient of the spectrum at each rotational phase. The top plot displays RMSD distribution. The plot to the right shows the change in continuum level across the phase. The minimum and maximum range of each the grey-scale images is indicated.

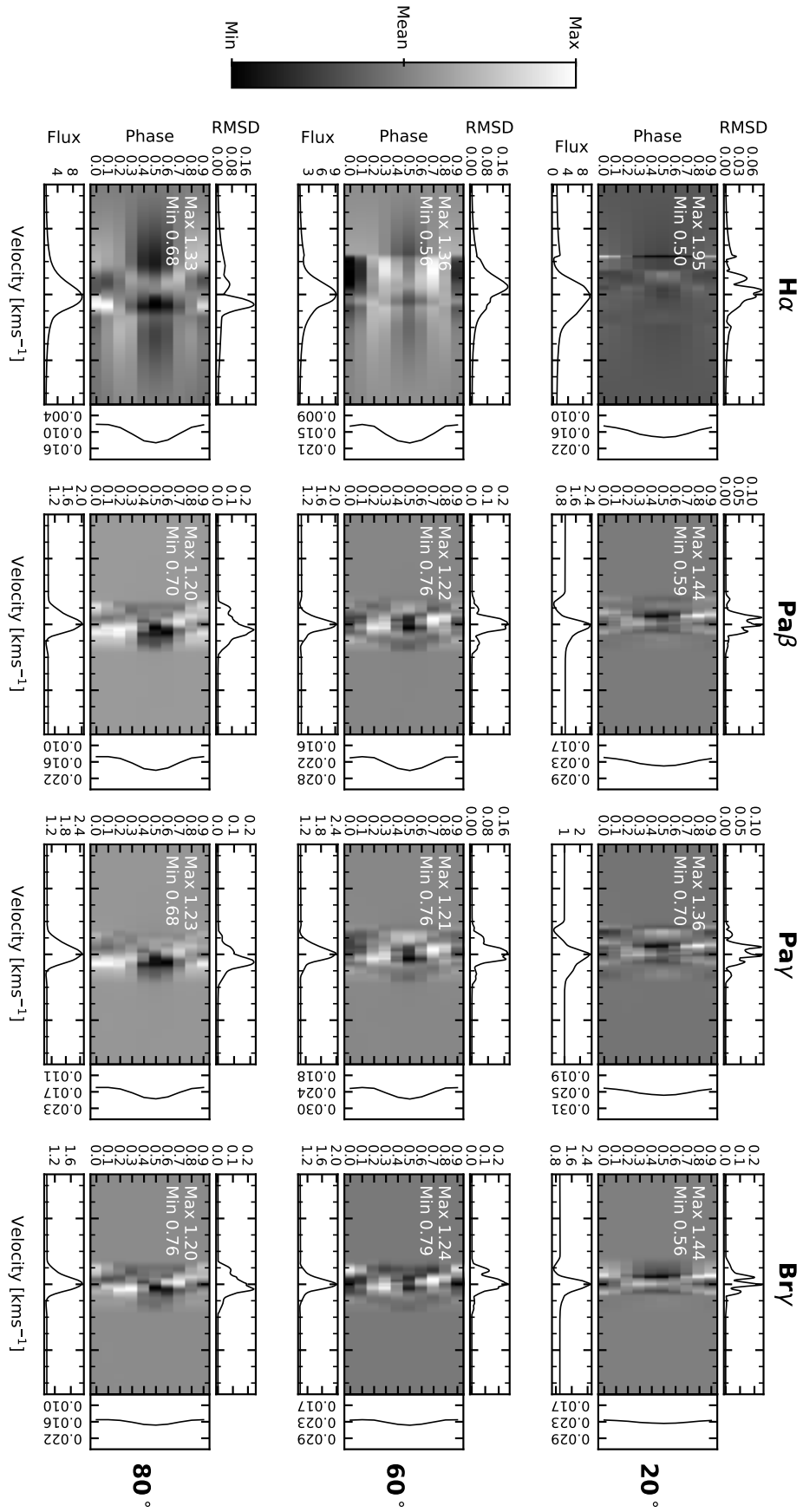


Figure B.1: Continued. Model 1.

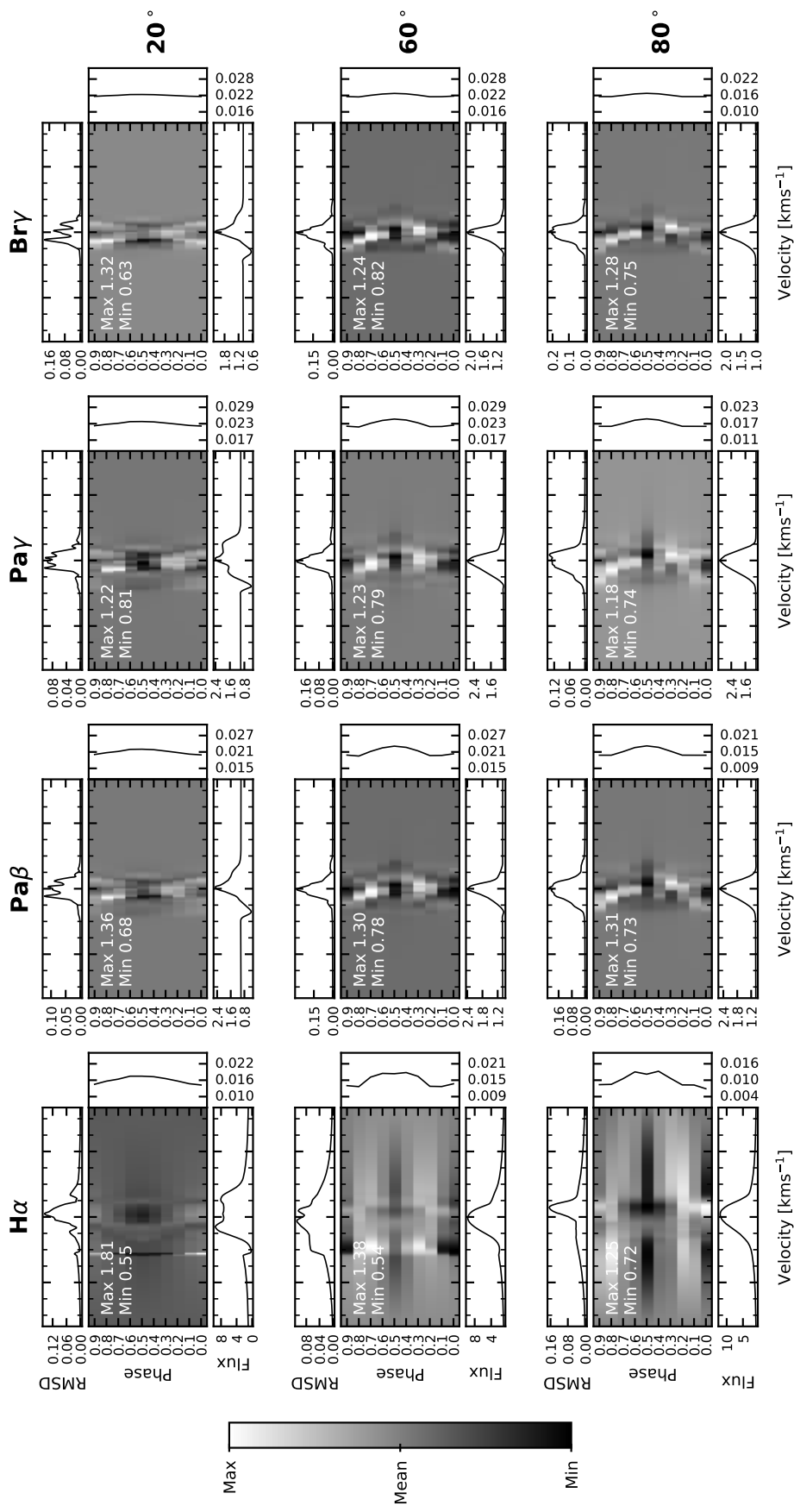


Figure B.1: Continued. Model 2.

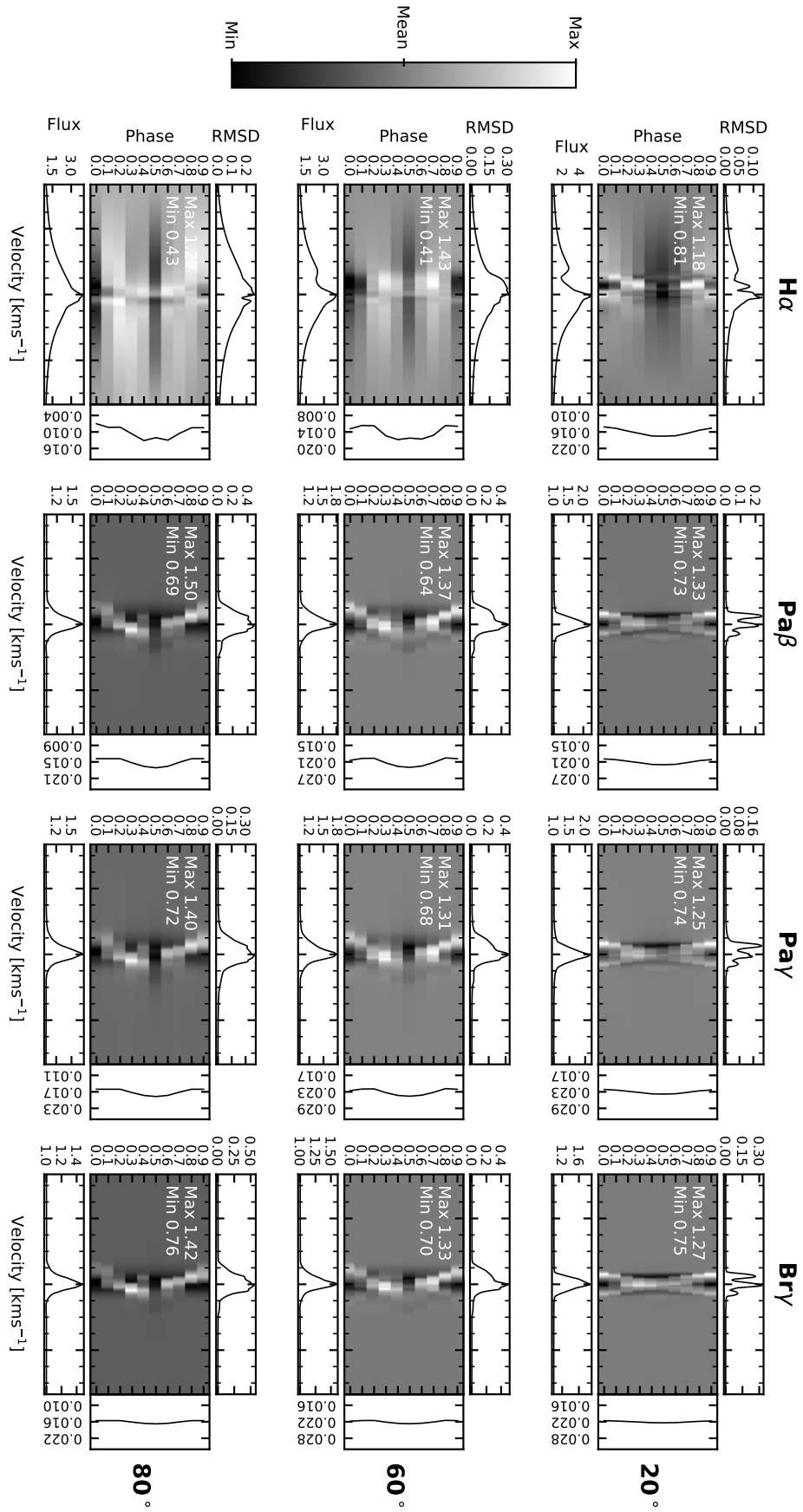


Figure B.1: Continued. Model 3.

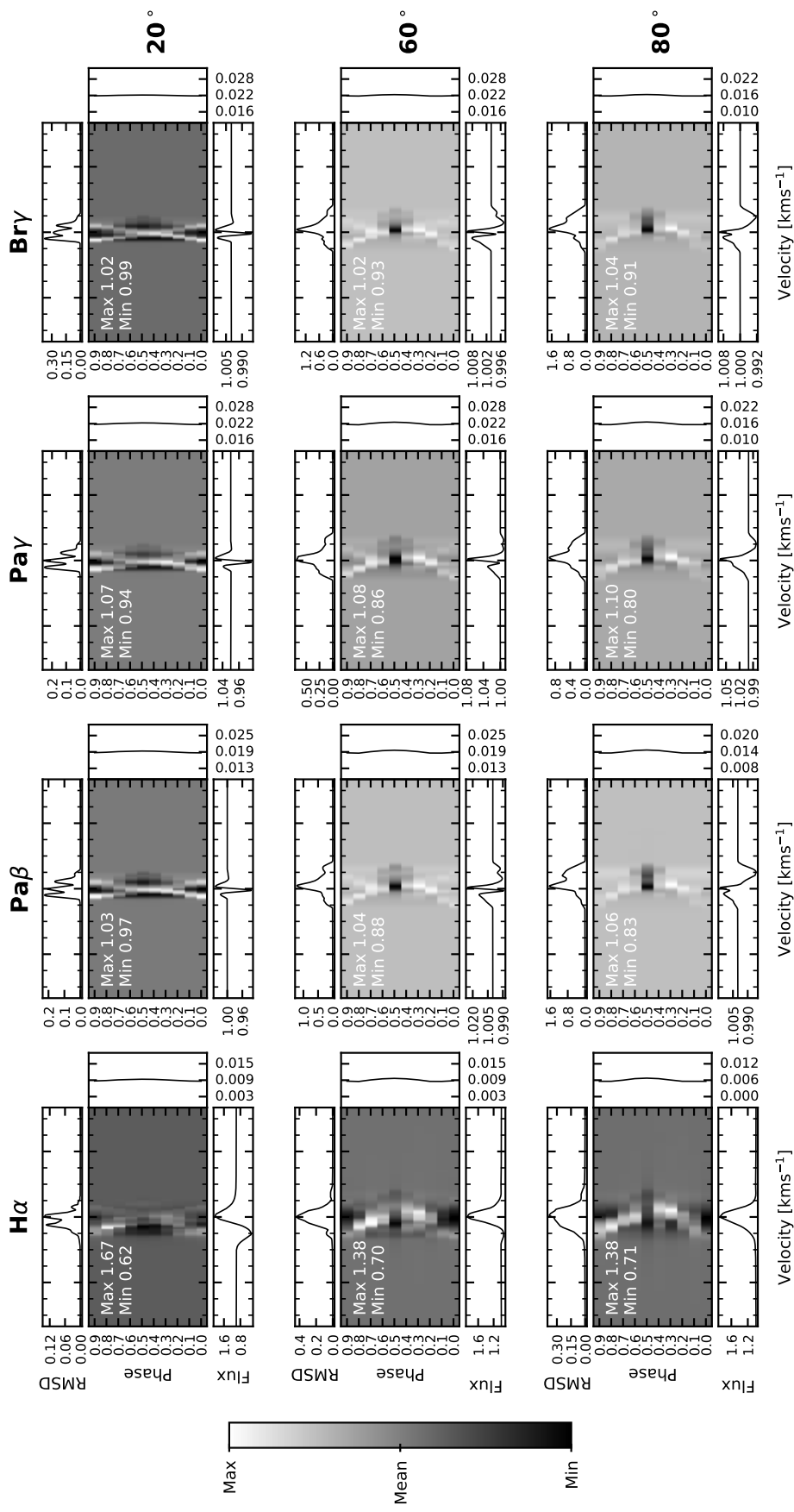


Figure B.1: Continued. Model 4.

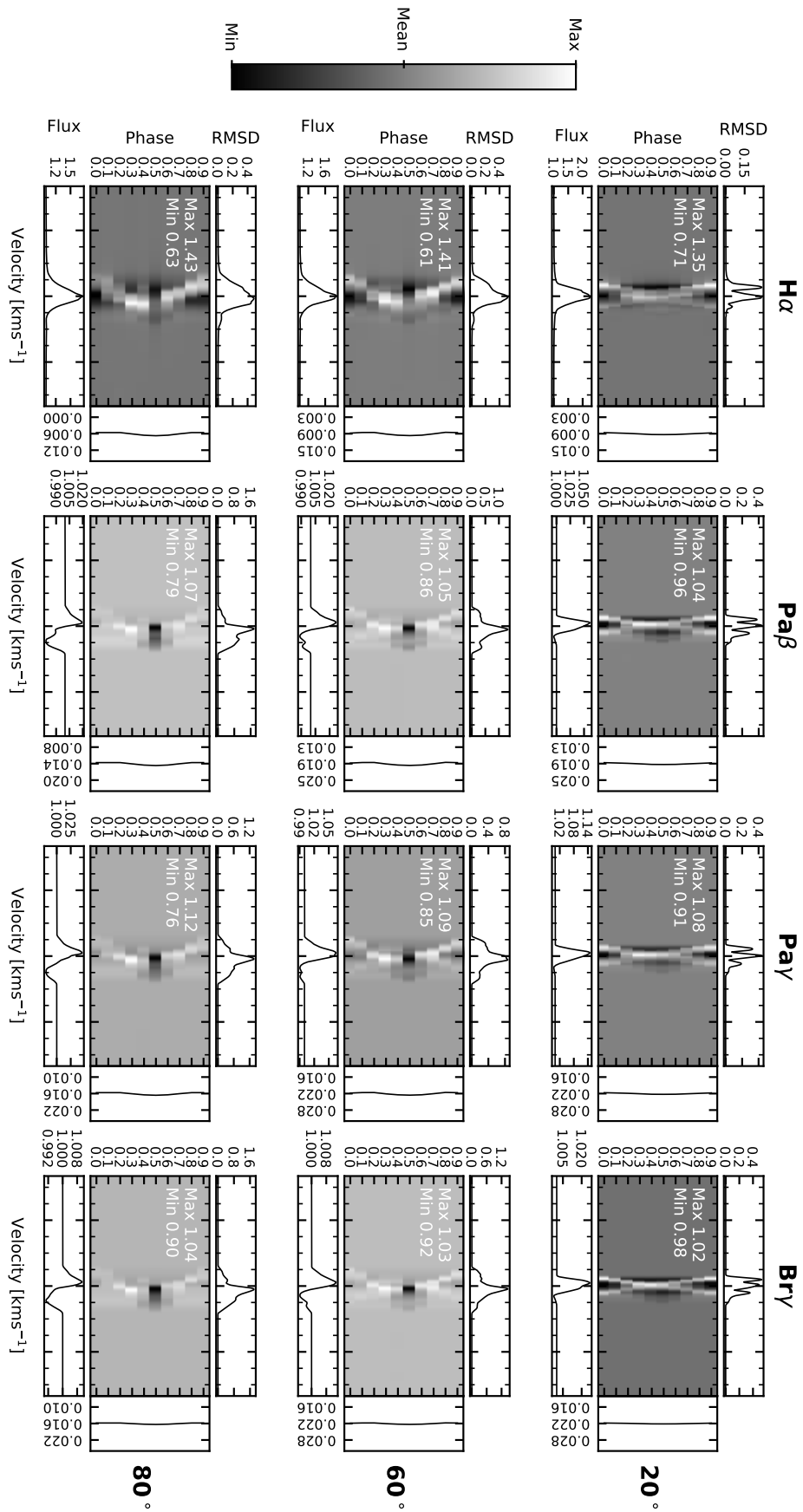


Figure B.1: Continued. Model 5.

Appendix C

Auto-Correlation Maps

Auto-correlation maps of the 3D T Tauri models with non-axisymmetric accretion and wind that are presented in Chapter 5.

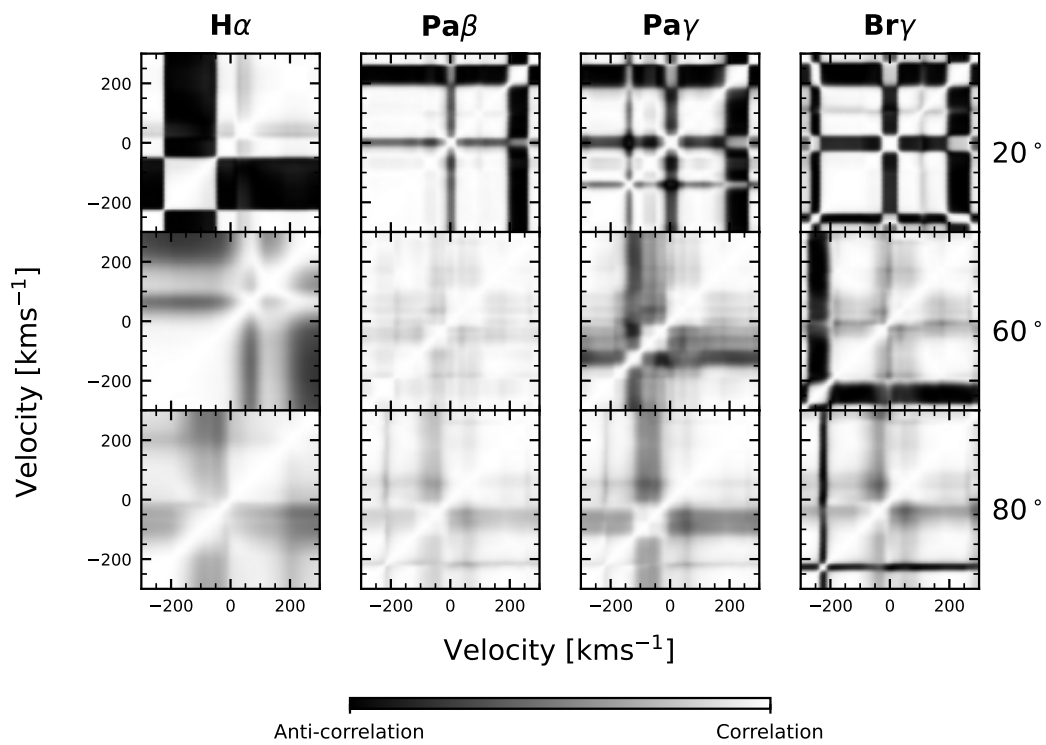


Figure C.1: Auto-correlation map for model 0. White areas correspond to a strong correlation and black areas strong anti-correlation. The images are symmetrical along the x-y diagonal.

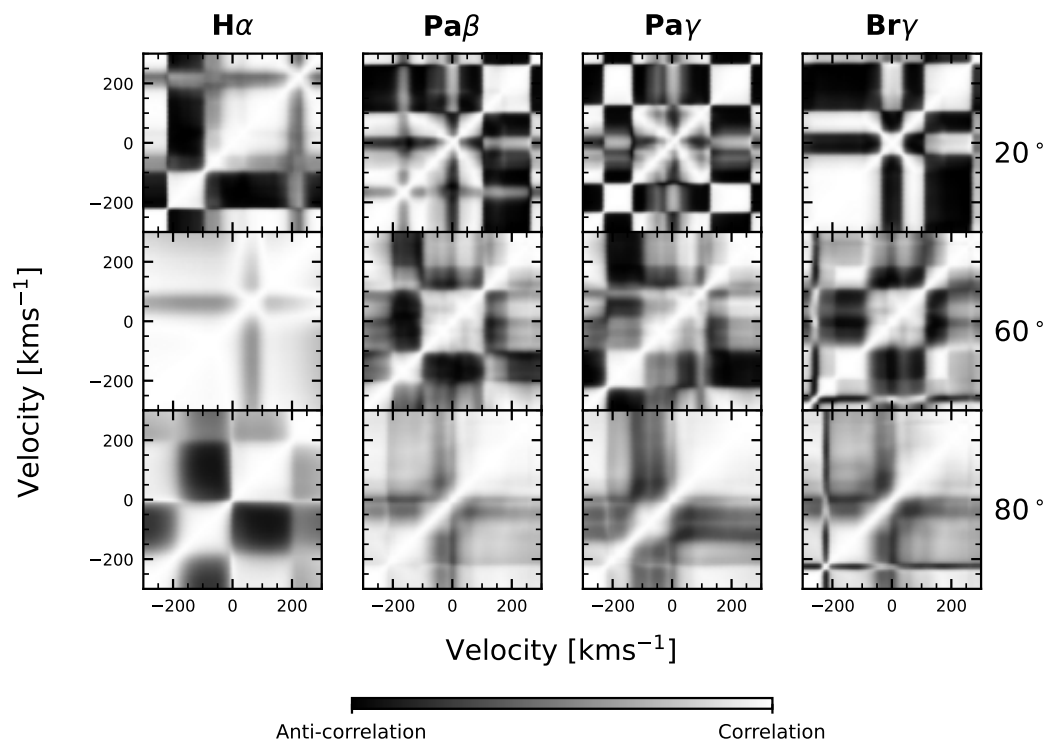


Figure C.2: Model 1

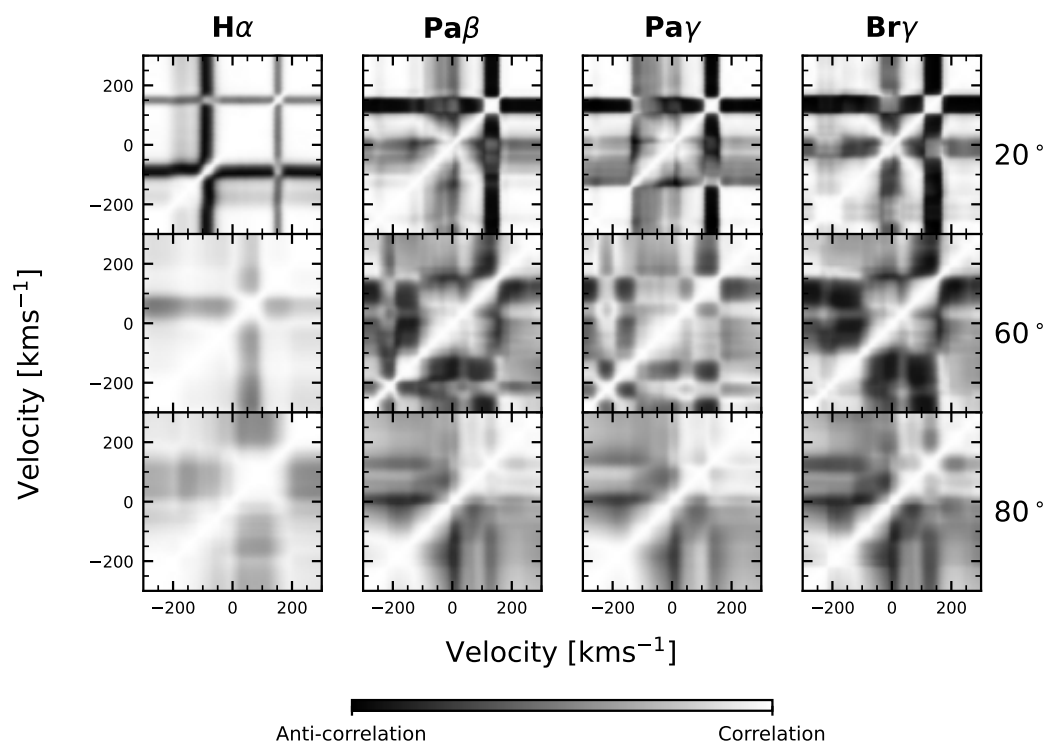


Figure C.3: Model 2

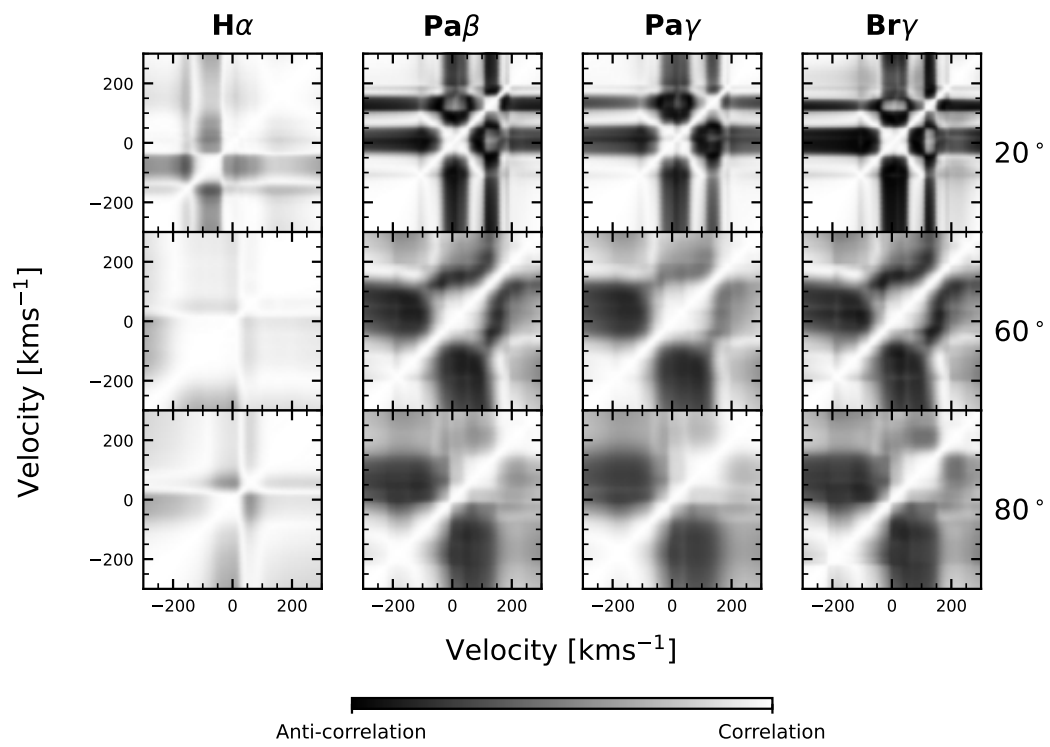


Figure C.4: Model 3

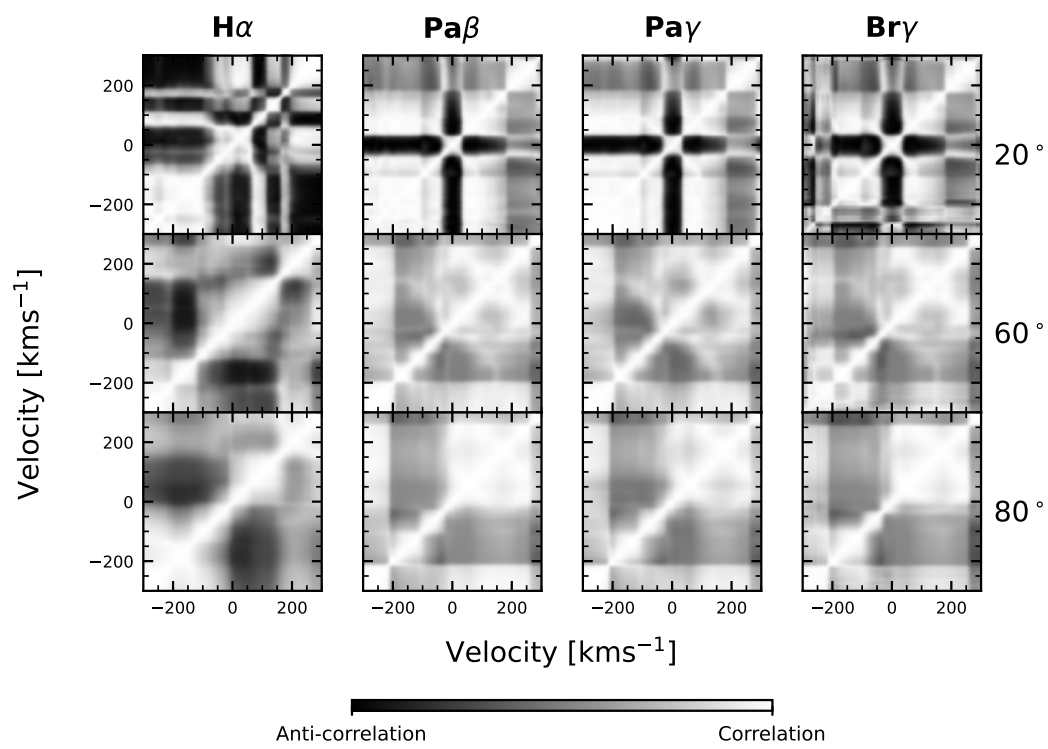


Figure C.5: Model 4

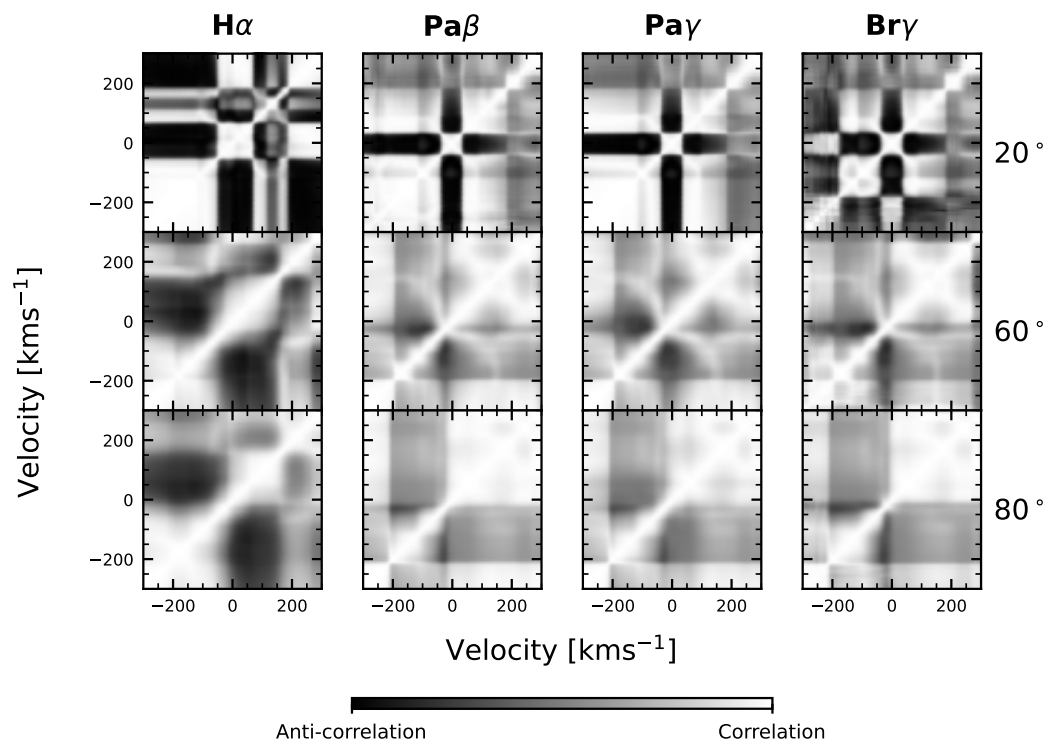


Figure C.6: Model 5